Characterization of Spot Weld Failure within Weld Groups under Predominantly Shear Loading

by

Cameron Jeffrey Tolton

A thesis

presented to the University of Waterloo

in fulfilment of the

thesis requirement for the degree of

Master of Applied Science

in

Mechanical and Mechatronics Engineering

Author's Declaration

I hereby declare that I am the sole author of this thesis. This is a true copy of the thesis, including any required final revisions, as accepted by my examiners.

I understand that my thesis may be made electronically available to the public.

Abstract

This thesis examines the failure behaviour of spot welded connections in components using three different aluminium-silicon coated hot stamped steels, Ductibor® 500-AS, Ductibor® 1000-AS, and Usibor® 1500-AS, with 1.2 mm and 1.6 mm sheet thicknesses. Spot weld connections are first characterized using single spot weld experiments. A novel experiment is then developed to characterize weld failure propagation within groups of welds under predominantly shear loading conditions. The experiments are modelled to evaluate how a calibrated weld failure model from single spot weld test data performs in predicting spot weld group response.

Tensile lap shear and cross tension single spot weld experiments were conducted under quasi-static conditions, according to the AWS D8.9M:2012 standard, for all materials and thicknesses considered in this work. Recorded force *versus* crosshead displacement curves and integrated absorbed energy *versus* crosshead displacement are reported for all single spot weld experiments. The higher strength materials, Ductibor® 1000-AS and Usibor® 1500-AS, exhibited brittle weld failure modes and thus absorbed almost no energy following failure initiation. The lap shear experiments showed similar levels of spot weld strength, around 15 kN, for all 1.2 mm specimens and approximately 20-26 kN for the 1.6 mm lap shear specimens. The cross tension experiments showed similar strength for the Ductibor® 500-AS and Ductibor® 1000-AS specimens, 7 kN for the 1.2 mm thickness and 12 kN for the 1.6 mm thickness. The peak loads for the Usibor® 1500-AS cross tension specimens were approximately 50% of the loads for the other two materials. The Ductibor® 500-AS specimens absorbed the most energy for the lap shear and the cross tension experiments which is attributed to increased parent metal deformation and more ductile weld failure characteristics.

A new mechanical test, termed the Caiman Mode III, was developed to promote shear failure within a group of spot welds in a manner similar to a mode III fracture mechanics specimen. A custom rail design using U-channels, that is fabricated in stages, is selected. The Caiman Mode III experiments are tested under quasi-static and dynamic loading rate conditions to examine the mechanical properties of spot welds in a structure in which the applied load can be shared across multiple spot welds. The Caiman Mode III experiments further showed that the three materials have similar peak loads and that the Ductibor® 500-AS spot welds have the highest toughness and most absorbed energy of the three materials tested. Spot weld failure timing was recorded to

characterize the extent and rate of spot weld failure propagation in the Caiman Mode III experiments. High speed thermal imagery was applied to determine precise spot weld failure times in both the quasi-static and the dynamic Caiman Mode III experiments since it was difficult to identify failure of specific weld from the force-displacement data. The Ductibor® 500-AS exhibited a slower rate of failure propagation through the weld group compared to the two higher strength alloys.

Two different spot weld material models were considered in numerical simulations of the single spot weld and Caiman weld group experiments. The first weld material model, *MAT_100_DA, is used commonly by industry in car crash simulations, while the second weld material model, *MAT_240, used a cohesive zone approach that enables more direct control over the spot weld post-failure behaviour. Both weld material models were calibrated to the single spot weld experiments with respect to force *versus* displacement. The *MAT_100_DA model showed no post-failure unloading response for the normal-tensile loading condition, thus under predicting the total absorbed energy. The *MAT_240 model enabled more accurate post-failure unloading for all of the single spot weld conditions tested.

Simulations of the Caiman Mode III experiments were performed to validate the calibrated single spot weld models. The *MAT_240 simulations and the *MAT_100_DA simulations show similar predictions for each material condition except for the Ductibor® 500-AS 1.6 mm model. The numerical simulations of the Caiman Mode III experiments were able to qualitatively predict the overall behaviour of the Caiman Mode III experiments, including aspects such as high initial load followed by load drops at each sequential weld failure and load drop off, as well as progressive failure propagation through the weld group. However, the simulations showed inconsistent peak force and energy absorption accuracy results when examining the results of different material and thickness simulations. The Caiman Mode III simulation inconsistencies for both material models suggests that the differences between the predictions and the experiments may be from physical inconsistencies between the design and the as-fabricated final specimens. Edge tear out failure was observed in the Caiman Mode III experiments due to 10 mm nugget-to-edge distance while the spot weld models were calibrated from single spot weld experiments with 20 mm weld-edge distance that exhibited button pull out failure instead.

Acknowledgements

I would like to thank my supervisor, Dr. Michael Worswick, for the opportunity to work on this project and to be a member of the Waterloo Forming and Crash Lab. The guidance that Dr. Worswick have given me has been invaluable towards both my professional development as an engineer and my personal development. Dr. Clifford Butcher has been very generous with his time and assistance in answering any of my questions, particularly with obscure problems in my numerical simulations. Dr José Imbert-Boyd has been an excellent mentor in the lab and played a key role in completing the dynamic testing portion of my thesis experiments. Cameron O'Keeffe, AKA "Mode I Cameron", was a huge help in getting started and laid the groundwork for the spot weld group testing that my work has built off of.

I'd like to acknowledge the project's supporting organizations: Honda R&D Americas, Promatek Research Center, ArcelorMittal, as well as The Natural Sciences and Engineering Research Council of Canada, the Canada Foundation for Innovation, the Ontario Research Fund, Ontario Centres of Excellence, the Ontario Advanced Manufacturing Consortium.

The assistance from Eckhard Budziarek, Tom Gawel, Andy Barber, Neil Griffett, and Doug Hirst ensuring that my experiments go smoothly, and the lab equipment is in tiptop shape is greatly appreciated.

A big shoutout to Matt Tummers who has become a close friend through our time at the university and travelling, and to Sante DiCecco who has also become a good friend despite, or perhaps because of, accounting for the large majority of my time spent stalling. I would also like to thank fellow past and present group members Ryan George, Amir Zhumagulov, Armin Abedini, Pedram Samadian, Cale Peister, Kaab Omer, Alireza Mohamadizadeh, and the rest whom are too many to name, for their advice and willingness to help in both the office and lab.

Thank you to my parents and family for their continued support to help me get to where I am.

Lastly, to Emilia, my fiancée, who has been by my side from start to end and whose support never wavered.

Table of Contents

Author's Declaration ii

Abstract iii

Acknowledgements v

List of Figures ix

List of Tables xv

1. Introduction 1

1.1. Motivation 1

1.2. Hot Stamping 4

1.3. Hot Stamped Steel Material Properties 6

1.4. Resistance Spot Welding Process 7

1.5. Standard spot weld characterization test methods 10

1.5.1. Lap shear 11

1.5.2. Cross tension 11

1.6. Advanced spot weld characterization test methods 12

1.6.1. Coach peel 12

1.6.2. KS-II 13

1.7. Weld group tests 14

1.7.1. H-Specimen 14

1.7.2. T-Joint Test 15

1.7.3. Caiman Mode I 15

1.8. Spot weld numerical characterization 17

1.8.1. *MAT_100/*Mat_Spotweld 19

1.8.1.1. Force resultant-based failure 19

1.8.1.2. Stress-based failure 20

1.8.1.3. User subroutine failure 22

1.8.1.4. Post-failure damage 22

1.8.1.5. Mesh Effects 23

1.8.2. *MAT_100_DA/*MAT_SPOTWELD_DIAMLERCHRYSLER 24

1.8.3. *MAT_240/*Mat_Cohesive_Mixed_Mode_Elastoplastic_Rate 26

1.8.4. *Constrained_Interpolation_Spotweld 28

1.9. Simulation of HAZ Material Failure 30

1.9.1. HAZ Properties from Hardness Scaling 31

1.9.2. HAZ Properties from Gleeble 33

1.9.3. HAZ Properties from Miniature Specimens 34
1.10. Simulation of Weld Groups (Structural Connections) 34
1.11. Current Work 37
2. Specimen Preparation 39
2.1. Furnace 39
2.2. Press 39
2.3. Material Preparation 40
2.4. Spot weld process 42
3. Single spot weld characterization 44
3.1. Single spot weld specimens 44
3.1.1. Lap shear 45
3.1.2. Cross tension 45
3.2. Single spot weld mechanical performance 46
3.2.1. Lap shear Test Results 47
3.2.2. Cross tension Test Results 50
3.3. Numerical model development 55
3.3.1. Parent metal constitutive models 56
3.3.2. Weld coupon mesh development 58
3.3.2.1. MAT_100_DA 60
3.3.2.2. MAT_240 62
3.4. Calibration Procedure 63
3.4.1. *MAT_100_DA Calibration 63
3.4.2. *MAT_240 Calibration 64
3.5. Single spot weld simulation results 66
3.5.1. Post-Failure Energy Absorption Correlations 71
4. Development of a shear group spot weld characterization test 74
4.1. Caiman Mode III Design 75
4.1.1. Initial Design Options 76
4.1.2. Custom U-channel Design 78
4.1.3. Validation Specimens 83
4.1.4. Final Design 87
4.2. Quasi-static testing methodology 88
4.3. Dynamic testing methodology 90
5. Caiman Mode III Results 93
5.1. Caiman Mode III mechanical performance 93

5.1.1. Quasi-Static Response 93
5.1.2. Dynamic 100
5.2. Caiman Mode III numerical model development 106
5.3. Caiman Mode III simulation results 109
6. Discussion / Analysis 119
6.1. Comparison of single spot weld and Caiman peak forces 119
6.2. Comparison of single spot weld and Caiman absorbed energy 120
6.3. Effects of interfacial weld failure 120
6.4. Spot weld nugget to edge distance 122
6.5. Loading rate effects in the Caiman experiments 123
7. Conclusions and recommendations 127
References 131
Appendix A 137
Material Card Parameters 137
Appendix B 138
Caiman Mode III 1.2 mm Drawing Package 138
Caiman Mode III 1.6 mm Drawing Package 144

List of Figures

Figure 1: Left) Actual and projected changes in the absolute amount and percentage of the total weight in North American vehicles [2]. Right) Steel strength ductility diagram [3]. 2

Figure 2: 2016 Honda Pilot body construction and high-strength steel content. [11] 3

Figure 3: (a) Top-hat channel section; (b) square channel section. Adapted from Tarigopula et al. [12]..... 3

Figure 4: Direct hot-stamping process diagram. [18] 5

Figure 5: Left) Iron-carbon diagram labelled with expected equilibrium phases for different combinations of carbon content and temperature [19, p. 319]. Right) The complete isothermal transformation diagram for an iron–carbon alloy of eutectoid composition: A, austenite; B, bainite; M, martensite; P, pearlite [19, p. 364]. 5

Figure 6: Generic RSW process with optional features. [35, p. 2] 7

Figure 7: Spot weld HAZ microstructure with respective peak temperatures shown on equilibrium diagram [39, p. 403]. 9

Figure 8: Tensile lap shear assembly and schematic of gripping in the tensile frame. 11

Figure 9: Cross tension assembly geometry and fixture schematic. 12

Figure 10: Coach peel test geometry (left) and modified KS-II test for peel (right). Arrows indicate direction of applied loading. 13

Figure 11: Different load cases for the KS-II test. Arrows indicate direction of applied loading. 13

Figure 12: H-specimen geometry used for multiple spot weld fatigue tests for (a) shear, and (b) peel, loading conditions [60] 14

Figure 13: T-joint model [50]. 15

Figure 14: Caiman Mode I [51]. 15

Figure 15: Force (left) and energy (right) versus pin displacement plots for quasi-static Caiman Mode I tests [51]. 16

Figure 16: Sample of four, eight, or sixteen solid elements used to construct a single spot weld assembly.[66] 19

Figure 17: Spot weld failure and damage. [73] 25

Figure 18: *MAT_240 Trilinear mixed mode traction-separation law. [67] 26

Figure 19: Tests and CAE correlation using *MAT_240 at coupon level of different loading conditions for self-piercing rivets (left [62] and right [72]). 27

Figure 20: Tests and CAE correlation using *MAT_240 at coupon level of different loading conditions for spot welds. [65] 27

Figure 21: Left) Schematic representation of *Constrained_Interpolation_Spotweld [55]. Right) Flow curve with damage and failure plastic equivalent displacements [52]. 29

Figure 22: Simulations results of KS-II and peeling tests with the *Constrained_Interpolation_Spotweld (left) [52] and the modified *Constrained_Interpolation_Spotweld (Model 2) (right) [79]. 30

Figure 23: Left) CAE-level finite element model with 2 mm shell element size, adapted from [70]. Right) Detailed model of spot weld with three sub-zones [82]. 31

Figure 24: Usibor® 1500-AS flow curves; Base metal tensile specimen (solid black), hardness scaled base metal (dashed black), Gleeble thermo-simulated tensile specimen (red). [57] 32

Figure 25: Force-displacement curves for experimental cross tension test and simulation model. Simplified FEA model (left) [70] and detailed model (right) [87]. 33

Figure 26: T-joint measured and predicted force-displacement responses from (a) Seeger et al. [50] (b) Yang et al. [56] (c) Bier and Sommer [52] (d) May et al. [63]. 36

Figure 27: Caiman Mode I measured and predicted force-displacement response for quasi-static tests [51]. Fully hardened condition shown on left and softened condition (using 700° in-die heating in the flange region) shown on right. 37

Figure 28: Picture of flat die with cooling channels present 41

Figure 29: Image of lower hot stamping rail die binder, punch, and cooling tubes. 42

Figure 30: Micrograph images of spot welds after failure (A) PHS600 (Ductibor® 500-AS) no expulsion; (B) PHS600 (Ductibor® 500-AS) with expulsion; (C) PHS1500 (Usibor^3 1500-AS) no expulsion; (D) PHS1500 (Usibor® 1500-AS) with expulsion. 43

Figure 31: Tensile lap shear assembly geometry and schematic of gripping in the tensile frame. [36] 45

Figure 32: Cross tension assembly geometry and fixture schematic. [36] 46

Figure 33: Possible spot weld fracture modes. [35] 46

Figure 34: Lap shear force versus displacement data for 1.2 mm specimens. 47

Figure 35: Lap shear force versus displacement data for 1.6 mm specimens. Dashed lines showed expulsion. 48

Figure 36: Lap shear energy absorbed versus displacement data for 1.2 mm specimens. 48

Figure 37: Lap shear energy absorbed versus displacement data for 1.6 mm specimens. Dashed lines showed expulsion. 48

Figure 38: Ductibor® 500-AS 1.6 mm lap shear specimen exhibiting expulsion. Burr from laser trimming expanded in detail. 49

Figure 39: Ductibor® 500-AS 1.6 mm lap shear specimen exhibiting double shared pull out failure mode (not classified by AWS). 50

Figure 40: Cross tension force versus displacement data for 1.2 mm specimens. Dashed lines showed expulsion. 51

Figure 41: Cross tension force versus displacement data for 1.6 mm specimens. Dashed lines showed expulsion. 52

Figure 42: Cross tension energy absorbed versus displacement data for 1.2 mm specimens. 52

Figure 43: Cross tension energy absorbed versus displacement data for 1.6 mm specimens. 52

Figure 44: Close up of the Ductibor® 500-AS 1.6 mm cross tension test showing shared asymmetric pull out. 53

Figure 45: Top Left) Coupon deformation showing vertical displacement measurement. Bottom Left) Al-Si coating missing where the coupon is pulled out of the clamping fixture. Right) Al-Si coating flakes off due to coupon contact with the clamping bolt. 54

Figure 46: Material flow curves for Ductibor®500-AS [27], Ductibor®1000-AS [101], and Usibor®1500-AS [4]. Curves of the same material show rate-sensitivity by increasing orders of magnitude from bottom to top..... 57

Figure 47: Fracture loci (left) and GISSMO mesh regularization factors (right) of Ductibor® 500-AS [104], Ductibor® 1000-AS [101], and Usibor® 1500-AS [22]. 58

Figure 48: Cross tension model mesh. 59

Figure 49: Close up view of the cross tension mesh showing the clamping fixture components and bolt ring. 60

Figure 50: Tensile lap shear model mesh. Top (red) coupon elements removed to show solid weld elements (green). 60

Figure 51: Effect of the cohesive element mesh patterns used to model a single spot weld nugget using *MAT_240. Data shown is for Ductibor® 500-AS 1.6 mm lap shear experiments. 63

Figure 52: Relation between *MAT_240 input parameters and resulting Traction-Separation law for the normal-tensile case. 65

Figure 53: a) Ductibor® 1000-AS 1.6 mm cross tension experimental force vs. displacement and output of *MAT_240 numerical model data confirming input values; b) Partial cross-section view of the *MAT_240 cross tension model showing applied forces; c) *MAT_240 normal-tensile traction-separation law; d) Measurement of coupon deformation from post-test coupon. 66

Figure 54: Tensile lap shear 1.2 mm and 1.6 mm experiments (red, blue, and purple lines) and numerical model simulation results (black lines). 68

Figure 55: Cross tension 1.2 mm and 1.6 mm experiments (red, blue, and purple lines) and numerical model simulation results (black lines). 69

Figure 56: Peak force data for lap shear (left) and cross tension (right) experiments and simulations. 70

Figure 57: Total energy absorbed for lap shear (left) and cross tension (right) experiments and simulations. 70

Figure 58: Ductibor® 500-AS 1.2 mm experiment, *MAT_100_DA, and *MAT_240 force vs. displacement response for (a) cross tension; and (b) lap shear. Red shaded areas indicate post-failure absorbed energy predicted by numerical models. 71

Figure 59: Post-failure energy absorption versus input parameter value for each simulation. (a) Lap shear simulations with *MAT_100_DA model; (b) Cross tension simulations with *MAT_240 model; (c) Lap shear simulations with *MAT_240 model. 72

Figure 60: Left) Tensile frame interface fixtures for quasi-static testing. Right) Crash sled fixtures for dynamic testing. 76

Figure 61: Left) Initial Caiman Mode III design idea to rotate a double hat channel to create shear stress weld failures. Arrows indicate applied load, F, on each hat channel. Right) Simulation of the initial design using Ductibor® 500-AS material showing the twisting and buckling occurring at the first spot weld on each flange. 77

Figure 62: Left) Initial design iteration showing the mirrored hat-channel rail. Fixed rails and desired weld failure indicated with black arrows. Impacted rails and direction are indicated with red arrows. Right) Simulation of the mirrored hat-channel rail design. 78

Figure 63: Interference between lower weld electrode and sidewalls when joining two overlapping die-formed U-channels. 79

Figure 64: Top) Custom U-Channel rail components. Bottom) Three step joining operations and final outer dimensions with spot weld spacing. 80

Figure 65: Left) Caiman Mode III Rev 1 simulation showing von Mises equivalent stress contour plot. Right) Complete U-channel buckling of the Caiman Mode III Rev 1 simulation. 81

Figure 66: Cross section of the custom U-channel design revisions. Centre of Mass symbol indicates location of the centroid for each cross section. 82

Figure 67: Simulation results of the Caiman Mode III Rev 2.1 (left) and Rev 2.2 (right) design options. Measurements show maximum out-of-plane displacement of the side walls during simulation. All models are shown at pin displacement = 118 mm. 83

Figure 68: Caiman Mode III Rev 2.2 validation specimen, labelled UW#2. 84

Figure 69: Caiman Mode III Rev 2.2 post-test validation specimen UW#1. 84

Figure 70: Caiman Mode III Rev 3 specimen, labelled UW#3. 85

Figure 71: Caiman Mode III Rev 3 post-test validation specimen UW#3. 85

Figure 72: Caiman Mode III Rev 4 specimen, labelled UW#2. 86

Figure 73: Caiman Mode III Rev 4 post-test validation specimen UW#2. 86

Figure 74: Caiman Mode III Rev 5 specimen, labelled UW#6, before and after testing. 87

Figure 75: Force (solid lines) and Absorbed Energy (dashed lines) versus crosshead displacement data for validation specimen revisions. 88

Figure 76: Quasi-static testing setup showing the group spot weld configuration. Thermal camera not seen here. 89

Figure 77: Left) Gier Dunkle DB-100 Reflectometer; Right) Emissivity measurements for Usibor® 1500 and Ductibor® 500. 90

Figure 78: Dynamic testing setup. Metal-halide floodlighting systems, Cameras 2 and 3, DAQ, and control computers not shown. 91

Figure 79: Comparison of measured and calculated sled displacement. 92

Figure 80: Caiman Mode III 1.2 mm quasi-static force versus displacement. 94

Figure 81: Caiman Mode III 1.6 mm quasi-static force versus displacement. 94

Figure 82: Average Caiman Mode III quasi-static energy absorbed versus displacement data for 1.2 mm (dashed lines) and 1.6 mm (solid lines) specimens. Experimental repeats are shown with thin faded lines. 95

Figure 83: Side view of post-mortem Caiman Mode III specimens. 96

Figure 84: End view of post-mortem Caiman Mode III specimens. 96

Figure 85: Caiman Mode III Usibor® 1500-AS 1.2 mm specimen exhibiting significant expulsion. 97

Figure 86: Left) Compact Tension specimen showing the updated crack size, 'a'. Adapted from ASTM E1820-15a [111]. Right) Caiman Mode III specimen drawing showing 'crack' extension measure, 'a'. . 98

Figure 87: Quasi-static Caiman Mode III thermal images showing different failure modes. Colour scale in °C. 98

Figure 88: Caiman Mode III quasi-static 'crack' extension growth. (a) 1.2 mm specimens; (b) 1.6 mm specimens. 99

Figure 89: Caiman Mode III Ductibor® 500-AS 1.6 mm quasi-static specimen that buckled. 100

Figure 90: First and last high-speed image of a Caiman Mode III dynamic experiment from each material and thickness 101

Figure 91: Caiman Mode III dynamic Ductibor® 500-AS wall-side force versus displacement. 102

Figure 92: Caiman Mode III dynamic Ductibor® 1000-AS wall-side force versus displacement. 102

Figure 93: Caiman Mode III dynamic Usibor® 1500-AS wall-side force versus displacement. 102

Figure 94: Caiman Mode III dynamic high-speed images of Usibor® 1500-AS 1.2 mm specimen showing pin and sled contact. Left) Initial contact; Centre) Loss of contact; Right) Secondary contact. 103

Figure 95: Average Caiman Mode III dynamic energy absorbed versus crush distance for 1.2 mm (dashed lines) and 1.6 mm (solid lines) specimens. Experimental repeats are shown with thin faded lines. 104

Figure 96: Thermal images captured for the Caiman Mode III dynamic experiments. Colour scale in °C. 105

Figure 97: Caiman Mode III dynamic 'crack' extension growth. (a) 1.2 mm specimens; (b) 1.6 mm specimens. 106

Figure 98: DP 980 experimental strain rate data and Cowper-Symonds (CS) constitutive model fit. [112] 107

Figure 99: Caiman Mode III numerical model mesh. Rigid components coloured grey. 108

Figure 100: Caiman Mode III numerical model tied contact locations. One quarter of the specimen shown here. 109

Figure 101: Caiman Mode III *MAT_100_DA simulation final frames. 110

Figure 102: Caiman Mode III *MAT_240 simulation final frames. 110

Figure 103: Caiman Mode III Ductibor® 500 experimental force versus displacement and *MAT_100_DA model output. 111

Figure 104: Caiman Mode III Ductibor®1000 experimental force versus displacement and *MAT_100_DA model output. 111

Figure 105: Caiman Mode III Usibor® 1500 experimental force versus displacement and *MAT_100_DA model output. 111

Figure 106: Caiman Mode III Ductibor® 500 experimental force versus displacement and *MAT_240 material model output. 112

Figure 107: Caiman Mode III Ductibor® 1000 experimental force versus displacement and *MAT_240 material model output. 112

Figure 108: Caiman Mode III Usibor® 1500 experimental force versus displacement and *MAT_240 material model output. 112

Figure 109: Peak Force data (left) and Total Energy Absorbed data (right) for Caiman Mode III experiments and simulations. 114

Figure 110: Caiman Mode III 1.2 mm quasi-static experiments (red, blue, and purple lines) and numerical model simulation (black lines) crack extension measurements. 115

Figure 111: Caiman Mode III 1.6 mm experiments (red, blue, and purple lines) and numerical model simulation (black lines) crack extension measurements. 115

Figure 112: Close up side view of Caiman Mode III Ductibor® 500-AS 1.6mm simulation showing side wall slippage.. 117

Figure 113: End view of Ductibor® 500-AS 1.2 mm Caiman Mode III quasi-static experiment and simulation end-collapse. 117

Figure 114: Total energy absorbed for Tensile Lap Shear and Caiman Mode III experiments. 120

Figure 115: Left) First to fourth spot welds post-failure for left and right sides of the Caiman Mode III Ductibor® 1000-AS 1.6 mm quasi-static specimens. Right) Corresponding experimental force versus displacement curves. 121

Figure 116: Ductibor® 1000-AS 1.6 mm quasi-static specimen #4 showing worse-case spot weld nugget to edge distance. 122

Figure 117: Usibor® 1500-AS 1.6 mm Caiman Mode III quasi-static specimen showing tear out failure... 123

Figure 118: Peak load data from Caiman Mode III quasi-static and dynamic experiments. 124

Figure 119: Caiman Mode III Ductibor® 500-AS quasi-static and dynamic 'crack' extensions. 125

Figure 120: Caiman Mode III Ductibor® 1000-AS quasi-static and dynamic 'crack' extensions. 125

Figure 121: Caiman Mode III Usibor® 1500-AS quasi-static and dynamic 'crack' extensions. 126

List of Tables

Table 1: ArcelorMittal material minimum characteristic values after hot stamping and paint baking simulation. [18] 6

Table 2: Maximum weight percent chemical composition of the three hot stamped steels considered and calculated carbon equivalent contents, from ArcelorMittal [18] 41

Table 3: Resistance spot weld schedule. 42

Table 4: Single spot weld test matrix. 44

Table 5: Lap shear geometry dimensions, all dimensions in mm. 45

Table 6: Cross tension geometry dimensions, all dimensions in mm. 46

Table 7: Summary of average data values for single spot weld tensile lap shear tests. 47

Table 8: Summary of average data values for single spot weld cross tension tests. 51

Table 9: *MAT_100_DA keyword card sample with Usibor® 1500-AS 1.2 mm weld properties. 61

Table 10: *Define_Connection_Properties keyword card example with Usibor® 1500-AS 1.2 mm weld properties. 61

Table 11: *MAT_240 keyword card example with Usibor® 1500-AS 1.2 mm weld properties. 62

Table 12: *MAT_240 T-S Law defining parameter descriptions. 64

Table 13: Lap shear single spot weld numerical simulation prediction and error results. 67

Table 14: Cross tension single spot weld numerical simulation prediction and error results. 67

Table 15: Ductibor® 1000-AS von Mises equivalent stress at time of failure for *MAT_100_DA cross tension and lap shear experiments, and the *MAT_100_DA yield stress parameter. 73

Table 16: Caiman Mode III quasi-static experimental data summary. 93

Table 17: Caiman Mode III dynamic experimental data summary. 101

Table 18: Caiman Mode III quasi-static numerical simulation prediction and error results. 113

Table 19: Average tensile lap shear peak forces and Caiman Mode III peak forces with percent differences in brackets. 119

Table 20: Caiman Mode III Ductibor® 1000-AS weld failure mode count. 124

Table 21: *MAT_100_DA material card parameters. 137

Table 22: *DEFINE_CONNECTION_PROPERTIES material card parameters. 137

Table 23: *MAT_240 material card parameters. 137

1. Introduction

1.1. Motivation

The Environment Protection Agency (EPA) and the National Highway Traffic Safety Administration (NHTSA) require manufacturers of passenger cars and light trucks to meet certain fuel consumption standards for vehicles sold in the United States. The fuel consumption is set through the Corporate Average Fuel Economy (CAFE) program. The CAFE program has been in effect since 1978 and the latest extension covers the model years (MY) 2017 to 2025. The program is estimated to save four billion barrels of oil and reduce the emission of greenhouse gases by the equivalent of approximately two billion metric tons over the lifetimes of the 2017-2025 MY vehicles [1].

One approach that vehicle manufacturers are investigating to reduce emissions is through vehicle light-weighting. Reducing the overall weight of the vehicle will require less energy, and thus burn less fuel, to operate the vehicle. While vehicle light-weighting has many facets, in this work the focus is on the light-weighting of automotive structures, i.e. the vehicle frame, through the development and application of higher strength materials. Increasing the strength of the material allows manufacturers to reduce the effective cross section of frame members while maintaining or improving the overall strength and safety of the structure.

To achieve weight savings through this method, manufacturers have been implementing Advanced High Strength Steels (AHSS) in vehicles. These alloys typically have higher strengths but do tend to have lower elongation, as shown in Figure 1. As the materials used in automotive applications increase in strength, it can be seen that there is an inverse relation with total elongation; as the materials become stronger the elongation decreases. This relationship limits the range of structural applications in which the highest strength materials can be used because forming parts with complex geometry is very difficult with such low total elongation values. Additionally, there will be lower energy absorption capacity due to the low ductility which can have negative effects on crash worthiness and passenger safety. Future material development for 3rd Gen AHSS grades, seen in the grey bubble labelled "3rd GEN AHSS" in Figure 1, is investigating different ways to maintain high tensile strength but increase the elongation through new chemistries, processing techniques, and material behaviour.

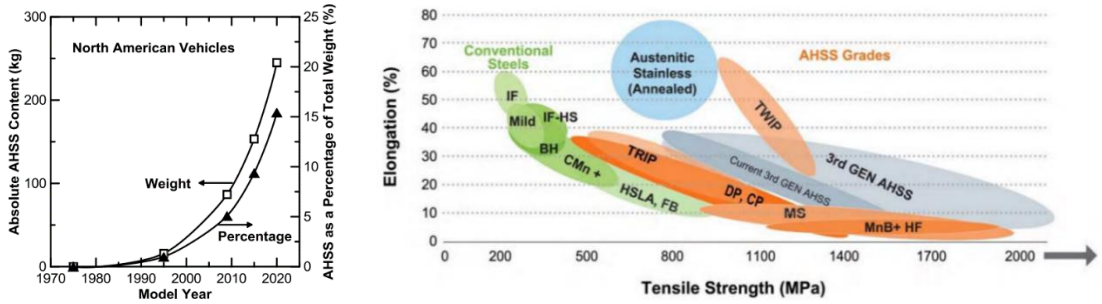

Figure 1: *Left) Actual and projected changes in the absolute amount and percentage of the total weight in North American vehicles* [2]. *Right) Steel strength ductility diagram* [3].

This thesis presents research that is a part of a larger effort investigating the application of hot stamped steels in the front end structure of automobiles. Hot stamped steels are among the highest tensile strength materials available, but also exhibit relatively low ductility. Typically, hot stamped steels have been limited to applications in which anti-intrusion is desired to protect the passenger compartment during a vehicle crash, such as in the vehicle door ring, seen in the red coloured sections in Figure 2. The passenger cabin is designed to be enclosed by a rigid shell that limits deformation and intrusion into the cabin (referred to as "intrusion protection") during crash events. The use of ultra high strength hot stamped steels in the front end structure, where a large amount of deformation is required for energy absorption, is a challenging task. Omer *et al.* [4] demonstrated that significant spot weld failure and the brittle behaviour of the martensitic UHSS material (UTS > 1,500 MPa) used in axial crush experiments led to catastrophic failure. Unstable or catastrophic failure is undesirable for front crash applications in vehicles where reliable energy absorption is required to design safe vehicles. Omer *et al.* [4] showed that tailoring properties via in-die-heating can lead to favourable crash performance. Múnera *et al.* [5] introduced Ductibor® 500 for Laser Welded Blanks to extend the application of hot stamp material to high energy absorption areas such as front and rear rails. More recent work by Peister [6] with Tailored Welded Blanks has demonstrated that somewhat lower strength hot stamped grades (UTS < 1,000 MPa) can absorb crash energy and may be suitable for front end structural applications.

With the increases in strength of materials being used in the construction of vehicles, it is becoming more important to understand the joining methods being used to assemble the structure. Accurate representation of the joint strength, and joint failure behaviour or fracture modes, is necessary to understand and predict a vehicle's global behaviour and response to a crash scenario. Resistance spot welding (RSW) is a major joining method utilized in the fabrication of automotive structures because of the low time required per weld and high suitability for automation, without

a requirement for additional filler material [7], [8]. Over 90% of assembly work in a car body is completed by RSW, totalling anywhere from 3000-6000 individual spot welds, depending on the vehicle [8]–[10]. Given its prominence in vehicle assembly, significant efforts are being applied to simulate the RSW process and subsequent structural and crash performance.

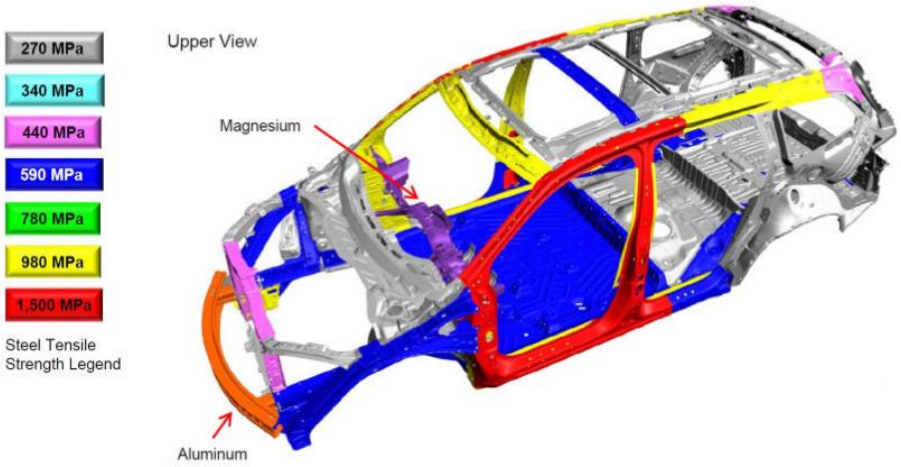

Figure 2: *2016 Honda Pilot body construction and high-strength steel content.* [11]

Implementation of high strength steels has measurably affected the structural performance of component level structures. Early work examining the effects of using a spot welded top-hat channel (Figure 3 (a)) instead of a square tube with a continuous seam weld (Figure 3 (b)) highlighted the importance of understanding and accurately modelling spot weld failure. Structural effectiveness is a parameter used to evaluate axial crush performance and is calculated by normalizing the average stress during an axial crush by the material tensile strength. It was shown the structural effectiveness was reduced for top-hat channel axial crush experiments when changing the material from lower strength (300 MPa) UTS mild steel to higher UTS materials [12]–[14]. However, the structural effectiveness was not affected when increasing the base metal strength in the square tube axial crush experiments.

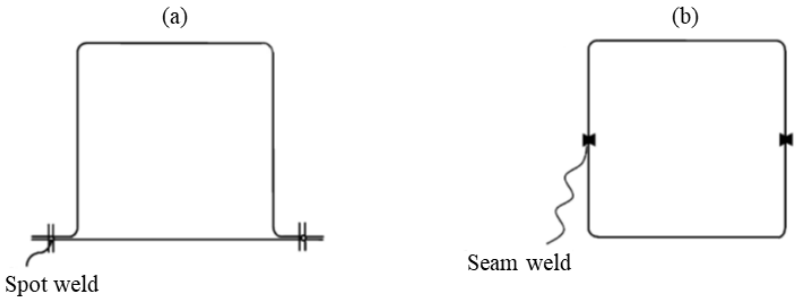

Figure 3: *(a) Top-hat channel section; (b) square channel section. Adapted from Tarigopula* et al. [12].

Schneider and Jones [15] established that there are many aspects that could explain a reduced structural effectiveness when increasing the material strength, but none of them explain why square sections did not exhibit the same phenomenon. These results indicate that the presence of the spot welds on the flange of a top-hat channel, in contrast to the seam welds used in the square section, is the cause of the structural effectiveness reduction when applying higher tensile strength materials to axial crush experiments. It was also noted that finite element simulations were not able to reproduce the different structural effectiveness for spot welded top-hat sections.

In this review, the hot stamping process and mechanical properties of the materials considered in this thesis are discussed. Following that, the resistance spot welding process is introduced and how it affects the microstructure of the hot stamped materials being used. Next, the commonly used single spot weld characterization tests and component-level weld group tests are reviewed. Lastly, the various methods of spot weld numerical modelling for FEA and the results of simulations from the current literature are discussed.

1.2. Hot Stamping

Increasing the strength of steel allows for thinner gauge sheet to be used in automotive applications while maintaining structural and safety integrity. However, increasing the strength of the steel sheet metal typically results in a reduction of the total elongation of the material, shown in Figure 1, making it impossible to form the complex geometry required in automotive structures. According to Mori *et al.* [16], cold-stamping UHSS that has a tensile strength greater than 1.2 GPa is unpractical because of the large amounts of spring back and tool wear. Mori *et al.* [16] also stated that the hot stamping process is ideal to overcome these issues because it is springback-free, parts have tensile strengths of 1.5 GPa after stamping, and during stamping there are low loads and increased ductility. In the hot stamping process, depicted in Figure 4, a blank is first heated in an oven until a completely austenite microstructure is obtained. Then, the blank is transferred from the oven into the press where the final geometry is formed while simultaneously rapidly cooling the part. The austenitization heat treatment process followed by the die quenching forms a 100% martensite or mixed martensite and ferrite or bainite microstructure, depending on the alloy [17].

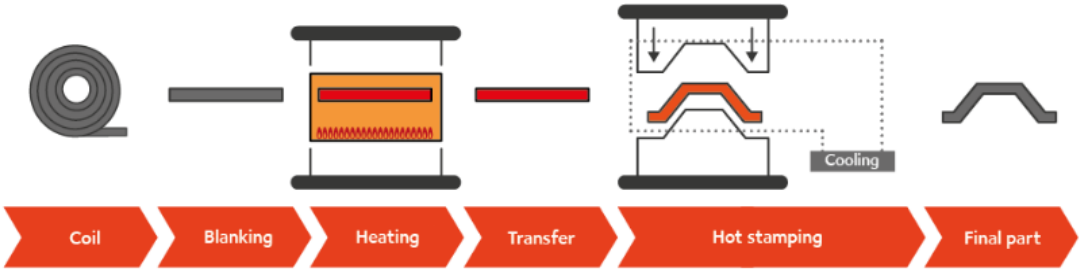

Figure 4: *Direct hot-stamping process diagram.* [18]

The mechanics of the hot stamping heat treatment can be further understood from the iron-carbon binary phase diagram and the isothermal transformation diagram, shown in Figure 5. The austenite microstructure is formed when an iron-carbon alloy with a carbon content of approximately less than 2% by weight is heated above the upper critical temperatures, A_3 or A_{cm}. Martensite is formed through the diffusionless transformation of austenite when it is rapidly cooled to low temperatures [19, p. 362]. Martensite does not appear on the iron-carbon phase diagram because it is a meta-stable, or non-equilibrium, microstructure. As the martensite transformation is diffusionless, it has the same chemical composition as the parent austenite phase [20]. The presence of alloying elements can significantly alter the phase transformation temperatures and carbon content in the phase diagram as well as change the time and shape of the isothermal transformation diagrams.

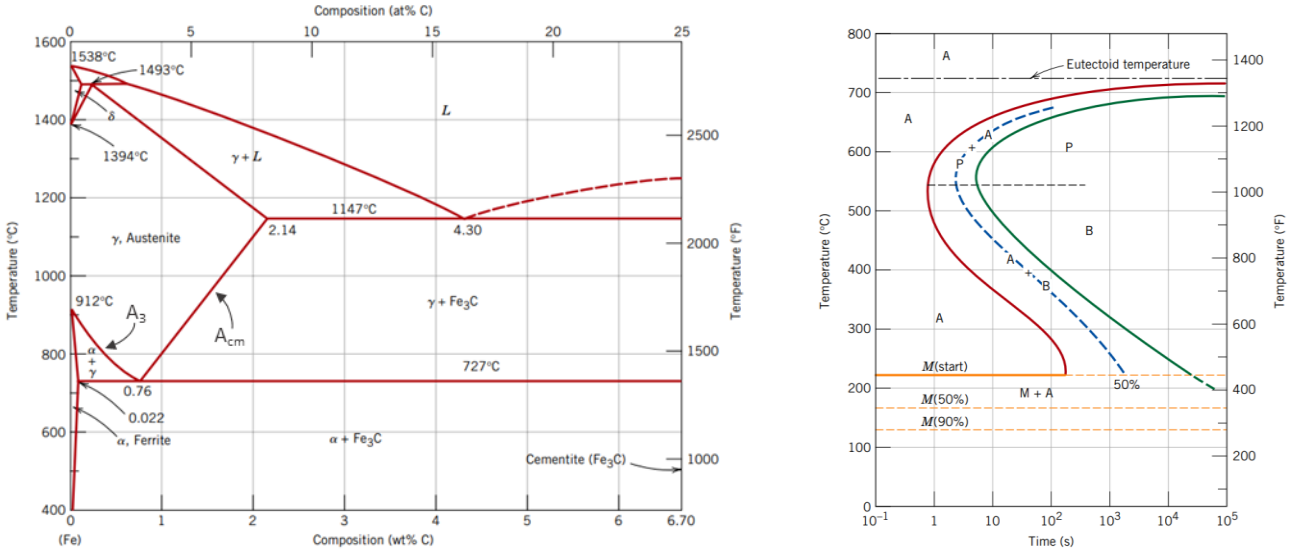

Figure 5: *Left) Iron-carbon diagram labelled with expected equilibrium phases for different combinations of carbon content and temperature* [19, p. 319]. *Right) The complete isothermal transformation diagram for an iron–carbon alloy of eutectoid composition: A, austenite; B, bainite; M, martensite; P, pearlite* [19, p. 364].

1.3. Hot Stamped Steel Material Properties

The hot stamped alloys considered in this work are Ductibor® 500-AS, Ductibor® 1000-AS, and Usibor® 1500-AS, supplied by ArcelorMittal. These grades of steel are micro alloyed with boron and coated with an aluminium-silicon alloy. The addition of boron to steel has been well studied and is known to increase hardenability by suppressing the nucleation of ferrite at the grain boundaries of austenite [21].

The mechanical properties for these three alloys are listed in Table 1 based on a heat treatment process of 5 to 10 minutes at 880°C to 930°C followed by a simulated paint bake cycle at 170°C for 20 minutes. All three steels in the as-received condition have a ferritic-pearlitic microstructure [22], [23]. A 100% austenite microstructure is formed during the heat treatment process before quenching. After die quenching, the Usibor® 1500-AS forms a 100% martensite microstructure [22]–[26] and the Ductibor® 500-AS microstructure consists of ferrite and martensite [23], [26], [27]. The Ductibor® 1000-AS also forms 100% martensite but has increased ductility-toughness through a micro-alloying addition of Nb [28]. The Nb addition in the steel composition contributes mainly to a more refined microstructure during hot stamping operations [29].

Table 1: *ArcelorMittal material minimum characteristic values after hot stamping and paint baking simulation.* [18]

Material	Yield stress [MPa]	Tensile strength [MPa]	Min. Elongation [%]	Bending angle
Ductibor® 500-AS	≥ 380	≥ 550	15	≥ 120
Ductibor® 1000-AS	≥ 800	≥ 1000	6	≥ 80
Usibor® 1500-AS	≥ 1050	≥ 1400	5	≥ 50

During the austenitization heat treatment, the sheet metal blank forms an oxide scale when in contact with air and undergoes surface decarburization [30]. Typically, a zinc-based or aluminium-based coating is applied to the steel sheet to prevent this from occurring. The material considered in this work has an Al-Si (10% wt.) coating applied by a hot-dip process [18]. During the austenitization process many different phases and layers are formed through the diffusion of iron from the base metal into the partially melted coating, assisting with adhesion of the Al-Si coating to the steel substrate [18], [31], [32]. The adhesion of the coating to the base metal substrate means that paint may be applied directly without additional processing. Alternatively, if no coating is applied, an extra shot-blasting process is required to remove the scale to allow good paint adhesion [32], [33]. Comparative work done by Ighodaro, Biro, and Zhou [34] found that the presence of

both Al-Si and zinc-based galvannealed (GA) coatings required increased welding current due to the increase of electrical resistance. The peak load of the spot weld joint (after welding) was not affected by the coatings because the strength depends solely on the size of the fusion zone. It was also found during weld failure testing that welded coupons with both coatings in the hot stamped condition exhibited similar levels of energy absorption, indicating that the different coatings do not affect the weld strength or toughness.

1.4. Resistance Spot Welding Process

Resistance spot welding (RSW) is a process to join two or more stacked metal sheets together by clamping the material between two copper electrodes and driving a large electric current through the stackup. The generated heat rapidly melts the material between the electrodes which then solidifies, creating a fusion zone that joins the sheets together. Heat is generated in this process as a function of the applied current, the electrical resistance of the components in the circuit, and the time the current is flowing, according to

$$Q = I^2Rt \tag{1}$$

in which Q is the heat generated, I is the welding current, R is the electrical resistance, and t is the time current is applied. The current has the largest effect on the total heat generated because the amount of heat generated is proportional to the square of the applied current. Increasing the current grows the nugget size but excessive current density will cause molten metal expulsion, weld cracking, and lower mechanical strength properties [10]. The primary parameters of the RSW process are controlling the current, welding time, hold time, and force applied by the electrodes. These controlling parameters are illustrated for a possible RSW process diagram seen in Figure 6.

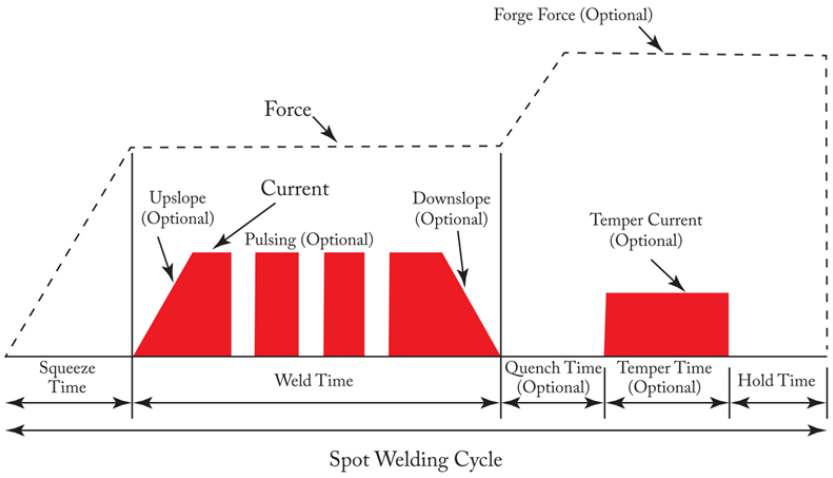

Figure 6: *Generic RSW process with optional features.* [35, p. 2]

The electrode geometry and internal water cooling are also parameters that can affect weld quality. The AWS D8.9M:2012 [36] standard provides specifications for all of the spot welding process parameters for sheet thicknesses ranging from 0.60 mm to 3.00 mm. For an AC power supply, the weld time is defined as number of cycles at a system frequency of either 60 Hz or 50 Hz, but can also be converted to seconds. Newer technology using DC power supplies provide better electrical efficiency and the more precise control of the spot welding process [35], [36]. The applied force directly relates to the contact resistance. As the clamping force increases, the surface asperities that offset the sheets from each other begin to yield. This reduces the average height of the asperities and increases the number of asperities in contact. The overall effect of this it to reduce the interface electrical resistance [35], [37], [38]. Acceptable weld quality is defined using the weld nugget size for a range of current amperes and time/cycles of current applied, referred to as the weld lobe [3]; there is a minimum and maximum weld nugget size that will provide acceptable mechanical properties. The minimum weld nugget size is $4\sqrt{t}$, in which t is the sheet thickness, and the maximum nugget size is limited by the occurrence of expulsion [36].

The thermal cycling from the resistance spot weld process alters the microstructure of the surrounding parent metal in all materials; however, the final microstructure is highly dependent on the initial microstructure and exact thermal cycle. Depicted in Figure 7, the microstructure of the spot weld is made up of different zones that experience different thermal cycles during the RSW process. The heat affected zone (HAZ) due to welding can be divided into four sub-regions: the coarse grained (CG), fine grained (FG), intercritical (IC), and the subcritical (SC) zones [39], [40]. These sub-regions extend from the fusion zone (FZ), where material is heated above the melting temperature and has a cast-like structure, to the base metal (BM) region, where the original microstructure is heated to below approximately 200°C and generally unaffected. In the CG and FG zones, the peak temperature exceeds the A_3 temperature and the local structure is fully austentized. The CG HAZ, which is closest to the FZ, undergoes a thermal cycle well above the A_3 and grain-coarsening temperature, thus promoting grain growth. The FG HAZ thermal cycle nucleates austenite grains but does not reach grain coarsening temperatures. Rapid cooling transforms the austenite into large martensite grains in the CG HAZ, whereas the FG HAZ produces an ultra-fine martensitic microstructure. The IC zone peak temperatures are between the A_1 and A_3 temperatures causing partial transformation of the ferrite phase to austenite resulting in a final martensite + ferrite microstructure. The SC zone temperatures are below the A_1 point and

temper the metastable martensite and bainite phases, if they exist, shown by Eller *et al.* [41]. Some materials, such as mild carbon or HSLA steel, may not show structural changes in this region.

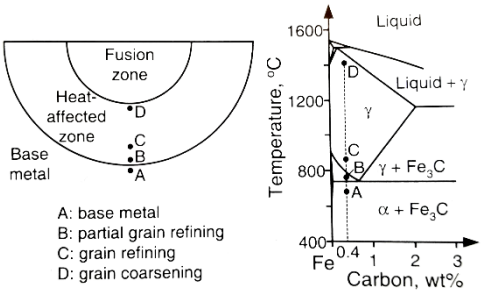

Figure 7: *Spot weld HAZ microstructure with respective peak temperatures shown on equilibrium diagram* [39, p. 403].

Early work by Kunishige *et al.* [42] showed that localized necking and fracture occurred during forming operations due to softening in the HAZ for DP grade steel, but not HSLA steel. The DP steel, which contains a mixture of martensite and ferrite, experienced tempering of the martensite in the base metal that was heated to above 600°C and below the A_{c1} temperature. Khan *et al.* [43] examined the microstructure and mechanical properties of several AHSS grades with reference to a conventional HSLA steel. The AHSS grades showed higher tensile strengths than the HSLA steel. The FZ was observed to have harder microstructures due to the complex chemical compositions of the AHSS when compared the HSLA steel. Baltazar-Hernandez *et al.* [44] studied the extent of softening in the SC HAZ in DP steel through the use of a nano indentation technique on each individual phase present. Micro indentation testing showed an average maximum drop in hardness of 31 HV at 100 µm from the start of the SC zone. The nano indentation measurements revealed that almost no softening occurs in the ferrite phase; all softening is due to the tempering of martensite and tempered martensite existed further from the FZ than the micro hardness data suggested. Biro *et al.* [45] studied more specifically the softening kinetics of the SC HAZ in laser welds in DP 600 and 780 steels. They found HAZ softening occurred through martensite tempering and that the heat input required for HAZ softening decreased as the carbon content of the martensite phases increased. The martensite tempered via decomposition into cementite and ferrite, and the formation of carbides due to alloying elements (Cr and Mo) reduces the effects of softening.

Fully quenched hot stamped boron steel (22MnB5) has a completely martensitic microstructure that exhibits microstructural changes in the HAZ from the thermal cycle of the spot welding process that are similar to those in the DP steels. Jong *et al.* [46] investigated the effects of RSW

parameters and post-weld microstructure of 1.2 mm Usibor® 1500-AS. The sub-regions and softening effects in the HAZ present in the Usibor® 1500-AS are the same as what was reported in the high strength DP steels. The CG and FG HAZ contained only martensite, the IC HAZ was a mixture of martensite and stable ferrite, and in the SC HAZ the pre-existing martensite formed stable ferrite and tempered martensite resulting in a softened region. The hardness at the weld fusion zone and the base metal was approximately 550 HV compared to approximately 320 HV in the SC HAZ. Lu *et al.* [47] also showed that for Usibor® 1500-AS, the same range of microstructures form in the HAZ from the RSW process as those identified by Jong *et al.* [46]. The weld nugget, CG HAZ, and FG HAZ microstructure consist of fresh martensite, followed by a duplex structure of martensite and ferrite in the IC HAZ, and lastly tempered martensite in the SC HAZ with the extent of tempering decreasing towards the BM. In a study by Burget and Sommer [48] to characterize and model fracture of spot welds in hot stamped grade steel, it was found that the measured elongation of a uniaxial tensile specimen was significantly reduced compared to the specimen with no spot weld. In work to develop a calibrated strain-based fracture model for RSW of tailored hot stamped boron steel, Eller *et al.* [41] showed a peak softening effect as a result of a short tempering cycle just below the A_{c1} temperature. The reduction of hardness scaled linearly with the base material hardness for the five tailored hardness grades examined. Additionally, the study by Eller *et al.* [41] and the earlier study by Burget and Sommer [48] both showed that for uniaxial tensile loading, strains localize in the softened HAZ leading to early fracture initiation for base metals with hardness of 250 HV or greater. The presence of the spot welds affects the overall deformation response of the tested specimens; this further shows the need to characterize weld failure when implementing higher strength materials in automotive structures and have accurate models.

1.5. Standard spot weld characterization test methods

Single spot weld characterization is performed to understand the joint strength under isolated loading conditions (in the absence of other spot welds). Single spot weld tests are used to objectively determine the strength of a weld and quantitatively compare the weld strength of joints using different welding process settings, sheet materials and thicknesses in a consistent manner. There are two basic test methods for determining the strength of a single resistance spot weld defined by the American Welding Society (AWS) in the AWS D8.9M:2012 standard [36]. These two methods are the tensile lap shear test and the cross tension test, as detailed in the following.

1.5.1. Lap shear

The lap shear test applies a tensile load acting along the plane of the weld interface to develop a shear stress in the weld nugget. Depending on material properties, this test only approximates a shear loading because the weld nugget rotates out-of-plane as the load increases. Mohamadizadeh *et al.* [49] showed for PHS600 (Ductibor® 500-AS) material that the lap shear test begins with an isolated shear loading condition but begins to transition into a mixed shear and normal loading as the weld nugget rotates while the higher strength PHS1500 (Usibor® 1500-AS) material had negligible normal force components. Nonetheless, the tensile lap shear is one of the most commonly adopted and simplest weld characterization tests in use. The coupon geometry is illustrated in Figure 8.

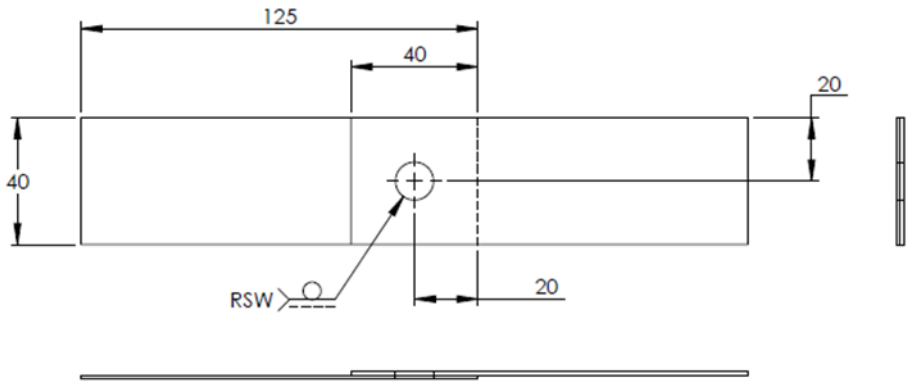

Figure 8: *Tensile lap shear assembly and schematic of gripping in the tensile frame.*

1.5.2. Cross tension

The cross tension test applies a tensile load normal to the interface plane of the spot weld to develop a normal stress in the weld nugget. This test requires significant fixtures to connect the welded specimen to the tensile frame grips. The applied load is centred on the weld nugget and is rotationally symmetric about the weld nugget so there is no transition from the initial isolated loading condition, unlike the coach peel test [50]. However, the cross tension test typically develops a large amount of coupon deformation away from the nugget which makes it difficult to characterize the local deformation conditions near the weld at the onset of failure [51]. Alternative spot weld characterization methods can help reduce this effect, such as the KS-II test discussed in Section 1.6.2. The welded assembly geometry for the cross tension test is shown in Figure 9.

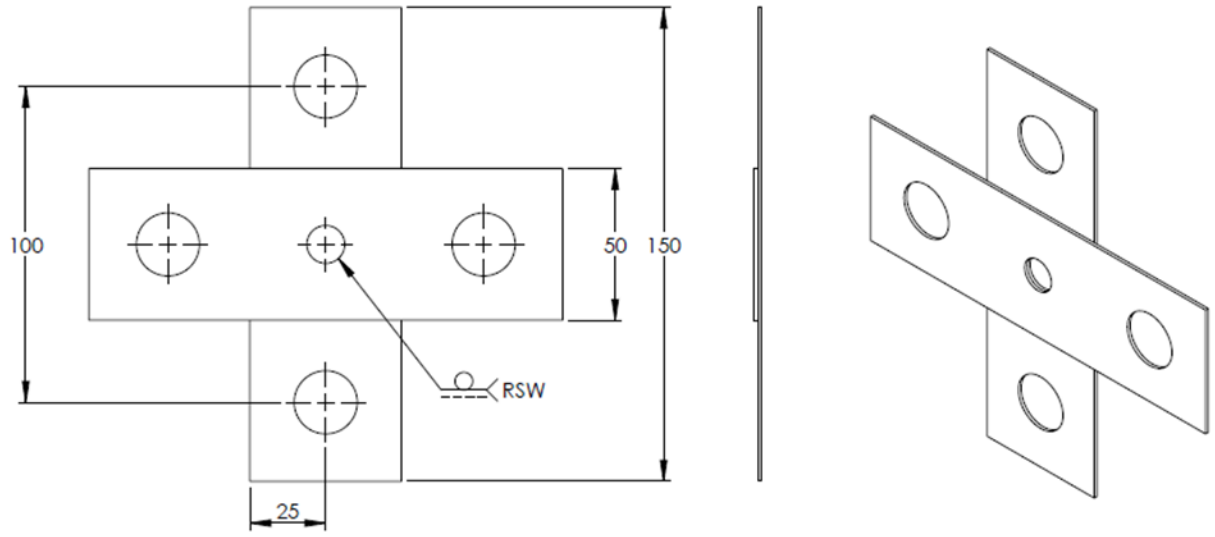

Figure 9: *Cross tension assembly geometry and fixture schematic.*

1.6. Advanced spot weld characterization test methods

There are several other methods of testing welds found in literature used for the characterization of spot welds in addition to the standard tensile shear and cross tension tests outlined in the AWS D8.9:2012 standard. These advanced characterization methods do not follow any particular standard and thus each specific implementation in different studies tend to vary slightly, especially with regards to coupon geometry. However, each characterization method has a specific use that is maintained regardless of implementation differences, such as load condition, ease of testing, or numerical model validation purposes. The more commonly found methods found in literature are discussed in detail here.

1.6.1. Coach peel

The coach peel test is useful for characterizing spot weld behaviour under bending loading conditions [50]. The geometry, seen in Figure 10, joins the flanges of two pieces of material that are formed into an L-shape. As the coupon is loaded, pull-out begins on one side of the spot weld and propagates around the weld nugget. The concentration of stress at the opening of the coach peel specimen results in reduced load carrying capacity (strength) in comparison to that of the symmetrically loaded cross tension specimen [52]. The coach peel test has been used to calibrate joint models that include a bending term in the failure model [50], [52]–[58].

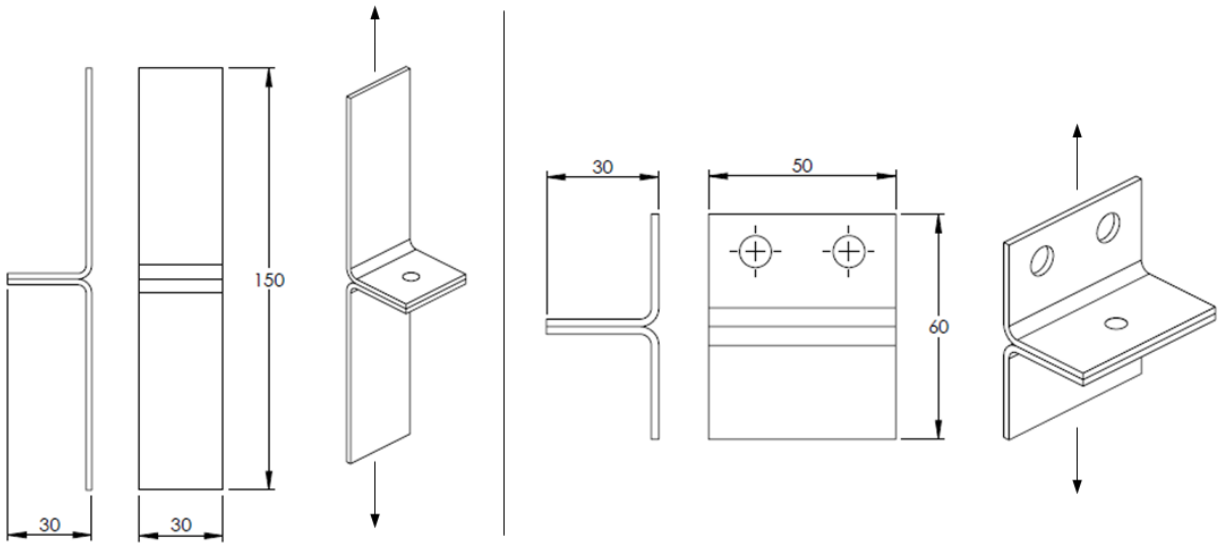

Figure 10: *Coach peel test geometry (left) and modified KS-II test for peel (right). Arrows indicate direction of applied loading.*

1.6.2. KS-II

The KS-II test [50] is used often in addition to or instead of the typical tensile shear test and cross tension test [48], [52], [56]–[59]. The KS-II weld coupon joins two formed U-channels, with the weld located at the centre of the mating surfaces. The assembly, shown in Figure 11, is then mounted into a tensile frame. The KS-II can be loaded at any loading angle from 0° (pure simple shear) to 90° (pure tension or opening mode). Particularly for tensile lap shear testing, there is significant weld nugget rotation that leads to a combined tensile and shear loading condition. The mixed mode loading makes calibrating the shear failure conditions for the spot weld models difficult but is avoided in the KS-II test because the specimen geometry provides more support to reduce the coupon deformation. Typically, loading angles of 0°, 30°, 45°, 60°, and 90° are used to investigate the relationship between normal and shear stresses, referred to as mixed loading condition, or mixed mode behaviour. The capability to apply isolated or mixed loading conditions with one geometry makes it convenient to calibrate failure behaviour for numerical models.

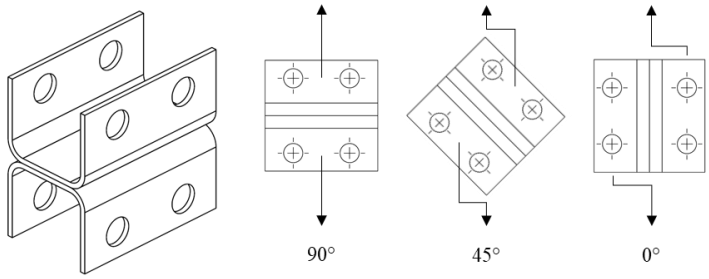

Figure 11: *Different load cases for the KS-II test. Arrows indicate direction of applied loading.*

1.7. Weld group tests

Weld group tests examine the behaviour of spot welds at the component level, which generally implies connections consisting of more than one spot weld. Spot welds in full vehicle crash scenarios have more complex loading conditions than what is represented in the single weld coupon tests. Also, when multiple spot welds are present in a deforming body the loads will be shared across multiple spot welds. A component level weld group test is used to verify that a weld model calibrated using one or more single spot weld tests will be able to accurately reproduce behaviour in the more complex loading conditions seen in vehicle crash analysis. The main results of a numerical simulation that are used to verify the weld material model are the weld failure location, deformation modes, and global force-displacement curves.

Apart from validation purposes, the presence of multiple spot welds allows for unique methods of characterizing weld failure behaviour. O'Keeffe [51] applied a "crack extension" metric to evaluate the rate of weld failure in the Caiman Mode I tests (detailed later). As the spot welds failed sequentially, referred to as unzipping, stronger material that had low energy absorption correlated to the fastest crack propagation.

1.7.1. H-Specimen

The H-specimen test is a multi-spot-welded fatigue test defined by the ISO 18592 standard [60], [61]. This test has the same form as the KS-II test but is larger in all dimensions to accommodate multiple spot welds in one specimen. The geometry is defined for shear and peel load conditions, as shown in Figure 12. The H-specimen test is a multiple weld group test, however, it is of limited utility for characterizing fracture propagation between spot welds since in this test all the spot welds see the same nominal loading simultaneously.

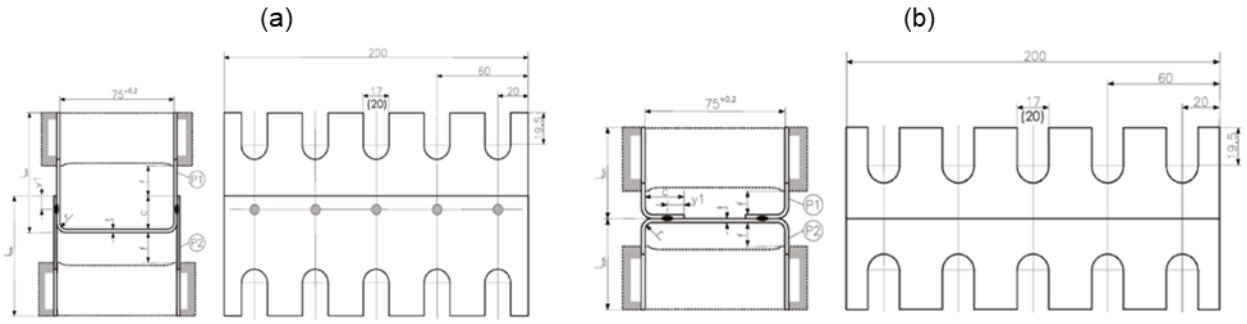

Figure 12: *H-specimen geometry used for multiple spot weld fatigue tests for (a) shear, and (b) peel, loading conditions* [60]

1.7.2. T-Joint Test

The T-component or T-joint weld group test is commonly used in literature as a weld model verification test [50], [52], [56], [62], [63]. The test is a simplified lab version of the lower section of a B-pillar and door ring seen in passenger vehicles, shown in Figure 13. It consists of two square rails that are joined to form a T-shape. The square rails are made from a hat-channel with a flat backing plate. The trunk of the 'T', which is representing the B-pillar, is loaded by the green impactor in Figure 13 as would be seen in a full vehicle side impact test. This test is used for weld model validation because it is relatively easy to fabricate and has many spot welds that undergo different loading conditions simultaneously.

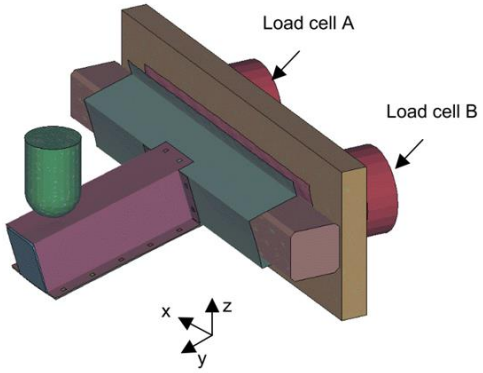

Figure 13: *T-joint model* [50].

1.7.3. Caiman Mode I

O'Keeffe [51] developed the Caiman Mode I weld group test to characterize how spot welds progressively fail in tension as a result of two components separating. The Caiman Mode I derives its name from the fracture mechanics failure type Mode I, not from the mixed mode loading definition used for the KS-II tests. The test uses a double hat-channel rail that has been partially joined along the length using with spot welds on the flange, seen in Figure 14.

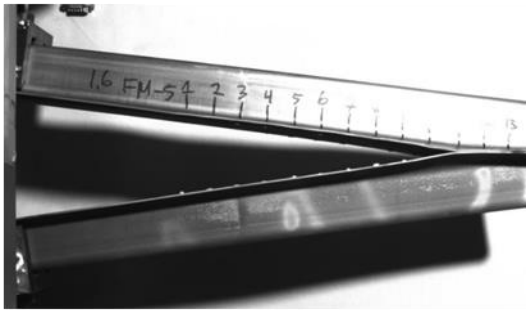

Figure 14: *Caiman Mode I* [51].

The Caiman Mode I test produces a unique characteristic force *versus* displacement response, seen in Figure 15, that is described by smooth loading up to the peak load followed by stepped force unloading as each progressive spot weld failure occurs. As the test progresses and the hat-channels separate, the spot welds on the flanges are loaded sequentially creating a propagating "crack". When comparing the results of single spot weld testing using different material conditions, O'Keeffe [51] found that the strength of single spot welds was not largely affected by parent metal strength or ductility but energy absorption was higher for the lower strength parent metal due to increased plastic deformation and change in weld fracture mode. The differences in weld toughness between the material conditions tested are clearly seen in the Caiman Mode I structural connections experiments; the specimens with softer material (labelled 400 °C and 700 °C) exhibited much higher energy absorption.

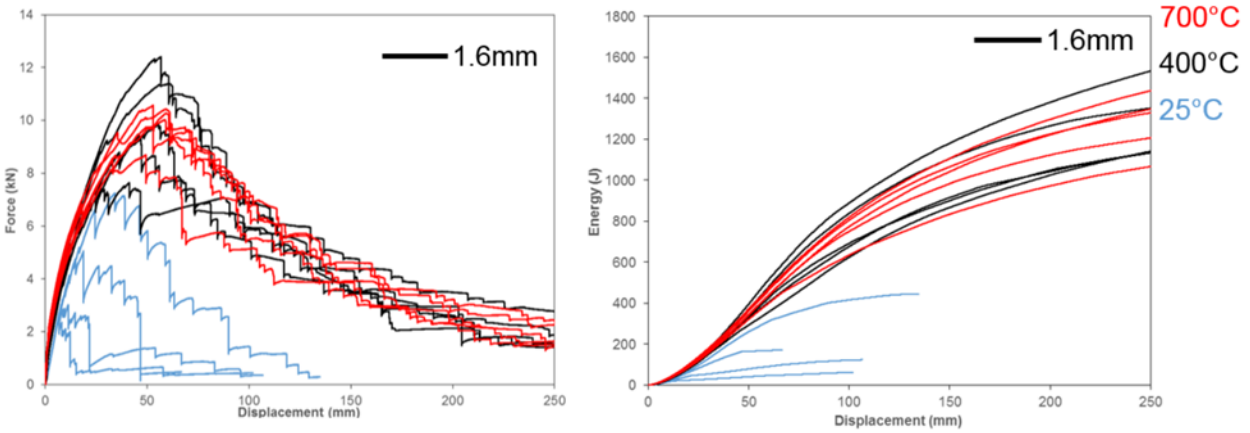

Figure 15: *Force (left) and energy (right) versus pin displacement plots for quasi-static Caiman Mode I tests* [51].

There are other geometries for large-scale weld group testing that use a full vehicle test or a section of a full vehicle, usually in conjunction with numerical simulations to predict local conditions within welds. One study looked at applying a weld model to the seat mounting point on a floor frame [54], another study compared the numerical and experimental results of a side crash test on a vehicle floor pan [64], and two studies looked at modelling and predicting the global deformation mode of the frontal structure during vehicle crash [58], [65]. Due to the large number of components and complex deformation that occurs in these assemblies, often only qualitative conclusions are drawn from a model validation perspective. Weld failure location and timing correlations are made as well as identifying similar trends in force-displacement plots. The complexity of these types of weld group tests makes them difficult to use as a weld model validation tool.

1.8. Spot weld numerical characterization

The development of models of failure of the various joints used in automotive structures is an on-going process, underway within many research groups in the automotive industry. Accurate representation of the joint strength and failure modes is necessary to understand a vehicle's global behaviour and response to a crash scenario. LS-DYNA is a non-linear finite-element solver that is commonly used for crash analysis for the automotive industry. There are already multiple simplified models for spot weld failure that have been developed and implemented within LS-DYNA [66], [67]. These methods are suitable for automotive CAE analysis in which shell elements are most commonly used that have a size on the order of 3-5 mm to enable reasonable solution times for full vehicle simulations. An alternative modelling approach is to use a detailed model with sub-millimetre solid elements that will capture the micromechanics at the meso-scale. This modelling strategy, discussed in Section 1.9, can predict force-displacement response and fracture modes at weld failure very well [41], [48], [57], [68]–[70] but is complex since it requires constitutive models for individual heat affected zones. For simulations at the automotive CAE-level, elements that are less than approximately 3 mm in size are considered prohibitively small and as such HAZ modelling has not yet been applied to full vehicle simulation in current literature.

The CAE-level methods, which are described in detail here, are all designed to accomplish the same general task but are based on different formulations and thus provide different results with varying levels of effectiveness or accuracy. There is a balance that must be determined by the user that involves aspects such as modelling complexity (*e.g.*, acquiring test data for calibration or meshing requirements), effects on run-time, and accuracy relative to real spot weld behaviour. All spot weld models require single spot weld test data to calibrate the model for various isolated loading conditions, ideally to enable accurate solutions for more complex loading conditions seen in component level or full vehicle crash tests. Typically, the standard single spot weld tests defined in the AWS standards [36] such as cross-tension and tensile-lap-shear are used [50], [51], [54], [68], [69], [71]. It is also possible to use other geometries such as KS-II that can provide various isolated and mixed loading conditions while only using one coupon geometry [48], [52], [55]–[57], [72], [73]. Some single spot weld tests require more preparation before testing can be performed, for example coach peel and KS-II tests need to have formed coupons before being spot welded whereas cross-tension and tensile-lap-shear use flat blanks. The spot weld modelling options have different meshing methods or sometimes can be meshed multiple ways. Different

meshing methods can impact the feasibility of implementing a weld model into existing component and vehicle meshes. A weld model may have a different response depending on how the weld elements and the joined surfaces are meshed, as well as how the weld is connected to the parent surfaces – all of which is referred to as mesh-dependence [41], [48], [50], [54], [55], [74]. A mesh-independent modelling method is preferred since a mesh-dependent weld may also require significant manual remeshing of the joined components or meshing with the use of custom macros or CAD tools. The element type and formulation can change depending on which weld model is being used. Each element type and formulation have a different method of determining the minimum time step required and can influence the total run time of the simulation. At the CAE level of analysis, it is impossible to capture the exact fracture mode of a spot weld due to the inability to capture crack propagation near the weld nugget or within the HAZ. Localized deformation in the HAZ as well as fracture through the nugget or parent material are not captured via a simplified weld model using beam or solid elements to connect shell elements representing the parent material. However, there are still differences between the weld models that will more or less accurately capture the stress state of the weld and the failure behaviour. Models that use solid elements can be refined to a higher density of elements in the nugget that will better capture peeling or use different damage formulations that are more representative of the physical mechanics [50].

Apart from the inherent difficulty of generating a CAE-level weld model that can predict the overall response of single spot weld tests, another difficulty faced is that not every spot weld is the same. Each of the thousands of spot welds placed on a car body will have minute differences that can affect the failure mode and weld strength. A spot weld model, however, will use the exact same properties that have been calibrated to a certain weld failure mode for every weld so it can be problematic when trying to represent spot welds on a component that do not fail the same way every time.

As stated earlier, there are many methods or different formulations for modelling a spot weld connection built into the finite element solver LS-DYNA [66], [67], [74]. The simplest connection method is a rigid connection that uses a tied contact or constrained nodal rigid body to couple the nodal rotations and displacements of the points of a nodal pair to each other. Later methods built on this foundation to provide failure criteria that will release the tied constraint of the nodal pair to simulate the failure of the spot weld. Instead of using a rigid connection, deformable beam or

solid elements, incorporating an appropriate constitutive model, have also been considered to introduce compliance of the connection to the model. Additionally, these methods can implement post-failure damage treatments that will gradually unload the connection as separation occurs. The more common and recent formulations that are commonly seen in automotive CAE analysis simulations (here focusing on LS-DYNA) are described in the following.

1.8.1. *MAT_100/*Mat_Spotweld

The *Mat_Spotweld is an elasto-plastic material model based on von Mises plasticity theory [67]. It can be applied to either beam elements or solid elements that are used to mesh the connection between two deformable or rigid surfaces. When connecting beam elements to shell surfaces, the elements have an unconstrained drilling degree-of-freedom which prevents torsional loads from developing; if torsional forces are expected, solid elements should be used instead of beam elements. A single solid element or an assembly of up to 16 solid elements, shown in Figure 16, can be used to mesh the connection.

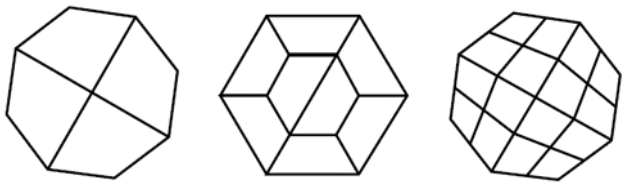

Figure 16: *Sample of four, eight, or sixteen solid elements used to construct a single spot weld assembly.*[66]

The spot weld material is modelled with isotropic hardening plasticity that can be coupled to failure models. In the simplest case, a failure strain is specified that defines when each integration point in the spot weld connection element fails. Alternatively, a variety of failure formulations that have been developed by different groups and are implemented into LS-DYNA can be used as the failure criterion instead of a single strain value [67]. The *OPT* parameter on the *MAT_100 material card is used to select which failure method is applied to the weld elements and is separate from the damage parameters and function.

1.8.1.1. Force resultant-based failure

Three normal (N_{rr}, N_{rs}, N_{rt}) and three moment resultants (M_{rr}, M_{ss}, M_{tt}) are used to define a failure surface that is either predefined, shown in Equation (2), or specified via a *DEFINE_FUNCTION card. Additionally, the failure function can be evaluated but not applied,

meaning no failure, to assist with the identification and analysis of spot welds that are likely to fail.

$$\left[\frac{Max\ (N_{rr},0)}{N_{rr_F}}\right]^2+\left[\frac{N_{rs}}{N_{rs_F}}\right]^2+\left[\frac{N_{rt}}{N_{rt_F}}\right]^2+\left[\frac{M_{rr}}{N_{rr_F}}\right]^2+\left[\frac{M_{ss}}{N_{ss_F}}\right]^2+\left[\frac{M_{tt}}{N_{tt_F}}\right]^2-1=0 \qquad (2)$$

1.8.1.2. Stress-based failure

The stress-based failure options uses normal stress, σ_{rr}, and shear stress, τ, in the weld material elements and a failure surface to determine failure, similar to the force resultant based option. The stresses used in these failure functions are calculated using the same force resultants that are used in the force resultant method. For the primary stress-based option (`OPT = 1`), the failure surface is defined by:

$$\left(\frac{\sigma_{rr}}{\sigma_{rr}^F}\right)^2+\left(\frac{\tau}{\tau^F}\right)^2-1=0 \qquad (3)$$

If rate effects are to be considered, Equation (3) becomes:

$$\left[\frac{\sigma_{rr}}{\sigma_{rr}^F(\dot{\varepsilon}_{eff})}\right]^2+\left[\frac{\tau}{\tau^F(\dot{\varepsilon}_{eff})}\right]-1=0 \qquad (4)$$

where $\sigma_{rr}^F(\dot{\varepsilon}_{eff})$ and $\tau^F(\dot{\varepsilon}_{eff})$ describe the function dependence of failure stress on strain rate and are defined with user input curves. There are alternate stress-based failure options (`OPT = 6,7,9`) that slightly alter the input method using extra *DEFINE cards but all follow the same base failure functions defined by Equations (3) and (4).

An approximate notch stress (`OPT = 3`) and stress intensity factor (`OPT = 4`) failure method, developed by Zhang [71], were implemented into *MAT_100 as failure options. The notch stress and stress intensity factors are developed by superposition of the approximate analytical solution maxima on the nugget edge for tensile shear, cross tension, and coach peel specimens. It was noted by Zhang [71] that the formulas were not validated for systematic variations with regards to specimen geometry, weld placement, or spacing. It was also assumed that the spot welds are at least two diameters away from the nearest edge and that there are at least four diameters between spot welds. The notch stress equation is given by:

$$\sigma_k = \alpha_1 \frac{4F}{\pi dt}\left(1 + \frac{\sqrt{3}+\sqrt{19}}{8\sqrt{\pi}}\sqrt{\frac{t}{\rho}}\right) + \alpha_2 \frac{6M}{\pi dt^2}\left(1 + \frac{2}{\sqrt{3\pi}}\sqrt{\frac{t}{\rho}}\right) + \alpha_3 \frac{4F_{rr}}{\pi d^2}\left(1 + \frac{5}{3\sqrt{2\pi}}\frac{d}{t}\sqrt{\frac{t}{\rho}}\right) \quad (5)$$

where

$$F = \sqrt{F_{rs}^2 + F_{rt}^2} \quad (6)$$

$$M = \sqrt{M_{ss}^2 + M_{tt}^2} \quad (7)$$

and α_i for $i = 1,2,3$ are input correction factors. F_{rs}, F_{rt}, M_{ss}, and M_{tt} are normal forces and moments about the local element axes *s* and *t*. The constant t is the sheet thickness, d is the nugget diameter, and ρ is the notch-root radius at the nugget edge. The structural stress intensity failure criterion is given by:

$$K_{eq} - K_{eqF} \geq 0 \quad (8)$$

where

$$K_{eq} = \sqrt{K_I^2 + K_{II}^2} \quad (9)$$

and

$$K_I = \alpha_1 \frac{\sqrt{3}F}{2\pi d\sqrt{t}} + \alpha_2 \frac{2\sqrt{3}M}{\pi dt\sqrt{t}} + \alpha_3 \frac{5\sqrt{2}F_{rr}}{3\pi d\sqrt{t}} \quad (10)$$

$$K_{II} = \alpha_1 \frac{2F}{\pi d\sqrt{t}} \quad (11)$$

For the stress intensity Equations (10) and (11), F, M, α_i, d, and t are the same as defined above for notch stress.

There is another stress based failure option (`OPT = 10`) that is described in the patent application by Lee and Balur [75] (current patent status is abandoned) based on the ratios of nominal/ultimate and static/dynamic for shear or normal stresses. The failure criterion, given in Equation (12), is similar in form to the failure surface defined by Equation (3) for `OPT = 1`.

$$\left(\frac{S_s}{S_{s,dynamic}}\right)^{\beta} + \left(\frac{S_n}{S_{n,dynamic}}\right)^{\beta} \leq 1 \quad (12)$$

where

$$S_{n,static} = S_{n,2} = S_{n,1}\left(\frac{S_{ut,2}}{S_{ut,1}}\right) \quad (13)$$

$$S_{s,static} = S_{s,2} = S_{s,1}\left(\frac{S_{ut,2}}{S_{ut,1}}\right) \quad (14)$$

$$S_{n,dynamic} = S_{n,static}\left[1.183 + 0.002963\left(\frac{\dot{P}}{0.1}\right) + 0.0458\, log\left(\frac{\dot{P}}{0.1}\right)\right] \quad (15)$$

$$S_{s,dynamic} = S_{s,static}\left[1.183 + 0.002963\left(\frac{\dot{P}}{0.1}\right) + 0.0458\, log\left(\frac{\dot{P}}{0.1}\right)\right] \quad (16)$$

The exponent β modifies the shape of the failure surface to better fit with the experimental failure points. $S_{ut,i}$ are the material specific ultimate tensile strengths, $S_{n,i}$ and $S_{s,i}$ are the material specific spot weld ultimate static normal and shear strengths, and $\dot{P}$ is the load rate. The subscripts 1 and 2 in Equations (13) and (14) denote strengths for base materials 1 and 2 respectively.

1.8.1.3. User subroutine failure

A user-written subroutine, named *uweldfail*, *uweldfail12*, or *uweldfail22*, can be defined that is run at every time step to evaluate if failure has occurred and optionally incorporate a damage model. In the failure only option, axial and shear forces, bending moments, torsional resultant, weld diameter, and user defined parameters can be used to evaluate a failure criterion. Once the criterion is met, sudden failure occurs and the weld elements will be deleted. In the failure and damage subroutine, the user has access to the same input parameters as the failure subroutine and additional strain related variables. The damage parameter is calculated in the user defined subroutine which is then used to determine the scaled true stress in the spot weld from the nominal stress.

1.8.1.4. Post-failure damage

The *MAT_SPOTWELD card also has options for implementing post-failure damage accumulation and weld unloading. If a rupture strain value is specified, then a damage counter is invoked, and a smooth drop-off of the resultant forces occurs as the effective plastic strain of each element reaches the user-defined rupture strain before deleting the weld element(s). The actual stress is calculated by modifying the nominal stress with the damage parameter.

$$\sigma_{nominal} = \frac{P}{A} \tag{17}$$

$$\sigma_{true} = \frac{P}{A - A_{loss}} \tag{18}$$

$$0 \leq \omega = \frac{A_{loss}}{A} \leq 1 \tag{19}$$

where P is the applied load, A is the surface area of the spot weld, A_{loss} is the void area, and ω is the damage parameter. The damage parameter can be a function of effective plastic strain in the weld, defined in Equation (20), or as a function of time, in Equation (21).

$$\varepsilon^p_{failure} \leq \varepsilon^p_{eff} \leq \varepsilon^p_{rupture} \rightarrow \omega = \frac{\varepsilon^p_{eff} - \varepsilon^p_{failure}}{\varepsilon^p_{rupture} - \varepsilon^p_{failure}} \tag{20}$$

$$t_{failure} \leq t \leq t_{rupture} \rightarrow \omega = \frac{t - t_{failure}}{t_{rupture}} \tag{21}$$

1.8.1.5. Mesh Effects

It has been found through a mesh discretization study by Seeger *et al.* [50] that a single solid weld element joining shell elements can have artificial parasitic contact forces causing unphysical and unpredictable failure. For certain meshes, the flange shell elements on either side of the weld element contact each other causing the internal forces of the spot weld, used for the failure criteria calculation, to be disturbed and differ from the external forces. Modifying the contact algorithm to reduce the contact thickness of the shell elements near the spot weld reduced the contact forces and prevents the artificial internal forces except for extreme deformation cases, which are not relevant because weld failure occurs first in practice. Malcolm and Nutwell [54] used an alternative solution by discretizing the single solid spot weld element into an assembly of 8 solid hex elements. The tied contact to the parent shell elements is more robust due to the weld consisting of an inner ring of nodes. The results reported by Malcolm and Nutwell [54] show there is minimal shell element pass-through of the weld elements for a shell mesh size of 5 mm. The internal forces are stable and closely match the external forces in 8-hex weld assemblies for positional cases and rotational cases used to evaluate mesh dependence. Malcolm and Nutwell [54] also reported that hour glassing effects introduced by this type of weld element meshing were minimal.

1.8.2. *MAT_100_DA/*MAT_SPOTWELD_DIAMLERCHRYSLER

The *MAT_100_DA weld material model developed by Seeger *et al.* [50] is a direct enhancement of the *MAT_100 weld material model that has been implemented within LS-DYNA. The primary enhancement is the addition of a new failure criterion, Equation (22), which includes a failure term for the bending stress component. In Equation (22), σ_n is the normal stress component, σ_b is the bending stress component, and τ is the shear stress component. The superscript F denotes the pre-defined failure stress parameter. Consideration of this loading component is important for accurately determining the failure of peeling dominated load cases.

$$f = \left(\frac{\sigma_n}{\sigma_n^F}\right)^{m_n} + \left(\frac{\sigma_b}{\sigma_b^F}\right)^{m_b} + \left(\frac{\tau}{\tau^F}\right)^{m_\tau} - 1 \tag{22}$$

Damage models are available to apply post-failure unloading behaviour and capture additional energy absorbed by the work of the spot weld failure instead of sudden load drop when the failure occurs. The damage models available for *MAT_100_DA are applied in a similar manner as the *MAT_100 material model: a scaling factor is calculated using a damage parameter and then applied to determine the true stress from the nominal stress. If damage growth is selected as a function of plastic strain (`DGTYP = 1`) then Equation (20) is used to determine ω and the true stress, $\hat{\sigma}$, is determined by

$$\hat{\sigma} = \frac{DGPR(1-\omega)}{\omega\left(\frac{1}{2} + \sqrt{\frac{1}{4} + DGPR}\right) + DGPR}\sigma \tag{23}$$

where `DGPR` is a user-defined damage parameter. *MAT_100_DA introduces a new method of describing the damage of the spot weld (`DGTYP = 4`) as a function of internal work done by the spot weld after the failure that uses a single input parameter, `GFAD`. The damage model is defined by the following set of equations:

$$\hat{\sigma} = (1-\omega)\sigma^{ep} \tag{24}$$

$$\omega = \frac{G_{used}}{2\,GFAD} \tag{25}$$

$$G_{used} = G_{used}^{n-1} + det\left(F_{ij}\sigma_{ij}^{ep}\Delta\varepsilon_{ij}\right) \tag{26}$$

$$\sigma^{ep} = \alpha\sigma^{wd} \tag{27}$$

$$\alpha = \frac{\sigma_{ij}^{n-1,ep}\Delta\varepsilon_{ij}}{\sigma_{ij}^{wd}\Delta\varepsilon_{ij}} \tag{28}$$

where F_{ij} is the deformation gradient, σ^{ep} is the scaled Cauchy stress tensor, σ^{wd} is the undamaged Cauchy stress tensor, n is the current simulation step, and `GFAD` is the fading energy parameter. The other available damage models (`DGTYP = 2,3`) are not used in reported literature and are not described here.

Studies by Yang *et al.* [56], Ghassemi-Armaki *et al.* [57], Khan *et al.* [73], and O'Keeffe [51] performed on resistance spot welds using the *MAT_100_DA weld material model show good agreement with the single spot weld tests used to calibrate the model up until the point of weld failure initiation (peak load). After weld failure initiates and the load has reached a peak value, measured force-displacement data exhibit different unloading behaviour that is dependent on the material and facture mode. Figure 17 shows the point in a load-displacement plot of a single spot weld when the weld fails and begins to accumulate damage, before final fracture. Yang *et al.* [56] did not apply a post-failure damage model and noted that the measured data showed higher loads than the predictions. Ghassemi-Armaki *et al.* [57] also did not apply a damage model in their predictions using *MAT_100_DA to capture the additional energy from post-failure unloading but stated that it will be a focus of a future study. Khan *et al.* [73] investigated the use of the weld damage model `DGTYP = 4` available with *MAT_100_DA and found that it did not work for all loading modes. Khan *et al.* [73] proposed an investigation of a loading path dependent damage model as part of future work. O'Keeffe [51] determined that the fade energy was critical to accurately predict the deformation of automotive structures, but only achieved a good correlation for post-failure unloading under shear loading conditions.

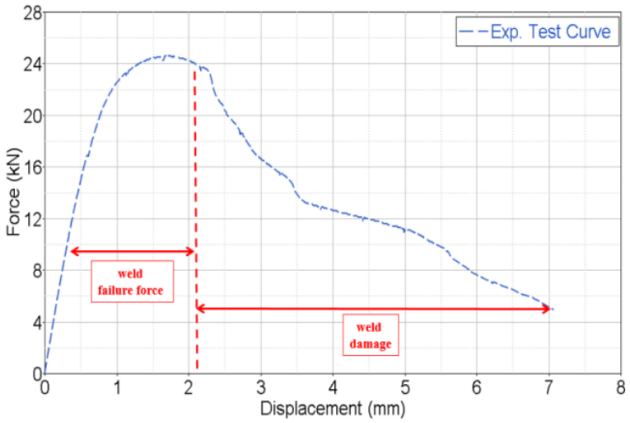

Figure 17: *Spot weld failure and damage.* [73]

An additional validation step has been performed by Seeger *et al.* [50] and Yang *et al.* [56] using their developed weld model in a T-component test (Figure 13) and by O'Keefe [51] using a newly designed component level test for an isolated loading condition (Figure 14). In all cases, the component level simulations showed reasonable accuracy up to initial weld failure and accurate weld failure locations. After weld failure, the simulations under predict the experimental force-displacement and total absorbed energy.

1.8.3. *MAT_240/*Mat_Cohesive_Mixed_Mode_Elastoplastic_Rate

The material model *MAT_240 is a rate-dependent, elastic-ideally plastic cohesive zone model developed by Marzi *et al.* [64], [76], [77] implemented into LS-DYNA. The model is defined by a tri-linear (trapezoidal) traction-separation law, seen in Figure 18, with a quadratic yield and damage initiation criterion in mixed-mode loading. The damage evolution is governed by a power-law formulation. Similar to the *MAT_100_DA weld model, the *MAT_240 material model also uses solid hex elements that are tied to the parent shell elements to represent the joint. The model was originally implemented to simulate adhesively bonded connections; however, there is also limited published work that considers this model to simulate other joining methods such as self-piercing rivets [62], [72] and spot welds [65], [78].

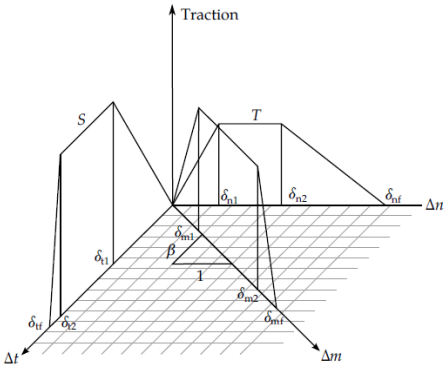

Figure 18: **MAT_240 Trilinear mixed mode traction-separation law.* [67]

The model has been calibrated for adhesive bonded joints by Marzi *et al.* [64] using a single lap-shear, T-peel, End-Loaded Shear joint (ELSJ) and Tapered Double Cantilever Beam (TDCB) tests and shows good correlation with validation tests using a side-impacted floor pan. The *MAT_240 material model has been calibrated for other joining methods using the KS-II geometry in various loading conditions, peel, and shear tests. A study on semi tubular self-piercing rivets by Bier *et al.* [62] recommended *MAT_240 due to its simple application and calibration procedure

and showed good correlation with the calibration experiments, but no validation experiments were performed. Sommer and Maier [72] investigated riveted joints using multiple different material models with KS-II and peel specimen tests concluded that *MAT_240 is the most promising model tested to describe the deformation and failure behaviour of the riveted joints. The correlations of the cohesive model and experimental tests are shown in Figure 19 for the self-piercing rivets.

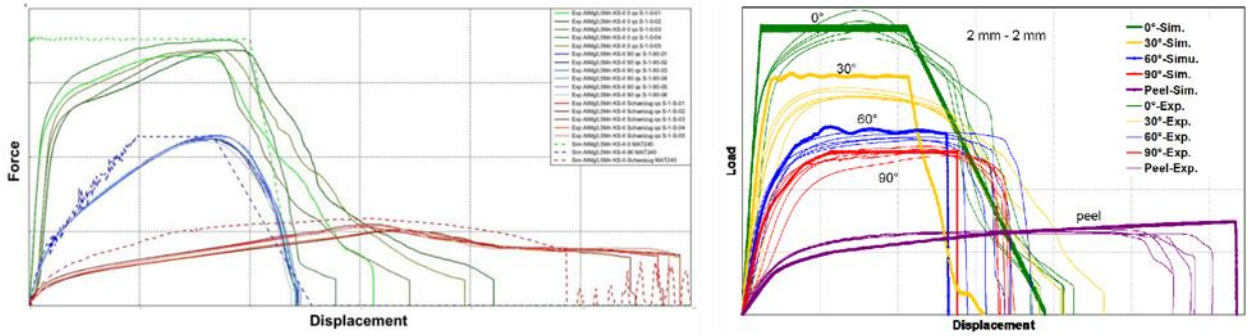

Figure 19: *Tests and CAE correlation using *MAT_240 at coupon level of different loading conditions for self-piercing rivets (left* [62] *and right* [72]*).*

Bier *et al.* [78] first considered the application of cohesive zone element formulations to describe spot welds in DC04 steel. Bier *et al.* [78] primarily examined the effects of meshing design dependence on failure predictions by modifying the spot weld rotation and position on the parent mesh. To date, only one other publication, due to Koralla *et al.* [65], implemented cohesive zone element formulations to describe spot welds in an unspecified material. The *MAT_240 cohesive material model showed that it can capture the post-weld failure unloading behaviour for both normal tensile and shear failure conditions. The correlations of the cohesive model and experimental tests are shown in Figure 20 for the spot weld joints.

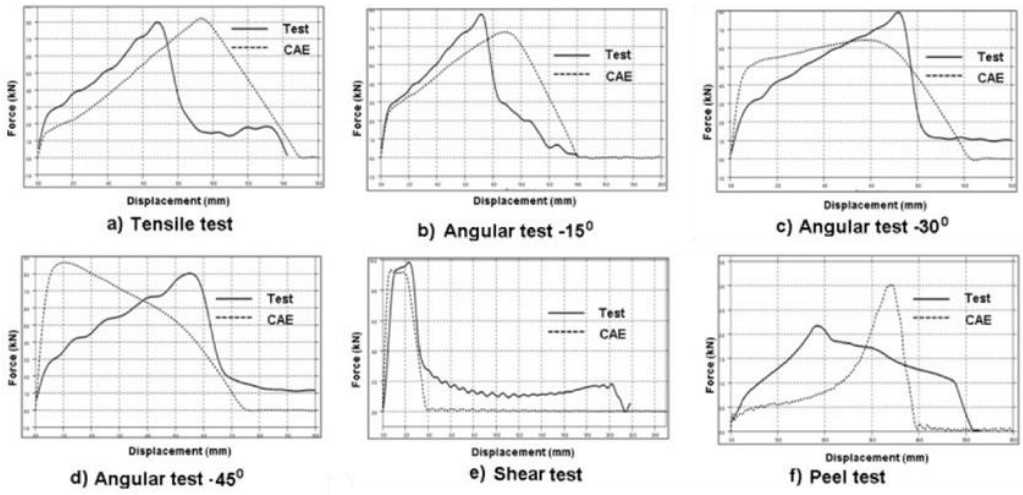

Figure 20: *Tests and CAE correlation using *MAT_240 at coupon level of different loading conditions for spot welds.* [65]

1.8.4. *Constrained_Interpolation_Spotweld

*Constrained_Interpolation_Spotweld, previously named *Constrained_SPR3, is a constraint formulation in LS-DYNA, rather than a material model, that is used to define a spot weld with failure [66]. The physical connection, whether it be a spot weld or self-piercing rivet (SPR), is not meshed when applying this method of modelling. A single node defines the centre of the joint connection and then constraints are applied to the appropriate nearby nodes of the connected shell parts, depicted in Figure 21 (left). A plasticity-damage model is incorporated that reduces the force and moment resultants to zero as the spot weld fails. This model, which has been detailed by Bier and Sommer [52], is similar to the self-piercing rivet model *Constrained_SPR2. The SPR2 model was introduced by Hanssen *et al.* [55] and showed that numerical results gave an acceptable fit the experimental force-displacement curves for the 0°, 45°, and 90° KS-II tests. When applied to the peeling test, however, the model over predicts the forces compared to the experimental behaviour. Small changes to the parameters were able to give a good fit to the peeling test without significantly affecting the fit of the other tests. It was also noted by Hanssen *et al.* [55] that the sensitivity to changes in mesh is minimal for the SPR2 model.

The elastic force calculations in Equation (29) are based on an averaging procedure of the normal relative displacement, δ_n, the tangential relative displacement, δ_t,and the relative rotation, ω_b, between the two connected sheets and the connection stiffness. The calculated forces and moment are uniformly applied to all the coupled nodes.

$$\tilde{\boldsymbol{f}} = [f_n, f_t, m_b] = STIFF \cdot [\delta_n, \delta_t, \omega_b] \tag{29}$$

The post-yielding, or plastic, the behaviour is defined using the flow function:

$$\left[\left(\frac{f_n + \alpha m_b}{R_n}\right)^{\beta} + \left(\frac{f_t}{R_t}\right)^{\beta}\right]^{\frac{1}{\beta}} - F^0(\bar{u}^{pl}) \leq 0 \tag{30}$$

where α determines the influence of bending moment on the failure, the exponent β controls the mixed loading behaviour and the flow curve $\mathrm{F}^0\left(\bar{\mathrm{u}}^{\mathrm{pl}}\right)$ is defined by the user.

The damage and failure behaviour are primarily defined by two plastic equivalent displacements, $\bar{u}_0^{pl}$, and $\bar{u}_f^{pl}$, shown in Figure 21 (right). The plastic equivalent displacement $\bar{u}_0^{pl}(\kappa)$ defines the point when damage initiation begins and $\bar{u}_f^{pl}(\kappa)$ defines when failure occurs.

Both these parameters are defined by the user as a function of load mixity, κ, seen in Equation (31), allowing for different normal and shear failure behaviour.

$$\kappa = \frac{2}{\pi} tan^{-1}\left(\frac{f_n + \alpha m_b}{f_t}\right) \tag{31}$$

Damage initiates when Equation (32) is satisfied, and the transmitted force is reduced linearly as defined by Equation (33). Failure occurs and the connection is deleted when Equation (34) is satisfied.

$$\bar{u}^{pl} - \bar{u}_0^{pl}(\kappa) = 0 \tag{32}$$

$$dmg = \frac{\bar{u}^{pl} - \bar{u}_0^{pl}(\kappa)}{\bar{u}^{pl} - \left(\bar{u}_0^{pl}(\kappa) + \bar{u}_f^{pl}(\kappa)\right)} \tag{33}$$

$$\bar{u}^{pl} - \left(\bar{u}_0^{pl}(\kappa) + \bar{u}_f^{pl}(\kappa)\right) = 0 \tag{34}$$

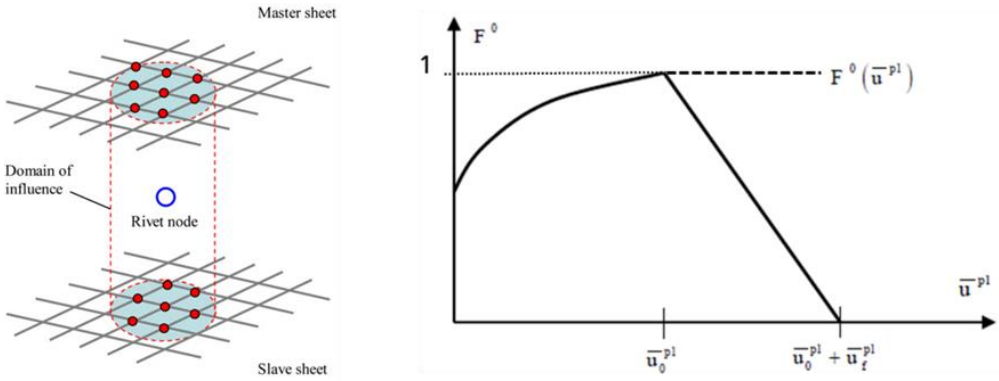

Figure 21: *Left) Schematic representation of *Constrained_Interpolation_Spotweld* [55]. Right) Flow curve with damage and failure plastic equivalent displacements* [52].

Studies that have used the *Constrained_Interpolation_Spotweld model primarily focus on self-piercing rivets. Bier and Sommer [52] showed that the model can reproduce the measured force-displacement curves of the KS-II test, specifically the maximum forces as well as the failure displacements of the experiments. This study also identified the weakness of this model when simulating the peel test. In a study on SPR modelling using several phenomenological models, Bier *et al.* [62] reported that the model shows good reproduction of the overall strength level but experienced oscillations that can be reduced with additional optimization within LS-DYNA. A modified model, called *Constrained_Interpolation_Spotweld (Model 2), was presented by Bier and Sommer and further detailed in two studies [52], [79]. *Constrained_Interpolation_Spotweld (Model 2) addressed the issue of the inability to capture the asymmetry of the peel test load

distribution and was able to accurately predict the peel test experimental behaviour. Shown in Figure 22, the *Constrained_Interpolation_Spotweld model over-predicted the coach peel maximum force and the failure displacement, whereas the *Constrained_Interpolation_Spotweld (Model 2) correctly predicts the maximum force and failure displacement.

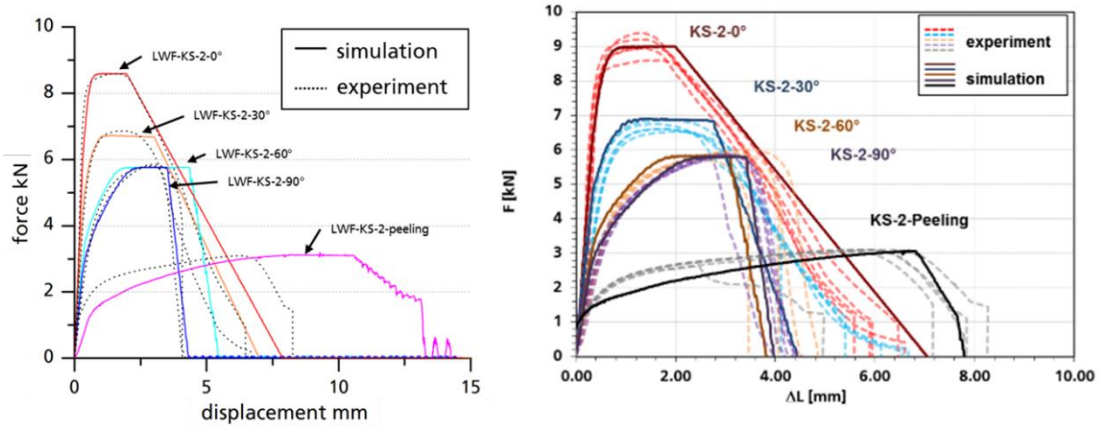

Figure 22: *Simulations results of KS-II and peeling tests with the *Constrained_Interpolation_Spotweld (left)* [52] *and the modified *Constrained_Interpolation_Spotweld (Model 2) (right)* [79].

1.9. Simulation of HAZ Material Failure

Current Gen 2 AHSS materials, and more so for new Gen 3 AHSS, cover a variety of complex microstructures and can contain many alloying elements that further complicate the issue of predicting weld failure behaviour. Button pull-out, for example, is a common failure mode in spot welds that can initiate from the weld notch through the CGHAZ, or initiate from the softened SCHAZ, or by ductile yielding of the base metal outside of the HAZ. As a result, considerable effort has been expended to develop models of HAZ failure. Failure models have been pursued at two levels: (i) CAE-level shell element-based models and (ii) meso-scale models incorporating fine brick element discretization. The CAE level analysis of HAZ modelling employs one or more rings of shell elements in the connected components around the weld nugget elements [48], [57], [59], [68], [70]. Conformal mesh dependent modelling of shell components is required to obtain the HAZ ring elements, which can increase the difficulty of applying the weld model to existing meshed components. There is also an effect on the time step size with this method of modelling the HAZ because each sub-zone of the HAZ is has dimensions of around 0.5-1 mm measured radially from the fusion zone, as reported by Eller *et al.* [41] for different hardness grades of Usibor®1500 and by Tamizi *et al.* [80] for MS 1400. Each concentric ring of HAZ elements must have one edge length at this size to capture the different constitutive properties that will cause them to become the limiting time step elements. Burget and Sommer [48] showed that larger elements

could be used that generalize the HAZ and use adjusted material models to predict the weld coupon behaviour to use HAZ failure modelling at the CAE-level.

As an alternative to shell element discretization of the HAZ, meso-scale analysis uses a detailed model with a mesh of fine solid elements from the fusion zone to the base metal region. In such models, the HAZ constitutive material properties are mapped onto the solid elements around the fusion zone of the weld nugget [41], [48], [53], [69], [81]–[85]. Such detailed models can more accurately predict the weld fracture modes and predict global behaviour better than the CAE-level methods, but cannot be applied at the CAE-level due to minimum time step constraints. Figure 23 shows an example of a CAE-level and meso scale finite element model for predicting spot weld failure with specific HAZ constitutive properties applied to the elements.

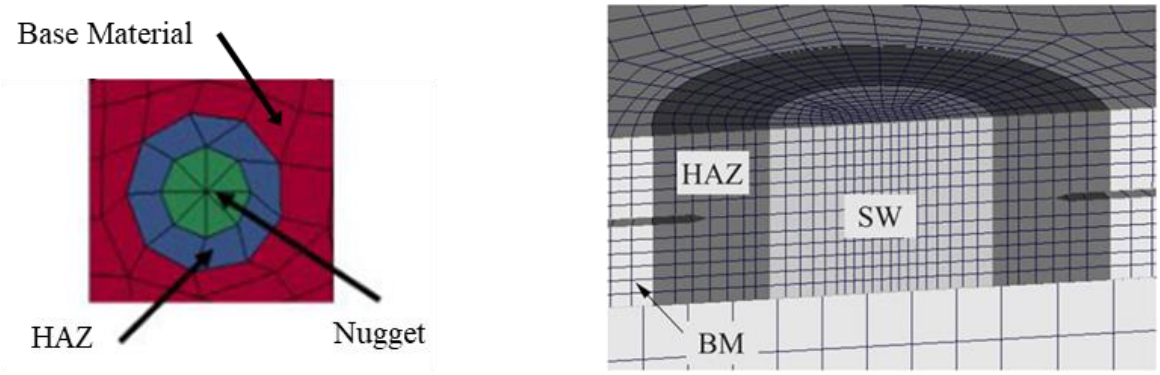

Figure 23: *Left) CAE-level finite element model with 2 mm shell element size, adapted from* [70]. *Right) Detailed model of spot weld with three sub-zones* [82].

The specific HAZ constitutive properties have been determined and implemented by many different methods in the literature. The publications, which are detailed below, use the following methods for obtaining HAZ properties: scaling base metal constitutive properties based on material hardness ratios, characterizing HAZ properties using specimens with reduced dimensions that are cut directly from the post spot welded material, and characterizing specimens that have undergone an experimentally simulated thermal process to recreate the HAZ microstructure using a thermo-mechanical simulation.

1.9.1. HAZ Properties from Hardness Scaling

HAZ sub-zone constitutive models for simulation models have been developed in multiple ways in recent literature. Seeger *et al.* [82] directly scaled the base metal tensile strength by the Vickers hardness of the different HAZ using the conversion table specified by the DIN 50150 (DIN EN ISO 18265:2013) standards. Lee and Choi [53] and Wang *et al.* [68] used a method

developed by Zuniga and Sheppard [86] that uses a relation between the hardness traverse data of the spot weld and the base metal properties to scale the constitutive model of the base metal and obtain HAZ material constitutive models. Nielsen [83] employed a similar tensile strength scaling method by developing a piecewise function that determines the material yield stress profile at any point in the HAZ by scaling the base metal yield stress by the mapped hardness. Kong *et al.* [84] used inverse modelling techniques and incrementally varied material properties until indentation load-displacement curves in the simulation matched the experimental curves. It is noted by the present author that for all the previously mentioned publications, the materials used did not exhibit a zone of reduced hardness lower than that of the base metal in the HAZ, which has been shown by Eller *et al.* [41] to be true for materials that have an ultimate tensile strength less than approximately 600 MPa or 180 HV0.1. Mohamadizadeh *et al.* [87] applied a strain-rate dependent Voce hardening rule for Usibor® 1500-AS, developed by Bardelcik *et al.* [88], based on hardness values measured across the spot weld. It has been identified by Ghassemi-Armaki *et al.* [70] that using the hardness data to scale the base metal constitutive data does not accurately capture the onset of yielding and the hardening behaviour of the different HAZ microstructures. Thermo-simulated "HAZ specimens" from the Gleeble (discussed later) provide more accurate hardening behaviour and fracture strain. Figure 24 shows the difference in experimental hardening data between the "HAZ specimens" from the Gleeble and data from scaling the base metal data using HAZ hardness.

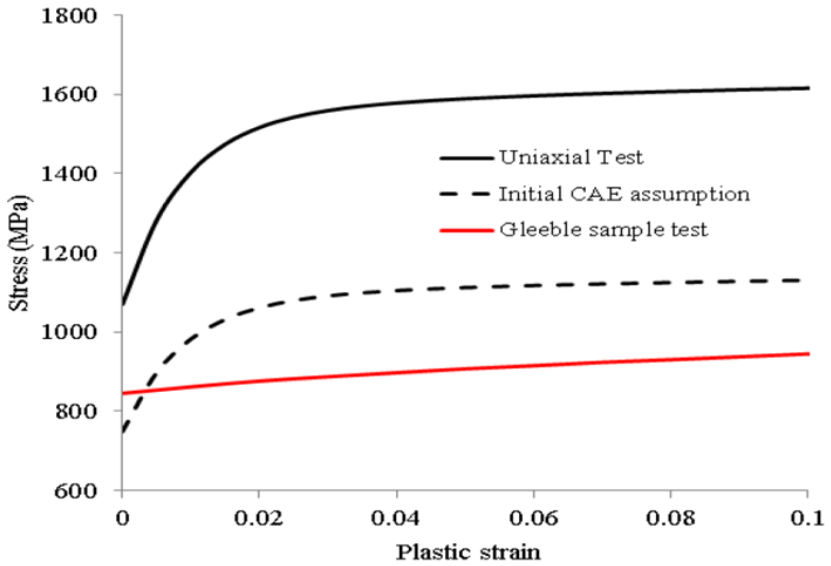

Figure 24: *Usibor® 1500-AS flow curves; Base metal tensile specimen (solid black), hardness scaled base metal (dashed black), Gleeble thermo-simulated tensile specimen (red).* [57]

1.9.2. HAZ Properties from Gleeble

Dancette *et al.* [89], Biro *et al.* [90], and Rezayat *et al.* [91], have shown that experimental simulations of the resistance spot welding thermal cycles can be performed with a Gleeble thermo-mechanical simulator in order to reproduce the local microstructures in the weld. Local heat affected zone material constitutive behaviour can be obtained using characterization tests carried out with the HAZ specimens produced with the Gleeble and used for modelling of the weld mechanical behaviour [48], [57], [69], [70], [89]. Burget and Sommer [48] compared the results of tensile tests and 3-point bend tests using detailed meso-scale models with simplified CAE level models. It was found that the calculated results of the detailed model accurately predicted the reduction of tensile strength due to the presence of the softened HAZ inside the tensile specimen. The simplified model required adjusting the material model properties to predict the stress-strain response of the tensile tests due to the element size being significantly larger than the actual width of the HAZ zone. As validation, the calculated results of the 3-point bend tests showed very good agreement with the experimental curves for the detailed model and the simplified model after the material models were adjusted. Other reported results by Dancette *et al.* [69] of a detailed model also showed good agreement of force-displacement curves and fracture behaviour using material models obtained from Gleeble tests. Using a simplified HAZ and weld model, Ghassemi-Armaki *et al.* [70] concluded that the FEA results of welded tensile and cross tension tests using input data Gleeble samples and tested welds show a good correlation to experimental characterization with respect to failure load, displacement, and failure location.

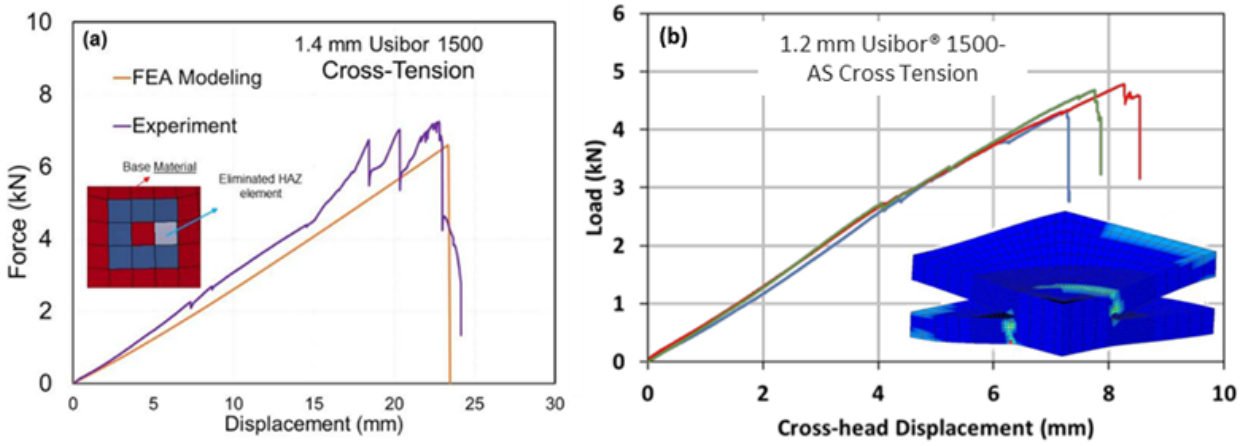

Figure 25: *Force-displacement curves for experimental cross tension test and simulation model. Simplified FEA model (left)* [70] *and detailed model (right)* [87].

1.9.3. HAZ Properties from Miniature Specimens

Nakayama *et al.* [81] developed a new testing technique utilizing tensile specimens with a gauge length of 1 mm to measure stress-strain relationships and ductility of the base metal and HAZs for RA590 and DP780. The failure strain and load of static tensile shear weld tests were predicted with good accuracy when applying their HAZ material properties to a meso scale model. Tao *et al.* [92] used miniature tensile specimens extracted from weld joint coupons to obtain material models for the base metal, heat-affected zone, and the fusion zone through the use of strain fields measured using DIC techniques. The material models were incorporated into a meso scale FE model to compare the predicted overall deformation behaviour and local stress-strain behaviour with that measured from the experiments. It was reported that the material models developed from the tensile coupons consisting entirely of one weld zone material (i.e., BM, HAZ, and fusion) can be used to simulate the deformation response of an entire spot weld in a finite element simulation to a reasonable degree of accuracy. Burget and Sommer [85] used inverse simulations to determine the parameters of the Gologanu model [93] (a modified Gurson model) and fracture criteria in a heterogeneous spot weld consisting of 22MnB5 and HC340LAD. Their study used reduced dimensions specimens for smooth tensile, notched tensile, and double notched shear specimens cut from the base metal, HAZ, and weld nugget. The authors showed simulations with their calibrated model reproduced the experimentally measured force *versus* displacement well using ABAQUS/Explicit except for the case of coach peel

1.10. Simulation of Weld Groups (Structural Connections)

The weld group tests, as discussed in Section 1.7, are used as validation tools for the spot weld model calibrated from single spot weld test data. The weld group test design, also referred to as component specimen tests, can follow either a mixed loading condition or an isolated loading condition methodology. The T-joint design emulates the lower section of a B-pillar in an easily manufacturable design that will validate the weld model in terms of predicting complex loading conditions and overall behavior in a crash scenario. The Caiman Mode I test isolates the loading conditions imposed on the spot welds such that one failure mode prediction (i.e. tensile) is validated. Isolated loading condition component tests ideally minimize the amount of deformation occurring in the base metal regions to reduce the impact of model parameters used for different loading conditions.

Seeger *et al.* [50] used the T-joint test to validate the *MAT_100_DA model that was calibrated using four different rotation angles of the single spot weld KS-II test and a peel test. The force *versus* displacement simulation results show accurate predictions of the peak load and displacement, seen in Figure 26 (a), as well as the initial weld failure location. After the peak load is reached and weld failure initiates, the sudden unloading predicted by the model fails to capture a large amount of absorbed energy since the overall structure continues to deform while the spot welds unload. The authors attributed the elastic material behavior of the spot weld to the sudden failure.

Yang *et al.* [56] similarly used the T-joint test with different material stack-ups and loading directions to validate calibrated spot weld models. The authors noted several differences between the simulation predictions and the measured results from testing, seen in Figure 26 (b). It was seen that the physical specimens had partial weld failure whereas the model predictions showed full separation of the welds. Additionally, it was noted that the calibrated weld failure model assumed sudden failure once failure initiated; crack propagation through damage modelling was beyond the scope of the study. This treatment led to under prediction of the peak force because in the physical specimen a partially failed weld still has a residual load carrying capacity that the model did not account for.

Bier and Sommer [52] apply their calibrated *Constrained_Interpolation_ Spotweld (Model 2) to the T-joint test for model validation of SPR connections. Their results, seen in Figure 26 (c), show a good prediction of the maximum force and reasonable trends in the force *versus* displacement data. It is seen though that the model slightly over predicts the final displacement before failure.

May *et al.* [63] developed a rate dependent cohesive zone model to predict adhesive bonds for high strength steel DP-K 30/50. The adhesive model was calibrated from data available in the literature and the adherend (parent material) properties were determined from tensile testing. The models developed were validated using T-joint components loaded in front impact and side impact configurations. The results of the measured and predicted values of the component testing for front impact under quasi-static conditions are seen in Figure 26 (d). The authors reported accurate predictions of the peak loads and the general shape of the force *versus* displacement curves for all loading conditions tested.

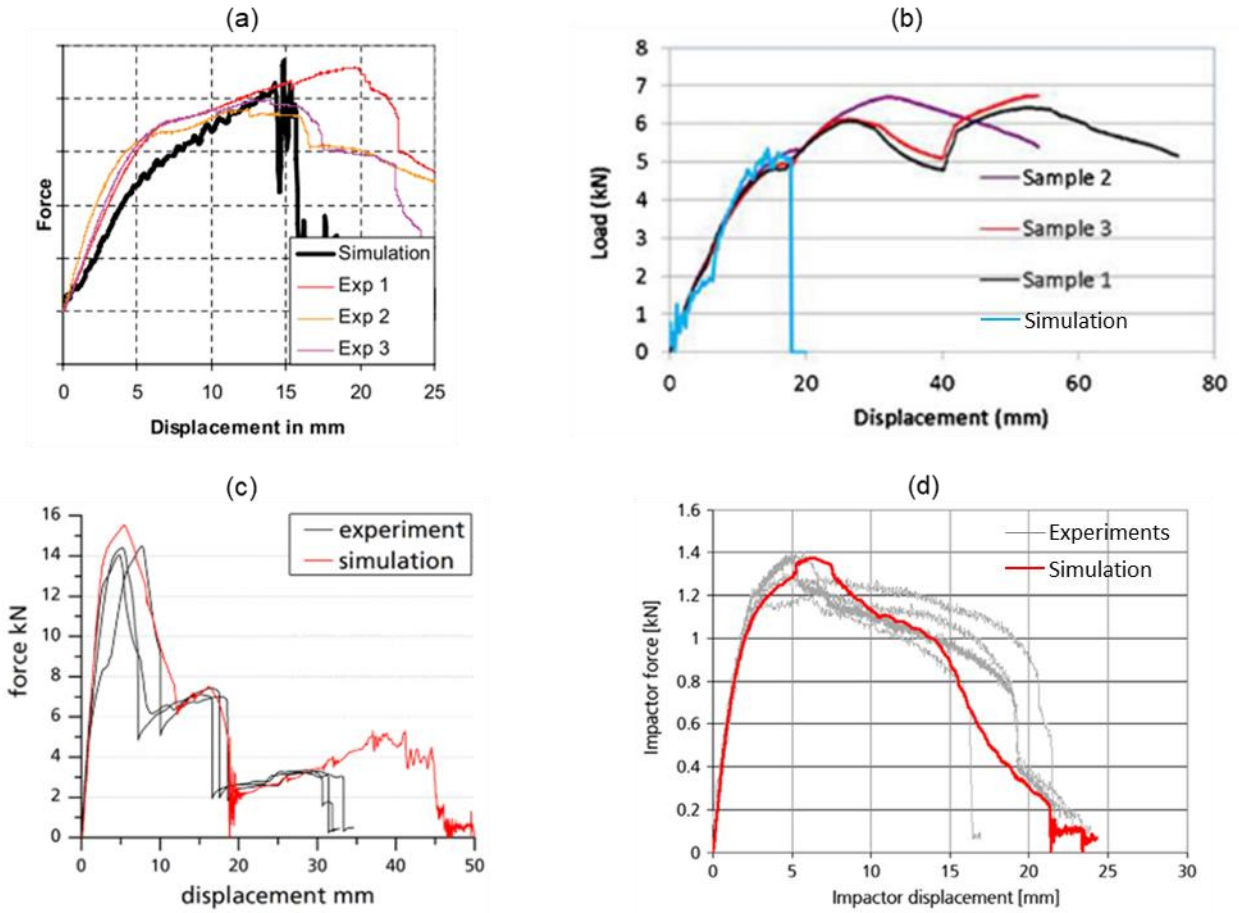

Figure 26: *T-joint measured and predicted force-displacement responses from (a) Seeger* et al. [50] *(b) Yang* et al. [56] *(c) Bier and Sommer* [52] *(d) May* et al. [63].

The Caiman Mode I test, developed by O'Keeffe [51] and shown in Figure 14, promotes weld failure within spot weld groups under a tensile/peel loading condition using two hat-channels that are spot welded along partial lengths of the flanges. O'Keeffe developed a model of this experiment using the *MAT_100_DA spot weld model calibrated using single spot weld cross tension and lap shear experiments. The model was assessed based on the Caiman Mode I test for Usibor® 1500-AS in the fully quenched and softened conditions (using 700° in-die heating in the flange region), as presented in Figure 27. The fully quenched predictions show an overly stiff response during elastic loading but match the rapid brittle failure modes seen in the experimental data. The softened predictions accurately match the force-displacement response of the experiments up to peak load, but the peak load is under predicted. The model predictions also show more rapid unloading than what is seen in the measured data for both material conditions, resulting in lower absorbed energy. O'Keeffe indicated the importance of calibrating the spot weld model to capture the post-failure response and accurately predict the total absorbed energy.

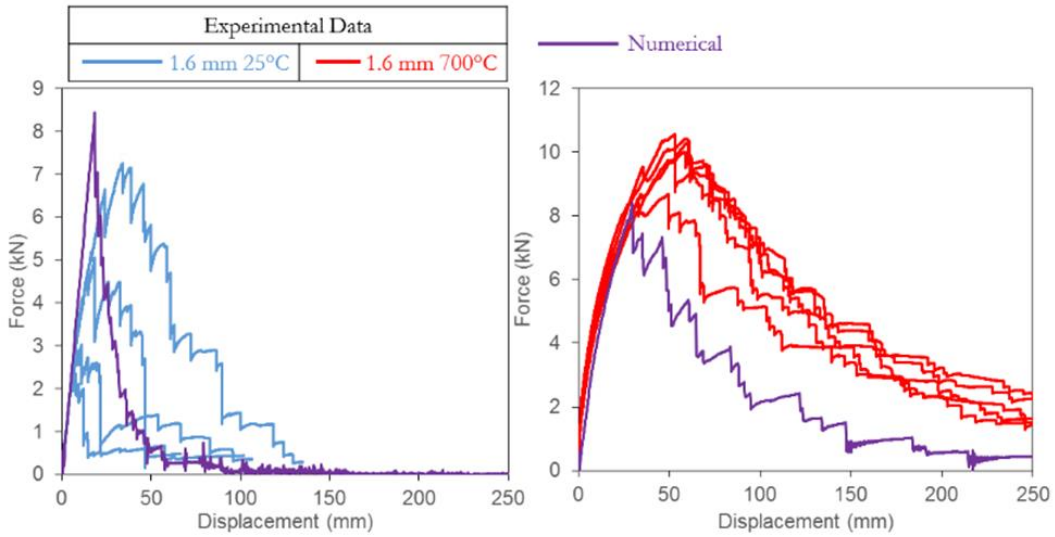

Figure 27: *Caiman Mode I measured and predicted force-displacement response for quasi-static tests* [51]*. Fully hardened condition shown on left and softened condition (using 700° in-die heating in the flange region) shown on right.*

1.11. Current Work

There exists a large variety of materials that are applied in the construction of an automotive BIW structure as well as a range of different joints and joint modelling techniques that need to be captured within CAE-level automotive crash simulations. For the application of hot stamped grade steels that are considered in the current thesis, there are very few published results on the modelling of spot welds. Furthermore, a consistent shortfall reported in the published literature is the need for improved predictions of the onset of failure and post-failure unloading behaviour of resistance spot welds, particularly in high strength steel alloys. Accurately capturing the post-failure behaviour of spot welds in numerical simulations for CAE analysis represents a significant need. The development of models of single spot welds that can predict the force *versus* displacement response for isolated loading conditions (tensile, shear, and bending), as well as mixed loading conditions is also a topic of current research. Weld group tests under various mixed loading conditions, such as the T-joint, have been employed successfully for qualitative model validation using metrics such as failure location and peak forces. The Caiman Mode I, a predominantly Mode I/peel loading condition weld group test, has been developed and quantitative analysis applied to validate the calibrated weld model. No test for weld groups under predominantly shear loading conditions exists.

Thus, the primary objective of this thesis is to develop the geometry and test setup for a component level test that will produce failure in weld groups under shear loading conditions. There

is also focus on exploring more accurate numerical models for spot welded connections that will fully capture mixed loading conditions and the overall weld failure behaviour seen in vehicle crash scenarios. This thesis examines weld failure in hot stamped Ductibor® 500-AS, Ductibor® 1000-AS, and Usibor® 1500-AS, of thickness 1.2 mm and 1.6 mm. These alloys are currently under consideration for integration within automotive front-end structures. Such structures are currently constructed from lower tensile strength cold-formed materials. This work builds in part on the work done by O'Keeffe [51] in developing the Caiman Mode I test for group weld failure under tensile-normal loading conditions. The intent of the weld group experiments is to provide a validation tool for the numerical models that are calibrated from single spot weld test data. The shear group weld component specimens developed here, termed the Caiman Mode III, are tested under quasi-static and dynamic conditions.

Tensile lap shear and cross tension single spot weld experiments are performed in this work to investigate mechanical behaviour and characterize RSW performance. Simulations of the single spot weld experiments were developed using the *MAT_100_DA spot weld model to remain consistent with previous modelling efforts, as well as a more novel approach considering *MAT_240 because it has been reported to better describe the deformation and failure behaviour of various connection methods. The *MAT_240 model has separate parameters for normal-tensile loading failure and shear loading failure. Applying *MAT_240 to spot welds is novel since the model was originally implemented to simulate adhesively bonded connections. The different weld models are calibrated to establish accuracy and feasibility for implementation into full vehicle simulations for the purpose of evaluating crash performance and safety.

The balance of this thesis is organized as follows: Chapter 2 presents the material and specimen preparation; Chapter 3 contains the single spot weld characterization experimental data and numerical model for single spot weld model calibration; Chapter 4 details the development process of the Caiman Mode III test; Chapter 5 presents the final design experimental and simulation results for validation; and lastly the final conclusions and future recommendations are in Chapters 6 and 7.

2. Specimen Preparation

A variety of equipment was used to prepare and test welded connections, and record data for all of the experiments. The furnace and press were used to process (hot stamp) the material into the fully quenched condition before spot weld welding and testing. The spot weld characterization was done under quasi-static conditions while the group spot weld testing was performed under both quasi-static and dynamic conditions. This chapter describes the equipment and process methodology used to prepare and weld the samples prior to mechanical testing. The actual testing methodology is described in Section 3.1 for the single spot weld specimens, and Section 4.2 and 4.3 for the quasi-static and dynamic group weld specimens, respectively.

2.1. Furnace

A Deltech DT-20 front load furnace was used for all of the thermal processing in this work. The furnace uses three heating elements on both the top and bottom surfaces of the interior to reach a maximum operating temperature of 1000 °C. Each top and bottom pair makes up a zone that is independently controlled and maintains a specified temperature using a thermocouple feedback system. During normal operation all three zones were set to the same desired temperature.

2.2. Press

The press used for quenching was a hydraulic, single-acting press manufactured by Macrodyne Technologies Inc. It has a 120 tonne actuator that is supplied by either a 150 GPM proportional valve or 30 GPM servo valve. The press is controlled by an MTS FlexTest SE servocontroller with custom LabView applications to provide analogue voltages and record digital displacement and load data. A National Instruments Multifunction I/O device, model USB-6216, is used to interface between the PC running LabView and the MTS FlexTest SE. The displacement is measured with a string potentiometer connected to the ram. The load is calculated using the actuator dimensions and pressure transducers at the inlet and outlet ports. The 150 GPM proportional valve is used under displacement control for high speed applications while the 30 GPM servo valve is used for load control applications.

Two different die sets were used for quenching material, depending on the size of the blank. There is a flat die, seen in Figure 28, with built-in water-cooling channels that can be used for blanks up to the dimensions 240 mm by 340 mm. This die is two separate pieces that are split in

the centre to allow one side to be raised with shims to accommodate multi-gauge tailor welded blanks (TWBs), which are not used in this project. The other die used is a rail forming die that is designed to form hot stamped hat channels and seen in Figure 29. It has an outer binder supported by nitrogen springs and a male punch fixed to the stationary platen on the hydraulic press. There is a female die and top binder surface fixed to the ram of the press. The binder surface on each side of the punch is 613 mm long and 110mm wide. The binder is supported by four DADCO U.0800 nitrogen springs with a maximum stroke length of 80mm. The nitrogen springs are pre-charged to 1500 psi that provides a total on-contact force of 4,565 lbf. In this current setup, the compressed stroke length when the dies are fully closed is 51.2 mm, resulting in a total final force of 6,144 lbf.

2.3. Material Preparation

The material used for this project are three different grades of press hardenable steels supplied by ArcelorMittal for the application of hot stamping. The three steels are Ductibor® 500-AS150, Ductibor® 1000-AS150, and Usibor® 1500-AS150, all with a nominal thicknesses of 1.2 mm and 1.6 mm. The total coating weight, including both the top and bottom surfaces, is 150 $^{g}/_{m^2}$ for all materials. The mechanical properties of these three hot stamped steels are listed in Table 1, and the hardening curves are presented in Figure 46 in Section 3.3.1. The chemical composition and the carbon equivalent percentages for each material are listed in Table 2. The CE_{IIW} carbon equivalent formula [94] was developed by the International Institute of Welding (IIW) as a weldability index, to determine how the alloying elements affect the maximum hardness in the HAZ. The CE_N carbon equivalent formula was developed by Yurioka *et al.* [95] to assess the susceptibility of steel to cold cracking for steels that have widely ranging carbon contents. Taylor *et al.* [96] used the CE_N formula in a study investigating 22MnB5 and 38MnB5 grades of boron hot-stamped steel. The carbon equivalent was found with two different methods, using Equations (35) [94] and (36) [96].

$$CE_{IIW} = C + \frac{Mn}{6} + \frac{Cu + Ni}{15} + \frac{Cr + Mo + V}{5} \tag{35}$$

$$CE_N = C + A(C) \cdot \left\{ \frac{Si}{24} + \frac{Mn}{6} + \frac{Cu}{15} + \frac{Ni}{20} + \frac{Cr + Mo + Nb + V}{5} + 5B \right\} \tag{36}$$

$$\text{where } A(C) = 0.75 + 0.25 \tanh[20(C - 0.12)] \tag{37}$$

Table 2: *Maximum weight percent chemical composition of the three hot stamped steels considered and calculated carbon equivalent contents, from ArcelorMittal* [18]

Material	C	Si	Mn	P	S	Al	B	Ti + Nb	Cr + Mo	CE_{IIW}	CE_N
Ductibor® 500-AS	0.1	0.5	1.9	0.03	0.025	0.015 - 0.2	0.001	0.24		0.417	0.356
Ductibor® 1000-AS	0.12	0.8	2	0.3	0.01	0.01 - 0.1	0.01	0.12	0.6	0.573	0.541
Usibor® 1500-AS	0.25	0.4	1.4	0.03	0.01	0.01 - 0.1	0.005	0.12	1	0.683	0.748

Using the calculated carbon equivalent for each material as an approximation of the carbon content and examining the carbon-iron binary phase diagram [19, p. 319] it can be seen that the materials are hypoeutectoid steels. The hot stamping process requires heating the material to a temperature above the upper critical temperature point (A_3) and holding at this temperature to achieve a complete austenite microstructure. For this work, the material was inserted into the oven at 930°C for six minutes before being removed and quenched between flat dies that were water cooled to maintain a temperature of approximately 25°C.

The provided material in the as-received condition was in large 1200 mm x 1500 mm sheets, that were cut from the coil, and were reduced to smaller blanks for hot stamping. For single spot weld characterization, the coupons range in dimensions from 50 mm to 150 mm. To prepare material for these coupons, 215 mm square blanks were sheared from the large sheets. After the austenitization process, the blanks were transferred into a flat quenching die, shown in Figure 28. For the single spot weld blanks, the smaller flat dies were installed, and the press was operating under load control for the quenching process. The clamping force during quenching was set to 136,000 lbf or 605 kN, resulting in a quench pressure of 13.1 MPa for the blank size used. The dies were held closed at this pressure for 15 seconds to ensure that the blanks cooled to a low enough temperature for the martensite transformation to complete.

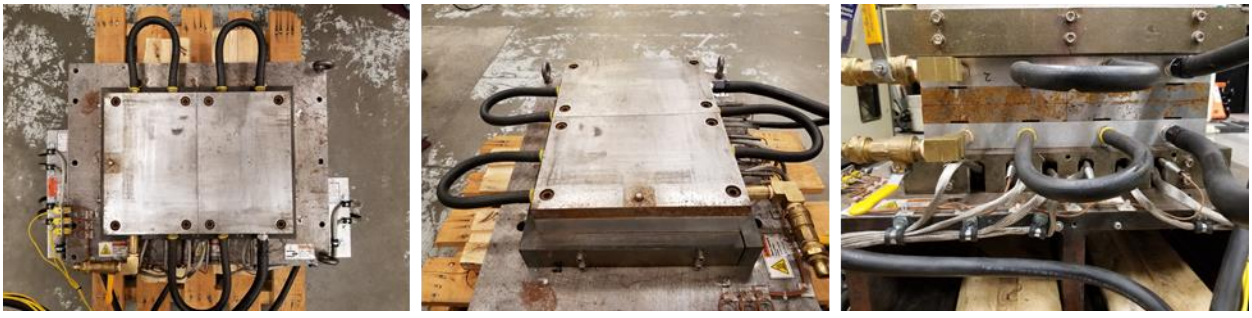

Figure 28: *Picture of flat die with cooling channels present*

The blanks used for the Caiman Mode III group spot weld tests are 600 mm long by 100 mm wide. These blanks were treated with the same hot stamping process as the smaller blanks used for

single spot weld characterization. The flat die that was used for the smaller blanks cannot accommodate the length of the Caiman Mode III blanks and another die must be used for quenching. The binder of the rail die show in Figure 29 is large enough to be used for this purpose. A dummy blank was placed on the opposite side binder surface to ensure that there was evenly distributed loading on the blank being quenched. The nitrogen springs supporting the binder initially only provided enough force to apply 0.5 MPa to the larger Caiman Mode III blanks. Steel blocks were place under the binder to stop the downward travel and allow the press to apply more pressure to the blanks. The clamping force was set to 136,000 lbf and created a quenching pressure of 10 MPa.

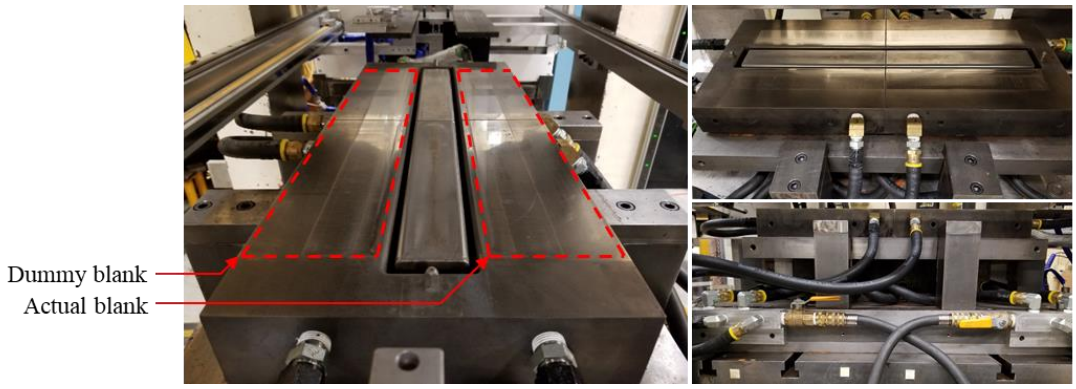

Figure 29: *Image of lower hot stamping rail die binder, punch, and cooling tubes.*

2.4. Spot weld process

The resistance spot welding process used for all specimens in this work was developed and performed by the Promatek Research Centre. Two different weld schedules were developed, one for each thickness used, that produce spot welds in all three materials to be consistent with industrial standards. The spot weld settings used are shown in Table 3. Micrographs, taken by Mohamadizadeh *et al.* [49], of the spot welds in the Ductibor® 500-AS material and the Usibor® 1500-AS material are shown in Figure 30. Note that these two materials are referred to as PHS600 and PHS1500 in the work by Mohamadizadeh *et al.* [49] but are from the same blanks as the material in this work.

Table 3: *Resistance spot weld schedule.*

Sheet Thickness	Force	Pre-Heat	Main Weld	Hold Time
1.2 mm	770 lbf	8 kA – 33 ms	7 kA – 400 ms	200 ms
1.6 mm	900 lbf	10 kA – 33 ms	7 kA – 400 ms	200 ms

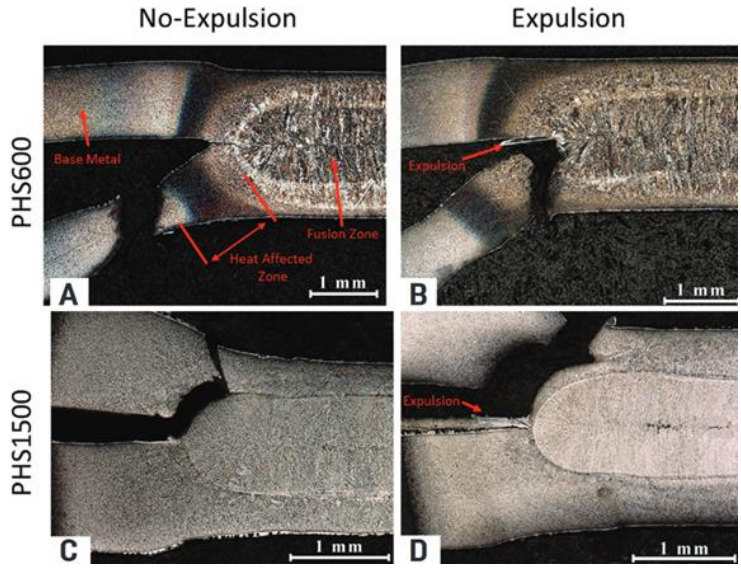

Figure 30: *Micrograph images of spot welds after failure (A) PHS600 (Ductibor® 500-AS) no expulsion; (B) PHS600 (Ductibor® 500-AS) with expulsion; (C) PHS1500 (Usibor³ 1500-AS) no expulsion; (D) PHS1500 (Usibor® 1500-AS) with expulsion.*

3. Single spot weld characterization

3.1. Single spot weld specimens

Single spot weld characterization is performed in this work to objectively determine the strength of the weld for each isolated loading condition and quantitatively compare the weld strengths of joints using different materials or thicknesses in a consistent manner. There are two basic test methods for determining the strength of a single resistance spot weld defined by the American Welding Society (AWS). These two methods are the tensile lap shear test and the cross tension test. The AWS D8.9:2012 standard dictates that the crosshead velocity shall be 10 mm/min and conducted at room temperature (20°C ± 5°C) [36]. Each test is considered complete when full separation occurs between the two welded coupons or when the total displacement extends beyond approximately 500% of the displacement at peak load. The test matrix used for the single spot weld testing regime is shown in Table 4. The AWS D8.9:2012 standard suggests at least three specimens are tested for each weld condition. Five repeats are selected here to assist with the weld model development.

Table 4: *Single spot weld test matrix.*

Material	Thickness [mm]	# of Lap Shear	# of Cross Tension
Ductibor® 500-AS	1.2	5	5
	1.6	5	5
Ductibor® 1000-AS	1.2	5	5
	1.6	5	5
Usibor® 1500-AS	1.2	5	5
	1.6	5	5

All single spot weld testing was performed under quasi-static conditions using an MTS Criterion® Model 45 tensile frame with a 100 kN load cell attached to the crosshead. The tensile frame was controlled via the MTS TestSuite™ TW Elite software. The tensile load and crosshead displacement were recorded at 500 Hz for the duration of the test. The single spot weld test specimens were gripped in the tensile frame using knurled hydraulic grips set to 2500 psi. The crosshead speed was determined by the specific test that was being performed. The single spot weld tests recorded the crosshead displacement, load cell force, and time data that was output from the MTS frame.

3.1.1. Lap shear

The lap shear test applies a tensile load along the weld interface plane to develop a shear stress in the weld nugget. This test results in only the approximate ultimate shear strength of the spot weld because the weld nugget begins to rotate out-of-plane as the load increases. The test begins with an isolated shear loading condition but begins to transition into a mixed shear and normal loading as the weld nugget rotates [49]. The geometry used is illustrated in Figure 31 and the dimensions used are listed in Table 5. Shims were used when installing the test specimens in the grips of the tensile frame to ensure that the coupons align properly.

Table 5: *Lap shear geometry dimensions, all dimensions in mm.*

Sheet thickness	Coupon length L	Coupon width W	Overlap O	Sample length SL	Unclamped length UL	Gripped length GL
1.2 / 1.6	125	40	40	210	130	40

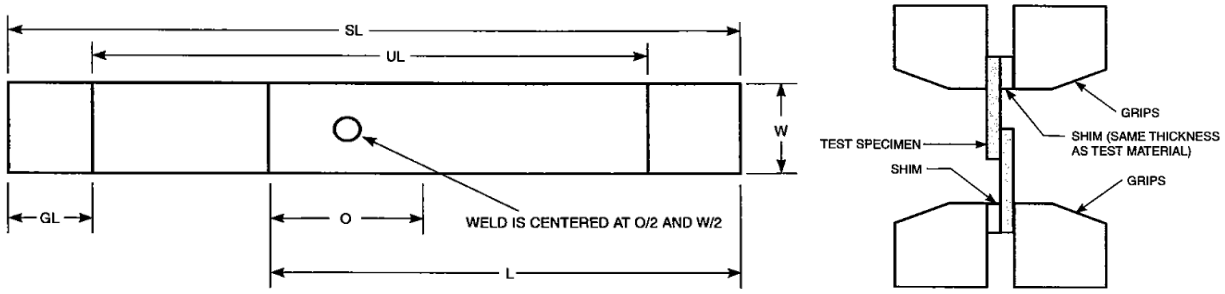

Figure 31: *Tensile lap shear assembly geometry and schematic of gripping in the tensile frame.* [36]

3.1.2. Cross tension

The cross tension test applies a tensile load normal to the interface plane of the spot weld to develop a normal stress in the weld nugget. This test requires significant fixtures to connect the welded specimen to the tensile frame grips. The applied load is centred on the weld nugget and is rotationally symmetric about the weld nugget so there is no transition from the initial isolated loading condition. However, the cross tension tests typically develop a large amount of coupon deformation which makes it difficult to determine the exact displacement before weld failure occurs. More analysis on this is discussed in detail in Section 3.2.2. The coupon and welded assembly geometry, and the fixture method for the cross tension test is shown in Figure 32. The dimensions used for the tests are listed in Table 6. The bolts that connect the bottom and top clamps to the weld specimen were torqued to 40 Nm, or 29.5 ft·lbf.

Table 6: *Cross tension geometry dimensions, all dimensions in mm.*

Sheet thickness	Coupon length L	Coupon width W	Overlap O	Hole spacing HS
1.2 / 1.6	150	50	50	100

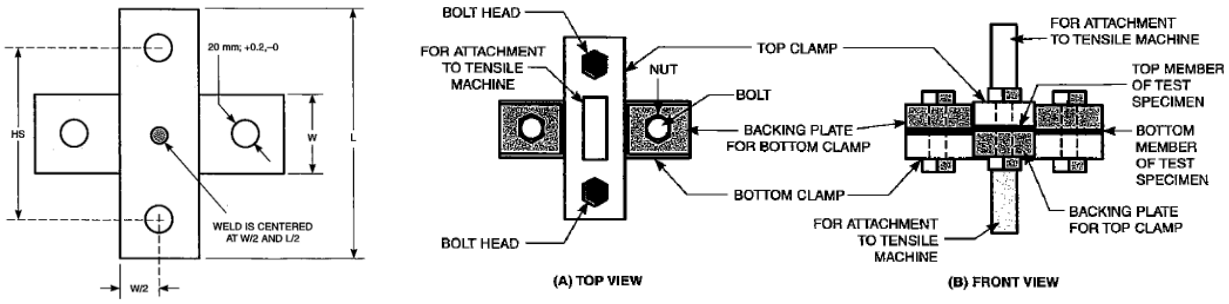

Figure 32*: Cross tension assembly geometry and fixture schematic.* [36]

3.2. Single spot weld mechanical performance

In this section, the single spot weld tensile lap shear and cross tension test results are reported, and the failure modes and behaviour are analysed. The data presented is the maximum load and the crosshead displacement when the maximum load occurs, which together are taken as the onset of failure initiation, as well as the total energy absorbed by the specimens until complete separation occurs. The failure modes, seen in Figure 33, are classified in the AWS D8.1M:2007 standards as interfacial failure, partial thickness fracture, full button pull out, or a mixed form thereof [35].

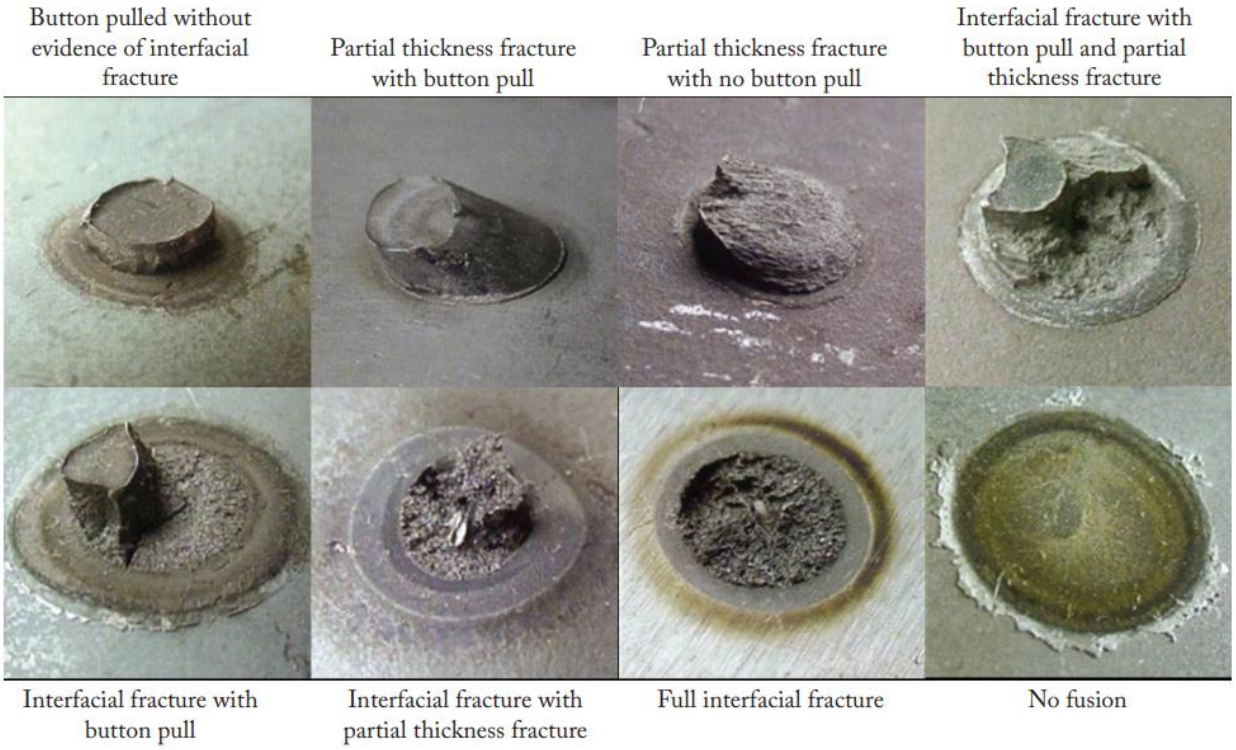

Figure 33: *Possible spot weld fracture modes.* [35]

3.2.1. Lap shear Test Results

The 1.2 mm thickness single spot weld tensile lap shear force *versus* displacement and absorbed energy *versus* displacement test results are presented in Figure 34 and Figure 36, respectively. The 1.6 mm thickness test results for force *versus* displacement and absorbed energy *versus* displacement are in Figure 35 and Figure 37, respectively. Note that spot welds that exhibited expulsion are indicated in these figures with a dashed line. The peak force, the displacement when the peak force occurred, and the total energy absorbed average values for each material condition are summarized in Table 7.

Table 7: *Summary of average data values for single spot weld tensile lap shear tests.*

Material	Thickness [mm]	Max Load [kN]	Displ @ max [mm]	Absorbed Energy [J]
Ductibor® 500-AS	1.2	14.2 ± 0.2	1.6 ± 0.1	29 ± 3
	1.6	19.3 ± 0.9	1.6 ± 0.3	43 ± 20
Ductibor® 1000-AS	1.2	16.8 ± 0.1	1.1 ± 0.03	16 ± 2
	1.6	21.0 ± 0.4	1.0 ± 0.03	14 ± 1
Usibor® 1500-AS	1.2	13.2 ± 0.1	0.6 ± 0.03	7 ± 2
	1.6	26.5 ± 2.4	1.0 ± 0.1	19 ± 3

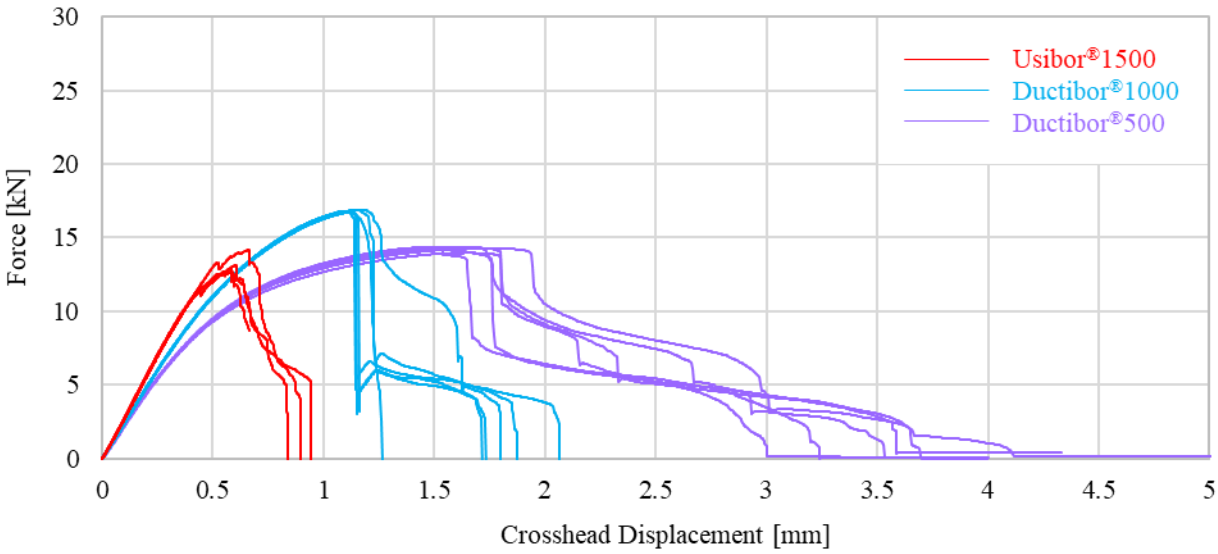

Figure 34: *Lap shear force versus displacement data for 1.2 mm specimens.*

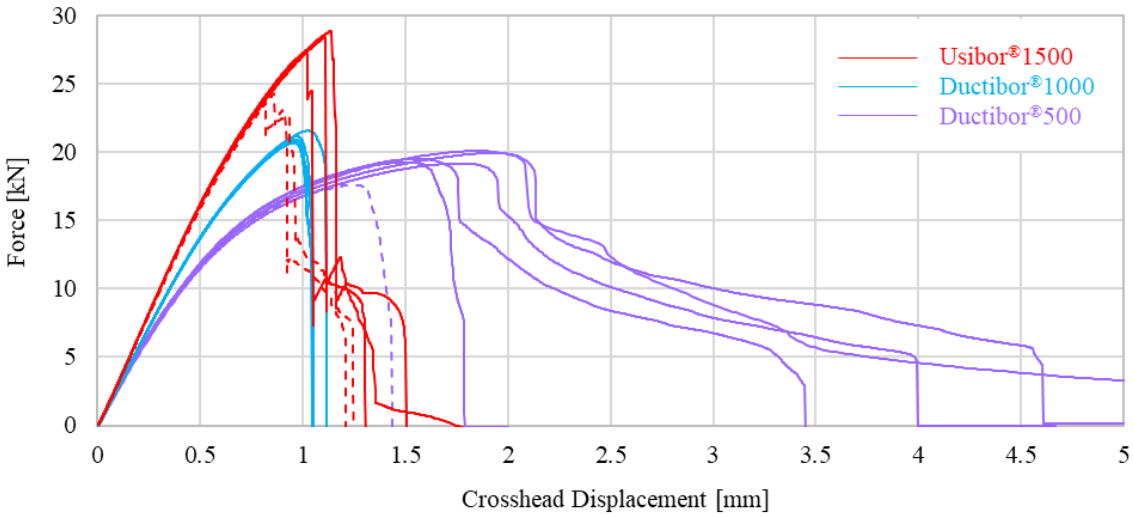

Figure 35: *Lap shear force versus displacement data for 1.6 mm specimens. Dashed lines showed expulsion.*

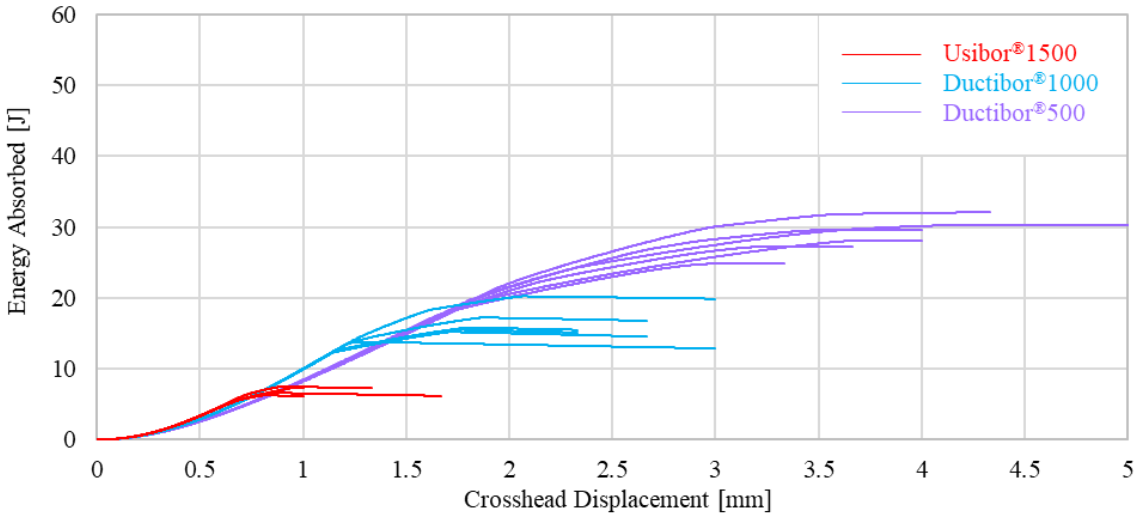

Figure 36: *Lap shear energy absorbed versus displacement data for 1.2 mm specimens.*

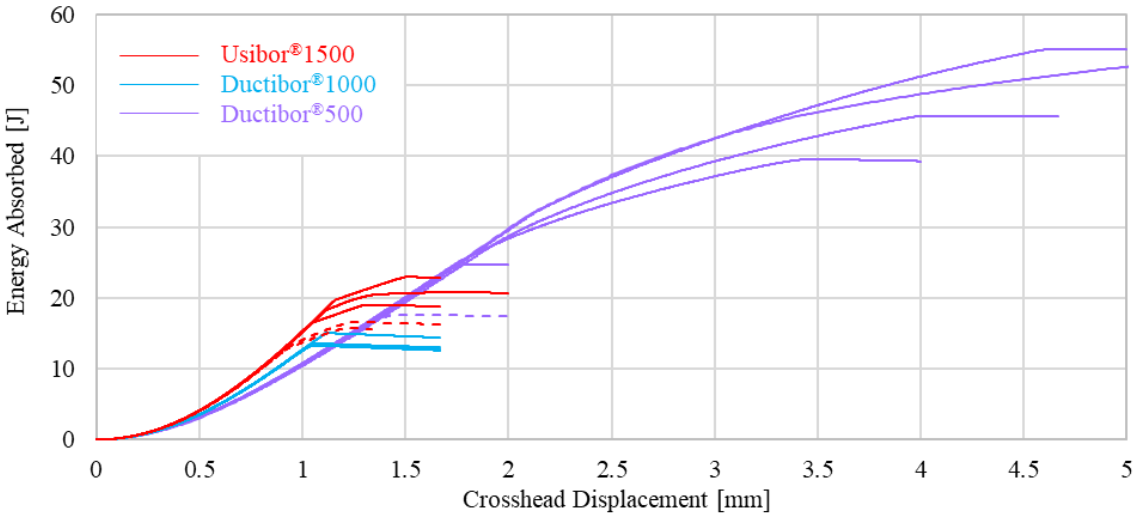

Figure 37: *Lap shear energy absorbed versus displacement data for 1.6 mm specimens. Dashed lines showed expulsion.*

It is seen from Table 7 that for all materials tested, the lap shear peak forces increased with thickness; however, increasing the thickness did not always correspond to an increase in the total energy absorbed for each material, as seen in the Ductibor® 1000-AS tests and discussed later. A few distinct behaviours are noted from these tests. When the load is decreasing after the peak force, termed the unloading region, the specimens often exhibit abrupt drops in load followed by periods of sustained loading. The sudden drops are the result of brittle crack growth through the heat-affected zone from the nugget to the outer surface of the specimens [97]. The sustained unloading regions occur when the brittle fractures are arrested, allowing for continued plastic deformation and ductile crack growth.

The lap shear experiments for each material condition exhibited consistent partial thickness fracture with button pull out (Figure 33), except for three outlier specimens for which expulsion occurred during spot welding. The specimens that contain expulsion from the welding process typically exhibit a reduced peak load and little-to-no unloading region (Figure 35) due to the rapid brittle interfacial failure that is triggered by excessive surface indentation and porosity formed when expulsion occurs [10], [38], [98], [99]. The expulsion that occurred in the Ductibor® 500-AS 1.6 mm specimen is attributed to a burr, seen in Figure 38, which was left over from the laser trimming operation to create the blank geometry. The burr created a gap between the two coupons that caused an unequal force distribution when they were spot welded together, allowing for the expulsion of melted material from the fusion zone.

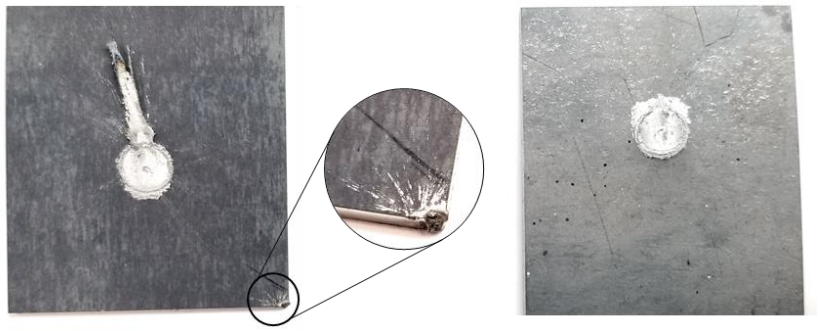

Figure 38: *Ductibor® 500-AS 1.6 mm lap shear specimen exhibiting expulsion. Burr from laser trimming expanded in detail.*

Also, one of the Ductibor® 500-AS 1.6 mm tests extends out of the plot area of Figure 35 before complete failure occurs. This specimen had a unique shared asymmetric pull out failure mode that is not classified in the AWS standards, shown in Figure 39. In this case the weld nugget was pulling out of both sides of the specimen at the same time and complete separation did not occur until the weld nugget rotated almost 180°.

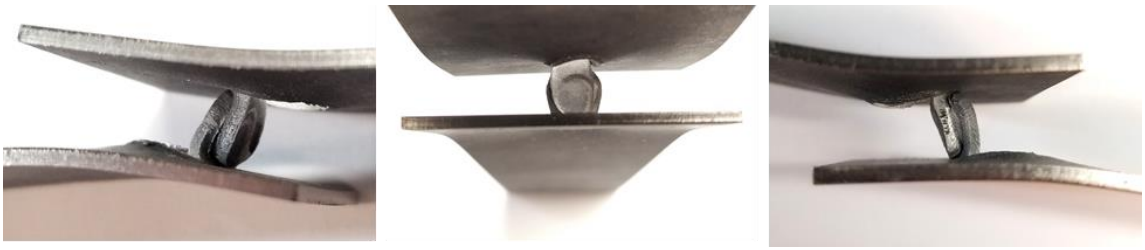

Figure 39: *Ductibor® 500-AS 1.6 mm lap shear specimen exhibiting double shared pull out failure mode (not classified by AWS).*

It can be seen in the force displacement data for the Ductibor® 1000-AS 1.6 mm lap shear tests (Figure 35) that there was very little unloading region after the peak load for any of the tested specimens. The 1.6 mm Ductibor® 1000-AS specimens all exhibited interfacial failure (Figure 33) and were the only material condition for lap shear tests, of the six material conditions tested, that exhibited no post-failure unloading behaviour. As a result, the absorbed energy for these samples was particularly low (see Table 7).

As previously mentioned, the average total energy absorbed during the lap shear tests increased when comparing the 1.6 mm thickness test specimens to the 1.2 mm specimens, except for Ductibor® 1000-AS lap shear tests. The Usibor® 1500-AS and the Ductibor® 500-AS test specimens both showed an increase of absorbed energy of approximately 13 J, or increases of 189% and 48% for a thickness increase from 1.2 to 1.6 mm, respectively, whereas the Ductibor® 1000-AS tests showed a decrease in total absorbed energy of 2.6 J. The total absorbed energy of the Usibor® 1500-AS 1.6 mm tests is higher than the Ductibor® 1000-AS 1.6 mm specimens. It is noted that an increase in the peak force does not always correspond to an increase in the total energy absorbed. The lack of relation of peak force to energy absorbed is attributed to the different heat affected zone microstructures for each material condition resulting in different failure modes. The Ductibor® 1000-AS 1.6 mm tests do not have any post-failure unloading behaviour and as a result there is less energy absorbed than in the thinner gauge material tests. This behaviour highlights the importance of the post-failure behaviour when optimizing the weld strength from a process perspective and the importance of capturing this behaviour in numerical models for simulation, as discussed in Section 3.5.

3.2.2. Cross tension Test Results

The 1.2 mm thickness single spot weld cross tension force *versus* displacement and energy absorbed *versus* displacement test results are presented below in Figure 40 and Figure 42, respectively. The 1.6 mm thickness test results for force *versus* displacement and energy absorbed

versus displacement are in Figure 41 and Figure 43, respectively. Specimens exhibiting expulsion are indicated with a dashed line. The peak force, displacement when the peak force occurred, and the total absorbed energy average values for each material condition are summarized in Table 8.

Table 8: *Summary of average data values for single spot weld cross tension tests.*

Material	Thickness [mm]	Max Load [kN]	Displ @ max [mm]	Absorbed Energy [J]
Ductibor® 500-AS	1.2	7.2 ± 0.7	17.2 ± 1.3	74 ± 10
	1.6	12.1 ± 0.6	18.3 ± 0.4	137 ± 12
Ductibor® 1000-AS	1.2	6.6 ± 0.8	10.6 ± 1.1	43 ± 6
	1.6	12.3 ± 0.5	14 ± 0.6	111 ± 9
Usibor® 1500-AS	1.2	4.0 ± 0.5	4.8 ± 0.7	14 ± 2
	1.6	5.5 ± 0.4	3.9 ± 0.7	17 ± 2

The cross tension tests showed similar behaviour as the lap shear tests in that the thicker 1.6 mm specimens recorded a higher peak force than the 1.2 mm thick specimens. From Table 8, the amount the cross tension test peak force increased by, for the Usibor® 1500-AS material specimens, was 1.5 kN for a thickness increase from 1.2 to 1.6 mm, while the Ductibor® 500-AS and the Ductibor® 1000-AS material specimens increased by 4.9 kN and 5.6 kN, respectively. All the single spot weld cross tension tests showed significantly reduced absorbed energy post-weld failure compared to their lap shear counterpart tests, with the exception of the 1.6 mm Ductibor® 1000-AS because neither supported load beyond initial weld failure. It is interesting to note that the Ductibor® 500-AS and Ductibor® 1000-AS cross tension experiments had similar or identical peak loads when comparing the same material thickness. The Ductibor® 500-AS welds displayed higher crosshead displacement than the Ductibor® 1000-AS, which is discussed below.

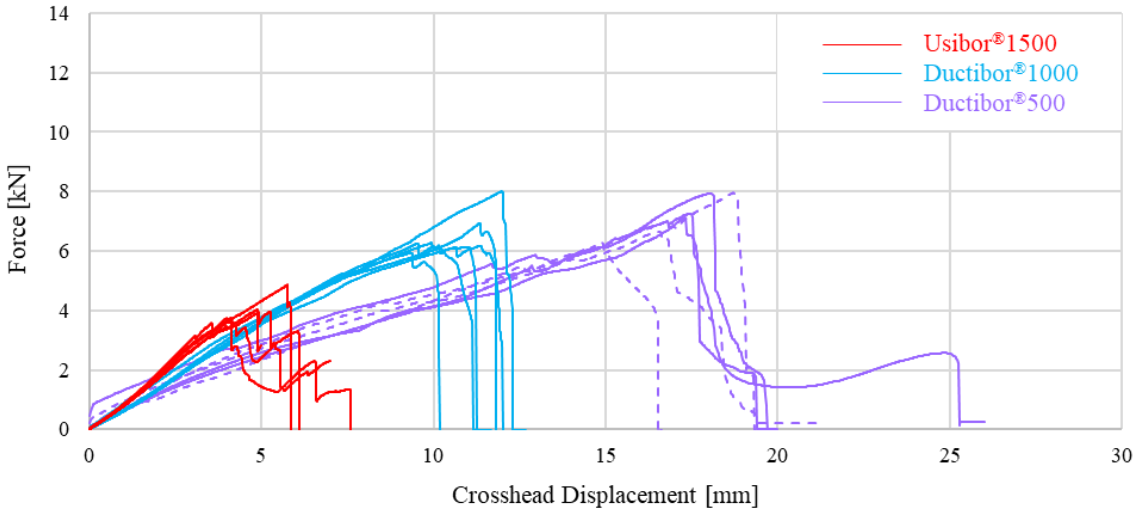

Figure 40: *Cross tension force versus displacement data for 1.2 mm specimens. Dashed lines showed expulsion.*

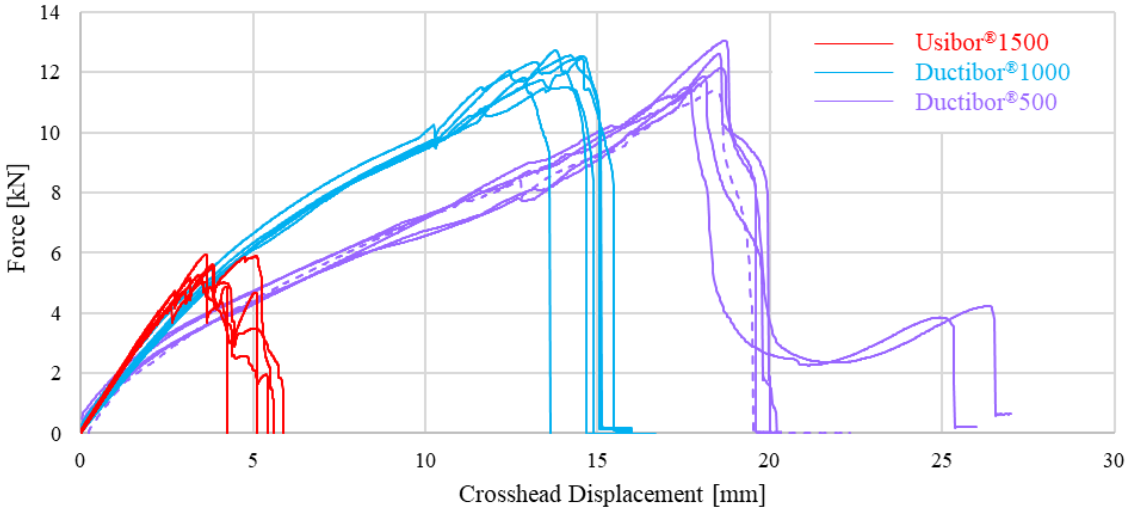

Figure 41: *Cross tension force versus displacement data for 1.6 mm specimens. Dashed lines showed expulsion.*

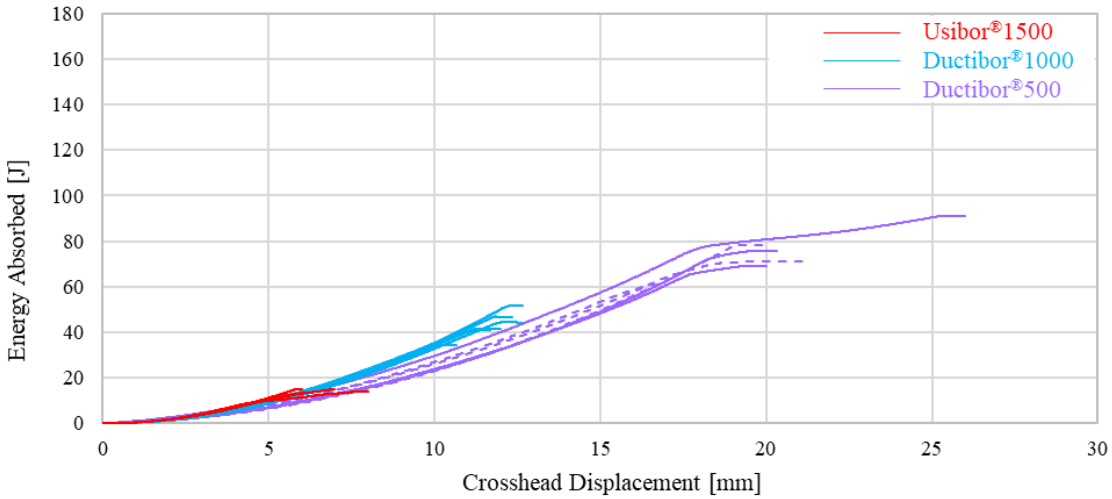

Figure 42: *Cross tension energy absorbed versus displacement data for 1.2 mm specimens.*

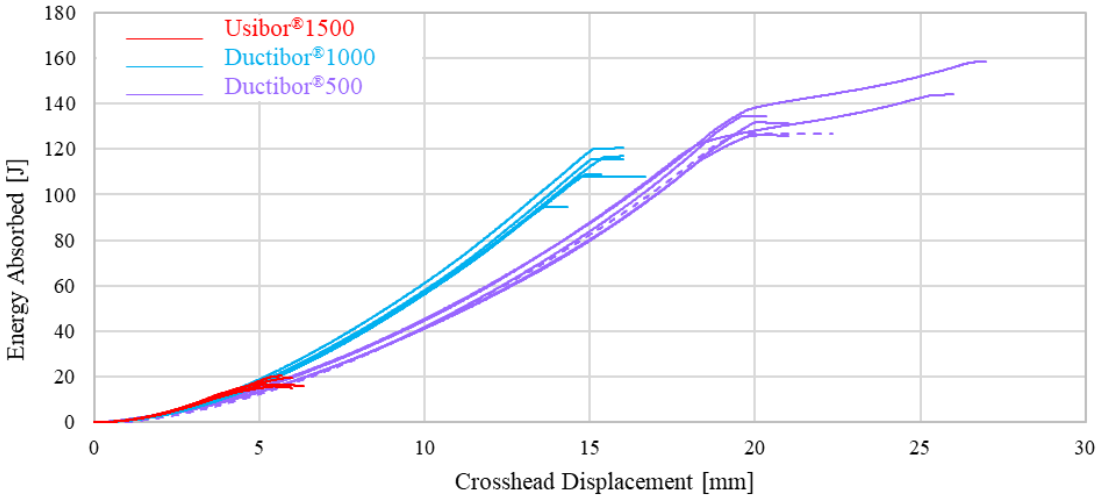

Figure 43: *Cross tension energy absorbed versus displacement data for 1.6 mm specimens.*

The absorbed energy *versus* displacement plots for the cross tension tests show similar trends as the lap shear tests but are more exaggerated due to the larger overall crosshead displacement. In Figure 42 and Figure 43, it is seen that the slopes of the energy *versus* displacement curves are different for each of the three materials tested. The strongest material, Usibor® 1500-AS, has the steepest slope while the softest material, Ductibor® 500-AS, has the lowest slope. These characteristics are also seen in the lap shear data but are not as noticeable because all the lap shear tests end before 5 mm of crosshead displacement. The cross tension test data shows progressively more absorbed energy as the base material softens except for the Ductibor® 500-AS and Ductibor® 1000-AS specimen tests which record similar values of total absorbed energy for the 1.6 mm specimens. The Ductibor® 1000-AS 1.6 mm final absorbed energy values (111 J) are almost three times larger than the 1.2 mm specimens (43 J) because of the change from brittle failure to more ductile failure mode.

Most cross tension specimens exhibited the partial or full button pull failure modes defined by AWS, examples of which were shown in Figure 33. Four of the Ductibor® 500-AS 1.2 mm and three of the 1.6 mm specimens did not exhibit partial or full button pull out failure modes. Some of the specimens had expulsion occur during the spot welding process and resulted in inconsistent peak forces and total energy absorbed (indicated with dashed lines in Figure 40 through to Figure 43). The other specimens not exhibiting the partial or full pull out failure mode had the shared asymmetric pull out failure mode, shown in Figure 44, that was discussed in the lap shear experimental results, Section 3.2.1. These tests show distinct characteristic behaviour in the force *versus* displacement plots shown in Figure 40 and Figure 41; there is a sharp drop in load after the peak followed by an increase in the load as the weld nugget rotates. As the nugget rotates approximately 90° the load begins to increase again until finally there is complete separation of the weld nugget from one of the coupons.

Figure 44: *Close up of the Ductibor® 500-AS 1.6 mm cross tension test showing shared asymmetric pull out.*

Another characteristic of the cross tension tests that was not present in the lap shear tests are the effects of coupon deformation on the force *versus* displacement response. The total crosshead displacement of the cross tension specimens was approximately 5 to 10 times larger than the lap shear tests. The softer materials, with lower ultimate tensile strength, deform more and result in a higher overall crosshead displacement. The direct cause of this behaviour is that the top and bottom coupons are pulling out of the fixtures and deforming, indicated by the arrows in the top left image of Figure 45. Post-test examination of the cross tension specimens reveals that slippage of the coupons in the fixtures was a key factor affecting the amount of coupon deformation. Shown in the right image of Figure 45, there are burnish marks on the coupons where the Al-Si coating has flaked off due to deformation from the coupon coming into contact with the bolts used for clamping the fixture. Once the coupon contacts the bolt, the slippage in the fixtures stops and further deformation is due to the spot weld fracture. The point that the coupon contacts the bolts is seen in the force *versus* crosshead displacement data as an upwards inflection point approximately 4 mm from the peak force. The strongest material tested, Usibor® 1500-AS, did not show this behaviour because there was very little coupon deformation.

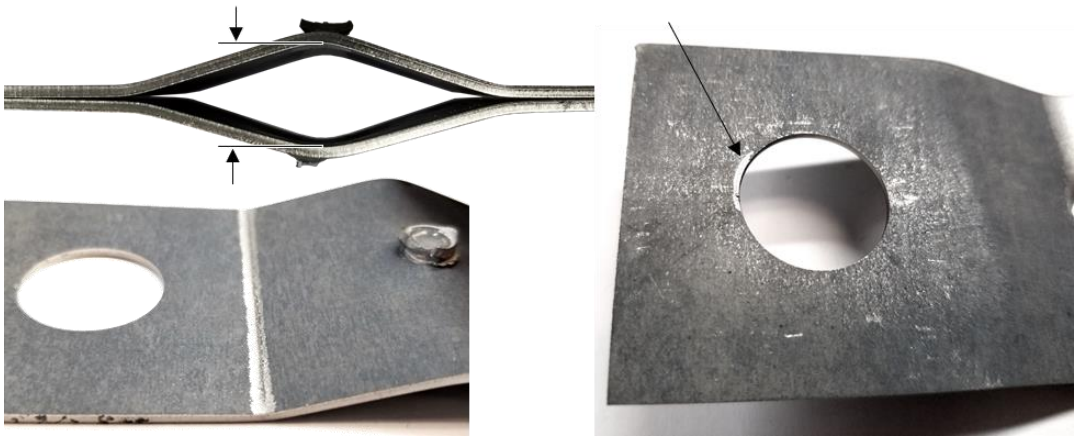

Figure 45: *Top Left) Coupon deformation showing vertical displacement measurement. Bottom Left) Al-Si coating missing where the coupon is pulled out of the clamping fixture. Right) Al-Si coating flakes off due to coupon contact with the clamping bolt.*

The three Ductibor® 500-AS cross tension specimens that exhibited the shared asymmetric pull out failure mode are easily identifiable on the absorbed energy *versus* displacement plots. There is a secondary region of increasing absorbed energy that begins when the specimens that had other failure modes end. This secondary region increases at a slower rate than primary region and is entirely due to the weld nugget pulling out of the parent coupons by shearing through the thickness of the sheets in the HAZ region. There is approximately 10-15% more total energy absorbed during this failure phenomenon.

3.3. Numerical model development

After the collection of the single spot weld test data, a numerical weld model is developed using the finite element analysis software LS-DYNA®. As introduced earlier, the weld model is a key aspect of the full vehicle simulation. As the parent metal strength increases and the cross sectional area of frame components is reduced to save weight, the stress developed in these automotive structures increases. A study by Li *et al.* [100] on the use of high strength steel for vehicle light-weighting identified that mild steel can be replaced with higher yield and failure strength steel, and lower depth (thickness) while maintaining impact energy absorption. The increase of stress throughout these structures has shifted the location of failures to the joints [15]. Thus, an accurate model of the spot welded joints is critical to generate accurate predictions at the component level and for full vehicle simulations. In this chapter, the development of two different weld material models is presented using the single spot weld test data for each material condition. The purpose is to determine if the weld material model is capable of capturing the weld failure characteristics, such as unloading behaviour, and mechanical performance for multiple load cases, since full vehicle simulations will induce complex loading conditions acting on the spot weld joints.

The spot welding process inherently contains a large amount of variability due to the different factors that affect the quality of a weld. During the weld process development, there is significant effort used to determine a weld schedule that will produce spot weld nuggets with a large diameter and no expulsion. A consistent spot weld will have predictable failure modes such as full button pull out. However, it is seen in the experimental data for the tensile lap shear and cross tensions test that there is a mix of fracture modes. Multiple inconsistent fracture modes poses another challenge for spot weld modelling because the numerical model will always predict the same result given a set of inputs and boundary conditions. One spot weld model is incapable of predicting a force *versus* displacement history of either interfacial failure or full button pull out failure for any one given loading condition. Due to this, the spot weld models are calibrated to the average experimental peak force and energy absorbed values recorded.

The spot weld nugget was modelled using an assembly of hexahedral fully integrated, selective reduced solid elements and are assigned the *MAT_100_DA material model [50] or modelled as cohesive elements and assigned the *MAT_240 material model [64], [76], [77]. The parent metal

is modelled using a 2.5 mm mesh of fully integrated shell elements. The *MAT_100_DA, or *MAT_SPOTWELD_DAIMLERCHRYSLER, is an elasto-plastic material model based on the von Mises plasticity with a failure criterion that uses the axial, shear, and bending stresses developed in the weld nugget. This material model also includes a fading energy parameter that defines additional energy absorbed after the weld failure. The material model *MAT_240, or *MAT_COHESIVE_MIXED_MODE_ELASTOPLASTIC_RATE, is a rate-dependent, elastic-ideally plastic cohesive zone model defined by a tri-linear traction-separation law with a quadratic yield and damage initiation criterion in mixed-mode loading.

The goal of the weld model calibration is to be able to accurately predict the peak load and total energy absorbed values of the single spot weld test data. This means the weld models are calibrated to the single spot weld test data and are then verified afterwards by insertion into a more complex loading case in a component level simulation. The two spot weld material constitutive models introduced use different set of parameters to define the spot weld behaviour but follow the same general calibration and evaluation processes. A mesh is required for both the cross tension and the tensile lap shear single spot weld tests. It is important that the mesh remains constant except for minor changes that are required for different weld material models so that comparisons made between the weld models are valid.

3.3.1. Parent metal constitutive models

The rate-sensitive stress-strain curves models used in the numerical simulations for three hot stamped materials are shown in Figure 46. The Ductibor® 500-AS constitutive model is from the work by Samadian *et al.* [27], the Ductibor® 1000-AS constitutive model is from Abedini and Samadian [101], and the Usibor® 1500-AS constitutive model is published by Omer *et al.* [4]. All three hot stamped materials are rate sensitive, with higher strain rates causing higher strength. Two different methods were originally employed to obtain these constitutive models. Flow curves for the Ductibor® 500-AS and Ductibor® 1000-AS material were created using a combination of uniaxial tensile and shear test data, following a procedure developed by Rahmaan *et al* [102]. High tensile strength materials tend to have low amounts of uniform elongation, making it difficult to extrapolate material hardening data to large strains. It was found that the hardening data from shear tests, which reach much higher strains due to the suppression of necking, could be used to extend the uniaxial tensile data. From the work of Omer *et al.* [4], the Usibor® 1500-AS flow curves were

generated using a method called the extended Tailored Crash Model (eTCM). The eTCM is an extension of the "Tailored Crash Model" (TCM) and the "Tailored Crash Model II" (TCM II) models developed by Bardelcik *et al.* [88], [103]. The TCM is a phenomenological strain rate sensitive model for quenched boron steel with tailored properties, via in-die heating, that varied from martensitic microstructure to bainitic. The TCM is based on the Voce hardening model with an additional strain rate sensitive term. It was later shown that the Vickers hardness and strength levels can be similar for as-quenched microstructure of bainite + martensite and bainite + martensite + ferrite, but the presence of ferrite can greatly affect the hardening behaviour. A new model, TCM II, was developed to account for this [103].

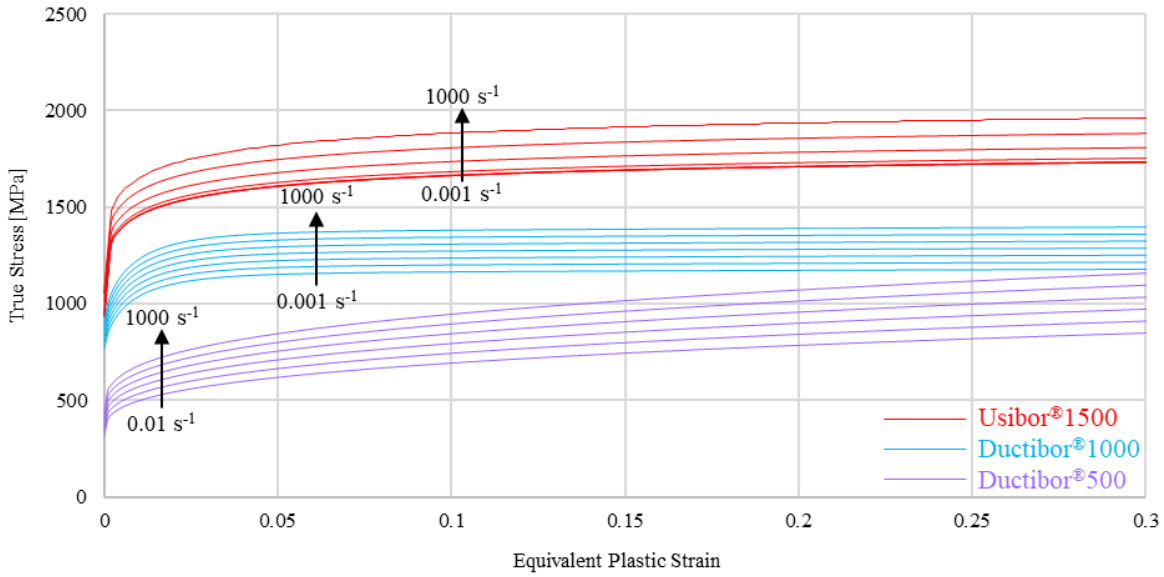

Figure 46: *Material flow curves for Ductibor®500-AS* [27], *Ductibor®1000-AS* [101], *and Usibor®1500-AS* [4]. *Curves of the same material show rate-sensitivity by increasing orders of magnitude from bottom to top.*

Fracture is modelled for the three hot stamped materials using the Generalized Incremental Stress State Model (GISMMO) in the 2-Dimension (plane stress) form. In this model, the fracture strain is a function of the instantaneous stress state, referred to as the stress triaxiality and defined in Equation (38) as the ratio of hydrostatic stress to the von Mises equivalent stress. The fracture loci used in GISSMO failure model was characterized by ten Kortenaar [22] for Usibor® 1500-AS, and characterized by Abedini and Samadian [101], [104] for Ductibor® 500-AS and Ductibor® 1000-AS. The GISSMO fracture treatment also applies a regularization factor to scale the fracture strain based on the element mesh size. The fracture loci are shown in the left image of Figure 47 and the mesh regularization is shown in the right image of Figure 47.

$$T = \frac{\sigma_{hyd}}{\sigma_{vm}} \tag{38}$$

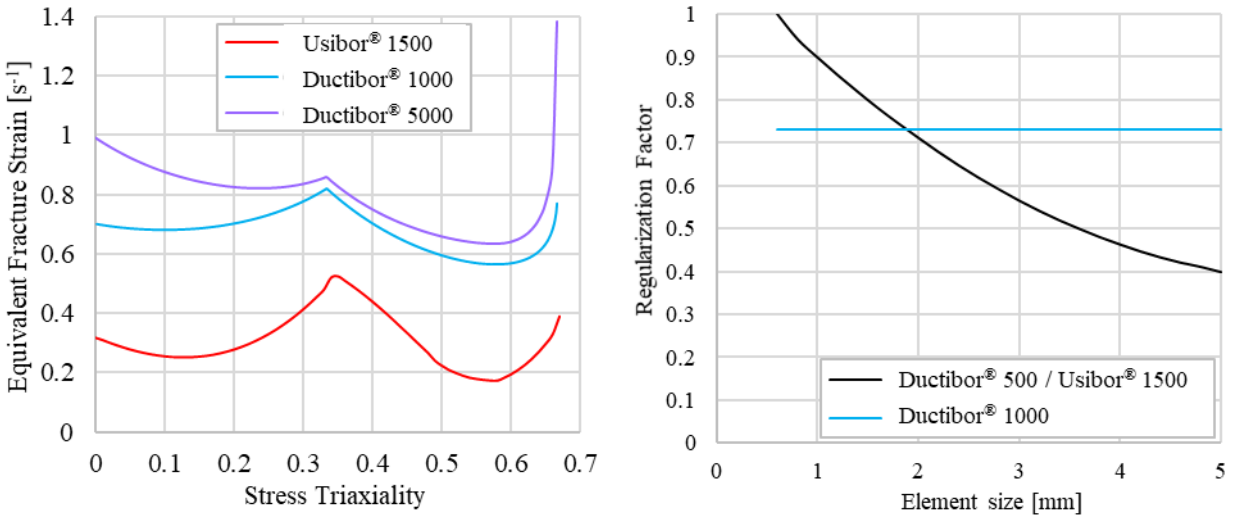

Figure 47: *Fracture loci (left) and GISSMO mesh regularization factors (right) of Ductibor® 500-AS [104], Ductibor® 1000-AS [101], and Usibor® 1500-AS [22].*

3.3.2. Weld coupon mesh development

The single spot weld coupons for the cross tension and tensile lap shear test simulation models are created using a combination of HyperMesh™ and LS-PrePost®. HyperMesh™ is used to create all of the mesh components in the model. LS-PrePost® is used to develop the rest of the keyword deck required for the simulations. This includes control cards, database outputs, boundary conditions, contact definitions, constraints, element section properties, node and part sets, and material model definitions. The cross tension and the tensile lap shear models share a common framework with only geometric differences. The parent metal material and section properties, and all of the control card parameters are consistent across the different models. The parent metal coupons are meshed with a 2.5 mm element size and assigned a fully integrated element formulation with five through-thickness integration points. The element thickness is 1.15 mm or 1.55 mm to account for removing the Al-Si coating thickness from of the 1.2 mm and 1.6 mm nominal thicknesses, respectively, since the coating adds no structural strength [105]. The *CONTACT_AUTOMATIC_SINGLE_SURFACE card is used to define contact between all components, including self-contact. The weld joint contact definition is dependent on the weld material model being used. For all models, the spot weld is meshed using solid elements that have a total cross section area of 28.3 mm^2, the same as a 6 mm diameter spot weld.

In the cross tension model, seen in Figure 48, there are two coupons (blue and red) being clamped with shells (grey) to mimic the fixtures. The fixture components are assumed to only deform elastically and are assigned a thickness of 12.7 mm to match the actual fixtures. The bottom fixture is fixed while the top fixture's movement is controlled by a prescribed boundary motion with the same velocity as the crosshead of the tensile frame, 10 mm/min. The bolt used to clamp the coupons within the fixtures is modelled by using an elastic beam that is constrained to the fixture shell element nodes at both ends, similar to a ring of spokes. To model the initial torque on the bolt, the beam is set to an initial pre-load of 10 kN before the top fixture begins moving. The pre-load tensile force is calculated from the applied torque by

$$F_i = \frac{T}{Kd} \tag{39}$$

where F_i is the pre-load tension, T is the applied torque, K is the torque coefficient, and d is the bolt major diameter [106, p. 430]. For a bolt diameter of 20 mm and an approximate friction coefficient of 0.20, the 40 Nm (29.5 ft·lb$_f$) applied torque equates to a 10 kN pre-load. It was found from the cross tension experiments that the coupons slide out of the fixtures until the coupon contacts the clamping bolt, placing an upper limit on the coupon sliding. To capture this behaviour, rings of rigid shell elements, representing the cylindrical surface of the bolt, were added, seen in Figure 49, to enforce contact with the shell edges of the coupons.

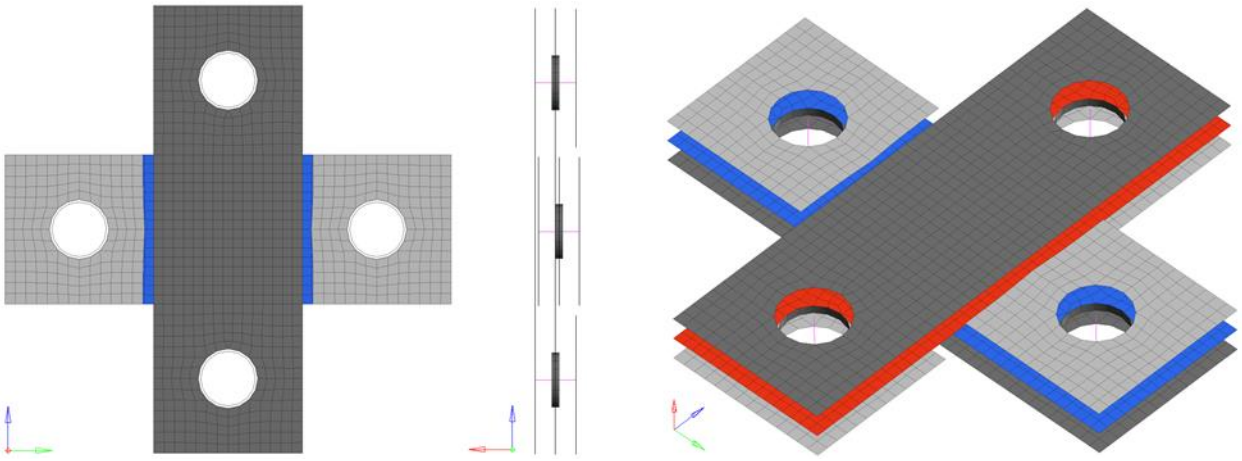

Figure 48: *Cross tension model mesh.*

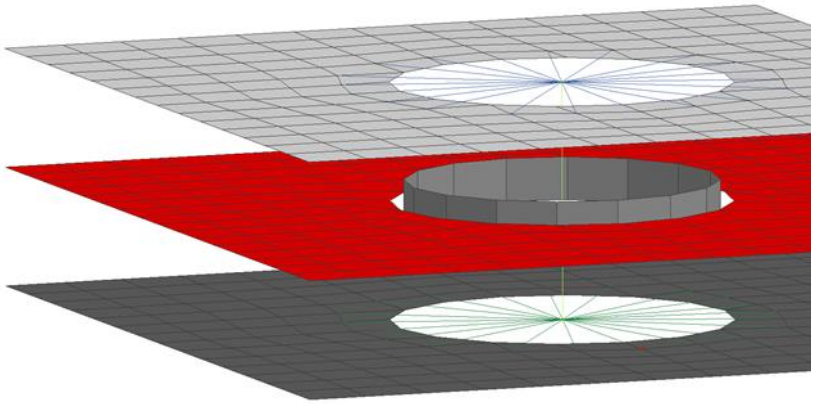

Figure 49: *Close up view of the cross tension mesh showing the clamping fixture components and bolt ring.*

The tensile lap shear model, seen in Figure 50, is a simpler model than the cross tension. There are no fixture components meshed for the lap shear model because the specimens insert directly into the hydraulics grips of the tensile frame. To replicate these boundary conditions in the simulation model, only the ungripped length of the specimens are meshed and single point constraints are applied to the top and bottom edge nodes. The bottom nodes are fixed in all 6 degrees of freedom and the top nodes are fixed in the y and z translational axis and about all three rotational axes.

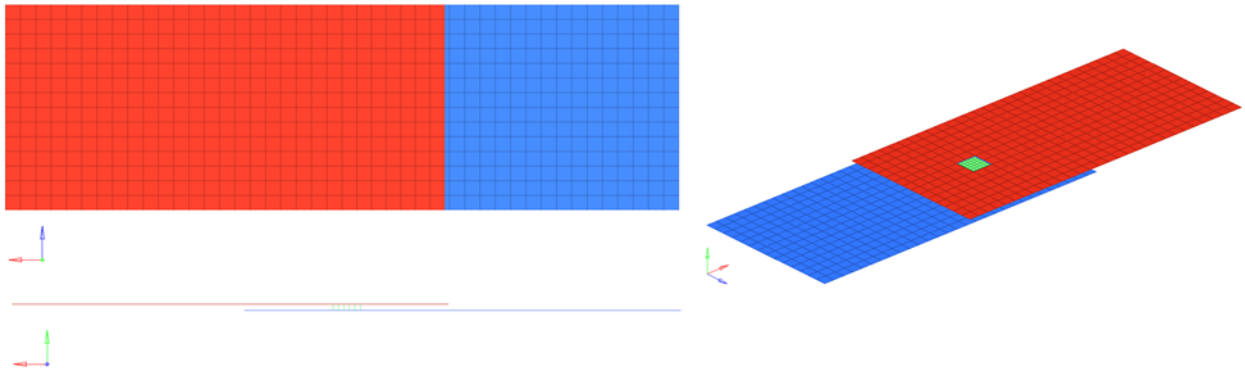

Figure 50: *Tensile lap shear model mesh. Top (red) coupon elements removed to show solid weld elements (green).*

3.3.2.1. MAT_100_DA

The *MAT_100_DA material model, as discussed in Section 1.8, assigns material properties to the solid hex elements that comprise the weld nugget mesh. These solid elements are grouped into an assembly of eight elements to create one weld nugget. The spot weld elements are connected to the parent material parts using the *CONTACT_TIED_SURFACE_TO_SURFACE contact definition. On this card, the spot weld part is defined as the slave and a part set including the two side wall parts being joined are defined as the master. One contact card is needed for each

side of the weld. The material card primarily inputs the parameters for the material elastic deformation behaviour, such as density, elastic modulus, Poisson's ratio, and specify the connection properties card ID. Basic weld failure conditions can be input on the material card, if desired, as well as other parameters to modify the weld nugget behaviour. An example of a complete *MAT_100_DA card is shown in Table 9 and a complete description of the material model is provided in the LS-Dyna Keyword Manual II [67].

Table 9: **MAT_100_DA keyword card sample with Usibor® 1500-AS 1.2 mm weld properties.*

Column	**1**	**2**	**3**	**4**	**5**	**6**	**7**	**8**
Variable	mid	ro	e	pr			dt	tfail
Value	6	7.83E-8	200000	0.3			0.0	0.0
Variable	efail							
Value	0.0							
Variable	rs			true_t	con_id			
Value	0.0			0.85	1			

The *MAT_100_DA material model uses the *con_id* variable value to connect to the *Define_Connection_Properties card that contains all of the related weld failure variables. The yield strength and the tangent modulus are defined to provide post yielding hardening behaviour. An example of a completed keyword card *Define_Connection_Properties is shown in Table 10 and a complete description is provided in the LS-Dyna Keyword Manual I [66]. Note that the *sb* and *exsb* variables are given a value of 1.0E14 because no bending experiments were performed in the current work and therefore it is assumed that no failure from bending occurs.

Table 10: **Define_Connection_Properties keyword card example with Usibor® 1500-AS 1.2 mm weld properties.*

Column	**1**	**2**	**3**	**4**	**5**	**6**	**7**	**8**
Variable	con_id	proprul	areaeq			dg_typ	moarfl	
Value	1	0	0			4	0	
Variable		sigy	etan	dg_pr	rank	sn	sb	ss
Value		1200.0	1200.0	1.0E10	0.0	182.0	1.0E14	600.0
Variable	exsn	exsb	exss	lcsn	lcsb	lcss	gfad	sclmrr
Value	1.0	1.0E14	1.0	0	0	0	230.0	1.0

3.3.2.2. MAT_240

A key aspect of this material model is the ability to model the post weld failure behaviour independently for different loading conditions (tensile, shear, mixed mode) to better predict joint failure. Similar to the *MAT_100_DA weld model, the *MAT_240 material model also uses solid hex elements that are tied to the parent shell elements to represent the joint. The solid elements are assigned the cohesive element formulation 20 on the section card. Two contact definitions are required for each part-to-part joint that is being modelled. The nodes of the cohesive elements' lower surface must be grouped into a node set that is then tied to the mating part. The same must be done for the cohesive elements' upper surface nodes. The *MAT_240 key word card contains the parameters that define the traction-separation law for both Mode I and Mode II/III crack opening conditions. An example of a complete *MAT_240 keyword card is provided in Table 11.

Table 11: **MAT_240 keyword card example with Usibor® 1500-AS 1.2 mm weld properties.*

Column	**1**	**2**	**3**	**4**	**5**	**6**	**7**	**8**
Variable	mid	ro	roflg	intfall	emod	gmod	thick	
Value	245	7.89e-9	1	1.0	200000.0	2800.0	1.0	
Variable	g1c_0	g1c_inf	edot_g1	t0	t1	edot_t	fg1	
Value	390.0	0.0	0.0	140.0	0.0	0.0	0.01	
Variable	g2c_0	g2c_inf	edot_g2	s0	s1	edot_s	fg2	
Value	240.0	0.0	0.0	473.0	0.0	0.0	0.10	

The same hexagon shaped assembly as the *MAT_100_DA is used, with the total cross section area of 28.27 mm^2 representing a 6 mm diameter spot weld. It was found that sudden increasing or decreasing irregularities were introduced into the force *versus* displacement response by using only one element to model the spot weld joint. It was determined that the irregularities were caused by shell elements belonging to the parent coupon parts contacting each other through the cohesive element. Increasing the element density of the spot weld nugget increases the number of tied points between the cohesive elements and the shell elements. More tied points help prevent the shell elements passing through the solid cohesive elements in a non-physical manner. It can be seen in Figure 51 that by increasing the mesh density by using the hex assembly mesh provides a stiffer and more accurate prediction of the experimental data for loading up to weld failure initiation with no irregularities. Additionally, using the hex assembly mesh pattern for the *MAT_240 cohesive elements maintains industry meshing practice which will provide fairer comparisons to the *MAT_100_DA models as well as ease the application of *MAT_240 to existing models.

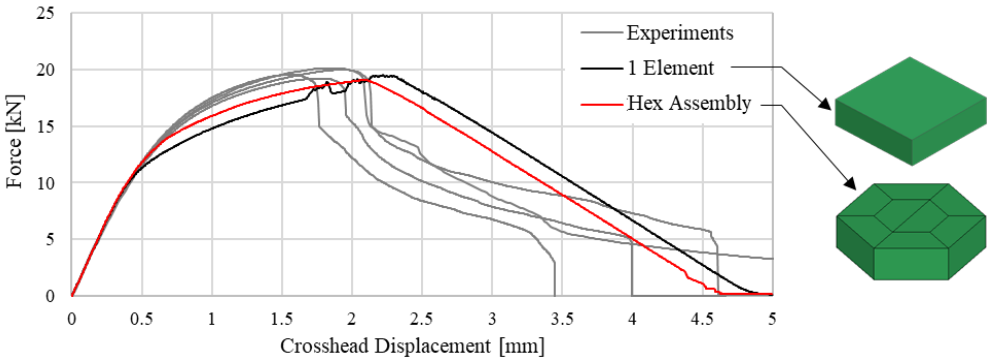

Figure 51: *Effect of the cohesive element mesh patterns used to model a single spot weld nugget using *MAT_240. Data shown is for Ductibor® 500-AS 1.6 mm lap shear experiments.*

3.4. Calibration Procedure

The calibration procedures for the two weld models (*MAT_100_DA and *MAT_240) follow the same general steps but vary slightly because there are different parameters that must be defined in each model. An initial estimation of parameter values is first made based on the force *versus* displacement data gathered from the experiments. The assumed parameters are confirmed to be correct by running the cross tension and lap shear numerical models and then comparing the output force *versus* displacement data to the measured data. The normal tensile parameters are first assessed with respect to the experimental cross tension data because the cross tension test is an isolated loading condition and there is little to no influence on the numerical model output associated with the shear failure parameters. It is typical that the assumed parameter values require slight adjustment to reduce the numerical error because of the necessary slight differences between the idealized numerical models and the actual test conditions. Once the normal tensile parameters are determined, the shear parameters are confirmed by comparing the numerical and measured lap shear force *versus* displacement response. The complete set of spot weld model parameters for *MAT_100_DA and *MAT_240 for all materials and thicknesses are given in Appendix A.

3.4.1. *MAT_100_DA Calibration

Calibrating the *MAT_100_DA model has proven to be difficult because of the limited number of parameters that are available to define spot weld behaviour as well as the inability to specify different post-failure or damage parameters for different loading conditions. It is straight forward to determine the failure values used in the failure criterion, shown in Equation (22), by calculating stress values using the measured peak force and weld nugget area by $\sigma = \frac{F}{A}$. However, the elastic modulus, e, Von Mises yield stress, $sigy$, and tangent modulus, $etan$, parameters from Table 9

and Table 10 control the constitutive behaviour. These three parameters pertain to the stress-strain relation of the weld elements and do not directly relate to the force *versus* displacement data that is being used for calibration. The only user input parameter that controls the damage model, shown in Equations (24)-(27) , is the *gfad* parameter and is taken here as having the units $[MPa \cdot mm]$ which can be converted to and interpreted as the energy release rate $\left[\frac{mJ}{mm^2}\right]$, where mJ is millijoules. It should be possible to calculate a value for Work $[J]$ done by the spot weld during unloading by multiplying *gfad* by an area but it is unclear if this is the proper way to interpret the physical meaning of this parameter since the documentation is limited. The correlation between the energy absorbed by the spot weld specimens and the input parameter *gfad* are investigated in more detail in Section 3.5.1. Additionally, the three constitutive parameters and the *gfad* parameter cannot be specified different values for different loading conditions. If there are different loading behaviours or fracture modes between the lap shear and cross tension tests, then the *MAT_100_DA model may not be able to accurately predict both conditions.

3.4.2. *MAT_240 Calibration

The *MAT_240 model enables more direct control over the spot weld behaviour and force *versus* displacement response of the numerical models. As discussed in Section 1.8.3, the *MAT_240 model defines one traction-separation curve for the normal-tensile loading (Mode I) and a second curve for the shear loading (Mode II/III) condition. There are four parameters used to define the Mode I/Mode II traction-separation (T-S) curve: *emod/gmod*, *t0/s0*, *fg1/fg2*, and *g1c_0/g2c_0*. The separation defined in the T-S curve is calculated by LS-DYNA from the element top surface to bottom surface displacement, relative to the element thickness. The cohesive element thickness is manually set to `1` via the *thick* parameter to directly equate the T-S separation to the actual element stretch. The other parameters on the keyword card that are not defined here are used for applying rate sensitivity to the material model. A brief description of each parameter is provided in Table 12 and an example of how the input parameters define the traction-separation curve for the normal-tensile case is shown in Figure 52.

Table 12: **MAT_240 T-S Law defining parameter descriptions.*

Parameter (Mode I / Mode II)	Description
emod / gmod	Elastic modulus
t0 / s0	Yield stress
fg1 / fg2	Ratio of area under plateau to total area
g1c_0 / g2c_0	Energy release rate

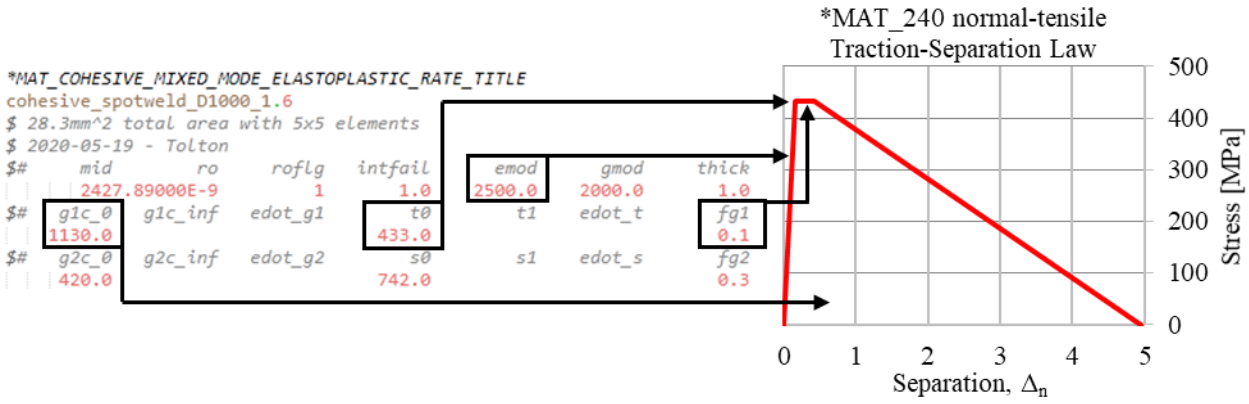

Figure 52: *Relation between *MAT_240 input parameters and resulting Traction-Separation law for the normal-tensile case.*

The elastic modulus parameter does not have much of an effect on the overall spot weld behaviour, as long as the initial stiffness is high enough that the coupon deformation is activated in softer materials, particularly Ductibor® 500-AS. The *MAT_240 model does not have any hardening, meaning that the yield stress is also the failure stress. The yield stress parameter can be easily determined in the same way as done for *MAT_100_DA by dividing the average measured peak force by the weld nugget area. Using the Ductibor® 1000-AS 1.6 mm cross tension test as an example: $sigy = \frac{F}{A} = \frac{12270\ N}{28.27\ mm^2} = 433\ MPa$. The length of the plateau at yield stress is set to match the behaviour seen in the measured data; for the cross tension model a small plateau is used while the lap shear model has a larger plateau. The final parameter, either *g1c_0* or *g2c_0*, is determined through analysis of the post-mortem experimental coupons. Shown in Figure 53 for the cross tension case, the final crosshead displacement can be broken into coupon deformation and the cohesive element separation. Note that in Figure 53, only half of the total coupon deformation is shown. The cohesive element separation can be calculated by subtracting the coupon deformation (both top and bottom coupons) from the final crosshead displacement. There is generally very little coupon deformation in the direction of applied load in the case of the lap shear experiments, so the amount of element separation is initially set to equal to the total crosshead displacement.

Following the process described here, the *MAT_240 material model required less iterations to achieve a calibrated model than the *MAT_100_DA model. This is attributed to the fact that the *MAT_240 material model parameters can be determined from experimental force *versus* displacement data and examination of the specimens more easily than the *MAT_100_DA parameters. In the following Section 3.5 it is shown that the *MAT_240 model predicted the experimental results better than the *MAT_100_DA model.

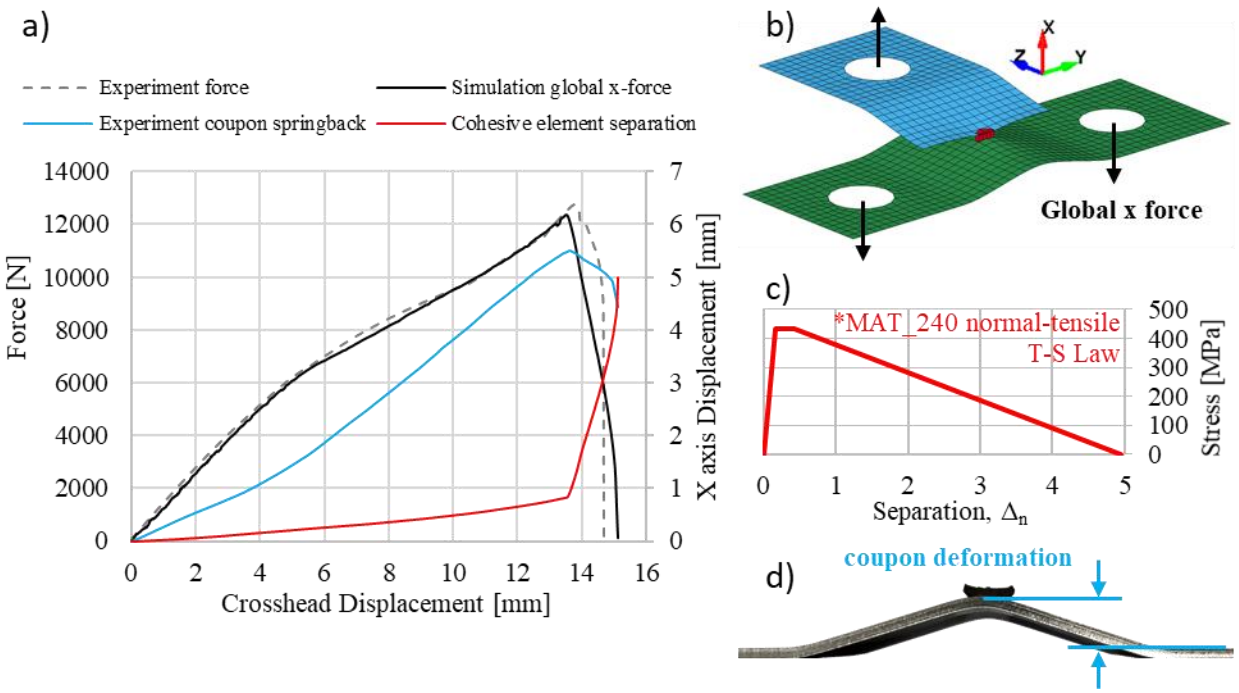

Figure 53: *a) Ductibor® 1000-AS 1.6 mm cross tension experimental force vs. displacement and output of *MAT_240 numerical model data confirming input values; b) Partial cross-section view of the *MAT_240 cross tension model showing applied forces; c) *MAT_240 normal-tensile traction-separation law; d) Measurement of coupon deformation from post-test coupon.*

3.5. Single spot weld simulation results

The *MAT_100_DA and the *MAT_240 weld material model simulations for tensile lap shear 1.2 mm and 1.6 mm are shown in Figure 54, and the cross tension 1.2 mm and 1.6mm results are shown in Figure 55. The simulation results for the predicted peak load and energy absorbed values are presented in

Table **13** and Table 14. Also, in these two tables, the error percentage values of the numerical predictions with respect to the average values for each of the corresponding experiments are presented. The predicted peak load and energy absorbed data from the simulations and the experimental are displayed together in Figure 56 and Figure 57, respectively.

Both the *MAT_100_DA and the *MAT_240 weld material model predictions for the lap shear tests are very accurate with respect to the experimental data. On average, the numerical predictions are within 5% percent error of the experimental results for the max load and the absorbed energy. There are no predicted values with a percent error larger than 20% for any lap shear test metric. For the modelling of shear dominant spot weld failure, either of the *MAT_100_DA and the *MAT_240 weld material models can be used.

Table 13: *Lap shear single spot weld numerical simulation prediction and error results.*

		***MAT_100_DA Simulations**		***MAT_240 Simulations**	
		Max Load [kN]	Energy absorbed [J]	Max Load [kN]	Energy absorbed [J]
Lap Shear 1.2 mm	Ductibor® 500-AS	14.1	28	13.4	29
	% error	1.0%	1.6%	6.4%	1.6%
	Ductibor® 1000-AS	16.7	16	16.4	16
	% error	0.5%	1.9%	2.4%	4.4%
	Usibor® 1500-AS	14.1	7	12.9	7
	% error	6.3%	9.5%	2.7%	3.1%
Lap Shear 1.6 mm	Ductibor® 500-AS	18.9	41	18.6	47
	% error	2.0%	2.9%	3.4%	9.5%
	Ductibor® 1000-AS	21.0	14	20.8	13
	% error	0.2%	0.4%	0.8%	6.4%
	Usibor® 1500-AS	26.2	19	26.0	19
	% error	1.3%	0.2%	2.1%	0.9%
	Average % error	**1.9%**	**2.8%**	**3.0%**	**4.3%**

Table 14: *Cross tension single spot weld numerical simulation prediction and error results.*

		***MAT_100_DA Simulations**		***MAT_240 Simulations**	
		Max Load [kN]	Energy absorbed [J]	Max Load [kN]	Energy absorbed [J]
Cross Tension 1.2 mm	Ductibor® 500-AS	8.6	62	7.4	72
	% error	16.0%	19.7%	2.1%	3.8%
	Ductibor® 1000-AS	7.8	38	6.8	43
	% error	15.6%	15.5%	3.0%	0.8%
	Usibor® 1500-AS	5.3	12	3.9	15
	% error	23.9%	13.5%	4.2%	8.4%
Cross Tension 1.6 mm	Ductibor® 500-AS	12.5	104	11.5	133
	% error	3.3%	31.6%	5.4%	2.6%
	Ductibor® 1000-AS	12.8	72	12.4	106
	% error	4.1%	53.4%	0.8%	5.0%
	Usibor® 1500-AS	5.6	7	5.5	16
	% error	0.9%	141.5%	1.5%	8.6%
	Average % error	**10.6%**	**45.9%**	**3.3%**	**8.8%**

The *MAT_100_DA numerical predictions for the cross tension tests are much worse than the lap shear test predictions. The Usibor® 1500-AS 1.2 mm cross tension test peak force numerical prediction error is 23.9% while the average peak force predictions error for all materials is 10.6%. The absorbed energy values for the *MAT_100_DA predictions for the 1.2mm cross tension tests are within the 20% requirement but the 1.6 mm cross tension test predictions are all above 20%. The *MAT_240 weld model predictions for the cross tension test peak forces and energy absorbed are all within 10% of the experiments.

The lap shear force *versus* crosshead displacement plots show that the numerical predictions for the weld material models match the experimental test results closely. Up until the peak load, when weld failure initiates, the test data is very consistent. There is more variation in the test data after failure initiates due to the uncertain nature of the crack growth from the nugget through the HAZ. The weld models are unable to predict the sudden drops in load and the subsequent extended regions of sustained load. Instead, the numerical models predict a smooth unloading that averages out the experimental unloading behaviour. This is most noticeable in the Ductibor®1000 1.2 mm lap shear simulation and experiments.

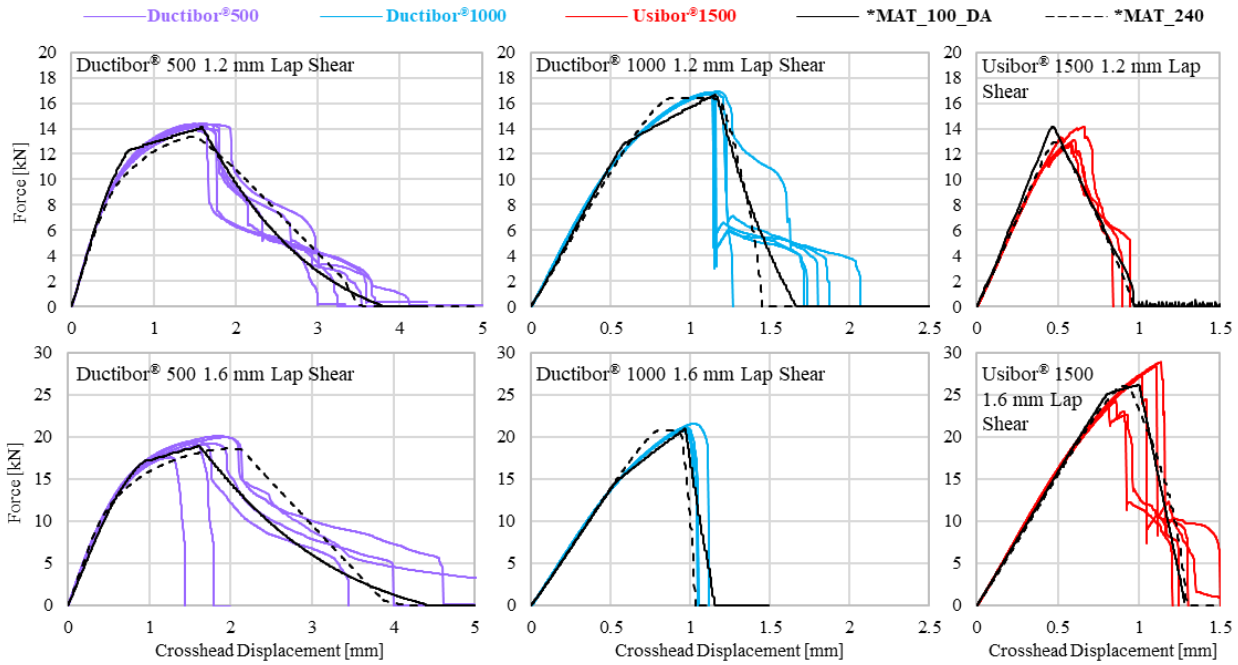

Figure 54: *Tensile lap shear 1.2 mm and 1.6 mm experiments (red, blue, and purple lines) and numerical model simulation results (black lines).*

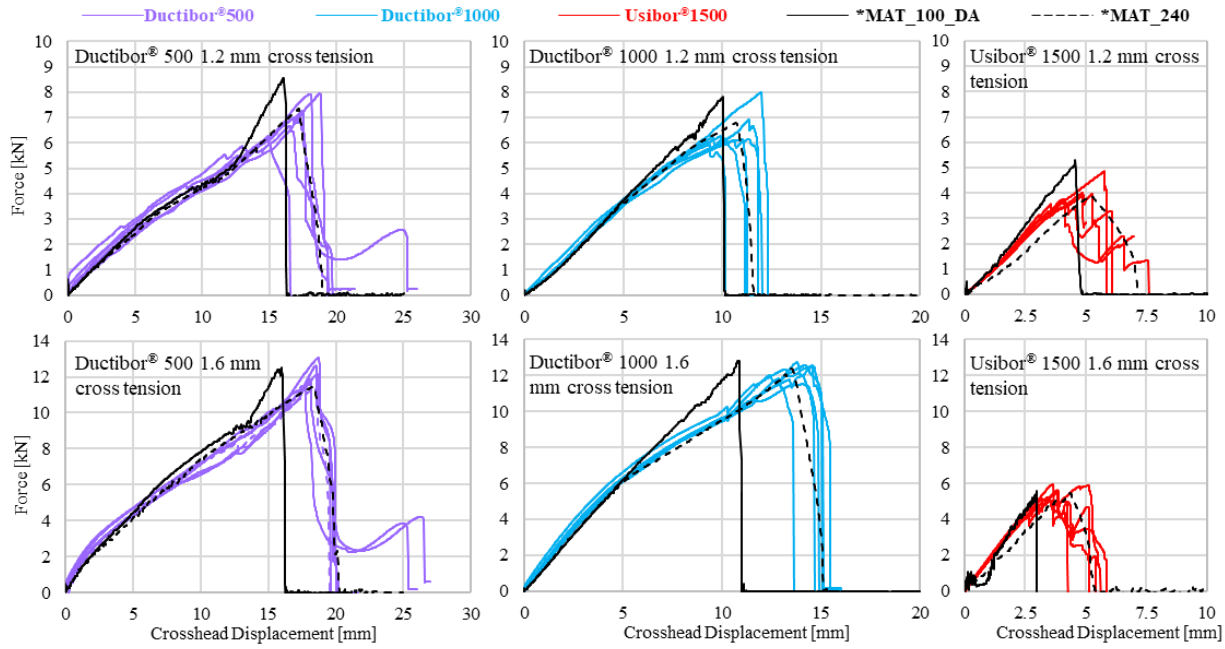

Figure 55: *Cross tension 1.2 mm and 1.6 mm experiments (red, blue, and purple lines) and numerical model simulation results (black lines).*

As discussed earlier, the cross tension test models predictions are not as accurate as the lap shear tests. This is mainly attributed to the large amount of coupon deformation and total crosshead displacement that occurs. The *MAT_100_DA models typically deviate from the experimental data as the force increases. The model accurately captures the peak load value but not the crosshead displacement when the peak load occurs. It was seen in the cross tension experiments using the softer materials, Ductibor® 500-AS and Ductibor® 1000-AS, the coupons are pulled out of the fixtures until they contact the bolts. The point that this occurs at is seen in the experimental data as an inflection change near the peak load. The cross tension mesh model includes a ring of shell elements to represent the bolt and capture this effect but this did not work well for the *MAT_100_DA model. The *MAT_240 material is defined using a traction-separation law curve so the total separation distance can be calibrated to match the experiments, for example, 4.4 mm for the Ductibor® 500-AS 1.6 mm cross tension model. This approach enables a much more accurate prediction of force and displacement when failure initiation begins. After failure initiation occurs, damage accumulates and the weld coupons begin to unload. The *MAT_100_DA material model has the *gfad* parameter to capture the energy released during unloading but for the cross tension tests it is observed that no post-failure unloading is predicted; the weld elements are deleted immediately after failure occurs. In addition, if the *gfad* parameter did induce unloading in the simulation there is no way to define a different value for shear failure or normal tensile failure.

The *MAT_240 material model is able to capture the post-weld failure unloading very well for all of the material conditions tested for the cross tension tests.

The evaluation of the two spot weld material models is that the *MAT_240 cohesive element weld material model can provide better numerical predictions of the spot weld for tensile lap shear and cross tension tests. The evaluation that *MAT_240 better predicted the experiments than *MAT_100_DA was determined through quantitative analysis of the experimental peak force and energy absorbed data, and qualitative comparisons of the force *versus* crosshead displacement predictions to the recorded data. The cohesive material model also showed that it is capable of capturing the post weld failure unloading behaviour for both normal tensile and shear failure conditions. Capturing the post weld failure unloading, and thus the total absorbed energy for the cross tension experiments, appears to be the largest benefit provided by the *MAT_240 model over the *MAT_100_DA model.

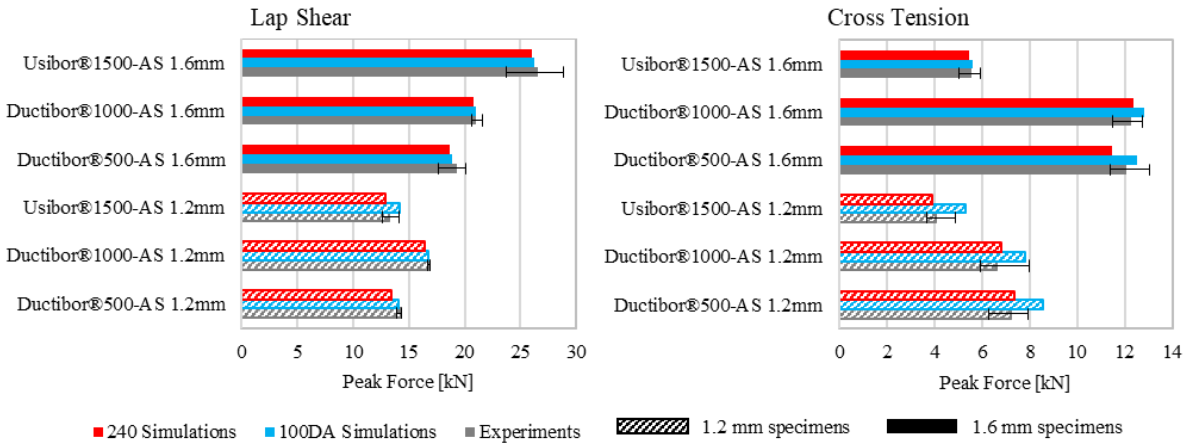

Figure 56: *Peak force data for lap shear (left) and cross tension (right) experiments and simulations.*

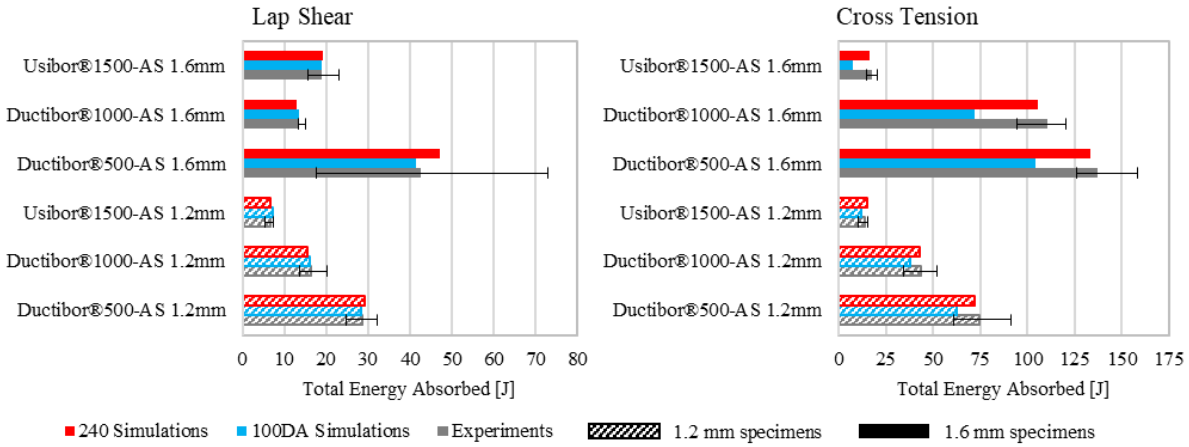

Figure 57: *Total energy absorbed for lap shear (left) and cross tension (right) experiments and simulations.*

3.5.1. Post-Failure Energy Absorption Correlations

Capturing the work done by the spot welds during post-failure unloading is critical to accurately predicting the spot weld strength and toughness. The cross tension experiments performed in this work, on average, had 15% of the total absorbed energy occur during post-failure unloading. The lap shear experiments absorbed on average 30% of the total energy during post-failure unloading. It was seen previously that input values on the material cards can be manipulated to produce numerical spot weld failure models that accurately predict the experimental force *versus* displacement responses. Here, it is examined if there are relationships or correlations that can be found between the material model input and the simulation output for the spot weld unloading behaviour. For the *MAT_100_DA model, the *gfad* parameter controls the post-failure energy absorption, however, possible correlations for the *MAT_100_DA cross tension simulations are not shown in the following (do not seems to exist) because there was no significant post-failure energy absorbed in these simulations. The parameters relevant to energy absorption for the *MAT_240 material model are either *g1c_0*, for cross tension, or *g2c_0*, for lap shear. As an example, the post-failure absorbed energy for the *MAT_100_DA and *MAT_240 Ductibor® 500-AS simulations are highlighted by the red regions in Figure 58.

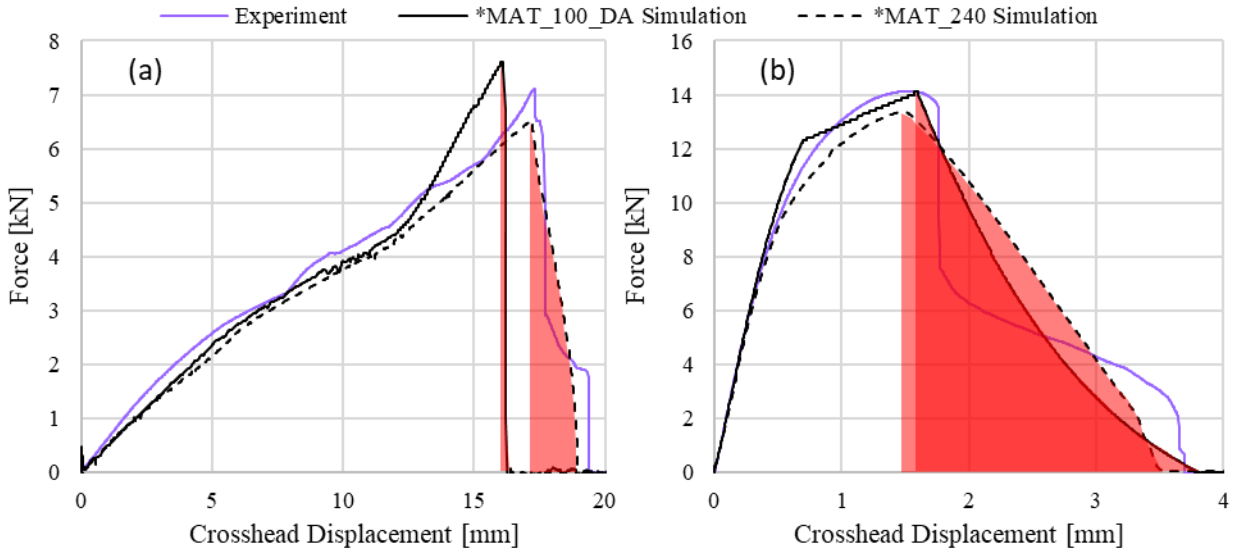

Figure 58: *Ductibor® 500-AS 1.2 mm experiment, *MAT_100_DA, and *MAT_240 force vs. displacement response for (a) cross tension; and (b) lap shear. Red shaded areas indicate post-failure absorbed energy predicted by numerical models.*

The energy absorbed during the spot weld unloading, as predicted by each numerical model, is plotted against the relevant input parameter for both the *MAT_100_DA and *MAT_240 material models in Figure 59. All of the plots in Figure 59 show a general trend that larger values input on

the material model keyword cards results in more energy being absorbed post-failure during the simulations. Although this is an obvious and expected trend, a larger input value did not always result in higher absorbed energy, even for simulations where the only difference was the thickness of the material. This indicates that there are other factors affecting the simulation post-failure behaviour, such as the failure stress in the weld elements, discussed below. Correctly defining the input parameters is important for calibrating the spot weld material models, however, there is no clear relation between the simulation output absorbed energy and the input parameter value that could be used to inform future spot weld model calibration efforts beyond what was discussed in Section 3.4.

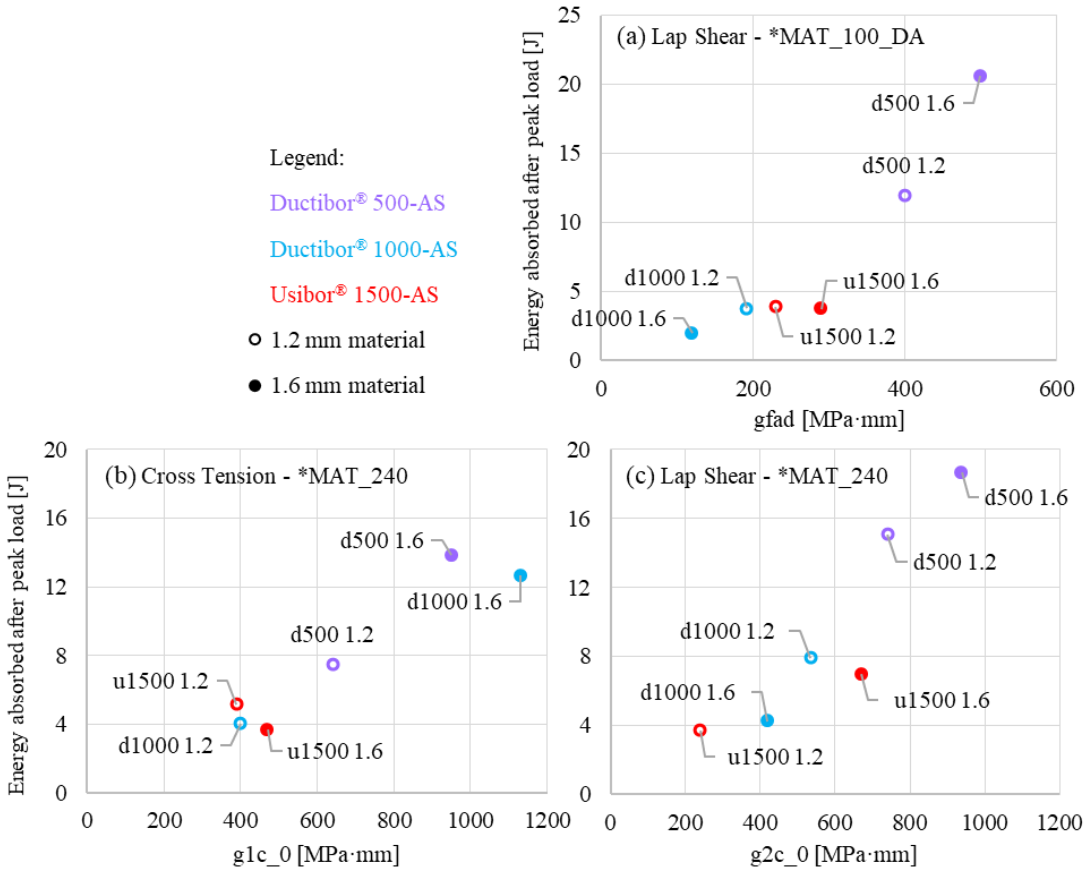

Figure 59: *Post-failure energy absorption versus input parameter value for each simulation. (a) Lap shear simulations with *MAT_100_DA model; (b) Cross tension simulations with *MAT_240 model; (c) Lap shear simulations with *MAT_240 model.*

The cross tension *MAT_100_DA plot is omitted in Figure 59 because there is negligible energy absorbed after the peak load for all cases and any comparison to input values would be meaningless. The *MAT_100_DA material model does not predict any post-failure unloading for the normal-tensile loading seen in cross tension tests because yielding in the spot weld elements is

determined by the von Mises equivalent stress but failure is determined from the stress tensor. To illustrate this point, the stress tensor at failure for the first solid hex element to fail within the spot weld for the Ductibor® 1000-AS 1.2 mm cross tension and lap shear simulations are given in Equations (40) and (41). Using these stress components, the von Mises equivalent stress at the time of failure was calculated for both simulations using Equation (42) and is shown in Table 15. Also shown in Table 15 is the yield stress parameter for the *MAT_100_DA model which was 780 MPa. From Table 15, it is evident that the von Mises stress does not reach the yield stress in the cross tension model before failure occurs. Thus, since the elements in the cross tension simulation do not first yield, the subsequent damage and unloading behaviour does not activate, resulting in the elements being deleted immediately after failure occurs.

Ductibor® 1000-AS 1.2 mm Cross Tension at failure:
$$\boldsymbol{\sigma_{ij}} = \begin{bmatrix} 170 & 0 & 31 \\ 0 & 170 & 11 \\ 31 & 11 & 335 \end{bmatrix} \quad (40)$$

Ductibor® 1000-AS 1.2 mm Lap Shear at failure:
$$\boldsymbol{\sigma_{ij}} = \begin{bmatrix} 402 & 0 & 555 \\ 0 & 147 & 0 \\ 555 & 0 & -20 \end{bmatrix} \quad (41)$$

$$\sigma_{vm} = \sqrt{\frac{1}{2}\left[\left(\sigma_x - \sigma_y\right)^2 + \left(\sigma_y - \sigma_z\right)^2 + (\sigma_z - \sigma_x)^2\right] + 3\left(\tau_{xy}^2 + \tau_{yz}^2 + \tau_{zx}^2\right)} \quad (42)$$

Table 15: *Ductibor® 1000-AS von Mises equivalent stress at time of failure for *MAT_100_DA cross tension and lap shear experiments, and the *MAT_100_DA yield stress parameter.*

Simulation	**σ_{vm} [MPa]**	**s_y [MPa]**
Cross Tension	175	780
Lap Shear	1029	780

4. Development of a shear group spot weld characterization test

A primary focus of the present work is to develop a test specimen that will capture shear failure behaviour in groups of spot welds. This new test specimen builds on the work by O'Keeffe on developing the Caiman Mode I test. Test specimens with a group of spot welds have been shown in literature with a variety of different designs, as discussed in Section 1.7. Some specimen designs are representative of an automotive structure component while others are designed to induce specific loading conditions on the spot welds.

Group spot weld tests are an extension of the single spot weld characterization tests and serve two purposes. One is to examine the experimental behaviour of weld failure in a component that contains a group of spot welds. It is understood that an automotive structure, such as the vehicle frame, contains upwards of several thousand resistance spot welds for its fabrication. In any crash scenario, an automotive structure will begin to deform and exert load on the spot weld joints. It will be possible to examine the effects of multiple spot welds in terms of peak forces and total energy absorbed by performing experiments on specimens that mimic an automotive structural component. This approach will help inform vehicle design in scenarios where, for example, the base material is of such a high strength that the weakest, and thus most critical, component of the structure is the joining method used. Group spot weld experiments are also used as a validation tool for the weld material models. Single spot welds are characterized to develop a material model for finite element analysis of the response of a vehicle to different crash scenarios. A good weld material model can predict the single spot weld experimental data that was used for calibration. A different test is required to validate that the weld model will predict accurate results for conditions other than the ones used for calibration. Group spot weld experiments fulfil this task.

The final group spot weld test specimen developed in this work section is a product of iterative design based off numerical analyses and validation experiments. The quasi-static and dynamic test methodology for the Caiman Mode III specimens are also discussed here in Sections 4.2 and 4.3. Each design concept is modelled in a 3D solid modelling CAD software to determine the specimen geometry. The solid model is then meshed and inserted into the LS-Dyna simulation keyword deck. The simulations are used as a tool to establish preliminary feasibility without having to spend time and effort fabricating prototype specimens, only to discover the design does not behave as desired. The numerical simulations are presented in more detail in Section 5.2. Once a design was

shown in the simulations to create successive shear weld failure in a controlled manner, a small batch of validation specimens were fabricated. These specimens were tested to confirm experimentally whether the design is viable for both fabrication and test data acquisition. Following the validation specimen experiments, a final design was completed after slight modifications. Subsequently, weld group specimens were fabricated using the three hot stamped materials, Ductibor® 500-AS, Ductibor® 1000-AS, and Usibor® 1500-AS, and were tested. The weld group design process and preliminary results are given in this chapter, while results of the mechanical testing and the numerical model simulations considering the three hot stamped alloys are reported in Chapter 5.

4.1. Caiman Mode III Design

The original weld group test developed by O'Keeffe [51], the Caiman Mode I, derived its name from the visual similarities seen between the opening of a caiman's mouth and the opened post-failure test specimen. The Mode I refers to fracture mechanics mode I opening type that develops when an edge crack is loaded with a normal tensile load. Continuing off of the work done to develop the Caiman Mode I test, it is desired to have a similar weld group test but one that predominately loads the spot welds under shear stress. This new test is named the Caiman Mode III, to indicate the predominantly shear, mode III fracture mechanics opening type. The design of the Caiman Mode III test was an iterative process that considered many factors, such as the specimen stability (suppression of buckling), fabrication feasibility, compatibility with Caiman Mode I fixtures, and specimen weight.

Compatibility with the Caiman Mode I fixtures requires that the Caiman Mode III design must interface with the tensile frame and the crash sled fixtures via pins that pass through inner and outer bosses. The quasi-static and dynamic test fixtures are shown in Figure 60. The pins will be reused, and the geometry of the inner and outer bosses can be altered as long as the pins pass through with no interference. For both the quasi-static and dynamic setups, the pins are hardened S7 steel that is ground to a final dimension and the bosses are machined from pre-hardened AISI 4140. The inner bosses and pins are processed to a nominal dimension of 24.13 mm or 0.950 inches and adhere to the H9/d9 tolerance specification to ensure that the pin can easily slide through the inner bosses. The outer bosses have at least a 0.5 mm clearance around the pins. For the MTS tensile frame, there are two custom designed clevises that replace the hydraulic grips (left image

in Figure 60). The lower clevis is fixed while the upper clevis is connected to the crosshead. The dynamic tests use a large fixture that is bolted to the wall to hold the specimen away from the wall such that the forks attached to the sled impact the longer pin (right image in Figure 60).

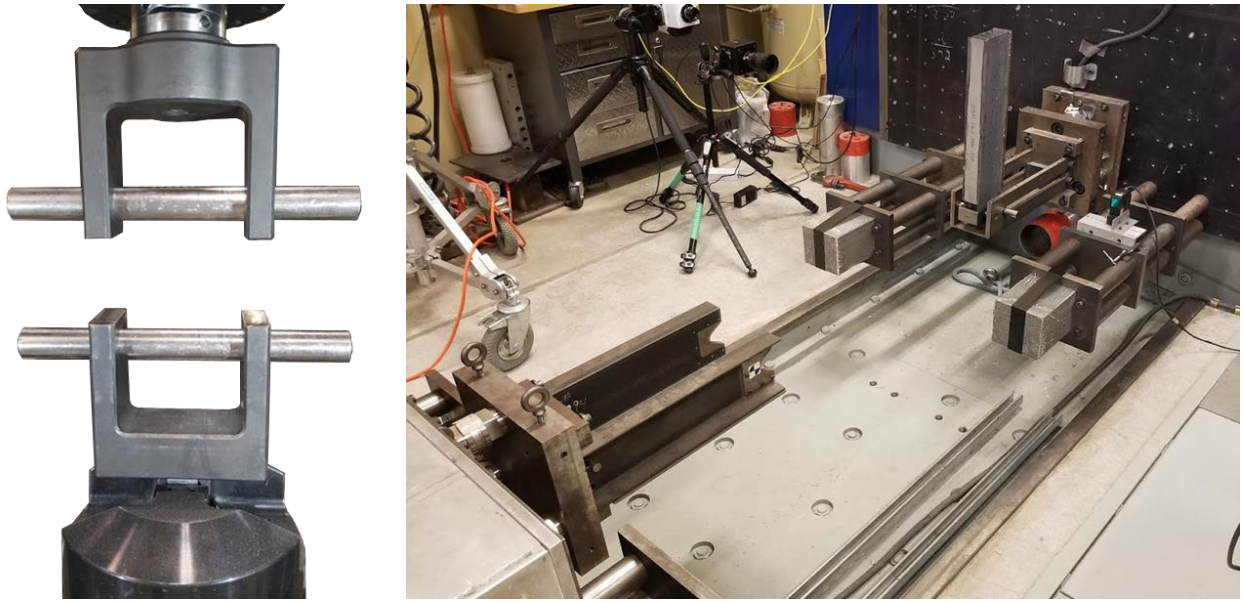

Figure 60: *Left) Tensile frame interface fixtures for quasi-static testing. Right) Crash sled fixtures for dynamic testing.*

4.1.1. Initial Design Options

The first option for the Caiman Mode III design was to use a double hat channel rail as the test specimen, similar to that adopted for the Caiman Mode I assembly by O'Keeffe [51]. To develop shear stress in the weld joints instead of the normal tensile stresses, the hat channel rail would have to be rotated axially 90°, as shown in Figure 61. This approach is attractive since a significant amount of equipment and expertise is readily available to form these parts and join them together [24], [49], [107], [108]. This existing equipment would greatly ease the fabrication process which is desirable for this work as well as any future work that would utilize this test. The arrows in Figure 61 indicate the applied loads, 'F', on each hat channel that are required to pull apart the specimen and create shear loads in the spot welds. Unfortunately, this specimen design exhibited a strong tendency to buckle prior to spot weld failure. Initial simulations were completed using hat channels that are assigned material properties corresponding to Ductibor® 500-AS (Figure 46) and the calibrated spot weld model. Ductibor® 500-AS is used for these initial simulations because this material has the lowest tensile strength of the three considered in this work and also has the toughest spot welds. It is shown in the right image of Figure 61 that the structure does not have enough stiffness to resist twisting due to the bending moments created by the applied loads that

are not on the central XZ-plane. Another factor for the rejection of this design is that the fixtures required to support the specimen as it is loaded would be a new design and impractical. For the quasi-static tests the fixture design is relatively straightforward as the tensile frame pulls the specimen from opposite sides. However, for the dynamic test using the crash sled, the fixture design is significantly more complex because one channel is fixed and offset from the wall while the other channel has to be impacted by the sled. Thus, this design was judged inadequate for achieving the goals of the Caiman Mode III test.

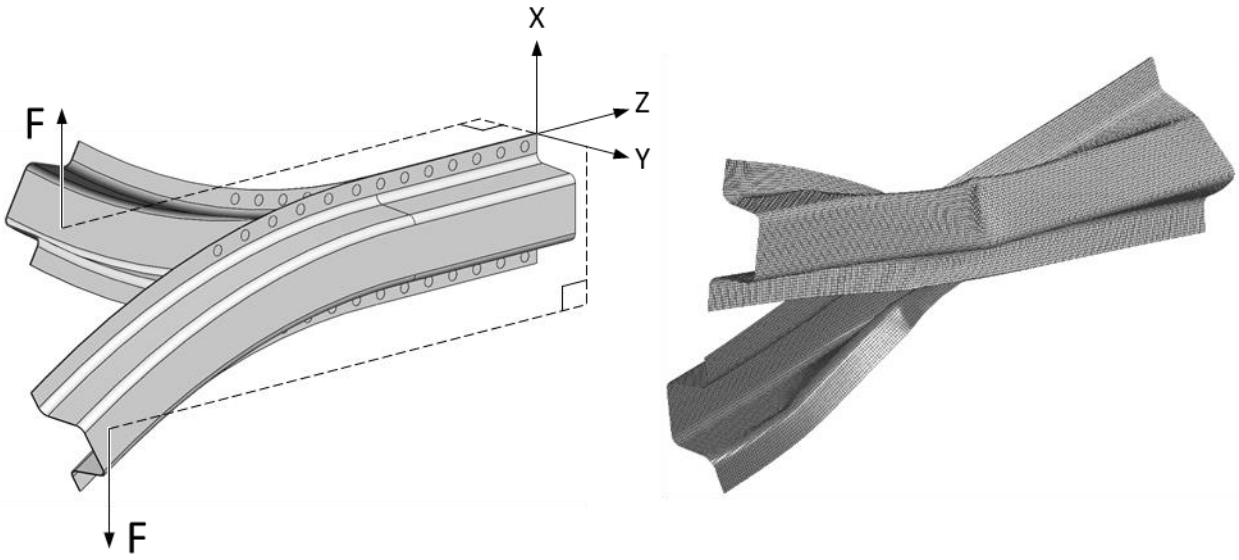

Figure 61: Left) *Initial Caiman Mode III design idea to rotate a double hat channel to create shear stress weld failures. Arrows indicate applied load, F, on each hat channel.* Right) *Simulation of the initial design using Ductibor® 500-AS material showing the twisting and buckling occurring at the first spot weld on each flange.*

An iterative design approach was undertaken to solve the fundamental issues with the initial design (Figure 61) that used a typical hat-channel rail. The main issue with the hat-channel rail is that it is predicted to be unstable during loading causing the specimen to twist and buckle before significant weld failure occurs. It is established that the main reason for this is that the loads being applied to each channel are offset from the centre plane.

The previous design is modified by doubling the hat-channel rail by mirroring the entire rail along one of the channel top faces, as seen in Figure 62. With this design, the two inner channels will be pulled or impacted together while the outer two rails will be fixed. It is hypothesized that this setup creates balanced forces so that a twisting moment or torque is not generated. However, there are other issues created by introducing a second hat-channel rail. A total of 56 spot welds

and 4 hat-channels are required for the assembly of one test specimen. This is a large amount of material that requires shearing, forming/quenching, and trimming operations which adds a significant cost and time to the fabrication of a specimen. Another possible issue is with the addition of a second hat-channel rail with more spot welds, there are four spot welds that will be initially loaded at the same time. As an approximation, the peak force for the strongest lap shear spot welds (26.5 kN for Usibor® 1500-AS 1.6 mm) multiplied by four indicates the peak load of this Mode III assembly. This equates to a theoretical peak load that could be upwards of 100 kN, or more if there is load sharing, which is at or above the limit of the load cell that is used in the tensile frame for quasi-static testing. Simulations of this design, shown in the right side of Figure 62, with the same input parameters as the previous design model shows that while twisting is suppressed by this more balance load application, significant local buckling still occurs.

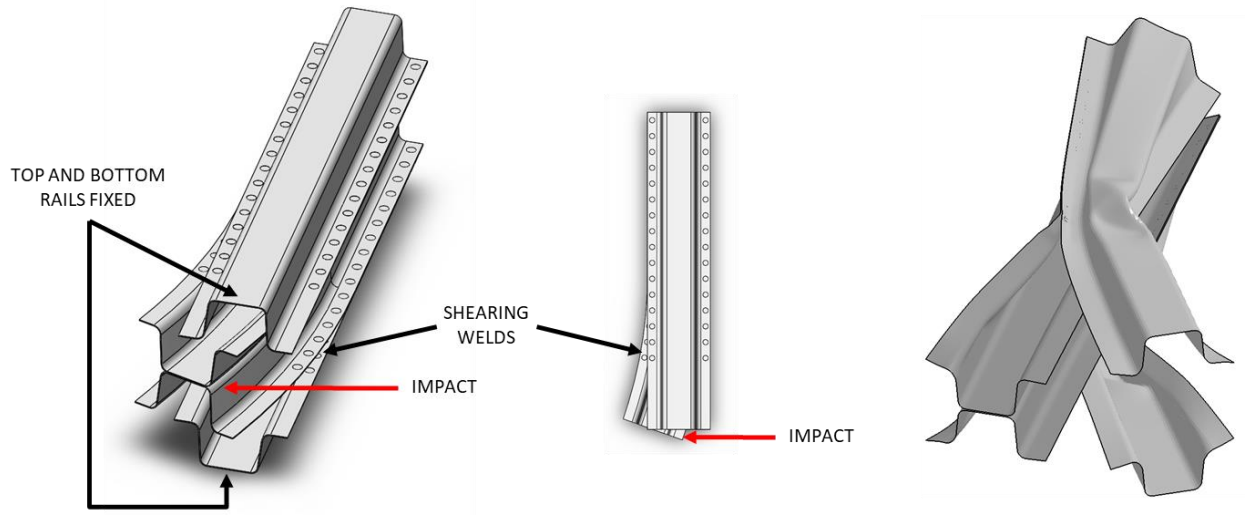

Figure 62: *Left) Initial design iteration showing the mirrored hat-channel rail. Fixed rails and desired weld failure indicated with black arrows. Impacted rails and direction are indicated with red arrows. Right) Simulation of the mirrored hat-channel rail design.*

From these initial design considerations and the validation simulations performed, it is established that the hat-channel rail geometry cannot be easily converted to a Mode III group weld shear failure test. Thus, a new rail geometry design is needed that will meet the requirements established for a successful test specimen.

4.1.2. Custom U-channel Design

Given the issues identified with the two preliminary designs using the available u-channel sections, it was decided to abandon development of a group spot weld Caiman Mode III testing using these sections. Instead, an entirely new specimen design was pursued.

The first design iteration, referred to as Caiman Mode III Rev 1, focuses on creating the shear loading condition in the spot welds and while maintaining ease of fabrication. It is understood that to create a shear loading condition, the interface plane of the spot weld joints needs to be parallel to the applied load, as seen in the tensile lap shear specimens. The simplest way to achieve this for the application of multiple spot welds is to extend the width of the tensile lap shear specimen coupons and apply more than one spot weld. This geometry would load all of the spot welds simultaneously, which is undesirable for examining weld failure unzipping. Alternatively, the specimen coupons could be gripped at one end but would be very unstable as they are pulled apart, similar to what was seen for the single hat channel rail design in Section 4.1.1. The first design option considered was to fabricate two U-channels that are spot welded together down the length of each side wall. This design attempts to replicate the design of the Caiman Mode I specimen except that instead of having the spot welds on the mating flanges of the two hat-channels, the spot welds are located on overlapping side walls of the U-channels. The clamping strategy using an inner and outer boss with through-pins is the same as the Mode I test. The boss geometry changes slightly since the rail geometry is different, but the pins are common across the Mode I and Mode III designs.

The fabrication of the U-channels presents a number of challenges that need to be resolved. It is infeasible to hot stamp a U-channel that has parallel vertical side walls because it is not possible to control the contact pressure, and thus quench rate, on the sidewalls. The other issue with joining two overlapping U-channels is that once the two channels are positioned in place to await the spot welds, there is no longer access for the spot welding electrodes on the inner side of the channels, illustrated in Figure 63.

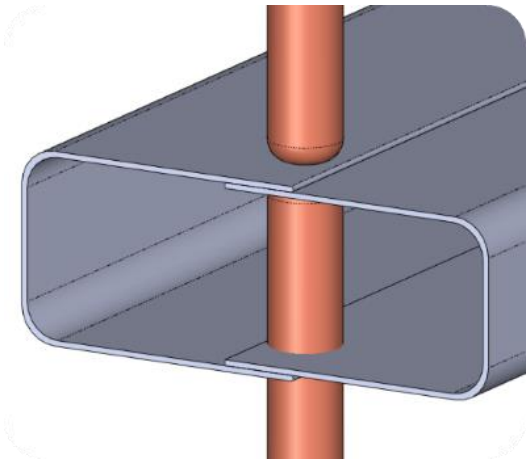

Figure 63: *Interference between lower weld electrode and sidewalls when joining two overlapping die-formed U-channels.*

To resolve the issues of fabrication, it is proposed that the entire specimen is built up by welding an assembly together in stages, as illustrated in Figure 64. To describe the U-channel design, specific nomenclature is used. The U-channel is fabricated from two side walls and one (or more) C-channels. Then, two U-channels make a complete rail specimen. Although, due to the actual fabrication sequence, a single U-channel is never actually obtained because the side walls of opposing U-channels are spot welded together first.

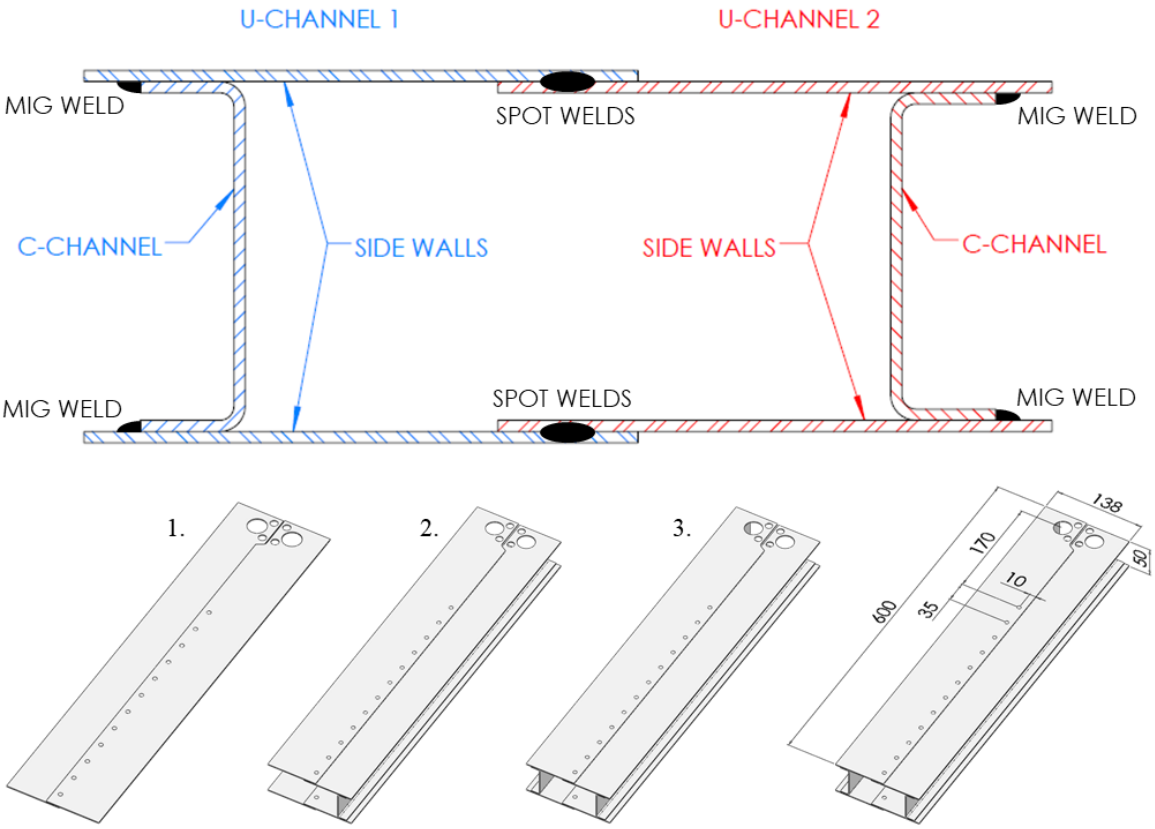

Figure 64: *Top) Custom U-Channel rail components. Bottom) Three step joining operations and final outer dimensions with spot weld spacing.*

First, the as-received sheet metal blanks are austenitized and then quenched using flat dies to mimic the hot stamped condition. After quenching, the blanks are laser cut to form the sidewalls of the specimen. Two sidewall blanks are then spot welded together in a fixture. This step is performed twice to create two spot welded sidewalls. Second, C-channels are formed using a high tensile strength material that can be cold formed, such as DP 980, which will be used to offset and support the spot welded side walls. A series of 25 mm long MIG welds, spaced 35 mm apart, are used to join the sidewall material to the DP 980 C-channels. The final product is essentially the same as two U-channels that are spot welded together along the overlapping side walls but

following a fabrication process enables flat, parallel sidewalls to be spot welded in a hot stamped condition.

Quasi-static simulation of the Caiman Mode III Rev 1 design[1] show that this assembly buckles at the first and second spot welds prior to progressive failure of the spot weld group. As the Caiman Mode III specimen is loaded, the two U-channels that have been joined with spot welds act as cantilevered beams that extend from the pins to the first spot weld. As the load increases, a bending moment is generated. For a cantilevered beam, the maximum moment occurs at the location furthest from the applied load, in this case the nearest load-bearing spot weld. At this location, the compressive stress causes the U-channels to buckle and create a hinge-like pivot point, seen in the right image of Figure 65. Once this occurs, the structural strength of the U-channel is compromised and weld failure halts, seen in the right image of Figure 65. From this simulation it is established that the channels making up the specimen require more strength and rigidity to promote spot weld failures.

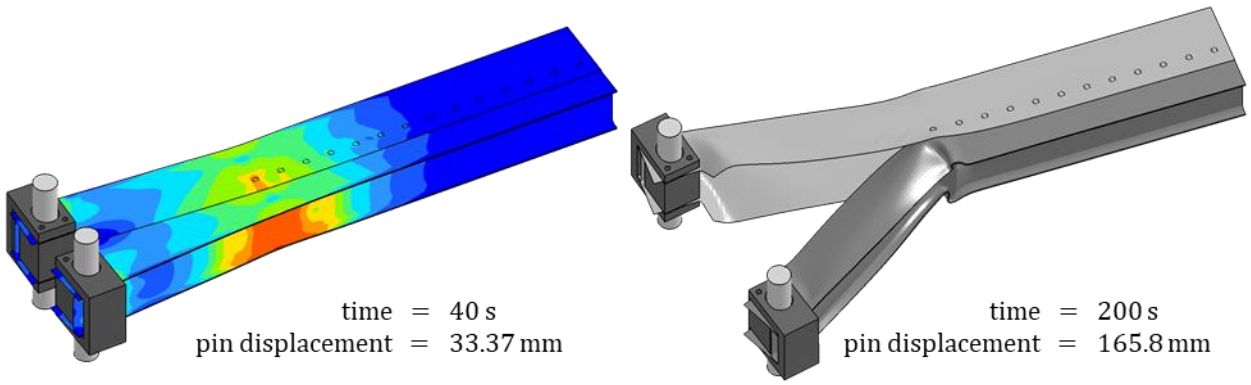

Figure 65: *Left) Caiman Mode III Rev 1 simulation showing von Mises equivalent stress contour plot. Right) Complete U-channel buckling of the Caiman Mode III Rev 1 simulation.*

There are three aspects that can be altered that will increase the specimen strength and rigidity to resist buckling: changing the material, changing the loads, and changing the geometry. The sidewall material cannot be changed since it is the focus of this project, however, in principle a stronger material with a higher yield and ultimate tensile stress could be selected for the C-channels. The material currently selected for the C-channels has an ultimate tensile strength of 980 MPa and a stronger material that is easily integrated into this design is not available, therefore it is not changed. Reducing the tensile load that induces the bending moment in the specimen U-

[1] Note that the finite element models of the Caiman Mode III experiments are documented in Section 5.2.

channels will lower the bending stress but to do this the weld strength would have to be reduced, which is counter to the goal of the project. The geometry of the specimen can be changed to increase the moment of inertia of area which will also reduce the effective bending stress that is causing the buckling. Two geometry changes are considered for the Caiman Mode III Rev 2 design, seen in Figure 66. The first option, Rev 2.1, is to double the C-channel thickness, which is 1.6 mm, by adding a second C-channel inside of the first one. The double C-channel design option is proposed because it adds more material at the location of folding initiation where buckling initiates. The other option, Rev 2.2, is also to add a second C-channel but have it offset from the first one, towards the spot welds. In addition to increasing the strength and stiffness of the rail, adding a second support in the Rev 2.2 option that connects the sidewalls to each other helps prevent twisting and out-of-plane motion of the sidewalls. Examining the simulation results, in Figure 67, it is seen that both geometry changes considered are predicted to prevent the specimen from buckling. The maximum out-of-plane displacement of the side walls is 23.8 mm for Rev 2.1 and 8.6 mm for Rev 2.2. The Rev 2.2 offset C-channel design is selected over the Rev 2.1 double C-channel option because the predicted results show less out-of-plane deformation of the side walls and less bending in the rails.

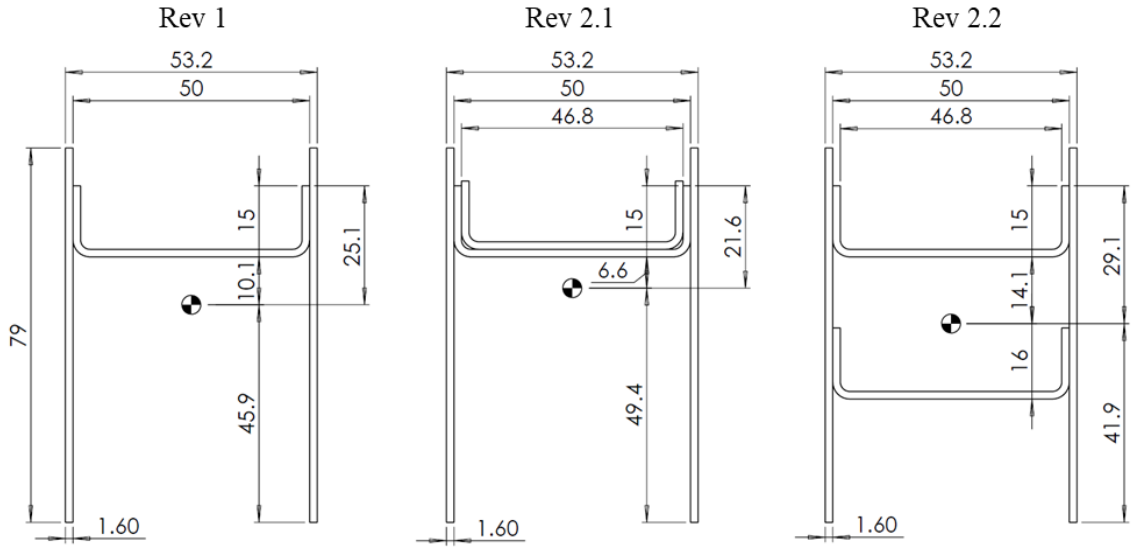

Figure 66: *Cross section of the custom U-channel design revisions. Centre of Mass symbol indicates location of the centroid for each cross section.*

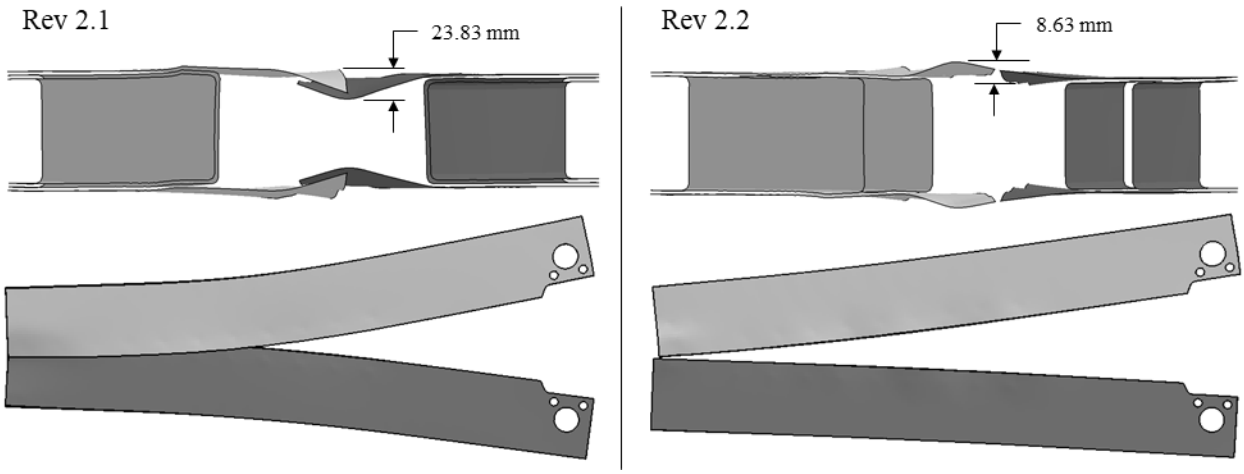

Figure 67: *Simulation results of the Caiman Mode III Rev 2.1 (left) and Rev 2.2 (right) design options. Measurements show maximum out-of-plane displacement of the side walls during simulation. All models are shown at pin displacement = 118 mm.*

4.1.3. Validation Specimens

Validation specimens are created using the Caiman Mode III Rev 2.2 design geometry. The purpose of the validation specimens is to ensure that the selected geometry can be fabricated and that the experiments produce progressive shear weld failure. To construct the validation specimens, as-received material (not hot stamped) is used for the side walls to reduce the time required for fabrication. The side wall blanks are laser cut from the large as-supplied sheets to the final shape. These blanks include hole features for the pins to pass through and for the bolts used to clamp the inner and outer bosses together. Since the side wall material for the validation specimens is not quenched, the weld schedule that was optimized for hot stamped sheet requires slight modification. The weld current is adjusted to eliminate expulsion and although this will not necessarily produce peak strength spot welds, it is assumed that this approach is adequate for the purpose of the validation process. Twelve spot welds are placed along the overlapping region of two individual side wall blanks, for a total of twenty-four welds. The sidewalls are joined to the DP980 1.6 mm C-channels using MIG welds that were 25 mm long with a spacing of 35 mm to reduce the amount of heat input into the side wall material. A completed validation test specimen is shown in Figure 68.

Figure 68: *Caiman Mode III Rev 2.2 validation specimen, labelled* UW#2.

The validation specimen tests are performed using the MTS tensile frame under quasi-static conditions (more detail is provided in Section 4.2). The crosshead speed is set to 50 mm/min and the test is stopped when the crosshead displacement reaches 250 mm. The pins each slide through a clevis to interface with the tensile frame. The first validation specimen tested, labelled *UW#1*, buckled after two weld failures occur on one side, shown in Figure 69. From the post-failure images, it is seen that there is significant out-of-plane deformation of the side wall material and the C-channel that the side walls are welded to. Closer examination shows that the buckle initiates between the MIG welds on both sides of the U-channel. On one side, the C-channel and the side wall fold together as the buckle occurs while on the other side the side wall separates from the C-channel. The cause of the buckling is attributed to a lack of a constraint that allows the side wall material to fold out of its initial plane.

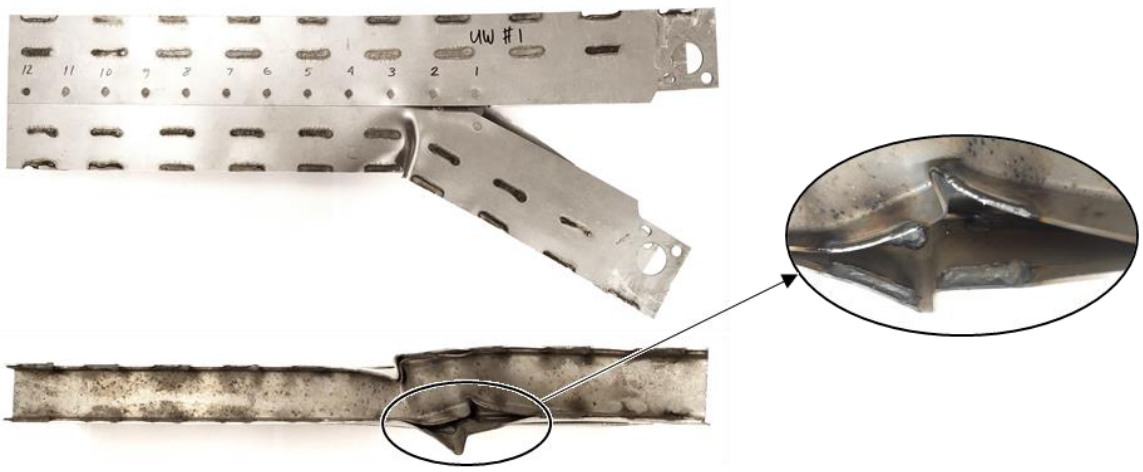

Figure 69: *Caiman Mode III Rev 2.2 post-test validation specimen* UW#1.

The next design revision, referred to as Rev 3 and labelled *UW#3* in Figure 70, is a modification of the previous validation specimen that was tested. It was seen in the test of Rev 2.2 that the cause of buckling is the folding deformation of the side wall and C-channels due to the compressive

stress as the rail is loaded. To prevent the folding, which was noted to occur between the spaced out MIG welds, the specimen is modified to have a continuous MIG weld joining the side walls to the C-channels for the entire length of the specimen.

Figure 70: *Caiman Mode III Rev 3 specimen, labelled* UW#3.

The test results of the *UW#3* specimen show that buckling is still occurring after one to two spot weld failures. The continuous MIG welds had the desired effect of constraining the side walls to the C-channels but the side wall folding behaviour still occurred. A more direct constraint on the side walls is required to prevent the folding. It is also noted that because the side walls fold and buckle instead of initiating progressive weld failure, the side wall material begins to split at the first spot weld and fracture towards the outer edge.

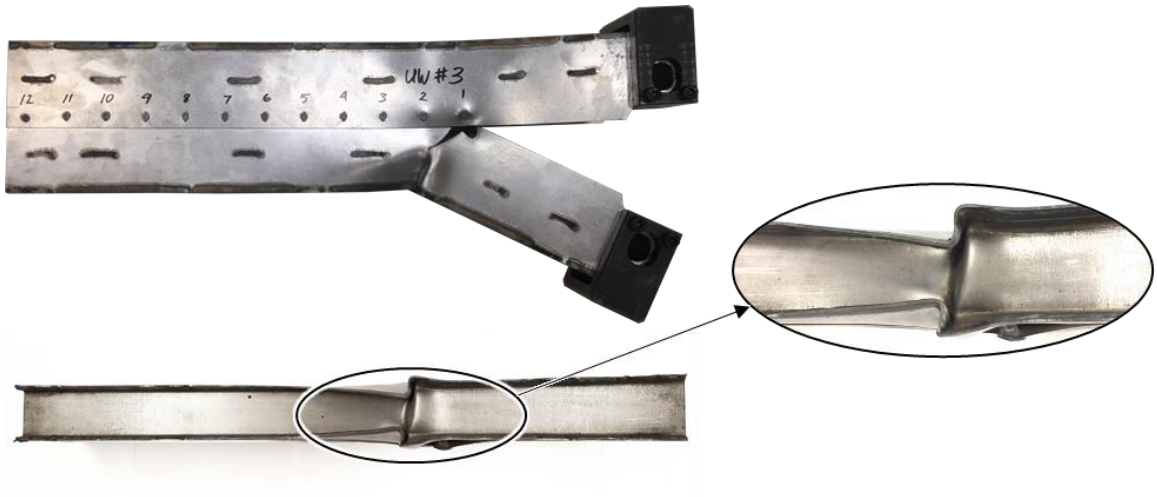

Figure 71: *Caiman Mode III Rev 3 post-test validation specimen* UW#3.

The Caiman Mode III Rev 4 design adds 1.25 x 1.25 x 0.188 inch angle iron that is welded into place along the outer C-channels, labelled *UW#2* in Figure 72. They key purpose of the angle iron is to fully constrain the side walls to prevent any out-of-plane motion. The angle iron significantly increases the moment of inertia of area and resistance to buckling for each U-channel. The

calculated moment of inertia of area for the Rev 4 design is 356914 mm^4 and the maximum vertical distance from the neutral axis is 18.1 mm.

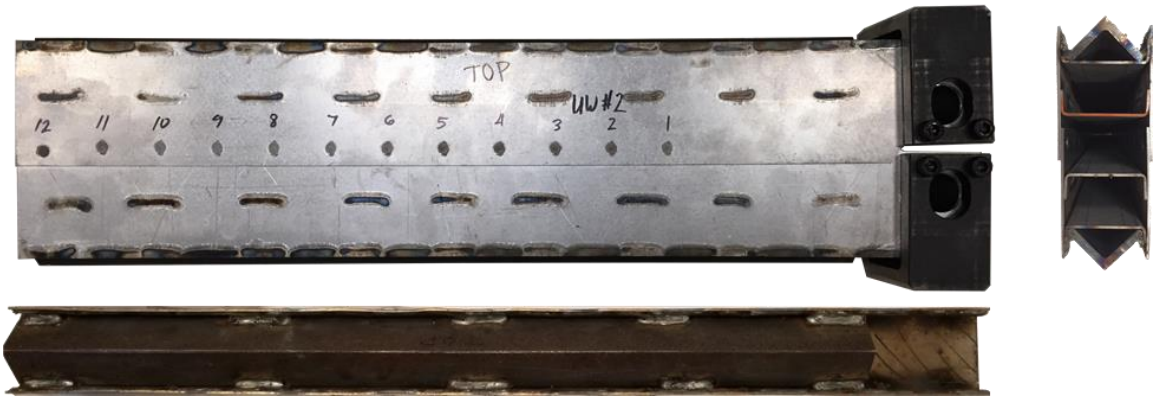

Figure 72: *Caiman Mode III Rev 4 specimen, labelled* UW#2.

The Rev 4 validation specimen experiment results, Figure 73, shows that the current design can produce stable and progressive shear weld failure up to approximately seven or eight spot welds per side. There is very little out-of-plane deformation in this specimen until the rail begins to collapse from spot weld #8 to the end. As the crosshead displacement increases and the weld failure progressed, the unconstrained end of the specimen began to collapse. The sidewalls separate from the inner c-channels that are supporting the structure and start to fold over. The collapsing behaviour is not desirable because the major deformation mode is changing and prevents further weld failure; however, since this collapse does not occur until over half of the spot welds have failed, it was not deemed a significant issue at this time.

Figure 73: *Caiman Mode III Rev 4 post-test validation specimen* UW#2.

4.1.4. Final Design

The final design adopted for the Caiman Mode III specimen is designated Rev 5, labelled *UW#6* in Figure 74. This revision is a modification from Rev 4 that replaced the angle iron addition with a flat sheet of DP 980 steel that acts as a closing cap along the length of the rail. It was established that the primary function of the angle iron was to prevent out-of-plane deformation of the side walls during the test and the flat cap continuously welded onto the side wall edges achieves this purpose. The angle iron increased the total cross section area, and thus volume and mass, of the rail by 65% whereas the flat closing cap in Rev 5 increased the total cross section area by only 20%. This lower inertia is more desirable to reduce higher inertial effects in the dynamic testing. A drawing package of the final design is provided in Appendix B

Figure 74: *Caiman Mode III Rev 5 specimen, labelled* UW#6*, before and after testing.*

The recorded force *versus* displacement data from each validation specimen revision is presented in Figure 75. The force response of the Rev 2.2 and Rev 3 specimen designs had a lower peak force and lower total energy absorbed because of the buckling failure mode. In addition to the higher peak force, the design modifications Rev 4 and Rev 5 (which did not buckle) had a longer sustained load as the weld failures propagate along the rail. In the same way as the single spot weld experiments showed, different weld failure modes can be seen in the data here. Sudden drops in the force for specimens Rev 5 and Rev 2.2 are caused by interfacial failures while all other weld failures seen in the validation specimens are shared asymmetric pull out. The rail collapse discussed earlier for specimen designs Rev 4 and Rev 5 after 7-8 weld failures per side occurred corresponds to the rapid load drop at approximately 90 mm of crosshead displacement.

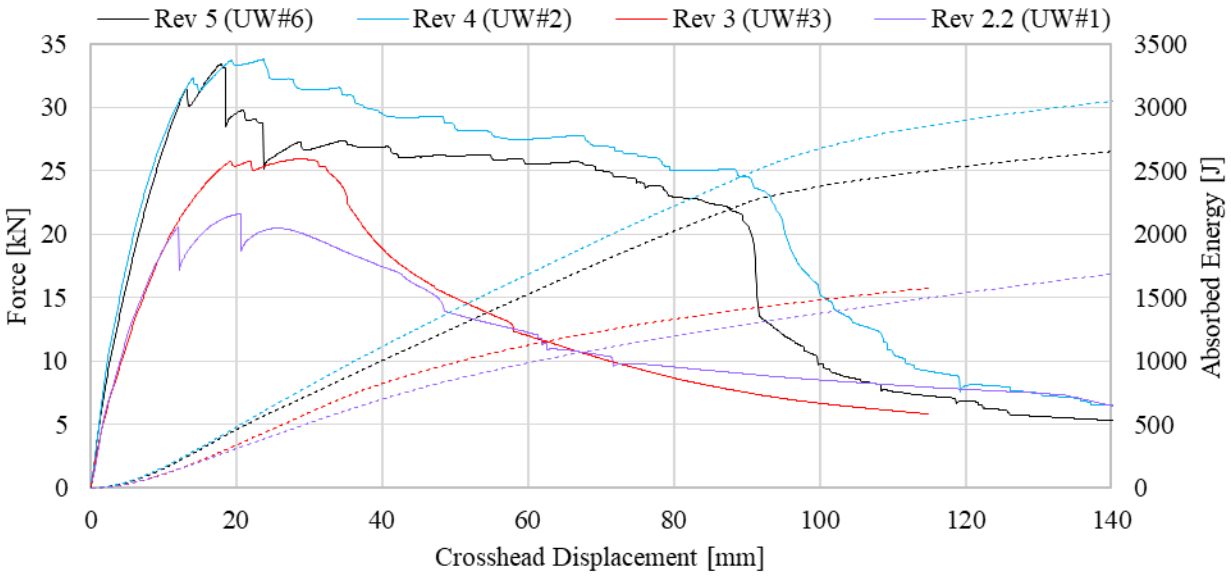

Figure 75: *Force (solid lines) and Absorbed Energy (dashed lines)* versus *crosshead displacement data for validation specimen revisions.*

4.2. Quasi-static testing methodology

The quasi-static Caiman Mode III specimens were tested using the same MTS tensile frame and setup documented in Section 3.1, with slight modifications. The quasi-static testing is performed with a crosshead speed of 50 mm/min and a maximum total displacement of 250 mm. The group spot weld tests recorded the same tensile load and crosshead displacement data as the single spot weld tests, as well as optical and thermal videography. The optical cameras were Point Grey GRAS-50S5M-C set to record at a frame rate of five frames per second. Two optical cameras used were to capture video of the left and right side of the specimens. Correlated Solutions Vic-

Snap software was used to record the camera videos and time synchronize with the force and displacement data from the MTS frame via a National Instruments Multifunction I/O device. A Telops Fast-IR-2K thermal camera was used to record infrared (IR) images during testing. O'Keeffe [51] reported that IR images can be used to detect the onset of weld failure due to the sudden local plastic work and heat released during strain localization. The RevealIR software was used to perform data collection and post-process to create videos. The thermal camera data acquisition was triggered using the rising edge of the load signal coming from the MTS frame. An example quasi-static setup showing the group weld Caiman Mode III specimen is seen in Figure 76.

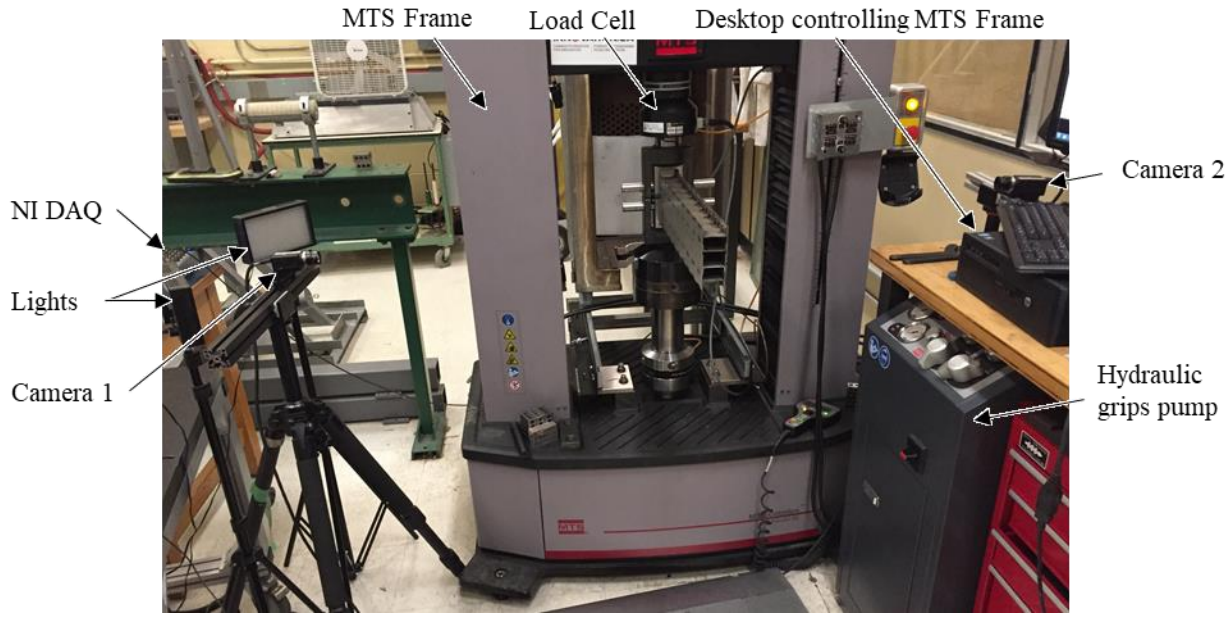

Figure 76: *Quasi-static testing setup showing the group spot weld configuration. Thermal camera not seen here.*

Emissivity measurements for use in the post-processing of the thermal images were made using a Gier-Dunkle DB-100 Reflectometer, shown in Figure 77. The DB-100 is an infrared reflectometer for accurately determining the total emittance of samples. The measurement is a broadband measurement (from 5 to 25 µm). Emissivity tests were performed in accordance with Method A of ASTM E408-13 [109]. In this work, all surfaces captured with the thermal camera were sand blasted. Ductibor® 500-AS emissivity values are used for Ductibor® 1000-AS surfaces.

Material	Thickness	Surface	Emissivity
Usibor® 1500	1.2	as-stamped	0.5
		sand blasted	0.41
	1.6	as-stamped	0.52
		sand blasted	0.39
Ductibor® 500	1.2	as-stamped	0.5
		sand blasted	0.42
	1.6	as-stamped	0.51
		sand blasted	0.41

Figure 77: *Left) Gier Dunkle DB-100 Reflectometer; Right) Emissivity measurements for Usibor® 1500 and Ductibor® 500.*

4.3. Dynamic testing methodology

The dynamic testing was performed for the Caiman Mode III group weld experiments using a Seattle Safety impact sled installed at the Waterloo Forming and Impact Lab. The dynamic test setup is discussed here while the Caiman Mode III specimen development and experimental results are detailed extensively in Section 5.1.2. The impact sled system uses a pressurized vessel to drive a large pneumatic piston that is connected to the sled via a rope. As the pressurized tank valve is opened, the piston is forced to advance and accelerates the sled. The sled weighs 850 kg in the configuration used and the system was pressurized to achieve a sled velocity of 7.1 m/s at the moment of impact. A custom fixture was developed to support the Caiman Mode I specimens for dynamic testing, and is detailed by O'Keeffe [51]. Seen in Figure 78, the fixture set up was made from two assemblies. The first assembly is attached to the wall and supports the specimen. The two pins that connect through the specimen are inserted through two slotted plates. The slotted plates also support the Fixed Pin and has a long slot that constrains the Impact Pin to move in only one direction during the impact. The slotted plate was connected to a load cell pack containing three 120 kN piezoelectric load cells in a triangle pattern. To acquire data, the load cells were sampled at 10,000 Hz. There are two standoffs from the wall that hold the honeycomb used to arrest the sled at a controlled deceleration rate. Plascore 5056 honeycomb with a nominal crush strength of 3.69 MPa (535 psi) [110] was used. The specimens have 75 mm of free crush distance before the sled engages with the honeycomb.

The other fixture assembly is attached to the front face of the sled. The sled-side assembly consists of a long fork subassembly (similar in shape to a tuning fork) that extends outwards ahead

of the sled. The fork subassembly passes on the outside of the slotted plates on the wall side assembly and catches the Impact Pin. As the sled moves forward, the Impact Pin is pushed with it and pulls the specimen apart. Forces from the sled-side of the impact are also recorded using a load cell pack in the same configuration as the wall-side to record. There are two accelerometers mounted to the sled, one on each side, that record the sled accelerations during each test at the same rate as the load cells. The sled displacement is calculated by integrating the accelerometer data and is also directly measured using a Keyence LK-G507 laser displacement sensor.

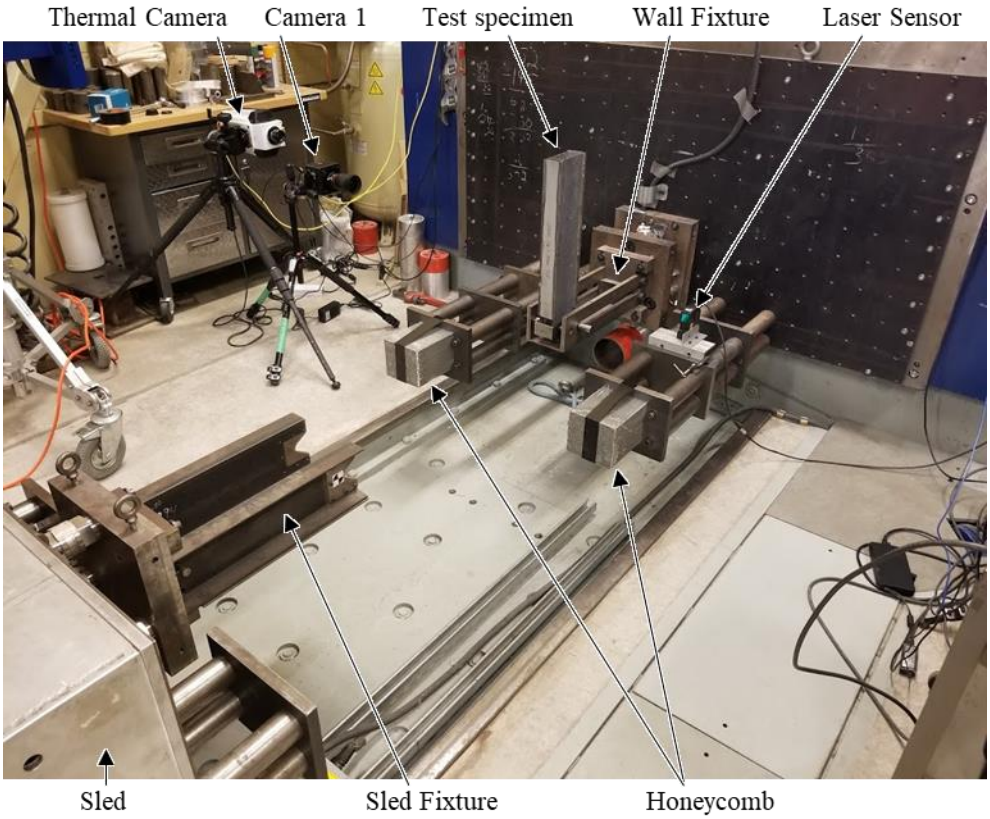

Figure 78: *Dynamic testing setup. Metal-halide floodlighting systems, Cameras 2 and 3, DAQ, and control computers not shown.*

The sled displacement was measured directly using a Keyence laser displacement sensor and was also calculated from the acceleration data recorded by the two accelerometers onboard the sled. In Equation (43), the raw accelerometer data is in units of g, which is converted to m/s^2 using the gravitational constant, 9.81, and averaged. Equations (44) to (47) are then used to determine the instantaneous displacement, as a function of time. In these equations, a is acceleration, t is time, v is velocity, and x is displacement. The subscript n refers to the sample point number, which was recorded at 10,000 samples per second. There is no difference between the two displacements

from initial sled-pin contact to the point the sled impacts the honeycomb, which is 75 mm of displacement. It was found that at the maximum sled crush distance, which ranges from 190 mm to 230 mm, the displacement calculated using acceleration data was consistently 4% below the directly measured displacement and continues to increase as the sled rebounds and travels backwards. Figure 79 shows the displacements from the two methods for a single Ductibor® 500-AS test and the difference between them. The displacement corresponding to honeycomb impact is also indicated. For all the dynamic experimental data presented in this work, the measured displacement using the Keyence laser displacement sensor is used.

$$\frac{a_{left} + a_{right}}{2}(9.81) = a_{avg}\left[\frac{m}{s^2}\right] \tag{43}$$

$$a_{avg,n} \cdot \Delta t_n = a_{avg,n} \cdot (t_n - t_{n-1}) = \Delta v_n \tag{44}$$

$$v_o + \sum \Delta v_n = v_{inst} \tag{45}$$

$$v_{inst} \cdot \Delta t_n = \Delta x_n \tag{46}$$

$$\sum \Delta x_n = x_{inst} \tag{47}$$

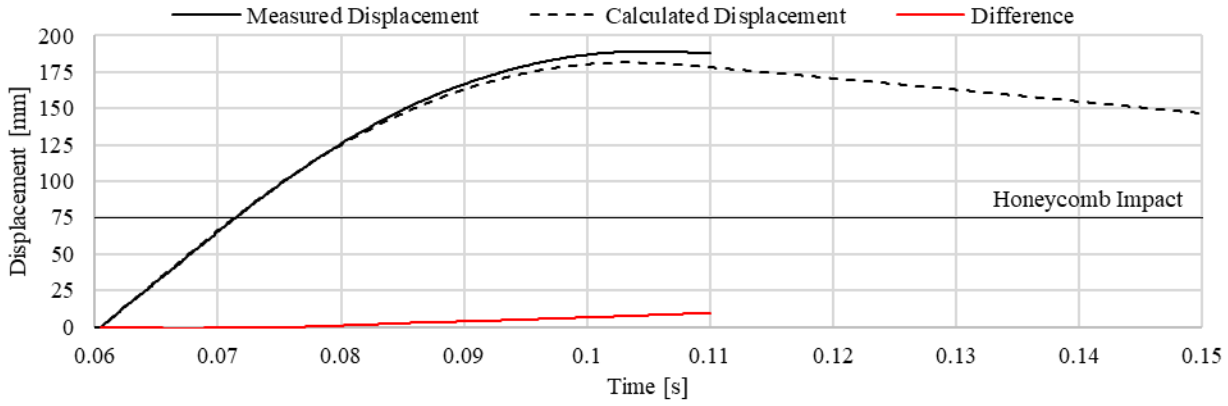

Figure 79: *Comparison of measured and calculated sled displacement.*

5. Caiman Mode III Results

The Caiman Mode III specimens fabricated according to the Rev 5 design (Section 4.1.4) were tested under quasi-static and dynamic conditions for all three hot stamped alloys and two thicknesses. The experimental results, analysis of the observed overall specimen behaviour, and spot weld failure modes are discussed here. The Caiman Mode III numerical model is developed, applying the calibrated weld material models from Chapter 3, and the simulation results are compared to the experiments and discussed.

5.1. Caiman Mode III mechanical performance

5.1.1. Quasi-Static Response

The quasi-static Caiman Mode III experimental data is summarized in Table 16. The quasi-static force *versus* crosshead displacement curves for the 1.2 mm specimens and 1.6 mm specimens are shown in Figure 80 and Figure 81, respectively. All tests initially show a sharp rise in load up to the first spot weld failure. As spot weld failure progresses, the load is sustained near the peak load values or slightly decreases. Sudden drops in the measured load are caused by individual brittle weld failure modes such as interfacial or partial button pull out, similar to what was observed for the single spot weld tests and the Caiman Mode III validation specimens. More ductile weld failure modes such as tear out still result in load drops but are less distinct than the brittle failure modes. Once spot weld failure has propagated to close to the end of the rails, the side walls tend to buckle away from the supporting inner C-channels and the load drops drastically. The rail end collapses occurred between 25 mm and 32 mm of crosshead displacement for the 1.2 mm thick specimens and between 35 mm and 80 mm for the 1.6 mm specimens.

Table 16: *Caiman Mode III quasi-static experimental data summary.*

Material	Thickness [mm]	Max Load [kN]	Energy absorbed [J]
Ductibor® 500-AS	1.2	21.4 ± 0.9	904 ± 64
	1.6	35.3 ± 0.4	2824 ± 254
Ductibor® 1000-AS	1.2	14.7 ± 0.9	367 ± 30
	1.6	29.3 ± 6.5	1030 ± 303
Usibor® 1500-AS	1.2	16.3 ± 0.8	348 ± 25
	1.6	33.7 ± 3.7	1108 ± 180

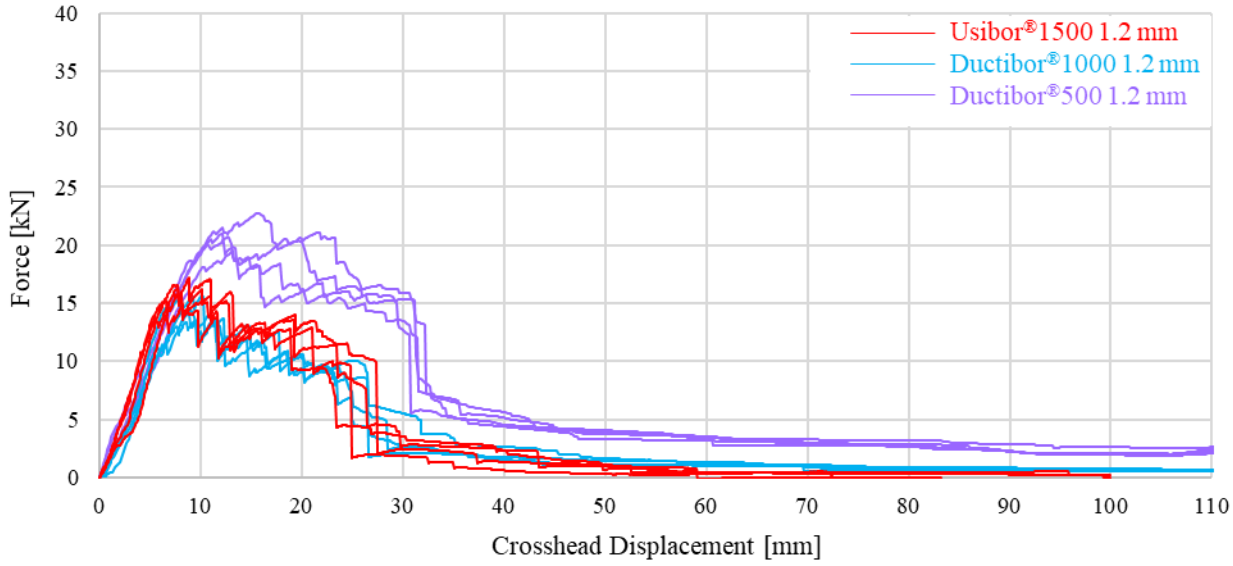

Figure 80: *Caiman Mode III 1.2 mm quasi-static force* versus *displacement.*

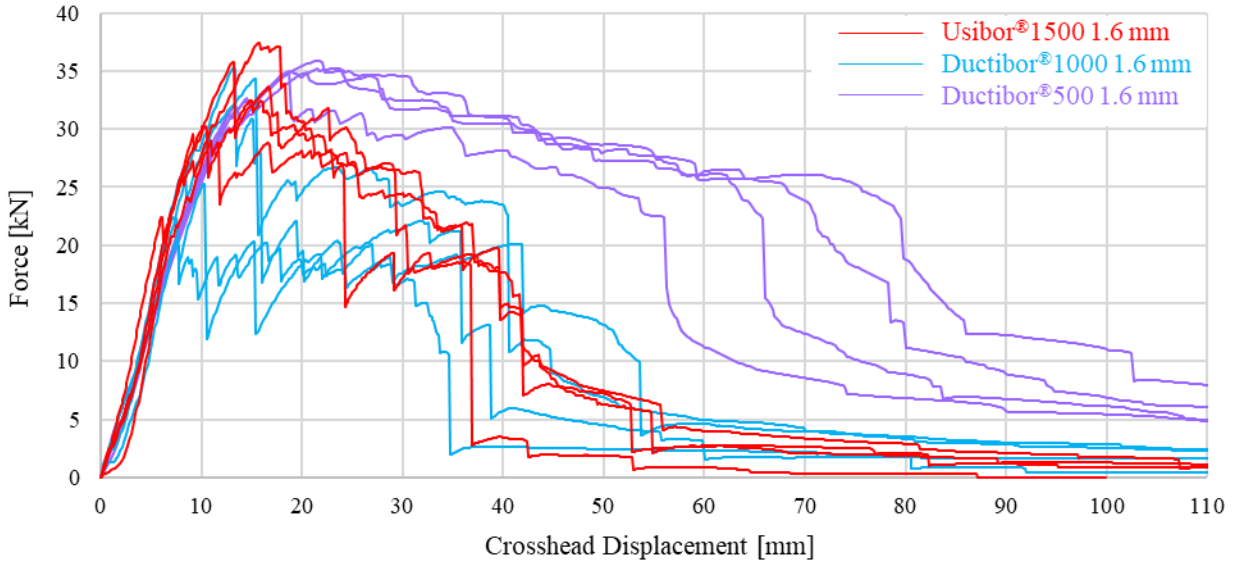

Figure 81: *Caiman Mode III 1.6 mm quasi-static force* versus *displacement.*

The average absorbed energy *versus* crosshead displacement for all specimens is shown with the heavy solid and heavy dashed lines in Figure 82. The experimental repeats are also shown in Figure 82 with the light faded lines. The maximum, or peak, load and the total energy absorbed increased for all specimens when the material thickness increased; the peak loads increased by approximately 100% while the absorbed energy increased by approximately 200%. All of the specimens resulted in progressive weld failures, as was desired, with the exception of one of the Ductibor® 500-AS 1.6 mm specimens which buckled, as discussed later.

The absorbed energy curves, Figure 82, show the weld toughness for the different materials and sheet thicknesses for the weld group specimens. For both the 1.2 mm and the 1.6 mm thicknesses, the Ductibor® 500-AS specimens have the highest absorbed energy. This is an expected result considering that the softer material doesn't have a softened SCHAZ zone, which has been shown in literature to cause early strain localization and fracture. The single spot weld lap shear experiments also showed that the Ductibor® 500-AS material exhibits ductile weld fracture modes and almost 50% of the total absorbed energy of the lap shear tests occurred after failure initiated during the unloading region. The Ductibor® 1000-AS and Usibor® 1500-AS specimens absorbed significantly less energy than the Ductibor® 500-AS specimens. It is interesting to note that for 1.2 mm specimens, the Ductibor® 1000-AS and Usibor® 1500-AS force and energy *versus* displacement are near identical. For the 1.6 mm experiments, the Ductibor® 1000-AS specimens absorbed less energy than the Usibor® 1500-AS specimens, which was an unexpected result based on the relative strength of these alloys. It was established in the single spot welding experimental results that the weld toughness is directly related to the weld fracture modes. The Ductibor® 1000-AS 1.6 mm specimens exhibited more interfacial weld failures than the Usibor® 1500-AS 1.6 mm specimens, resulting in poorer energy absorption.

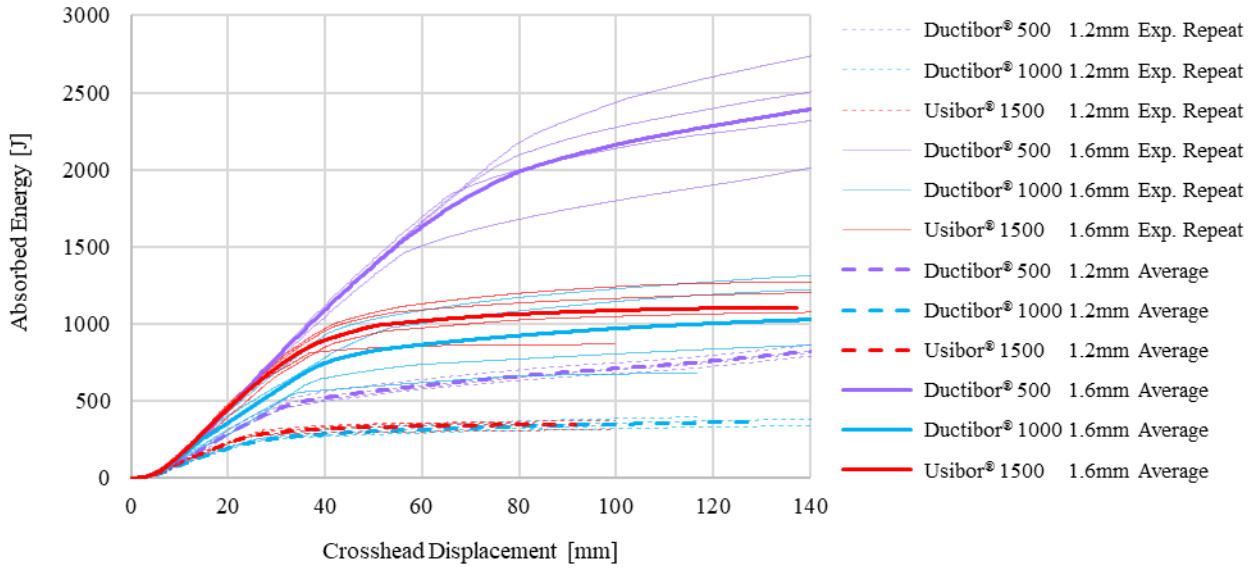

Figure 82: *Average Caiman Mode III quasi-static energy absorbed* versus *displacement data for 1.2 mm (dashed lines) and 1.6 mm (solid lines) specimens. Experimental repeats are shown with thin faded lines.*

Figure 83 shows a side view of one of each specimen condition tested and Figure 84 shows the collapsed or partially collapsed rail ends for each specimen condition. It is seen that that higher strength materials Usibor® 1500-AS and Ductibor® 1000-AS exhibit less end-collapsing than the

Ductibor® 500-AS rails. It was also observed that more spot welds fail as the strength of the material increases and the rail end collapse behaviour is reduced; spot weld failure stops once the rail end collapses in this manner. Ductibor® 500-AS specimens consistently had 7-8 spot welds, per side, fail before the rail end collapsed. The Ductibor® 1000-AS specimens had 9-10 spot welds fail per side. Three of the Usibor® 1500-AS specimens had 11 spot welds fail per side and one specimen had all 12 spot welds on each side fail, causing the two halves to separate.

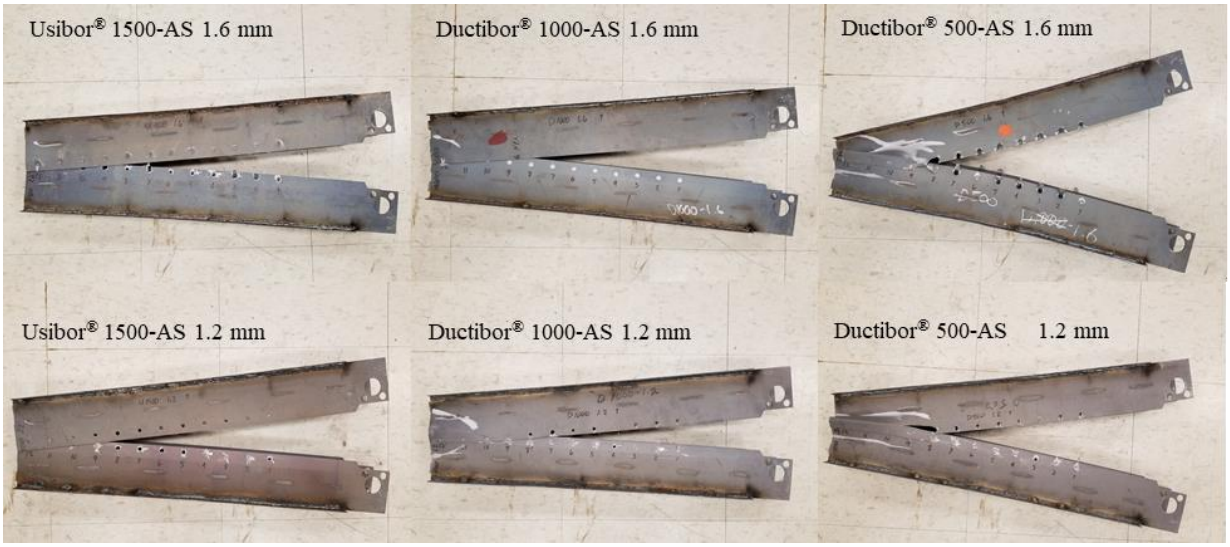

Figure 83: *Side view of post-mortem Caiman Mode III specimens.*

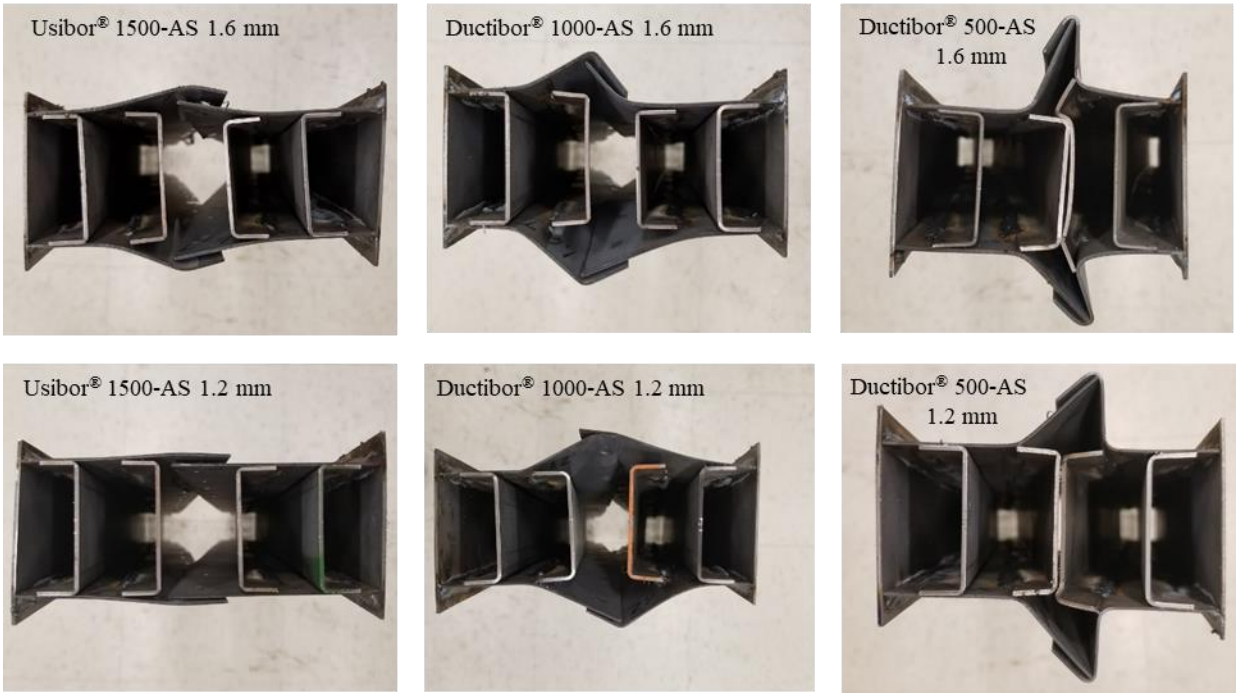

Figure 84: *End view of post-mortem Caiman Mode III specimens.*

Multiple different weld failure modes are present in each of the specimens, but each material and thickness condition tend to have a dominant failure mode. The Usibor® 1500-AS 1.6 mm specimens contained equal proportions of partial button pull out and tear out failure modes (refer to Figure 33). The Usibor® 1500-AS 1.2 mm specimens showed exclusively partial button pull out failures. The Ductibor® 1000-AS 1.6 mm specimens contained many interfacial failures along with smaller quantities of full or partial pull out and tear out failure modes. The Ductibor® 1000-AS 1.2 mm specimens exhibited almost all partial pull out with only a couple of spot welds across the four specimens tested exhibiting tear out. The Ductibor® 500-AS 1.6 mm specimens displayed mostly tear out and double shared tear out, which was defined in Section 3.2.1, along with a small amount of pull out failures.

Expulsion was present for approximately 50% of the Caiman Mode III specimens tested under quasi-static conditions, with the exception of the Ductibor® 500-AS 1.6 mm specimens. Figure 85 shows a Caiman Mode III specimen exhibiting a large amount of expulsion. Although it is not fully understood why there was so much expulsion present in these group weld specimens, considering that the weld schedule used was the same as what was used for the single spot weld specimens it is suspected that there were electrode or part alignment issues. It's also possible that or other fabrication related variables were different during the welding process that resulted in excessive expulsion, but it is not possible to identify them post testing.

Figure 85: *Caiman Mode III Usibor® 1500-AS 1.2 mm specimen exhibiting significant expulsion.*

The effects of different weld failure modes and the overall weld toughness are best seen in the absorbed energy trends and the histories of 'crack' extension *versus* load point displacement. The 'crack' discussed here is not a true crack in the Caiman specimens, but rather a representation of the progression of successive spot weld failures through the weld group. If the Caiman specimens are visualized as a Compact Tension specimen used in fracture mechanics, as shown in Figure 86, the 'crack' is taken as the distance "*a*" from the pins used for loading up to the nearest load bearing (intact) spot weld.

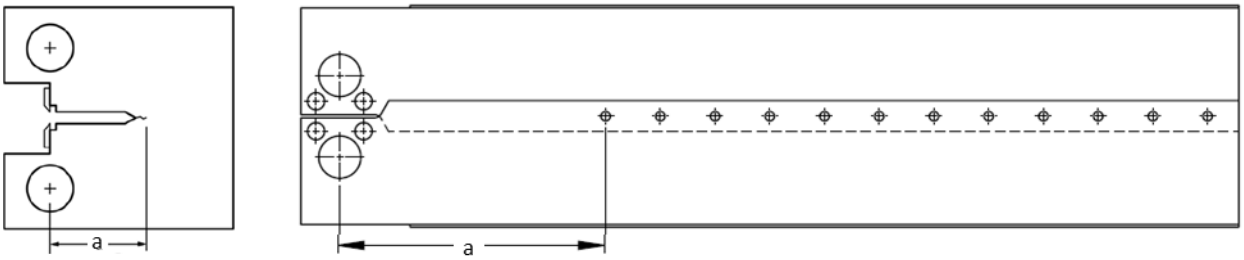

Figure 86: *Left) Compact Tension specimen showing the updated crack size, 'a'. Adapted from ASTM E1820-15a* [111]. *Right) Caiman Mode III specimen drawing showing 'crack' extension measure, 'a'.*

Weld failure was detected using an IR imaging technique first developed by O'Keeffe [51] for the Caiman Mode I specimen. In this method, the local spike in temperature due to the increase in plastic work and heat generation associated with spot weld failure can be used to identify when weld failure occurs. Thermal images were captured using a Telops Fast-IR-2K IR camera for the first six spot welds of each quasi-static Caiman Mode III specimen. Images captured during the testing of two Ductibor® 500-AS specimens, in Figure 87, highlight the different thermal distribution of various failure modes. In the upper image, double shared tear out and button pull out are present in the first two spot welds of the Ductibor® 500-AS 1.6 mm #1 specimen and in the lower image, the Ductibor® 500-AS 1.6 mm #2 specimen shows tear out failure occurring at different stages for the first four spot welds. Tear out failure modes generate more heat than pull out failure due to increased plastic work, which is consistent with the energy absorbed for these failure types as seen in the tensile lap shear experiments (Figure 37). Regardless of the failure mode, the peak temperature rise seen during the quasi-static testing was around 10 °C. The long test time of the quasi-static experiments leads to heat conduction into the surrounding parent. It is not expected that constitutive softening effects are occurring due to the low temperature rise.

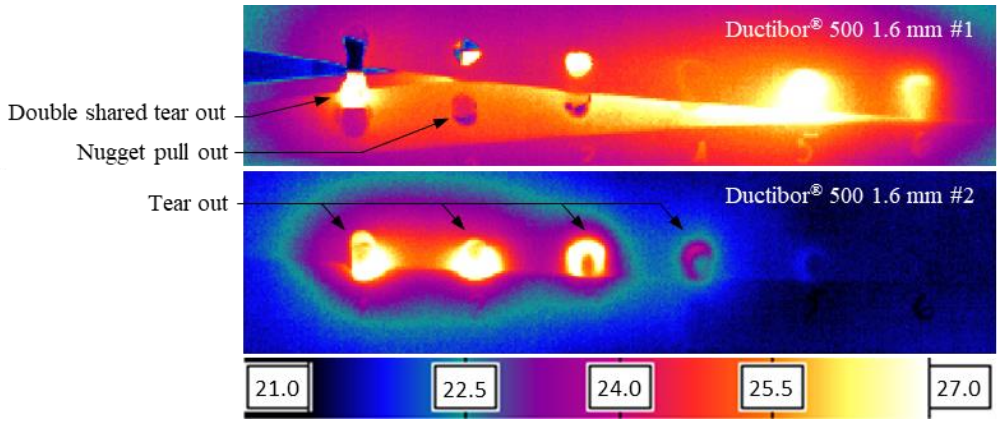

Figure 87: *Quasi-static Caiman Mode III thermal images showing different failure modes. Colour scale in °C.*

The crack extension *versus* load point displacement plots for the Caiman Mode III specimens tested in this work are shown in Figure 88. As each spot weld fails, the 'crack' extends in a stepwise manner. Each vertical step indicates a weld failure and increases the crack extension by 35 mm, which is the weld spacing used for the specimens. The horizontal step occurs between weld failures while the crosshead displacement (the x-axis) continues to increase and the current spot weld is loaded. It is noted that for these plots the weld failure is simplified to occur instantaneously at the crosshead displacement when weld failure begins. This is not strictly accurately for all weld failure modes, such as tear out, that are ductile failure modes with drawn out failure before complete separation occurs. There were some instances in the higher strength materials, Usibor® 1500-AS and Ductibor® 1000-AS, for which brittle interfacial weld failure occurred, and multiple spot welds fail at the same time. In these cases, the crack extension increases by multiples of 35 mm at one crosshead displacement. The precise weld failure time and corresponding crosshead displacement was determined using a combination of the thermal images and the force *versus* displacement curves in which load drops correspond to weld failures. The Ductibor® 500-AS experiments have slower 'crack' propagation than the other two materials for both thicknesses. All three 1.6 mm materials consistently had slower 'crack' propagation than the 1.2 mm experiments.

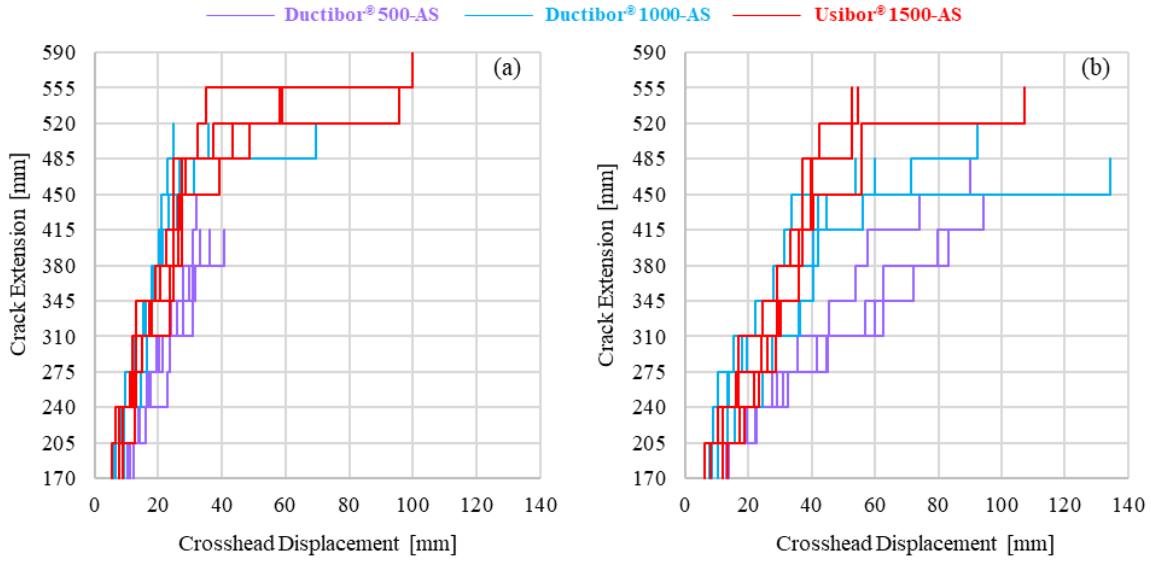

Figure 88: *Caiman Mode III quasi-static 'crack' extension growth. (a) 1.2 mm specimens; (b) 1.6 mm specimens.*

One of the Ductibor® 500-AS 1.6 mm experimental specimens buckled in a manner similar to the early design validation specimens but exhibited the same force *versus* displacement curve as the experiments that did not buckle. It was expected that the Ductibor® 500-AS 1.6 mm specimen that buckled would have a force response similar to the Caiman Mode III validation specimens

that buckled (Rev 2.2 and Rev 3, Figure 75) – but it did not. Examining the post-mortem Ductibor® 500-AS 1.6mm #3 specimen in Figure 89 revealed the cause of the specimen to buckle. During the experiment, the MIG weld that joined one of the inner C-channels to the side walls failed. This behaviour is different than what occurred during the validation experiments in which the buckling was caused by the sidewalls folding out-of-plane under compressive loading. Once the MIG welds failed, the upper half of the specimen lost the support of the C-channel and then fracture extended from spot weld #3 into the parent metal region. The force *versus* displacement curve of this specimen is indistinguishable from the other specimens that did not buckle because of the high number of spot weld failures that occurred before the buckling began. In contrast, in the validation specimens, only one or two spot welds failed on either side before buckling started. Looking at the Caiman Mode III Ductibor® 500-AS 1.6 mm #3 specimen in Figure 89, the first five spot welds on each side have started tear out failure.

Figure 89: *Caiman Mode III Ductibor® 500-AS 1.6 mm quasi-static specimen that buckled.*

5.1.2. Dynamic

The Caiman Mode III specimens were tested at dynamic rates for the 1.2 mm and 1.6 mm sheet thicknesses of Ductibor® 500-AS, Ductibor® 1000-AS, and Usibor® 1500-AS. Initial and final images from a high-speed camera for each different specimen condition are shown in Figure 90. The Caiman Mode III dynamic test results are summarized in Table 17. The wall-side total force *versus* sled displacement curves for Ductibor® 500-AS, Ductibor® 1000-AS, and Usibor® 1500-AS, are shown in Figure 91, Figure 92, and Figure 93, respectively. The peak load for the Ductibor® 500-AS and the Ductibor® 1000-AS dynamic experiments increased by approximately 40% when changing from 1.2 mm to 1.6 mm thick sheets. The Usibor® 1500-AS peak load increased by 20% when changing to the thicker material. All three materials experienced increases in total absorbed energy between 100% and 200% when increasing the sheet thickness from 1.2 mm to 1.6 mm.

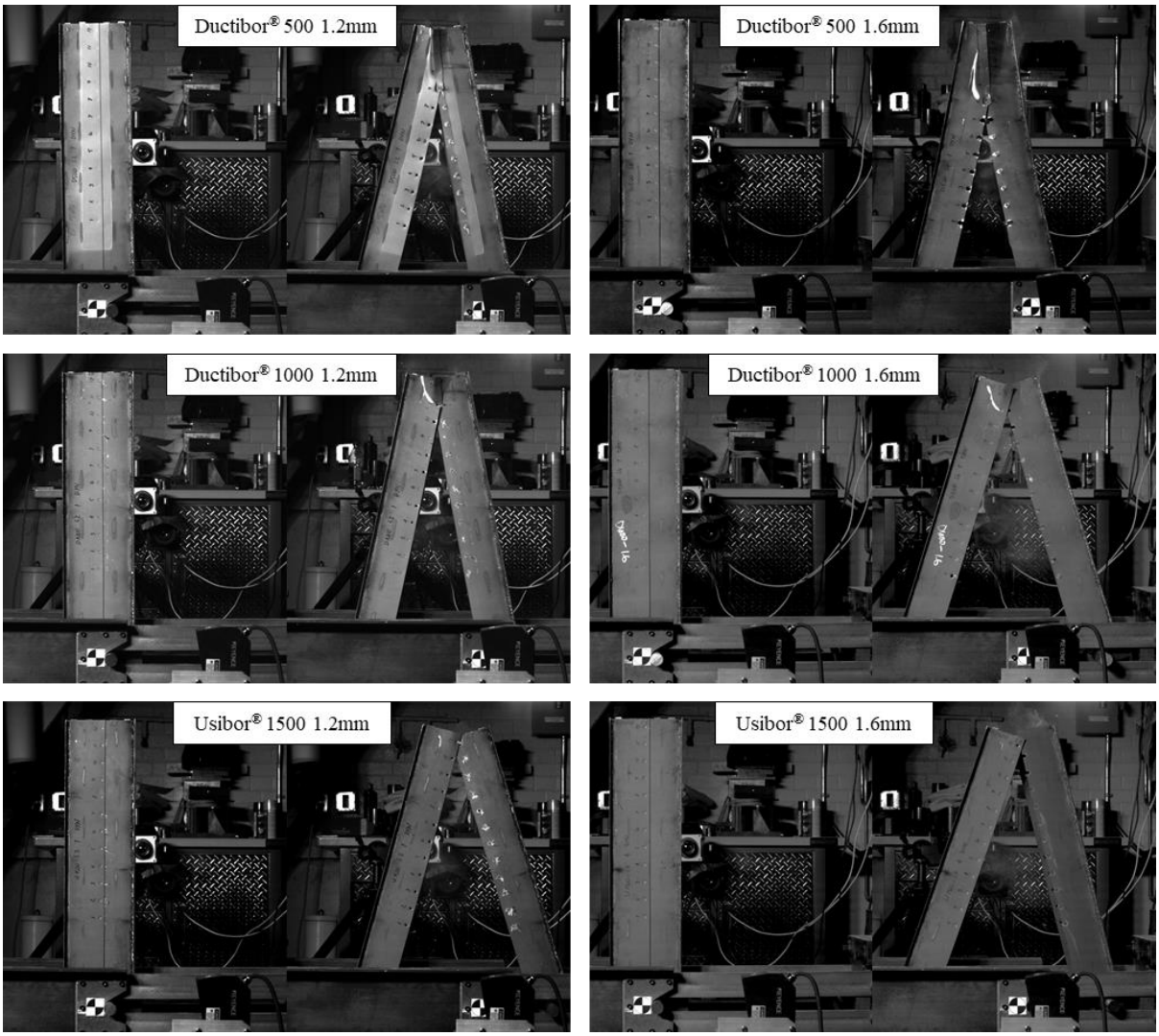

Figure 90: *First and last high-speed image of a Caiman Mode III dynamic experiment from each material and thickness.*

Table 17: *Caiman Mode III dynamic experimental data summary.*

Material	Thickness [mm]	Max Load [kN]	Energy absorbed [J]
Ductibor® 500-AS	1.2	37.6 ± 4.5	1090 ± 43
	1.6	50.1 ± 2.0	2615 ± 78
Ductibor® 1000-AS	1.2	37.1 ± 1.3	664 ± 32
	1.6	52.4 ± 5.1	1433 ± 132
Usibor® 1500-AS	1.2	44.3 ± 2.6	406 ± 56
	1.6	53.9 ± 4.4	1132 ± 114

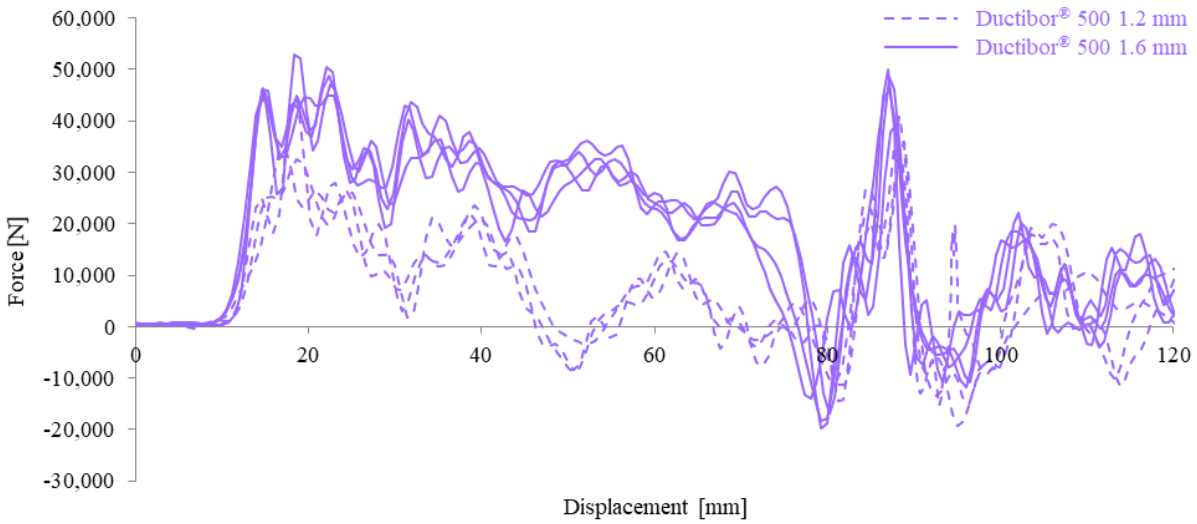

Figure 91: *Caiman Mode III dynamic Ductibor® 500-AS wall-side force* versus *displacement.*

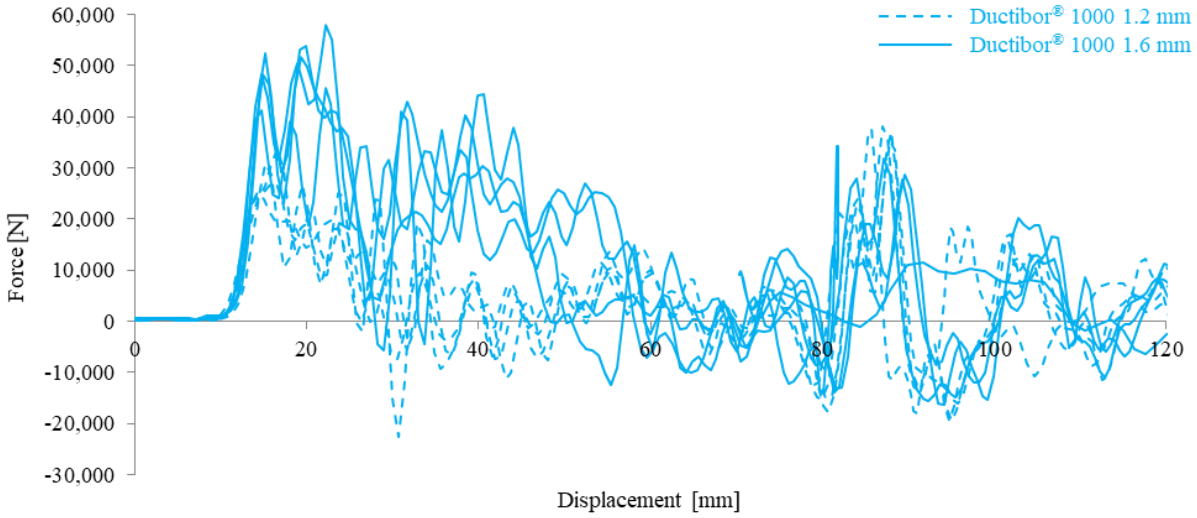

Figure 92: *Caiman Mode III dynamic Ductibor® 1000-AS wall-side force* versus *displacement.*

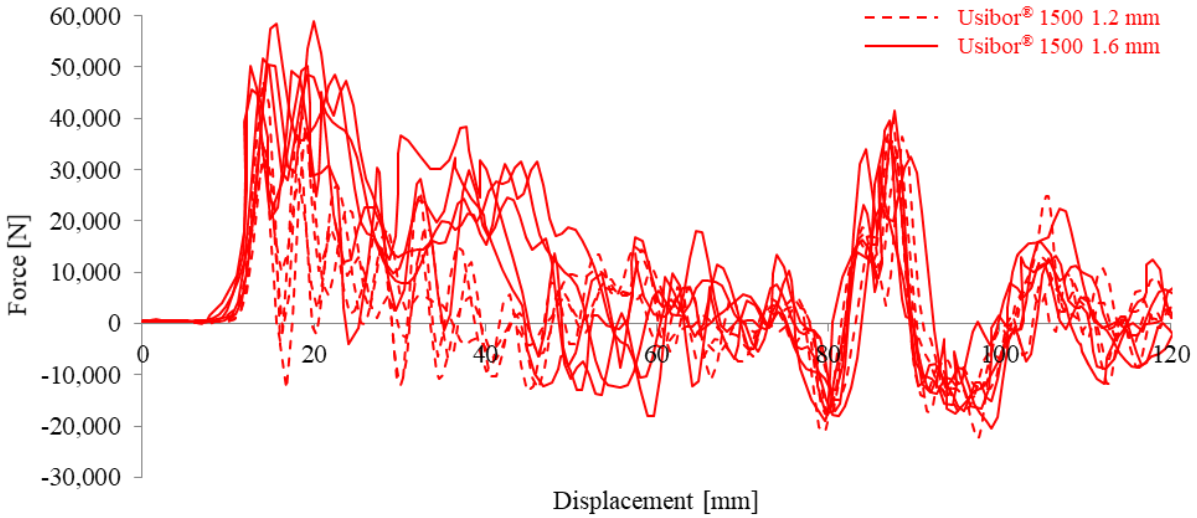

Figure 93: *Caiman Mode III dynamic Usibor® 1500-AS wall-side force* versus *displacement.*

The force *versus* displacement curves from the dynamic testing are more difficult to interpret than the quasi-static data curves. The initial sled velocity at the time of impact, which is approximately 25.5 kph, or 7.1 m/s, causes significant inertial effects that obscure the loading response from the specimens. Images from the high-speed cameras were used to find the time that sled-pin impact occurs for each test and align the data such that sled-pin impact occurs at $x = 0$ for all tests. It can be seen, however, that in the force *versus* displacement curves (Figure 91, Figure 92, and Figure 93), there is approximately 10 mm of sled displacement before the load begins to increase. This delay in loading is due to the elastic deformation and flexing of the fixture and pins. There is also a slight amount of shifting of the bosses inside of the specimens that is unavoidable at the impact rates used in the dynamic testing. At 75 mm of sled displacement, the sled impacts the honeycomb which slows down the sled and momentarily causes the Impact Pin to lose contact with sled. Once the sled catches back up to the Impact Pin there is a spike in the load, which can be seen to occur at 85 mm of displacement. The momentum of the pin and bosses attached to the specimen cause the Impact Pin to travel beyond the sled as the sled impacts the honeycomb. Then, the force on the spot welds that are joining the impacted side of the specimen to the fixed side reduces the momentum until the sled contacts the pin again. The Ductibor® 1000-AS and Usibor® 1500-AS specimens exhibit more brittle weld failure, which absorbs less energy, and lose contact between the sled and the pin more than the Ductibor® 500-AS specimens. This is seen in the high-speed images in Figure 94 as well as the force *versus* displacement curves where the force decays and fluctuates around zero load before spiking back up when sled-pin contact resumes.

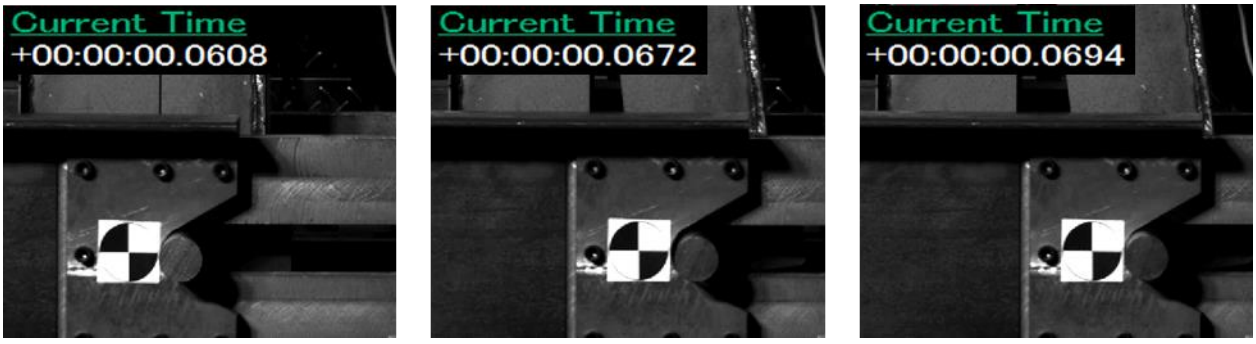

Figure 94: *Caiman Mode III dynamic high-speed images of Usibor® 1500-AS 1.2 mm specimen showing pin and sled contact. Left) Initial contact; Centre) Loss of contact; Right) Secondary contact.*

The force data recorded by the wall-side load cells was integrated over the sled displacement from the laser displacement sensor to obtain the energy absorption. The experimental repeats and average energy absorbed *versus* sled displacement curves for each specimen are shown in Figure

95. The Ductibor® 500-AS specimens absorbed twice as much energy as the other Ductibor® 1000-AS and Usibor® 1500-AS specimens for both thicknesses. The Ductibor® 1000-AS and Usibor® 1500-AS specimens performed quite similarly up to the honeycomb impact, after which the Ductibor® 1000-AS absorbed slightly more than the Usibor® 1500-AS specimens. It is seen that noise was introduced to the absorbed energy data once the sled impacts the honeycomb. The same phenomenon was observed by O'Keeffe [51] for the Caiman Mode I dynamic experiments.

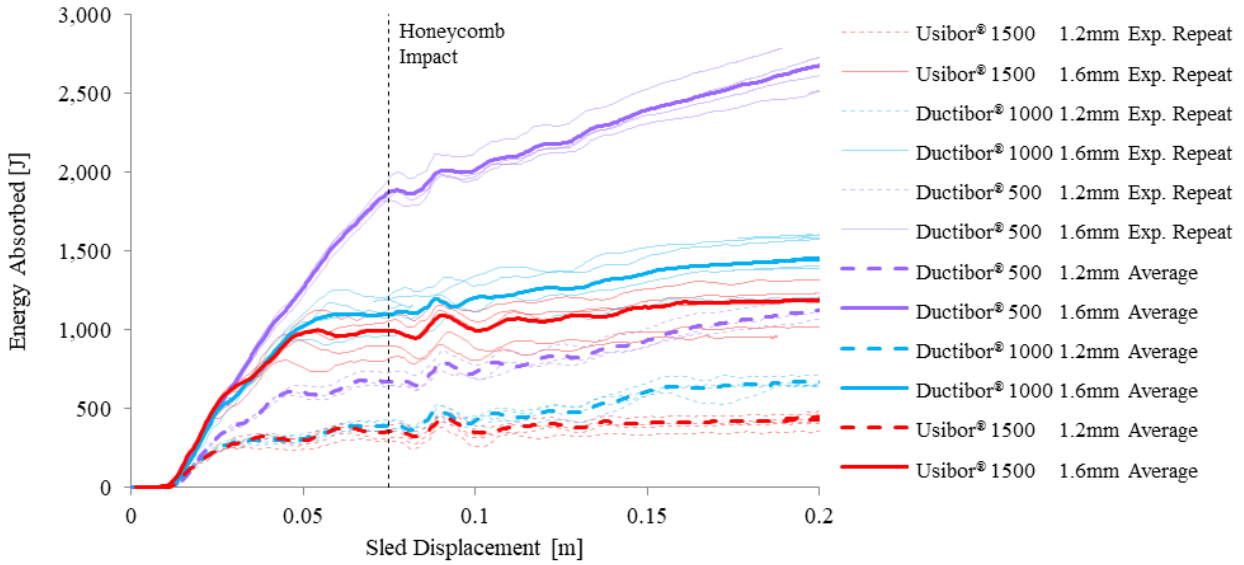

Figure 95: *Average Caiman Mode III dynamic energy absorbed* versus *crush distance for 1.2 mm (dashed lines) and 1.6 mm (solid lines) specimens. Experimental repeats are shown with thin faded lines.*

Thermal images captured using the Telops Fast-IR-2K IR camera from one specimen from each material condition are shown in Figure 96. As each spot weld fails, the surrounding HAZ and parent metal regions deform and heat up due to the plastic work. Peak temperatures at spot welds that failed via tear out or button pull-out reach up to 230-240 °C in the HAZ on the outer surface. The visible outer surface of interfacial weld failures only reaches to 30-40 °C. As the two halves of the specimen separate and the inner surface becomes visible, peak temperatures of approximately 160 °C are recorded on the fracture surface of interfacial failure spot welds. The temperature of the fracture surface itself is only an approximate value because the emissivity of the fracture surface is not known. Emissivity values were calibrated for the hot stamped material in the as-stamped and sand-blasted condition (Section 4.2). Note that the thermal colour scale used in Figure 96 has a peak temperature of 60 °C to increase specimen and spot weld clarity; the peak temperatures on specific pixels in the images reach the higher temperatures discussed here. It is also seen that the heating within each spot weld during failure is adiabatic at these elevated loading

rates since there is almost no temperature increase in the surrounding base metal regions. The thermal images, which are synced with the optical images and load cell data, are useful for determining precise spot weld failure timing in the dynamic experiments. The unfiltered dynamic load data does not produce the well-defined step-like force *versus* displacement that is captured in the quasi-static tests. As such, the dynamic load data cannot be used to determine individual spot weld failure.

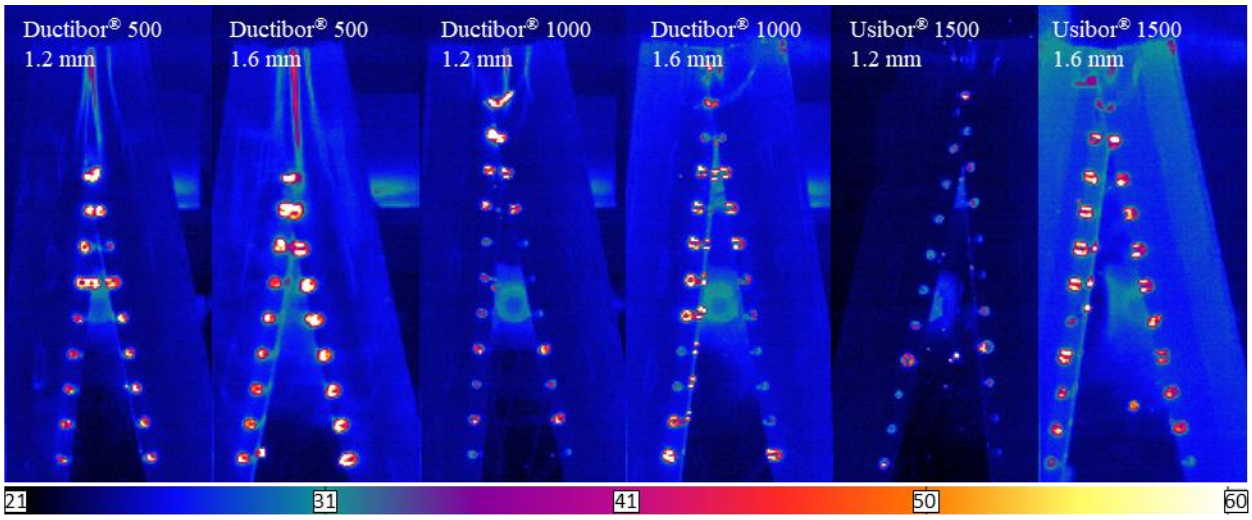

Figure 96: *Thermal images captured for the Caiman Mode III dynamic experiments. Colour scale in °C.*

The 'crack' extension data, used to characterize the extent of spot weld failure propagation, for the Caiman Mode III dynamic tests are shown in Figure 97. The timing of each spot weld failure was determined using the thermal images and then cross-plotted using the time axis with the recorded displacement data for each experiment. Note that each vertical step of 35 mm in 'crack' extension corresponds to a spot weld failure. The 'crack' extension results are consistent with the absorbed energy curves reported for the same experiments in Figure 95. Failure propagation is slower in the Ductibor® 500-AS specimens relative to the specimens made from the other two higher strength materials because the Ductibor® 500-AS spot welds are tougher and absorb more energy before complete failure. The Ductibor® 1000-AS and the Usibor® 1500-AS specimens have nearly identical failure propagation rates, with the Usibor® 1500-AS 1.6 mm being slightly faster than the Ductibor® 1000-AS 1.6 mm specimens near the final spot weld failures. It is also clear in these two 'crack' extension plots that the number of spot welds that failed reduced as the parent metal strength decreased; this behaviour can be attributed to earlier collapse of the end of the specimen for the lower strength materials.

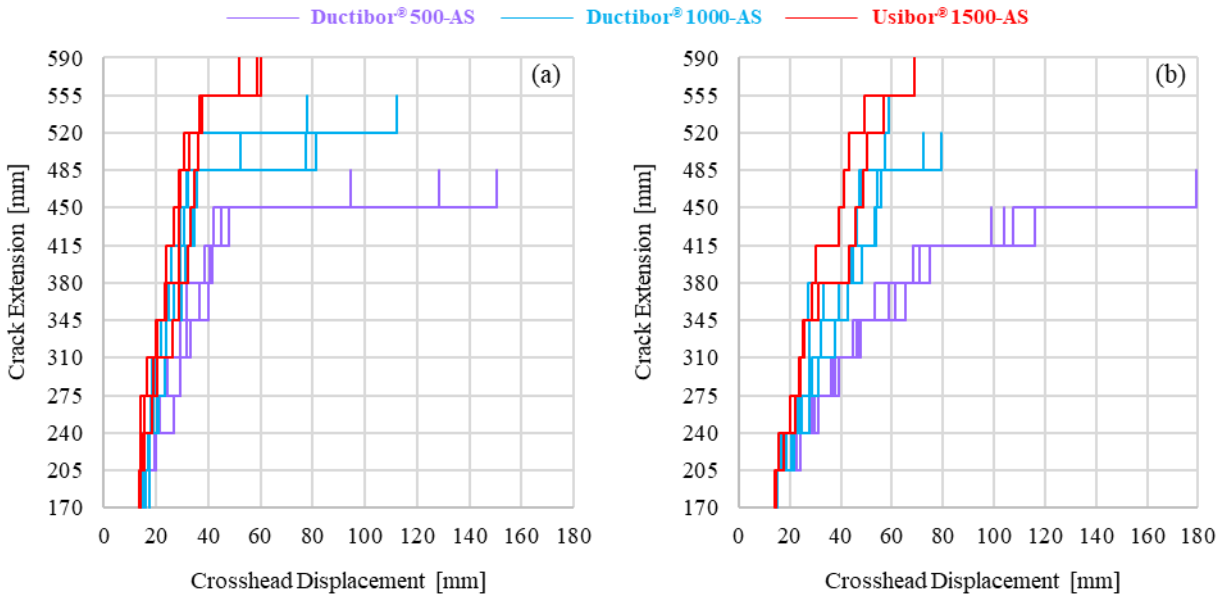

Figure 97: *Caiman Mode III dynamic 'crack' extension growth. (a) 1.2 mm specimens; (b) 1.6 mm specimens.*

5.2. Caiman Mode III numerical model development

Numerical models of the Caiman Mode III experiments have been developed for assessment of the calibrated single spot weld models presented in Section 3.3. The model assessment studies focused on the quasi-static experiments instead of the dynamic experiments since the quasi-static force *versus* displacement curves are cleaner, without the excessive dynamic oscillation present in the dynamic data. Each weld failure produced a distinct load drop that can be compared to the predicted force *versus* displacement output. In addition, in the quasi-static setup, there is only the large clevis between the pin and the load cell, seen in Figure 60 and Figure 76. In the dynamic setup there are the long, slotted plates and a thick plate that is part of the load cell pack, seen in Figure 60 and Figure 78. If the dynamic condition were to be used for model validation, the slotted plates and load cell pack components would have to be modelled as solid elements to capture the dynamic effects. All of the quasi-static experiments, except for one, had at least one spot weld that did not fail by the time the test stopped. As a result, there remains a small load after the rail end collapses due to parent metal deformation and fracture. For the purpose of the spot weld model validation, the Caiman Mode III experiment is considered complete after the rail end collapses, spot weld failure has stopped, and the load has dropped off and is slowly reducing to zero.

As was done for the single spot weld models, a Caiman Mode III model was developed for both the 1.2 mm and 1.6 mm specimen geometries. Apart from geometrical differences from the

change in specimen geometry, the Caiman Mode III models use the same material properties and control cards as the single spot weld models, developed in Section 3.3. For each model, the constitutive properties of the three materials, Ductibor® 500-AS, Ductibor® 1000-AS, or Usibor® 1500-AS, (presented in Figure 46) and fracture limits (Figure 47) are assigned to the deformable shell elements. Zhumagulov *et al.* [112] developed a constitutive model for DP 980, which is used in the Caiman models in the current work. Figure 98 shows the constitutive model fit to the experimental data for an unspecified DP 980 material. Due to the nature of the industrial consortium that provided the material in the work by Zhumagulov *et al.* [112], it is not possible to know if the constitutive model is for the same DP980 material used here, which was supplied by ArcelorMittal. In the single spot weld model development, it was established that a single spot weld mesh assembly consisting of eight hexagonal brick elements can be used for both the *MAT_100_DA and *MAT_240 material models. The element formulation applied to the brick elements in the weld region changes between the material models, but the mesh remains the same.

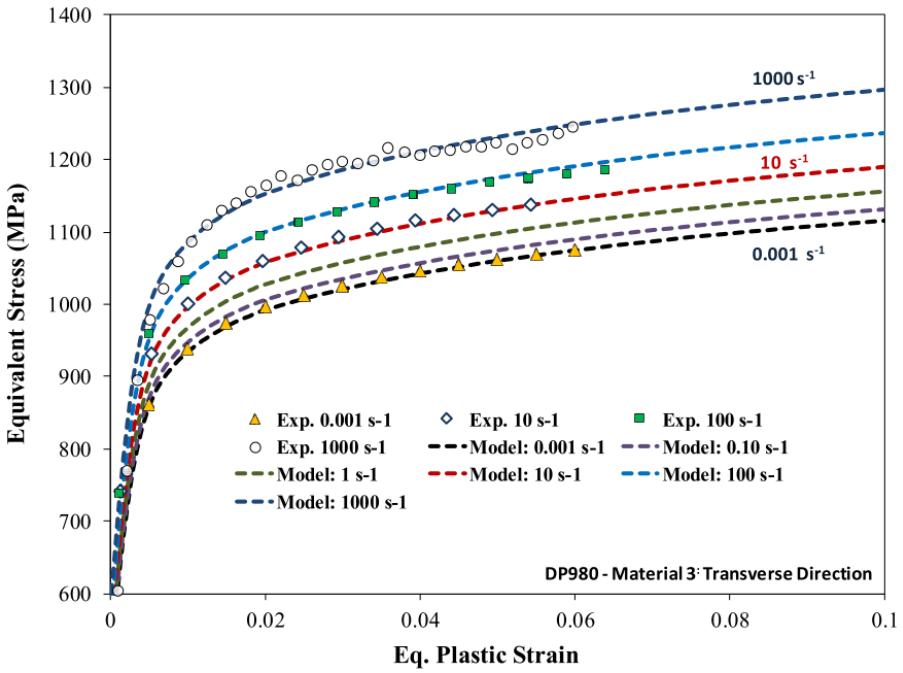

Figure 98: *DP 980 experimental strain rate data and Cowper-Symonds (CS) constitutive model fit.* [112]

With the absence of inertial effects, it is possible to model the fixturing components as rigid shells instead of using elastic solid brick elements. The Caiman Mode III mesh is shown in Figure 99. The model uses rigid shell elements for the bosses and pins in a configuration that matches the clamping of the specimen in the experiments. The pins are beams defined using a node at either

end and are connected to the inner bosses using the *JOINT_REVOLUTE constraint. This allows the inner boss to rotate freely around the pin beam while the top pin beam is translated by the boundary condition. The numerical models have the quasi-static boundary conditions applied to them; a prescribed boundary condition of 50 mm/min is applied to the top pin beam and the bottom pin beam has fixed x, y, and z translational degrees of freedom. Since the numerical model is simulating the quasi-static experiments, time scaling is applied to reduce the simulation run time to 3-4 hours. 100x time scaling is applied to the Usibor® 1500-AS simulations, 400x is applied to the Ductibor® 1000-AS simulations, and 600x is applied to the Ductibor® 500-AS simulations. Different time scaling values, and end times, are used because there is less crosshead displacement before the load drops to 1-2 kN for the higher strength materials that exhibit a more brittle weld failure mode.

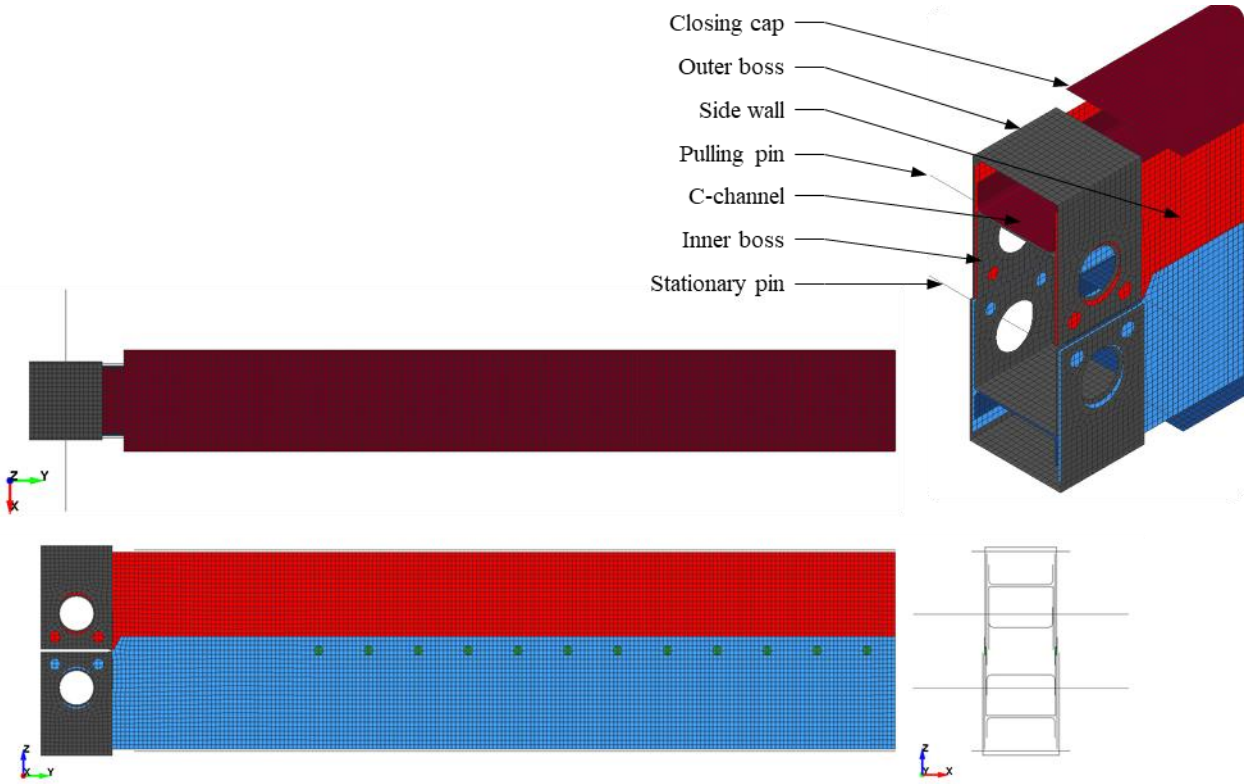

Figure 99: *Caiman Mode III numerical model mesh. Rigid components coloured grey.*

In the numerical models, the specimen is constructed in a manner similar way to the actual specimens. The specimens use stitch pattern MIG welds to join the C-channels to the side walls; 25 mm long MIG welds are spaced 35 mm apart. The flat closing cap that was added in the final design, Rev 5, is joined to the sidewalls using a continuous MIG weld the entire length of the specimen. In the model, the C-channels are tied with a rigid beam that is offset to the side wall

parts via a *CONTACT control card, following the same spacing as the MIG welds. The flat closing caps are tied to the edge of the side walls using a *CONTACT control card and a node set. As detailed in Section 3.3, the spot weld nugget mesh elements are tied to the side wall parts. Figure 100 shows the tied contact nodes and segments for a quarter of the specimen model. Contact is defined for all the shell components of the specimen using the automatic single surface algorithm. The contact for the bosses is also defined using automatic single surface and the specific specimen parts that they contact.

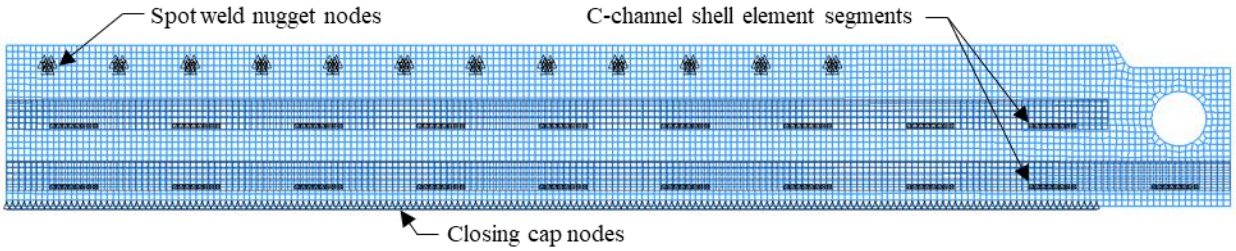

Figure 100: *Caiman Mode III numerical model tied contact locations. One quarter of the specimen shown here.*

The force applied in the direction the crosshead moves is extracted from the *jntforc* database output. The pin displacement is assumed to be equal to the crosshead displacement and is recorded in the simulation by tracking one of the nodes of the top pin beam. The displacement data of the top pin beam node is extracted using the *nodout* database output. The node displacement *versus* time and the force *versus* time are cross plotted using time to generate force *versus* displacement curves that can be compared to the experimental force *versus* displacement curves from the MTS tensile frame. Weld failure time is obtained from *dcfail* database output for *MAT_100_DA models and from individual element history data for *MAT_240 models

5.3. Caiman Mode III simulation results

The Caiman Mode III quasi-static simulations are completed for each material condition using both *MAT_100_DA and *MAT_240 calibrated material cards for the welded joints. The peak, or maximum, force and the total absorbed energy are the two main parameters that are used to evaluate the calibrated single spot weld models. The predicted force *versus* displacement response is also compared to the experimental data curves for qualitative analysis, as is the extent of failure propagation through the spot weld group as a function of displacement. The final deformed state of the simulations for each 1.6 mm material model are shown in Figure 101 and Figure 102, for *MAT_100_DA and *MAT_240, respectively.

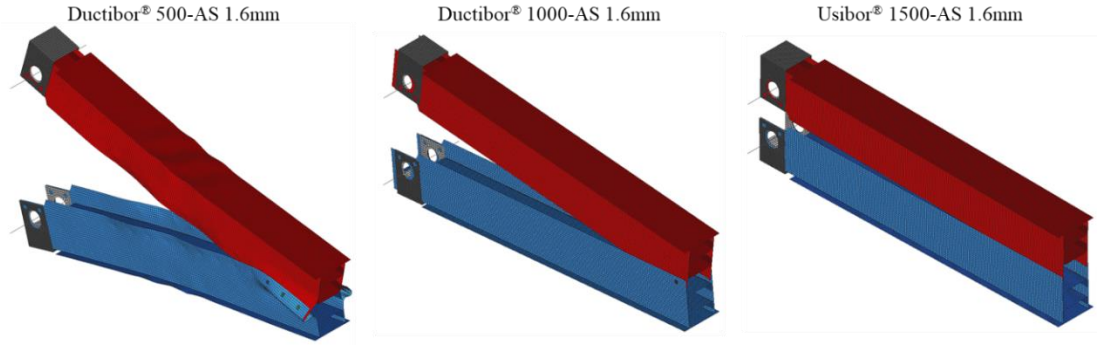

Figure 101: *Caiman Mode III *MAT_100_DA simulation final frames.*

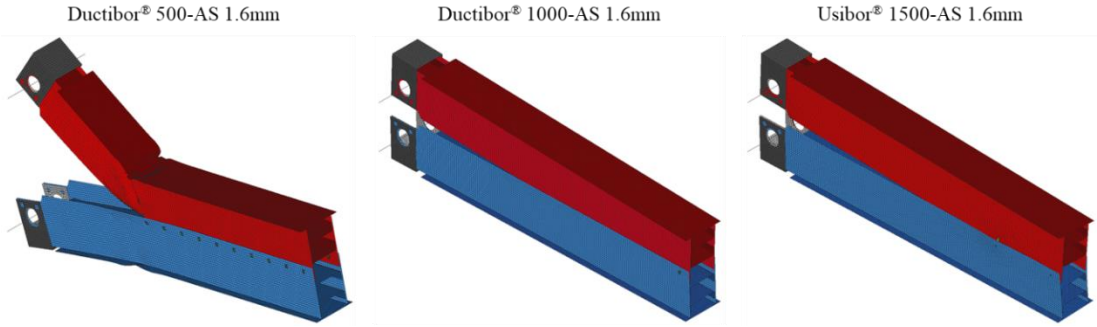

Figure 102: *Caiman Mode III *MAT_240 simulation final frames.*

The simulated outputs of the Caiman Mode III quasi-static numerical model using the *MAT_100_DA weld material model are compared to the experimental curves for Ductibor® 500-AS, Ductibor® 1000-AS, and Usibor® 1500-AS, in Figure 103, Figure 104, and Figure 105, respectively. The outputs of the Caiman Mode III quasi-static model using the *MAT_240 weld material model are compared to the experimental curves for Ductibor® 500-AS, Ductibor® 1000-AS, and Usibor® 1500-AS, in Figure 106, Figure 107, and Figure 108, respectively. The *MAT_240 simulations show similar trends to the *MAT_100_DA simulations. The peak forces are close to the experimental data and although there is still a large discrepancy in the absorbed energy values, the *MAT_240 model has on average about 50% error while the *MAT_100_DA absorbed energy values have more than 80% error on average. The step-like behaviour that is characteristic of the quasi-static Caiman experiments is captured relatively well by the models. The weld models that were calibrated to have higher energy absorption after weld failure initiates tend to have a smoother predicted force *versus* displacement curve, as seen in the Ductibor® 500-AS 1.2 mm and 1.6 mm predictions that have the largest $gfad$ parameter values. The weld models with larger energy absorption have larger separation distance before failure which distributes the applied load across multiple spot welds. Since multiple spot welds are sharing the load, when one fails there is less of a load drop and thus a smoother force response. Conversely, the Ductibor® 1000-AS *MAT_100_DA models have the smallest $gfad$ parameter values and the largest drops in the predicted force *versus* displacement curves.

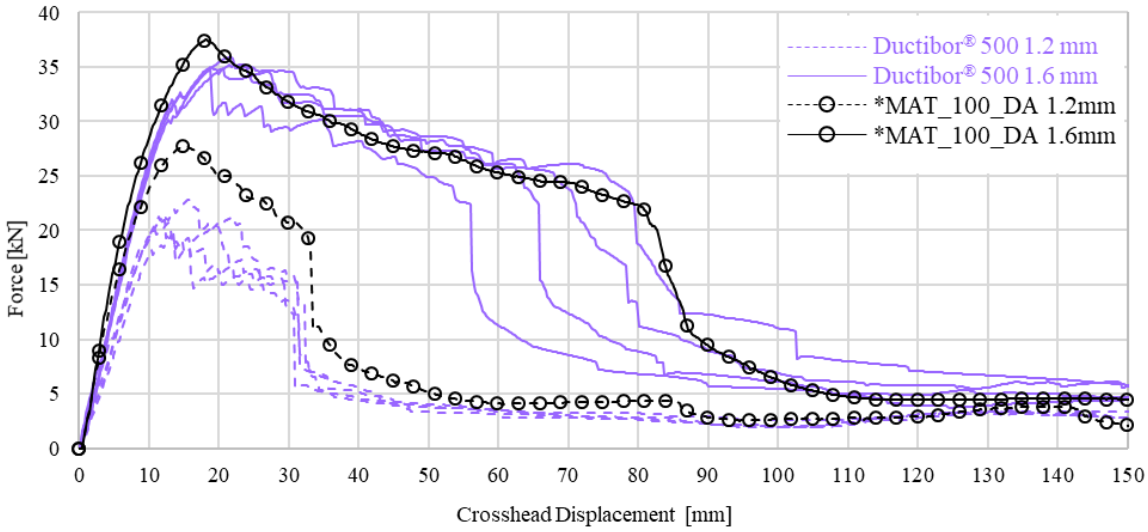

Figure 103: *Caiman Mode III Ductibor® 500 experimental force* versus *displacement and *MAT_100_DA model output.*

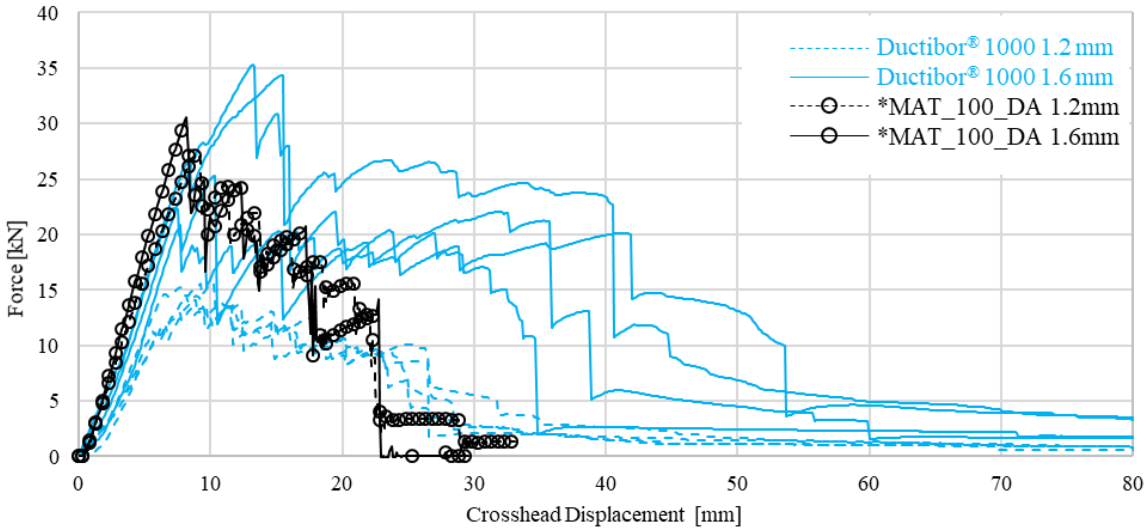

Figure 104: *Caiman Mode III Ductibor®1000 experimental force* versus *displacement and *MAT_100_DA model output.*

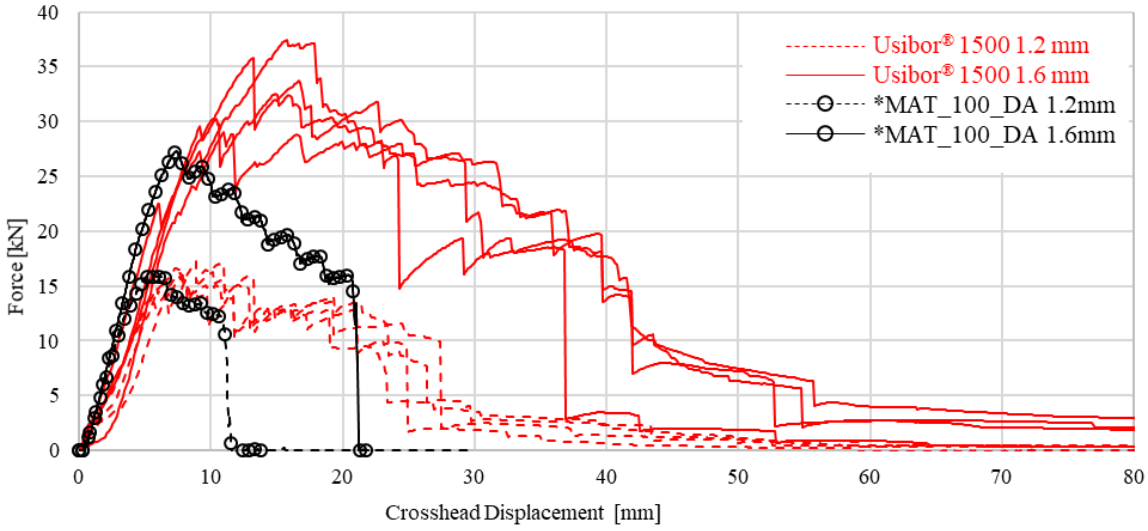

Figure 105: *Caiman Mode III Usibor® 1500 experimental force* versus *displacement and *MAT_100_DA model output.*

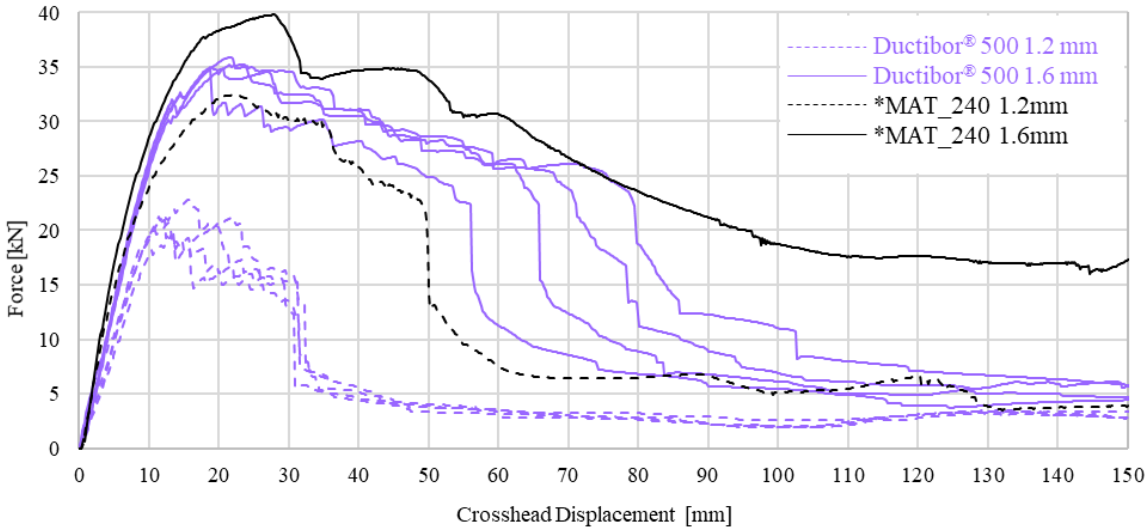

Figure 106: *Caiman Mode III Ductibor® 500 experimental force* versus *displacement and *MAT_240 material model output.*

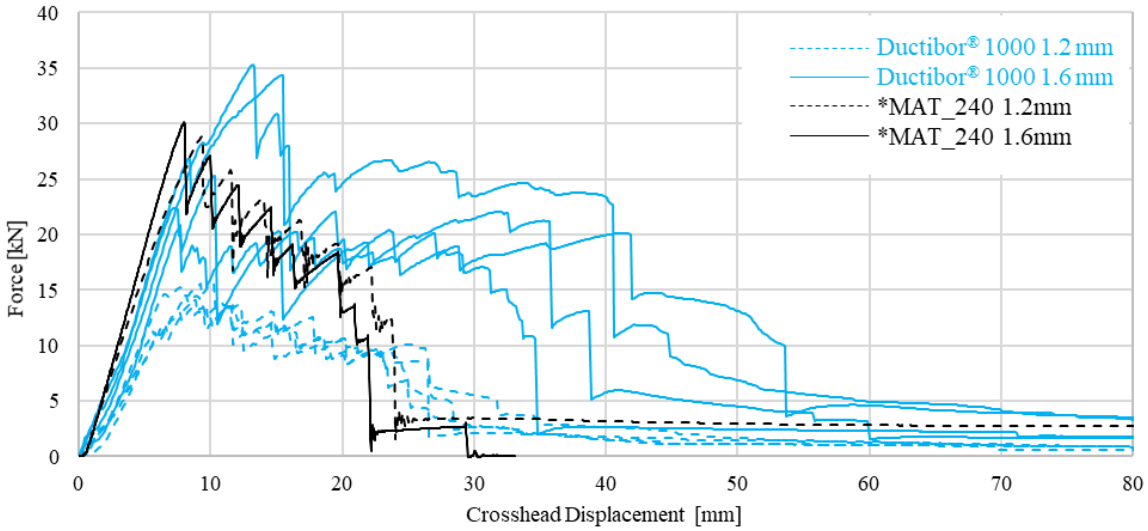

Figure 107: *Caiman Mode III Ductibor® 1000 experimental force* versus *displacement and *MAT_240 material model output.*

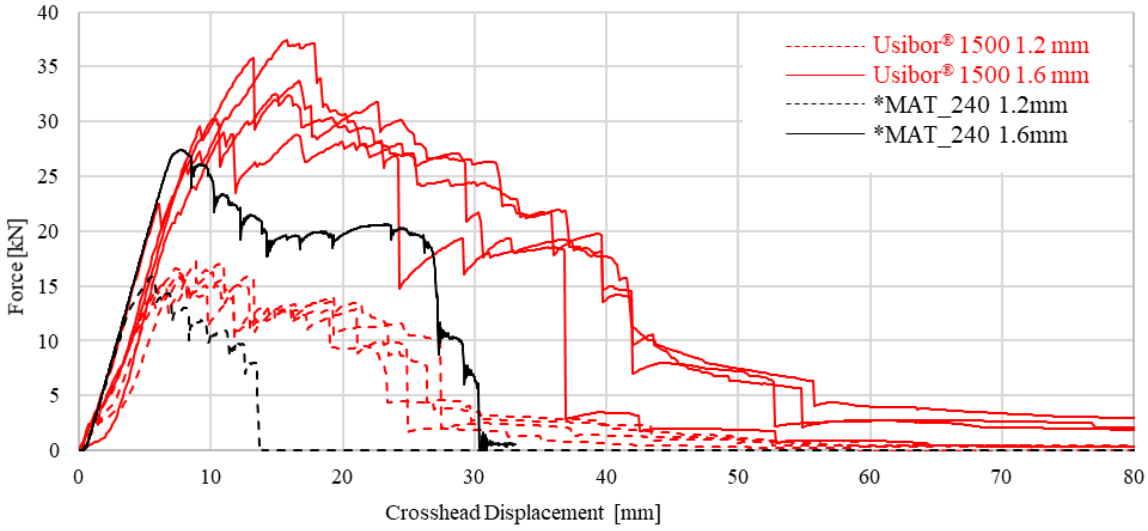

Figure 108: *Caiman Mode III Usibor® 1500 experimental force* versus *displacement and *MAT_240 material model output.*

The peak forces and total absorbed energy are listed in Table 18 and are presented graphically in Figure 109 to better visualize the results of the simulations and experiments. When comparing the *MAT_100_DA and the *MAT_240 models, they both predict similar peak force and energy absorption results for each Caiman Mode III simulation, except for the energy in the Ductibor® 500-AS material simulations. The *MAT_240 model largely over predicted the absorbed energy for both thickness of Ductibor® 500-AS in the simulations. However, there are changes in behaviour when comparing the force *versus* displacement response of one model, either *MAT_100_DA or *MAT_240, to a different material condition simulation using the same model. The Ductibor® 500-AS simulations over predict the peak force and the total absorbed energy but the Usibor® 1500-AS simulations show the opposite trend, under predicting the peak force and total energy. For the Ductibor® 1000-AS simulations, the models don't consistently over or under predict both 1.2 mm and 1.6 mm specimens, but the *MAT_100_DA and *MAT_240 models both predict very similar force responses.

Table 18: *Caiman Mode III quasi-static numerical simulation prediction and error results.*

		***MAT_100_DA Simulations**		***MAT_240 Simulations**	
		Max Load [kN]	Energy absorbed [J]	Max Load [kN]	Energy absorbed [J]
1.2	Ductibor® 500-AS	27.8	1288	32.5	2049
	% error	23%	30%	34%	56%
	Ductibor® 1000-AS	27.2	401	28.8	595
	% error	46%	9%	49%	38%
	Usibor® 1500-AS	15.9	128	15.9	137
	% error	3%	173%	3%	153%
1.6	Ductibor® 500-AS	37.5	2789	39.8	4237
	% error	6%	1%	11%	33%
	Ductibor® 1000-AS	30.5	375	30.1	403
	% error	4%	175%	3%	156%
	Usibor® 1500-AS	27.3	387	27.4	545
	% error	24%	186%	23%	103%
	Average % error	**9%**	**83%**	**12%**	**47%**

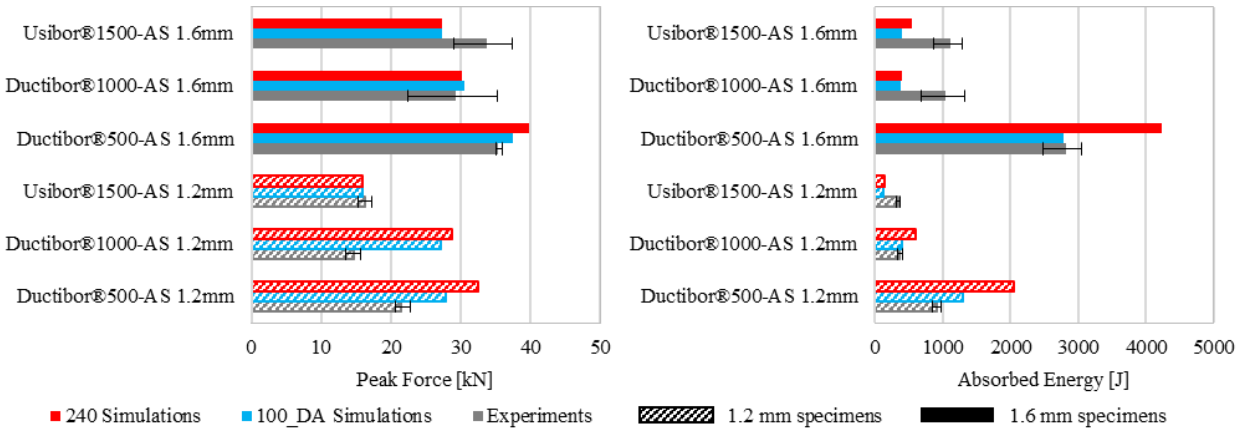

Figure 109: *Peak Force data (left) and Total Energy Absorbed data (right) for Caiman Mode III experiments and simulations.*

All the Caiman Mode III simulations using *MAT_100_DA and *MAT_240 predicted progressive weld failure behaviour, except for the *MAT_240 material model for the Ductibor® 500-AS 1.6 mm material. In this case, the force applied by the pins reached nearly 40 kN before the structural integrity of the specimen failed and one U-channel of the specimen began to buckle. The change in global failure behaviour to a buckling mode produced a force-displacement response that is distinctly different from all the other simulations. Although the predicted force response from the Ductibor® 500-AS 1.6 mm simulation that buckled does not match the Ductibor® 500-AS 1.6 mm experiment that buckled, it is the same as the experimental force *versus* displacement curve recorded from the validation experiments that buckled, Rev 2.2 and Rev 3.

The predicted "crack" extension is overlaid with the corresponding measured "crack" extension in Figure 110 for the 1.2mm cases and Figure 111 for the 1.6 mm cases. For *MAT_100_DA, the `dcfail` database output showing the failure function (Equation (22)) is used to determine the predicted weld failure timings; failure initiates when the failure function reaches unity. The *MAT_240 model does not have a dedicated database output and instead element history data is used to identify the point of failure for each spot weld location. Failure initiation is taken to occur when the von Mises stress in the inner most spot weld nugget element reaches a peak value. The *MAT_100_DA numerical model predicted weld failure timings that were very similar to that observed in the Ductibor® 500-AS and Ductibor® 1000-AS experiments. The Usibor® 1500-AS predictions from the *MAT_100_DA model propagated weld failure at similar rates as the experiments for the first half of the spot welds. Then the model predicts sudden weld failure of all the remaining spot welds, which does not correspond to behaviour shown in the experiments. The *MAT_240 predicts inconsistent behaviour for the three different materials. The

*MAT_240 1.2 mm numerical model over predicts the crosshead displacement at each spot weld failure. Recall that the *MAT_240 1.6 mm model buckled after two weld failures and cannot be used for comparison. The *MAT_240 numerical models predicted nearly identical results as the *MAT_100_DA models for the Ductibor® 1000-AS and Usibor® 1500-AS materials.

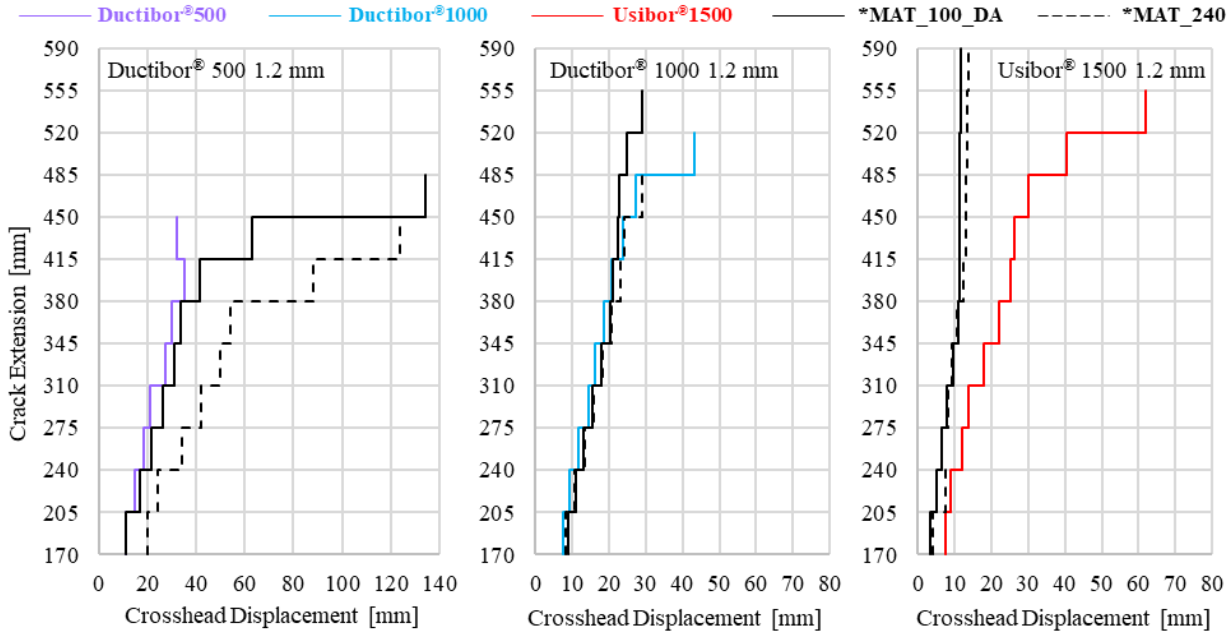

Figure 110: *Caiman Mode III 1.2 mm quasi-static experiments (red, blue, and purple lines) and numerical model simulation (black lines) crack extension measurements.*

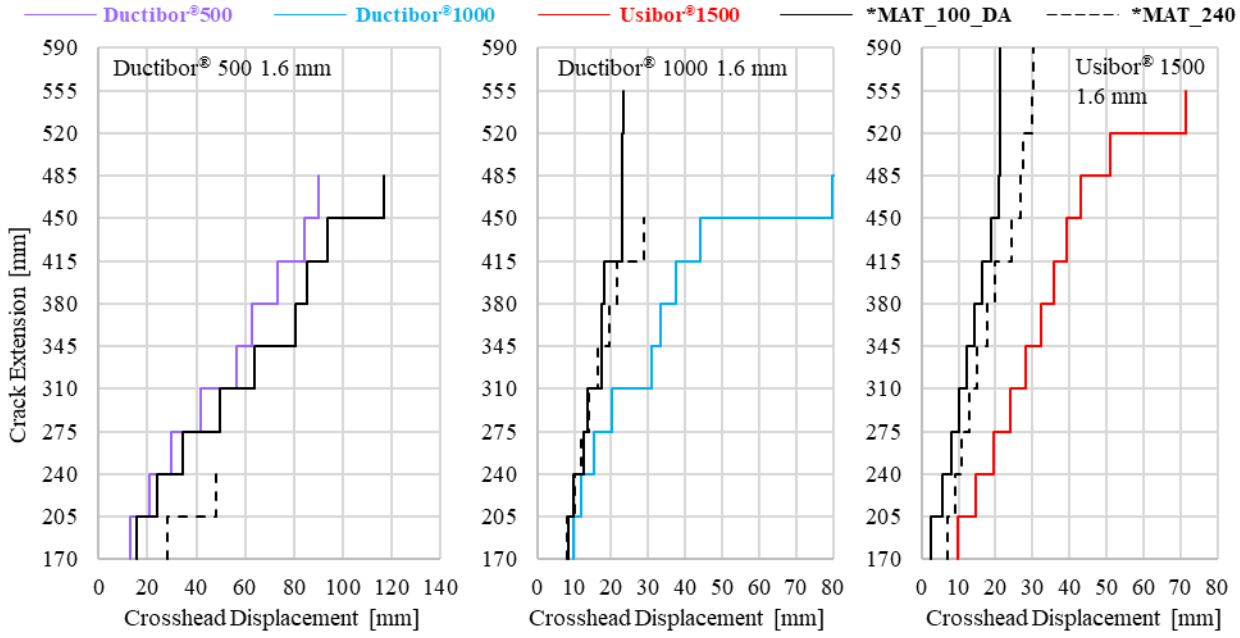

Figure 111: *Caiman Mode III 1.6 mm experiments (red, blue, and purple lines) and numerical model simulation (black lines) crack extension measurements.*

The similarities between the *MAT_100_DA and *MAT_240 simulations show that the Caiman Mode III models predict consistent results with different weld material models. The consistency of the two weld models here suggests that the differences between the predictions and the experiments may be from physical inconsistencies between the design and the as-fabricated final specimens, which is discussed in detail in Chapter 6. In particular, the distance of the weld nugget to the edge of the sheet metal changed from the tensile lap shear coupons to the Caiman Mode III specimens and is discussed in Section 6.4. Alternatively, differences could also arise from inaccuracies or simplifications made in the creation of the numerical model. The parent shell mesh element size and section properties, as well as the spot weld nugget mesh and connection details remained the same between the calibrated tensile lap shear simulations and the Caiman models. Since these aspects of the model were present in the calibrated coupon models, it is unlikely that they are the cause of numerical prediction differences seen in the Caiman models.

Newly introduced components that are only in the Caiman models are the bosses and pins, the DP980 inner C-channel parts, and the tied contact definitions used to represent the MIG welds connecting the C-channels to the side walls. The concern with the modelling of the bosses is that it is possible that the specimen sidewalls slip within the bosses and alter the real or effective displacement that is being applied to the specimen. The tied contact definitions do not have failure and could result in different specimen behaviour. The DP980 material constitutive model used in the work presented here was developed by Zhumagulov *et al.* [112]. No fracture was observed in the DP 980 components in any of the experiments, and so the applied constitutive model is not of a concern here.

The Caiman specimens are clamped using two inner boss and outer boss pairs. The boss pairs in the experiments are bolted together while in the model they are rigid parts that are constrained to move together to mimic the real bolt connections. The contact definition in the simulation applies a friction coefficient of 0.4 between the bosses and specimen side wall parts but the simulation does not apply a clamping force since the boss parts are rigid. Shown in Figure 112, the Ductibor® 500-AS 1.6 mm simulation had the largest amount of specimen movement within the rigid bosses, measured to be 2.1 mm. In the experiments, the presence of the pin limits the amount the side walls can move within the bosses. In the simulation, the specimen side wall (coloured red) does not slide into the region the pin would occupy (white region within bosses), thus the limited amount of slippage in the simulation is not thought to be a concern.

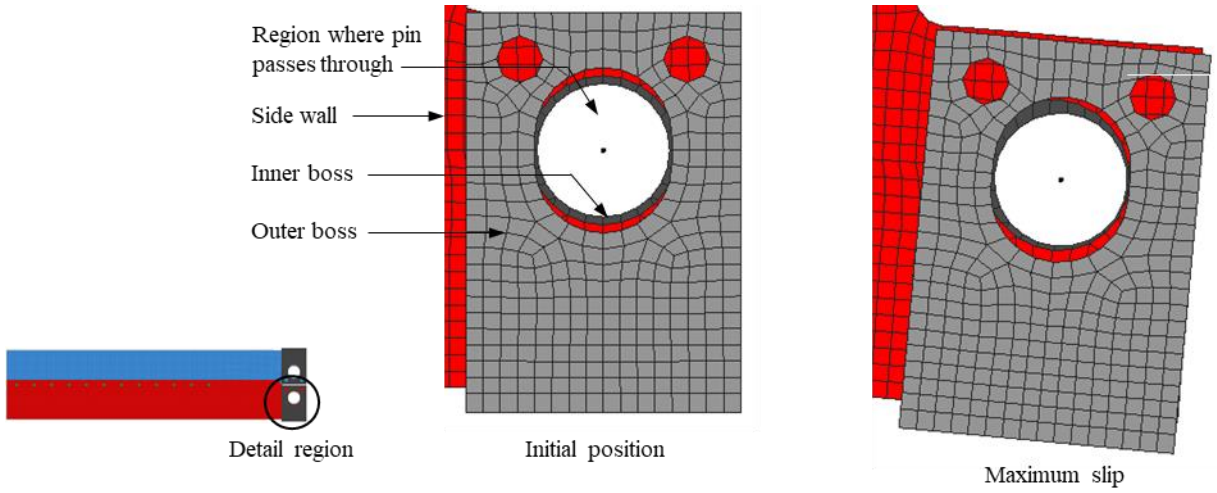

Figure 112: *Close up side view of Caiman Mode III Ductibor® 500-AS 1.6mm simulation showing side wall slippage..*

There was a concern that the simulation would not predict the same end-collapse folding behaviour that was observed in the experiments. The tied contact definitions used on the C-channels are approximately in the same locations as the MIG welds used on the actual specimens but do not have a failure condition. In Figure 114, on the left is the post-mortem image of the end of the Caiman rail for the Ductibor® 500-AS 1.2 mm quasi-static test and in the right image is the equivalent screen capture from the simulation output. The experiment and the simulation show remarkably similar folding behaviour at the end of the test. Although the shell segments that are tied to the C-channels remain tied throughout the simulation, the Ductibor® 500-AS parent metal shell elements around the tied segments fracture and are deleted. Folding that is very similar to the experiments occurs after the shell elements are deleted.

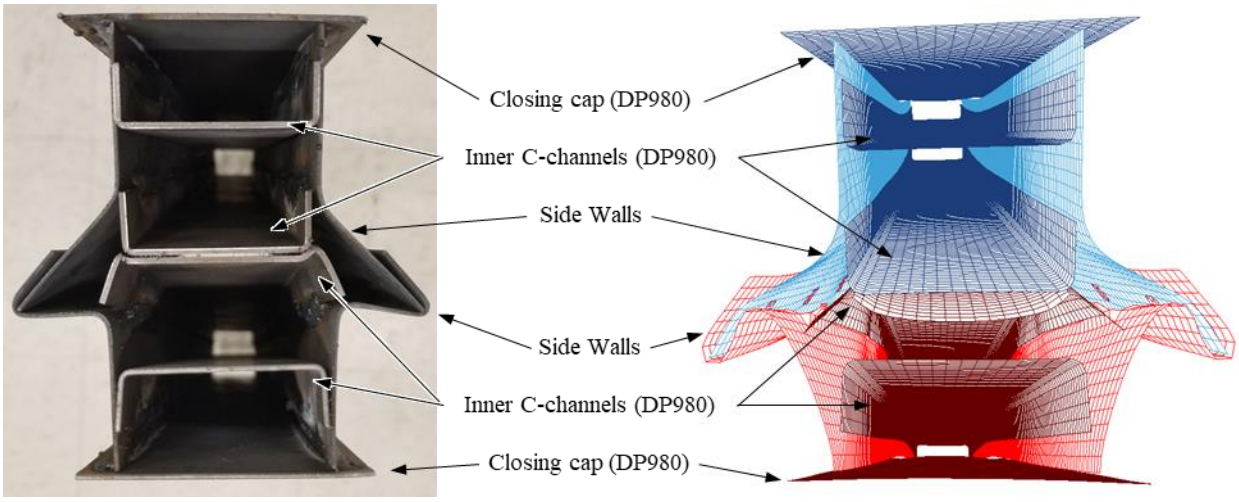

Figure 113: *End view of Ductibor® 500-AS 1.2 mm Caiman Mode III quasi-static experiment and simulation end-collapse.*

There were three concerns regarding new aspects introduced when developing the Caiman simulations, which are the side walls slipping within the rigid bosses, the uncertainty of the DP980 material constitutive model used, and the effect of tied constraints joining the DP980 parts to the side walls. None of these concerns definitively explain the differences seen between the numerical models using *MAT_240 or *MAT_100_DA weld material models and the experimental force *versus* displacement results. It is more likely that the differences between model predictions and experiments arise due to changes in spot weld strength and toughness, and corresponding changes in failure modes. As discussed in Chapter 6, changes in spot weld strength and toughness could be from spot weld quality or physical deviations from the design, or both.

6. Discussion / Analysis

In this chapter, aspects of the single spot weld characterization tests and the Caiman Mode III group weld validation tests are compared and analysed, for both the experiments and the simulations. The peak forces, total amount of energy absorbed, and weld failure modes of the single spot weld and group weld tests are examined, and any unexpected behaviour is discussed. The effects of loading rate (quasi-static *versus* dynamic) on the response of the Caiman Mode III weld group specimens is also discussed.

6.1. Comparison of single spot weld and Caiman peak forces

In Section 4.1, which describes the design of the Caiman Mode III specimen, an assumption was made that the approximate peak load that the group weld specimen would experience is at least double the peak load that was measured for the single spot weld tensile lap shear tests. In the group weld specimens, there are two spot welds that are loaded at a time while the lap shear specimens have just one spot weld. It was also possible that load sharing between multiple spot welds, as the first two welds begin to deform, would further increase the peak load. The measured peak forces from the Caiman Mode III quasi-static and dynamic experiments are compared to the peak forces in the single spot weld lap shear experiments in Table 19. The peak forces during the Caiman Mode III quasi-static experiments never reached a value of double that of the tensile lap shear experiments. Moreover, the 1.2 mm Ductibor® 1000-AS Caiman Mode III quasi-static specimens had a lower peak force than seen in the corresponding tensile lap shear specimens. The low peak force increase for the Caiman Mode III quasi-static experiments suggests the presence of poorer quality spot welds. The effects of changing loading rate are discussed in Section 6.5.

Table 19: *Average tensile lap shear peak forces and Caiman Mode III peak forces with percent differences in brackets.*

Material		Tensile Lap Shear [kN]	Caiman Mode III Quasi-Static [kN]	Caiman Mode III Dynamic [kN]
1.2 mm	Ductibor® 500-AS	14.2	21.4 (50%)	37.6 (164%)
	Ductibor® 1000-AS	16.8	14.7 (-12%)	37.1 (121%)
	Usibor® 1500-AS	13.2	16.3 (23%)	44.3 (234%)
1.6 mm	Ductibor® 500-AS	19.3	35.3 (83%)	50.1 (160%)
	Ductibor® 1000-AS	21.0	29.3 (40%)	52.4 (150%)
	Usibor® 1500-AS	26.5	33.7 (27%)	53.9 (103%)
Average % difference:			**(35%)**	**(155%)**

6.2. Comparison of single spot weld and Caiman absorbed energy

There is no direct analysis to be made by comparing the values of the total absorbed energy for the tensile lap shear experiments to that of the Caiman Mode III experiments. The Caiman Mode III specimens are fabricated using twenty-four spot welds whereas the tensile lap shear specimen has only one. There is also a large amount of work being done to deform the parent metal for the softer Ductibor® 500-AS Caiman Mode III specimens. Instead, in Figure 114 the total absorbed energy for the tensile lap shear and Caiman Mode III tests are plotted, with the lap shear values on a separate scaled axis. Overall, there is an increase in the total absorbed energy, *ie*. weld toughness, as the parent material strength decreases and the elongation increases. Comparing the Usibor® 1500-AS results to those for the Ductibor® 500-AS, there was a consistent trend for the absorbed energy to decrease, for both the single and weld group specimens, as the parent metal strength increased. The results for the Ductibor® 1000-AS samples were less consistent and, in some cases, the absorbed energy for the lap shear and/or Caiman Mode III Ductibor® 1000-AS samples was lower than that of the Usibor® 1500-AS specimens (most notably the 1.6 mm Ductibor® 1000-AS lap shear and Caiman samples and the 1.2 mm Caiman samples).

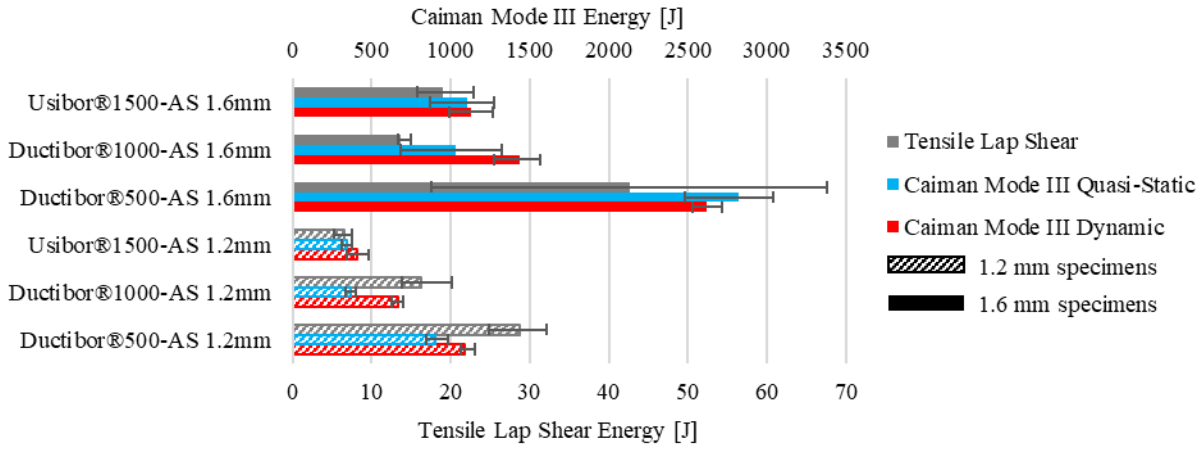

Figure 114: *Total energy absorbed for Tensile Lap Shear and Caiman Mode III experiments.*

6.3. Effects of interfacial weld failure

As mentioned, there are several aspects of the experiments that could lead to the observed deviation between the models and experimental results. In particular, it was noted for all of the Caiman Mode III specimens that there was a large amount of expulsion present (Figure 85). Expulsion can reduce the mechanical strength and toughness of the spot welds by creating stress

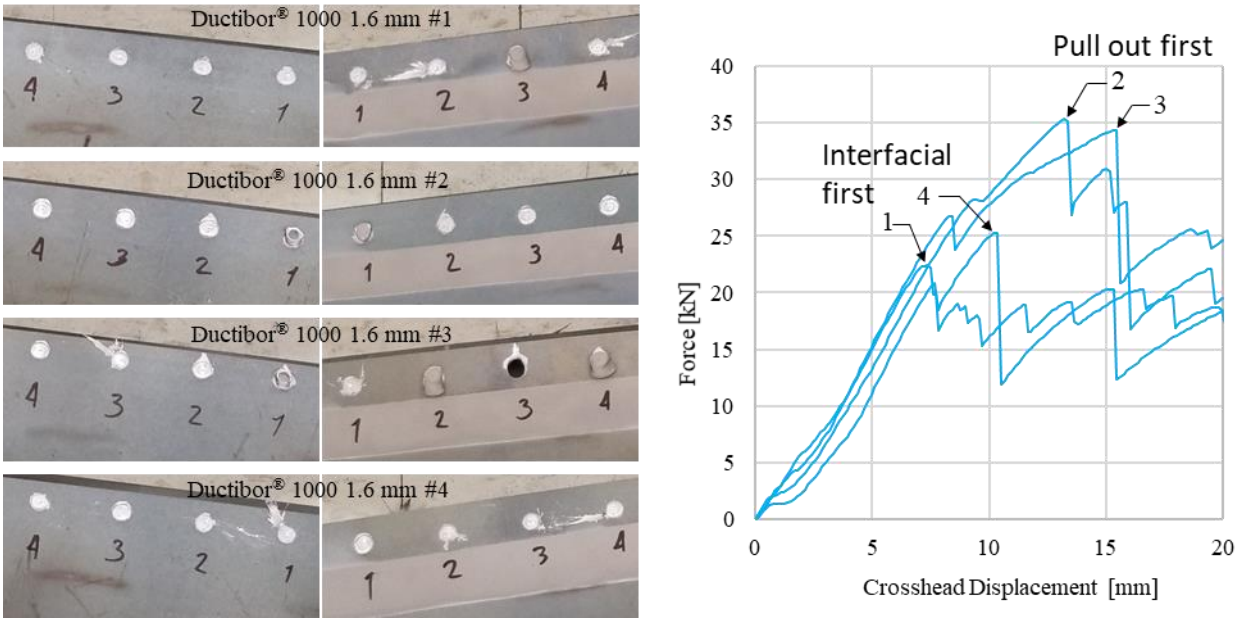

Figure 115: *Left) First to fourth spot welds post-failure for left and right sides of the Caiman Mode III Ductibor® 1000-AS 1.6 mm quasi-static specimens. Right) Corresponding experimental force versus displacement curves.*

concentrations that lead to interfacial or partial pull out failure modes. Using the Ductibor® 1000-AS 1.6 mm specimens as an example, it is shown in Figure 115 that two specimens, #1 and #4, have interfacial failure for the first spot welds on both sides. The other two specimens, #2 and #3, have at least one spot weld with pull out or tear out failure for the first spot weld. The corresponding force *versus* displacement curves exhibit significantly lower local peak loads prior to the load drops associated with each weld failure, demonstrating that interfacial failures result in lower weld strength and lower energy absorption (toughness) by the Caiman specimens. This effect of the weak and brittle interfacial failure mode it not just limited to the Ductibor® 1000-AS 1.6 mm Caiman Mode III specimens shown in Figure 115; it has been observed in many of the different experiments conducted in this work, including the single spot weld and the validation specimens.

Possible reasons for the excessive amounts of expulsion in the quasi-static Caiman Mode III samples were discussed briefly in Section 5.1.1. The spot welding process has many parameters that can affect the possibility of expulsion occurring; reducing electrode face diameter, increasing electrode force, increasing current, and increasing current cycle time can all increase the likelihood of expulsion occurring. In addition to those process parameters, there could be fixturing issues causing part misalignment which can also cause expulsion. For the Caiman Mode III specimens that were fabricated in this work, the process parameters were unchanged from the single spot weld

specimens. The expulsion also occurred across all three different materials and two different thicknesses. The single spot weld coupons had very limited expulsion, thus suggesting that the cause for expulsion may be due to a fixturing issue during the Caiman Mode III fabrication.

6.4. Spot weld nugget to edge distance

Another difference observed between the tensile lap shear and the Caiman specimens is the distance from the centre of the spot weld to the edge of the sheet. On the tensile lap shear specimens, the nugget is located 20 mm from the edge of the coupons. However, the Caiman specimens only have 10 mm from the nugget centre to the edge of the side wall components. Specifying a 10 mm nugget-to-edge spacing for the Caiman Mode III specimens was done to maintain consistency with the Caiman Mode I specimens tested by O'Keeffe [51]. The weld locations in the Caiman Mode I specimens were limited due to the size of the hat channel flanges. The flanges are not wide enough to accommodate 20 mm spacing from nugget to the edge used on the lap shear specimens, so it was reduced. While the Caiman Mode III design does not have this limitation, it was decided at the time that it was more important to keep the nugget-to-edge dimension consistent with the Mode I design. Future work should consider larger weld offset from the sheet metal edge to ascertain the effect of this design parameter.

There were also fabrication issues found on a few of the Caiman Mode III specimens. The side walls were misaligned with respect to the placement of the spot weld electrodes in the spot-welding fixture, causing some of the spot welds to be closer than 10 mm to the edge. Figure 116 shows the worst case found on a Ductibor® 1000-AS 1.6 mm specimen. Spot welds #11 and #12 are so close to the edge that the parent material was pushed outward due to the electrode clamping force and thermal softening during welding. It is not thought that the low peak force for the Caiman Mode III quasi-static specimens is caused by this particular fabrication issue since only a small number of specimens showed it and it only occurred to spot welds near the end of the rail, which did not fail before the test completed.

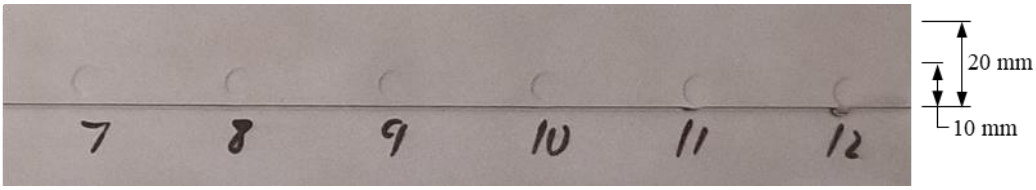

Figure 116: *Ductibor® 1000-AS 1.6 mm quasi-static specimen #4 showing worse-case spot weld nugget to edge distance.*

The reduced nugget to edge distance had a noticeable impact on the weld failure mode observed in the Caiman Mode III 1.6 mm experiments compared to the tensile lap shear 1.6 mm experiments. The Usibor® 1500-AS 1.6 mm tensile lap shear experiments and post-failure images, presented by O'Keeffe [51], show exclusively button pull out failure for this material. The Ductibor® 1000-AS 1.6 mm tensile lap shear experiments conducted in this work also show only pull out or partial pull out failure modes. In the Caiman Mode III experiments, tear out failure (shown in Figure 117) occurred in 47% of the failed spot welds for Usibor® 1500-AS 1.6 mm specimens and in 23% of the failed spot welds for Ductibor® 1000-AS 1.6 mm. The precise impact that the tear out failure has on the weld strength and toughness compared to the pull out failure mode observed in the tensile lap shear experiments is not quantified. It's also possible that the change in failure mode from pull out to tear out is because of the constraints on the material deformation that the Caiman Mode III structure introduces, and not the nugget-to-edge distance. The single spot weld tensile lap shear experiments would need to be repeated with the 10 mm nugget-to-edge spacing (versus the current 20 mm used for lap shear) that was used in the Caiman experiments to characterize the weld strength and observe if the failure mode changes to tear out.

Figure 117: *Usibor® 1500-AS 1.6 mm Caiman Mode III quasi-static specimen showing tear out failure.*

6.5. Loading rate effects in the Caiman experiments

The peak loads recorded for the quasi-static and the dynamic Caiman Mode III experiments are shown in Figure 118 (predicted values are listed in Table 19). The increased loading rate in the dynamic testing has positive strengthening effect on the peak loads for all the materials and thicknesses tested. This increase is largely attributed to inertial effects during the early stages of impact loading of the Caiman samples, but would also be due in part to the positive strain rate sensitivity of these material [4], [27], [101]. The total absorbed energy values, shown previously in Figure 114, do not show any significant strain rate effects on the weld toughness for the

Ductibor® 500-AS and Usibor® 1500-AS materials. Ductibor® 1000-AS showed an increase in total absorbed energy when comparing the quasi-static to dynamic experiments, for both material thicknesses.

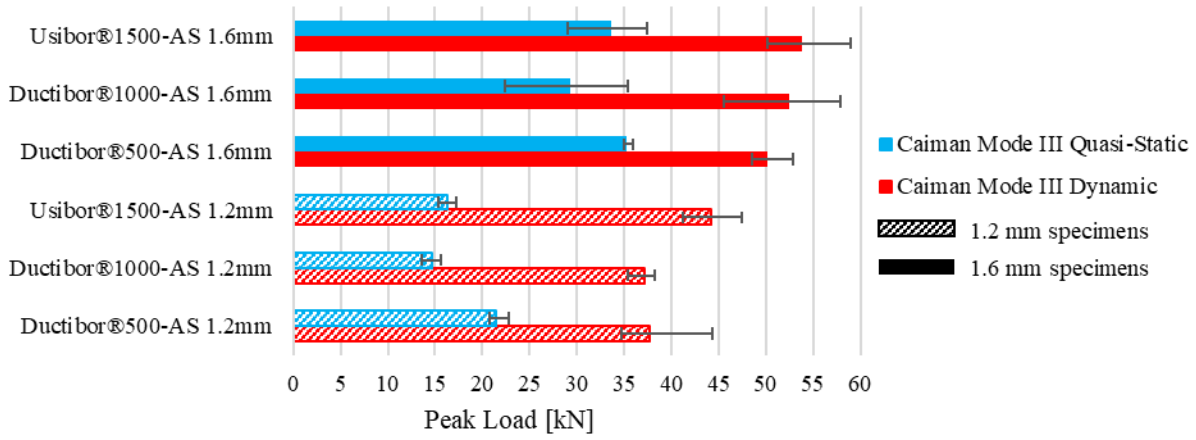

Figure 118: *Peak load data from Caiman Mode III quasi-static and dynamic experiments.*

It is thought that the increase in absorbed energy seen in the dynamic Ductibor® 1000-AS experiments was caused by the reduced number of interfacial failures observed. As previously discussed, the interfacial weld failure occurs when sudden brittle fracture propagates through the weld interface and has been shown in single spot weld testing to absorb less energy than more ductile weld failure modes, such as button pull out or tear out. The total number of weld failure types are counted for of all the Ductibor® 1000-AS Caiman specimens in Table 20. It is noted that the pull out weld failure counts include both partial pull out and full button pull out. The percentage of interfacial failure spot welds present in the 1.6 mm specimens largely decreased when comparing the quasi-static testing to the dynamic testing. However, the 1.2 mm specimens had low amounts of interfacial weld failure for both the quasi-static and the dynamic experiments, and so the proposed cause of increase in total absorbed energy due to number of interfacial failures is not supported.

Table 20: *Caiman Mode III Ductibor® 1000-AS weld failure mode count.*

Material		Interfacial		Tear out		Pull out	
		# of fails	% of total	# of fails	% of total	# of fails	% of total
1.2 mm	Ductibor® 1000-AS Quasi-static	0	0%	2	3%	78	98%
	Ductibor® 1000-AS Dynamic	8	10%	8	10%	63	80%
1.6 mm	Ductibor® 1000-AS Quasi-static	47	60%	20	26%	11	14%
	Ductibor® 1000-AS Dynamic	21	21%	32	40%	28	35%

The Caiman Mode III average ‘crack’ extension step curves from the quasi-static and dynamic testing are shown in Figure 119, Figure 120, and Figure 121, for the Ductibor® 500-AS, and Ductibor® 1000-AS, and Usibor® 1500-AS samples, respectively. There is no significant difference between the ‘crack’ propagation rate of the quasi-static and dynamic experiments fabricated from the Ductibor® 500-AS and the Usibor® 1500-AS materials. The Ductibor® 1000-AS 1.2 mm dynamic experiments had a slightly slower ‘crack’ propagation than the quasi-static experiments, identified by larger displacements for the same ‘crack’ extension measurement. The slower ‘crack’ propagation seen in the dynamic Ductibor® 1000-AS 1.2 mm experiments corresponds to the large increase in absorbed energy seen in Figure 114.

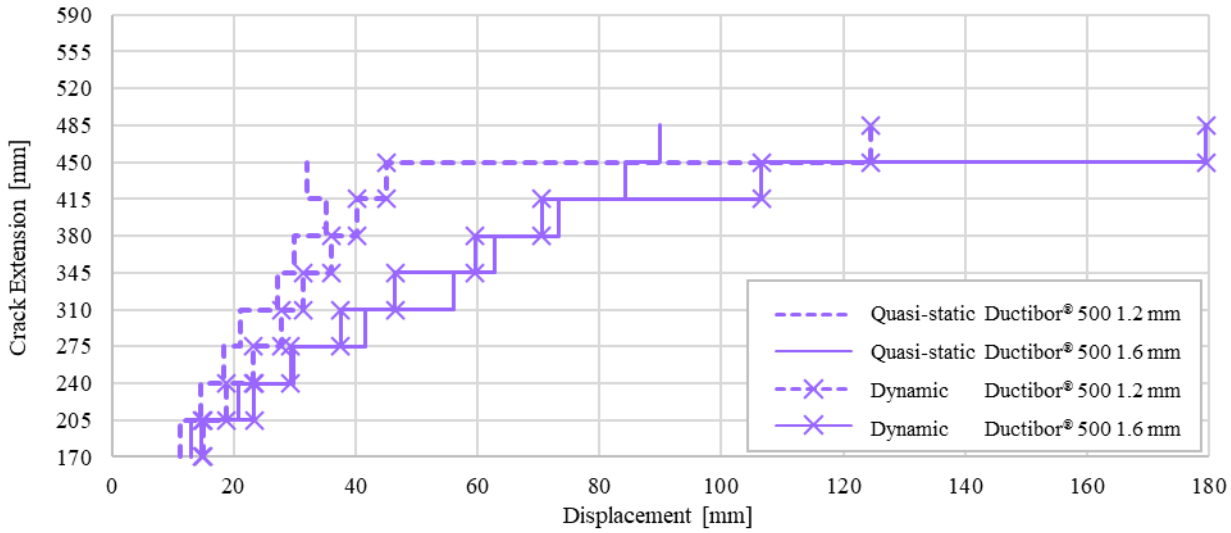

Figure 119: *Caiman Mode III Ductibor® 500-AS quasi-static and dynamic ‘crack’ extensions.*

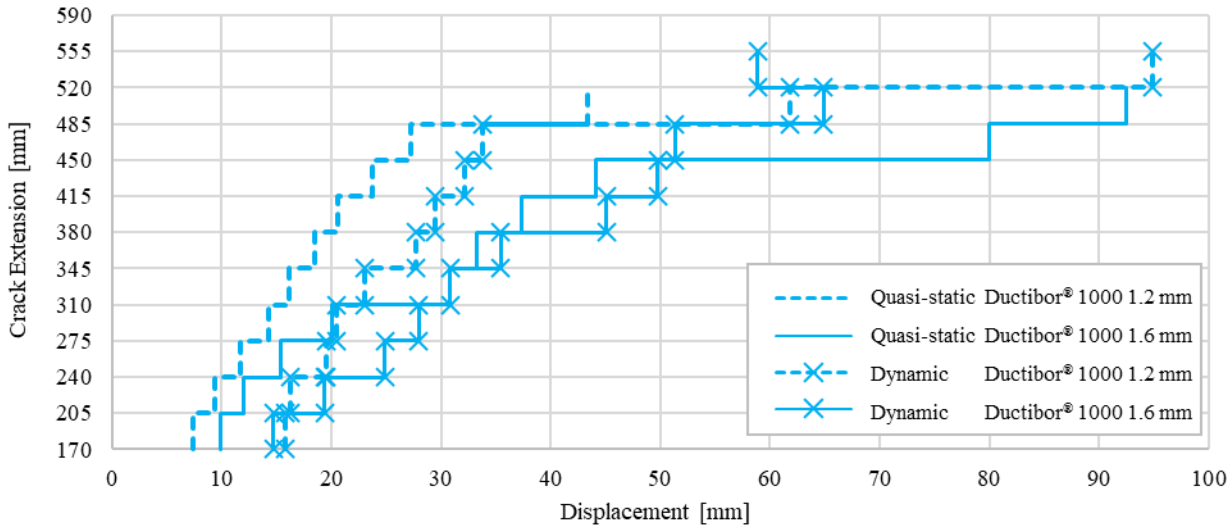

Figure 120: *Caiman Mode III Ductibor® 1000-AS quasi-static and dynamic ‘crack’ extensions.*

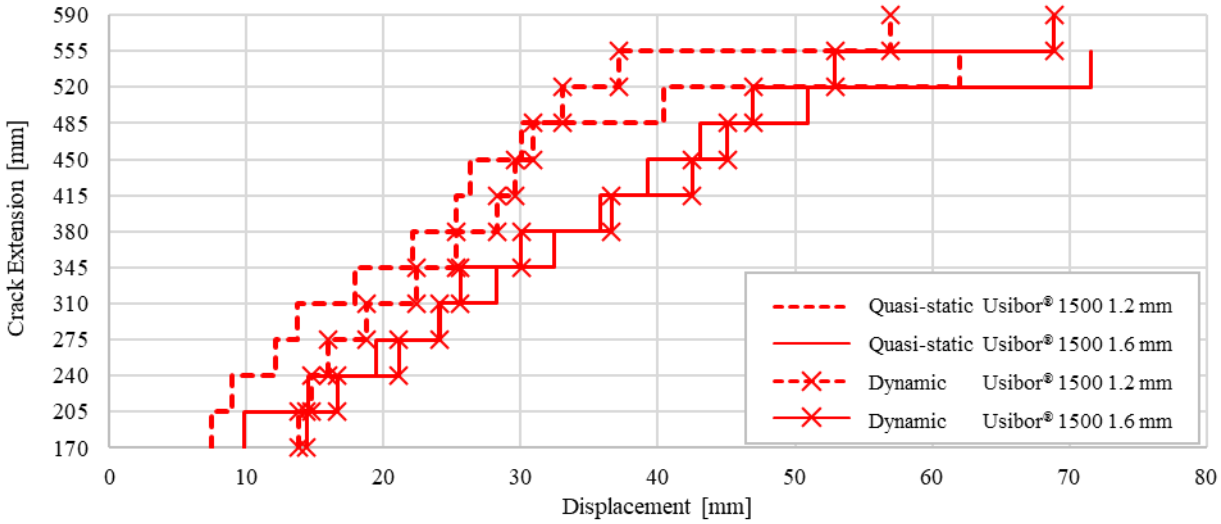

Figure 121: *Caiman Mode III Usibor® 1500-AS quasi-static and dynamic 'crack' extensions.*

7. Conclusions and recommendations

The following conclusions are made from the work presented in this thesis:

- For the three hot stamped sheet metal materials examined, Ductibor® 500-AS, Ductibor® 1000-AS, and Usibor® 1500-AS, the tensile lap shear and cross tension single spot weld experiments showed that peak weld strength and weld toughness increased with material thickness. The lap shear experiments showed similar levels of spot weld strength, around 15 kN, for all 1.2 mm specimens and approximately 20-26 kN for the 1.6 mm lap shear specimens. The cross tension experiments showed similar strength for the Ductibor® 500-AS and Ductibor® 1000-AS specimens, 7 kN for the 1.2 mm thickness and 12 kN for the 1.6 mm thickness. The peak loads for the Usibor® 1500-AS cross tension specimens were approximately 50% of the loads for the other two materials. As parent metal strength increased, and elongation decreased, the weld toughness decreased.

- Weld failure mode has a significant effect on the post-failure unloading behaviour of single spot weld coupons. Brittle weld failure modes like interfacial failure and, to an extent partial pull out, reduce the total absorbed energy by up to 50%.

- The *MAT_240 material model parameters can be determined from the measured force *versus* displacement data and examination of the specimens more easily than the *MAT_100_DA parameters. The *MAT_240 material model required less iteration to achieve a calibrated model than the *MAT_100_DA model.

- For the single spot weld tensile lap shear simulations, both the *MAT_100_DA and the *MAT_240 weld material model predictions were accurate to within 5% of the measured peak force and total absorbed energy.

- For the single spot weld cross tension simulations, the *MAT_240 material model simulations were able to accurately predict the force and total absorbed energy to within 3% and 9% of the measured values, respectively. The *MAT_100_DA model was only able to predict the peak force values to within 10% of the experiments while the absorbed energy predictions varied widely, with an average error of approximately 50%.

- The amount of energy absorbed in the single spot weld experiments post-failure varied from 0% up to 50% of the total energy, depending on the parent metal strength and weld failure mode. It was identified that predicting the post-failure energy in the weld models is critical, but that it is also difficult to accurately predict the total absorbed energy. The energy absorbed post-failure in the numerical simulations was plotted against the material keyword parameters that control the post-failure energy absorption, namely the `g1c_0` and `g2c_0` parameters for *MAT_240 and the `gfad` parameter for *MAT_100_DA. Although increasing these parameters saw an increase in the post-failure absorbed energy, the increase in absorbed energy was inconsistent and it was identified that there are other factors affecting the simulation post-failure behaviour.

- A new weld group component test termed the Caiman Mode III was developed and validated. A custom U-channel configuration, fabricated through several welding steps, was selected as the final design. The Caiman Mode III test proved useful to promote progressive failure and characterize the loads and absorbed energy for weld groups under shear loading.

- The peak force and total absorbed energy measured in the Caiman Mode III experiments increased when the material thickness increased. When the material strength increased, the peak force and the absorbed energy both tended to decrease. The energy absorbed in the static and dynamic Caiman Mode III experiments was similar, while much higher peak loads were measured in the dynamic experiments, which was attributed to inertial and strain rate hardening effects.

- Increased parent metal ductility and the occurrence of more ductile weld failure modes was shown to reduce the rate of spot weld failure propagation through the weld group.

- The numerical simulations of the Caiman Mode III experiments were able to qualitatively predict the overall behaviour of the Caiman Mode III experiments, including aspects such as high initial load followed by load drops at each sequential weld failure and load drop off, as well as progressive failure propagation through the weld group. The *MAT_240 and the *MAT_100_DA model simulations predicted similar results for each material condition simulated except for the Ductibor® 500-AS 1.6 mm model. However, the simulations were

unable to accurately predict the peak force and load-displacement history.

- Differences in the Caiman Mode III design and the single spot weld specimens led to a change in failure modes observed in the Caiman Mode III experiments that were not captured during the calibration using the single spot weld specimens. The nugget-to-edge distance in the Caiman Mode III specimens was 10 mm, half of the 20 mm used in the lap shear specimens, which led to change in failure mode, and thus weld toughness, from button pull out to tear out.

- The specified 10 mm weld offset from the sheet edge, as well as other physical inconsistencies between the design and the as-fabricated final specimens, were identified as possible reasons for the Caiman Mode III simulation inconsistencies with experiment.

The following recommendations are made for future work stemming from this thesis:

- A bending load case single spot weld test (e.g. coach peel test) should be performed to calibrate the bending term of the *MAT_100_DA material model. The *MAT_100_DA material model uses three stress parameters for failure determination, but in this work, only normal-tensile and shear stress failure parameters were calibrated. Such tests could also be used to assess the *MAT_240 model calibrations.

- KS-II specimens should be tested in the normal-tensile orientation to obtain failure loads *versus* displacement under conditions for which coupon deformation is less pronounced. It was noted during the single spot weld model calibration that the cross tension experiment displacement was dominated by coupon deformation, making it difficult to calibrate an independent weld failure model.

- Future work should consider constraining the end of the Caiman Mode III rails to prevent collapse which results in earlier arrest of weld failure propagation. Particularly for the Ductibor® 500-AS experiments, rigidly supporting the end of the rail geometry can promote propagation of failure to the last spot weld on either side but may have other (unknown) effects on the overall specimen behaviour.

- Considering that one of the Caiman Mode III Ductibor® 500-AS 1.6 mm specimens buckled, make the Caiman sections deeper to increase bending strength for cases in which the weld strength is high relative to the parent metal strength (e.g. Ductibor® 500-AS).

- The overall Caiman Mode III specimen design could be modified to remove some of the fabrication complexity such as using bolted connections to connect the sidewalls to a stiffer spine, eliminating the need to MIG weld the C-channels into place.

- Perform tensile lap shear tests with the same nugget to edge dimension as the Caiman Mode III to see if the peak forces and energy are more in line with the Caiman experiments. The nugget-to-edge distance was 10 mm for the Caiman Mode III experiments, but for the tensile lap shear experiments the distance was 20 mm. The weld models were calibrated using the 20 mm dimension and as a result could be over predicting the strength or toughness of spot welds in the Caiman experiments.

- Ensure proper fixturing of the side walls during Caiman Mode III specimen fabrication to prevent misalignment resulting in reduced nugget-to-edge distances as well as significant amount of expulsion that could affect failure modes of the spot welds.

- Improve the Caiman Mode III numerical model to be more physically accurate relative to the experimental specimens. This includes adding a clamping force on the external bosses and more accurate modelling of the MIG welds to include failure.

References

[1] Environmental Protection Agency and National Highway Traffic Safety Administration, "2017 and Later Model Year Light-Duty Vehicle Greenhouse Gas Emissions and Corporate Average Fuel Economy Standards," *Fed. Regist.*, vol. 77, no. 199, pp. 62624–63200, 2012.

[2] D. K. Matlock, J. G. Speer, E. De Moor, and P. J. Gibbs, "Recent Developments in Advanced High Strength Sheet Steels For Automotive Applications An Overview," *JESTECH*, vol. 15, no. 1, pp. 1–12, 2012.

[3] S. Keeler, M. Kimchi, and P. J. Mooney, "Advanced High-Strength Steels Apllication Guidelines Version 6.0," *WorldAutoSteel*, vol. 6, no. September, p. 314, 2017.

[4] K. Omer, L. ten Kortenaar, C. Butcher, M. Worswick, S. Malcolm, and D. Detwiler, "Testing of a hot stamped axial crush member with tailored properties – Experiments and models," *Int. J. Impact Eng.*, vol. 103, pp. 12–28, 2017, doi: 10.1016/j.ijimpeng.2017.01.003.

[5] D. D. Múnera, A. Pic, D. Abou-Khalil, F. Shmit, and F. Pinard, "Innovative press hardened steel based laser welded blanks solutions for weight savings and crash safety improvements," *SAE Int. J. Mater. Manuf.*, vol. 1, no. 1, pp. 472–479, 2009, doi: 10.4271/2008-01-1076.

[6] C. Peister, "Axial Crush Performance of Hot Stamped Tailor Welded Blanks," University of Waterloo, 2019.

[7] S. Subramaniam, R. Koganti, A. Joaquin, A. Elliott, T. Coon, and A. Wexler, "Considerations for spot welding of advanced high strength steels," *SAE Tech. Pap.*, no. 724, 2006, doi: 10.4271/2006-01-0089.

[8] Y. Lee, H. Jeong, K. Park, Y. Kim, and J. Cho, "Development of numerical analysis model for resistance spot welding of automotive steel," *J. Mech. Sci. Technol.*, vol. 31, no. 7, pp. 3455–3464, 2017, doi: 10.1007/s12206-017-0634-y.

[9] Y. B. Li, Z. Q. Lin, Q. Shen, and X. M. Lai, "Numerical analysis of transport phenomena in resistance spot welding process," *J. Manuf. Sci. Eng. Trans. ASME*, vol. 133, no. 3, pp. 1–8, 2011, doi: 10.1115/1.4004319.

[10] M. R. Rawal and K. H. Inamdar, "Review on Various Optimization Techniques used for Process Parameters of Resistance Spot Welding," *Int. J. Curr. Eng. Technol.*, no. Special Issue-3, pp. 160–164, 2014.

[11] American Honda Motor Co. Inc., "2016 Pilot : Body Repair Information," 2019.

[12] V. Tarigopula, M. Langseth, O. S. Hopperstad, and A. H. Clausen, "Axial crushing of thin-walled high-strength steel sections," *Int. J. Impact Eng.*, vol. 32, no. 5, pp. 847–882, 2006, doi: 10.1016/j.ijimpeng.2005.07.010.

[13] M. D. White and N. Jones, "Experimental quasi-static axial crushing of top-hat and double-hat thin-walled sections," *Int. J. Mech. Sci.*, vol. 41, no. 2, pp. 179–208, 1999, doi: 10.1016/S0020-7403(98)00047-2.

[14] F. Schneider and N. Jones, "Impact of thin-walled high-strength steel structural sections," *Proc. Inst. Mech. Eng. Part D J. Automob. Eng.*, vol. 218, no. 2, pp. 131–158, 2004, doi: 10.1243/095440704772913927.

[15] F. Schneider and N. Jones, "Influence of spot-weld failure on crushing of thin-walled structural sections," *Int. J. Mech. Sci.*, vol. 45, no. 12, pp. 2061–2081, 2003, doi: 10.1016/j.ijmecsci.2003.11.004.

[16] K. Mori *et al.*, "Hot stamping of ultra-high strength steel parts," *CIRP Ann. - Manuf. Technol.*, vol. 66, no. 2, pp. 755–777, 2017, doi: 10.1016/j.cirp.2017.05.007.

[17] M. Naderi, M. Ketabchi, M. Abbasi, and W. Bleck, "Analysis of microstructure and mechanical properties of different high strength carbon steels after hot stamping," *J. Mater. Process. Technol.*, vol. 211, no. 6, pp. 1117–1125, 2011, doi: 10.1016/j.jmatprotec.2011.01.015.

[18] ArcelorMittal, "Steels for hot stamping - Usibor® and Ductibor®." [Online]. Available: https://automotive.arcelormittal.com/products/flat/PHS/usibor_ductibor. [Accessed: 26-Sep-2019].

[19] W. D. Callister and D. G. Rethwisch, *Materials science and engineering: An introduction*, 8th ed. John Wiley & Sons, Inc., 2010.

[20] A. K. Sinha, “Martensite,” in *Physical Metallurgy Handbook*, 1st ed., McGraw-Hill Professional, 2002, pp. 8.3-8.17.

[21] K. A. Taylor and S. S. Hansen, “The boron hardenability effect in thermomechanically processed, direct-quenched 0.2 Pct C steels,” *Metall. Trans. A*, vol. 21, no. 6, pp. 1697–1708, 1990, doi: 10.1007/BF02672586.

[22] L. ten Kortenaar, “Failure Characterization of Hot Formed Boron Steels with Tailored Mechanical Properties,” University of Waterloo, 2016.

[23] P. Samadian, M. A. Wells, and M. J. Worswick, “Failure Characterization of Multi-Alloy and Multi-Gauge Hot-Stamped Tailor-Welded Blanks,” *IOP Conf. Ser. Mater. Sci. Eng.*, vol. 418, no. 1, 2018, doi: 10.1088/1757-899X/418/1/012082.

[24] A. Bardelcik, C. P. Salisbury, S. Winkler, M. A. Wells, and M. J. Worswick, “Effect of cooling rate on the high strain rate properties of boron steel,” *Int. J. Impact Eng.*, vol. 37, no. 6, pp. 694–702, 2010, doi: 10.1016/j.ijimpeng.2009.05.009.

[25] H. Güler, “Investigation of Usibor 1500 Formability in a Hot Forming Operation,” *Mater. Sci.*, vol. 19, no. 2, pp. 144–146, May 2013, doi: 10.5755/j01.ms.19.2.1484.

[26] M. Kang and C. Kim, “Laser welding for hot-stamped tailor-welded blanks with high-strength steel/high-energy absorption steel,” *J. Laser Appl.*, vol. 26, no. 3, p. 032007, Aug. 2014, doi: 10.2351/1.4881279.

[27] P. Samadian, M. A. Wells, and M. J. Worswick, “Constitutive Modelling of the Flow Behavior of the Different Microstructures of Ductibor®500 Steel,” in *International Conference on Impact Loading of Structures and Materials (ICILSM 2018)*, 2018, no. May, pp. 2–5.

[28] S. Sarkar, P. Drillet, M. Beauvais, N. Ramisetti, and L. Dormegny, “Ductibor 1000® AlSi: A New PHS Development for a Crash Dctility Optimization,” in *6th International Conference on Hot Sheet Metal Forming of High Performance Steel, CHS^2-2017*, 2017, pp. 591–599.

[29] D. Bhattacharya, “Microalloyed Steels for the Automotive Industry,” *Tecnol. em Metal. Mater. e Mineração*, vol. 11, no. 4, pp. 371–383, 2014, doi: 10.4322/tmm.2014.052.

[30] H. Karbasian and A. E. Tekkaya, “A review on hot stamping,” *J. Mater. Process. Technol.*, vol. 210, no. 15, pp. 2103–2118, 2010, doi: 10.1016/j.jmatprotec.2010.07.019.

[31] M. Windmann, A. Röttger, and W. Theisen, “Formation of intermetallic phases in Al-coated hot-stamped 22MnB5 sheets in terms of coating thickness and Si content,” *Surf. Coatings Technol.*, vol. 246, pp. 17–25, 2014, doi: 10.1016/j.surfcoat.2014.02.056.

[32] C. Allély, L. Dosdat, O. Clauzeau, K. Ogle, and P. Volovitch, “Anticorrosion mechanisms of aluminized steel for hot stamping,” *Surf. Coatings Technol.*, vol. 238, pp. 188–196, 2014, doi: 10.1016/j.surfcoat.2013.10.072.

[33] Z.-X. Gui, K. Wang, Y.-S. Zhang, and B. Zhu, “Cracking and interfacial debonding of the Al-Si coating in hot stamping of pre-coated boron steel,” *Appl. Surf. Sci.*, vol. 316, no. 1, pp. 595–603, 2014, doi: 10.1016/j.apsusc.2014.08.043.

[34] O. L. Ighodaro, E. Biro, and Y. N. Zhou, “Comparative effects of Al-Si and galvannealed coatings on the properties of resistance spot welded hot stamping steel joints,” *J. Mater. Process. Technol.*, vol. 236, pp. 64–72, 2016, doi: 10.1016/j.jmatprotec.2016.03.021.

[35] M. Kimchi and D. H. Phillips, *Resistance Spot Welding: Fundamentals and Applications for the Automotive Industry*, vol. 1, no. 2. 2017.

[36] American Welding Society, *AWS D8.9M:2012 - Test Method for Evaluating the Resistance Spot Welding Behavior of Automotive Sheet Steel Materials*. 2012.

[37] S. S. Babu, M. L. Santella, Z. Feng, B. W. Riemer, and J. W. Cohron, “Empirical model of effects of pressure and temperature on electrical contact resistance of metals,” *Sci. Technol. Weld. Join.*, vol. 6, no. 3, pp. 126–132, 2001, doi: 10.1179/136217101101538631.

[38] K. Zhou and L. Cai, “Study on effect of electrode force on resistance spot welding process,” *J. Appl. Phys.*, vol. 116, no. 8, 2014, doi: 10.1063/1.4893968.

[39] S. Kou, *Welding metallurgy*, 2nd ed. Hoboken, N.J.: Wiley-Interscience, 2003.

[40] H. Zhang and J. Senkara, *Resistance welding : fundamentals and applications*, 2nd ed. Boca Raton, FL: CRC Press, 2012.

[41] T. K. Eller *et al.*, “Plasticity and fracture modeling of the heat-affected zone in resistance spot welded tailor hardened boron steel,” *J. Mater. Process. Technol.*, vol. 234, pp. 309–322, Aug. 2016, doi: 10.1016/j.jmatprotec.2016.03.026.

[42] K. Kunishige, N. Uamauchi, T. Taka, and N. Nagao, “Softening in Weld Heat Affected Zone of Dual Phase Steel Sheet for Automtive Wheel Rim,” *SAE Tech. Pap. Ser.*, 1983.

[43] M. I. Khan, M. L. Kuntz, E. Biro, and Y. Zhou, “Microstructure and Mechanical Properties of Resistance Spot Welded Advanced High Strength Steels,” *Mater. Trans.*, vol. 49, no. 7, pp. 1629–1637, 2008, doi: 10.2320/matertrans.MRA2008031.

[44] V. H. Baltazar-Hernandez, S. K. Panda, Y. Okita, and N. Y. Zhou, “A study on heat affected zone softening in resistance spot welded dual phase steel by nanoindentation,” pp. 1638–1647, 2010, doi: 10.1007/s10853-009-4141-0.

[45] E. Biro, J. R. McDermid, J. D. Embury, and Y. Zhou, “Softening Kinetics in the Subcritical Heat-Affected Zone of Dual-Phase Steel Welds,” 2010, doi: 10.1007/s11661-010-0323-2.

[46] Y.-S. Jong, Y.-K. Lee, D.-C. Kim, M.-J. Kang, I.-S. Hwang, and W.-B. Lee, “Microstructural Evolution and Mechanical Properties of Resistance Spot Welded Ultra High Strength Steel Containing Boron,” *Mater. Trans.*, vol. 52, no. 6, pp. 1330–1333, 2011, doi: 10.2320/matertrans.M2011005.

[47] Y. Lu, A. Peer, T. Abke, M. Kimchi, and W. Zhang, “Subcritical heat affected zone softening in hot-stamped boron steel during resistance spot welding,” *Mater. Des.*, vol. 155, pp. 170–184, Oct. 2018, doi: 10.1016/j.matdes.2018.05.067.

[48] S. Burget and S. Sommer, “Characterization and modeling of fracture behavior of spot welded joints in hot-stamped ultra-high strength steels,” *11th LS-DYNA Forum*, 2012.

[49] A. Mohamadizadeh *et al.*, “Spot weld strength modeling and processing maps for hot-stamping steels,” *Weld. J.*, vol. 98, no. 8, pp. 241S-249S, 2019, doi: 10.29391/2019.98.021.

[50] F. Seeger, M. Feucht, T. Frank, B. Keding, and A. Haufe, “An Investigation on Spot Weld Modelling for Crash Simulation with LS-DYNA,” *4th LS-DYNA User Forum*, pp. 1–12, 2005.

[51] C. O’Keeffe, “Investigation of Resistance Spot Weld Failure in Tailored Hot Stamped Assemblies,” University of Waterloo, 2017.

[52] M. Bier and S. Sommer, “Advanced investigations on a simplified modeling method of self-piercing riveted joints for crash simulation,” *11th LS-DYNA Forum*, 2012.

[53] H. Lee and J. Choi, “Overload analysis and fatigue life prediction of spot-welded specimens using an effective J-integral,” *Mech. Mater.*, vol. 37, no. 1, pp. 19–32, Jan. 2005, doi: 10.1016/j.mechmat.2003.12.006.

[54] S. Malcolm and E. Nutwell, “Spotweld Failure Prediction using Solid Element Assemblies,” in *6th European LS-DYNA Users Conference*, 2007, pp. 47–56.

[55] A. G. Hanssen, L. Olovsson, R. Porcaro, and M. Langseth, “A large-scale finite element point-connector model for self-piercing rivet connections,” *Eur. J. Mech. A/Solids*, vol. 29, no. 4, pp. 484–495, 2010, doi: 10.1016/j.euromechsol.2010.02.010.

[56] Y. P. Yang, J. Gould, W. Peterson, F. Orth, P. Zelenak, and W. Al-Fakir, “Development of spot weld failure parameters for full vehicle crash modelling,” *Sci. Technol. Weld. Join.*, vol. 18, no. 3, pp. 222–231, Apr. 2013, doi: 10.1179/1362171812Y.0000000082.

[57] H. Ghassemi-Armaki, Q. Khan, A. Singh Gill, and S. Zilincik, “Characterization and Modeling of Spot-Weld Joints in Press Hardening Steels Associated with Softening in Heat Affected Zone,” *11th Eur. LS-DYNA Conf.*, 2017.

[58] S. Patil and H. Lankarani, “Characterisation and modelling the strength of EHSS steel grade spot weld for automotive joints and its application for frontal impact load-case,” *Int. J. Crashworthiness*, vol. 24, no. 1, pp. 13–23, Nov. 2017, doi: 10.1080/13588265.2017.1389628.

[59] X. Yang, Y. Xia, and Q. Zhou, “A simplified FE model for pull-out failure of spot welds,” *Eng. Fract. Mech.*, vol. 77, no. 8, pp. 1224–1239, May 2010, doi: 10.1016/j.engfracmech.2010.02.029.

[60] Stahlinstituts VDEh, “Testing and Documentation Guideline for the Joinability of thin sheet of steel - Part 2: Resistance Spot Welding,” *Verlag Stahleisen GmbH*, no. August, 2011.

[61] International Organization for Standardization, *ISO 18592:2019 Resistance welding - Destructive testing of welds - Method for the fatigue testing of multi-spot-welded specimens*. 2019.

[62] M. Bier, H. Klamser, and A. Haufe, “Phenomenological driven Modeling of Joints,” in *8th European LS-DYNA Conference*, 2011.

[63] M. May, H. Voß, and S. Hiermaier, “Predictive modeling of damage and failure in adhesively bonded metallic joints using cohesive interface elements,” *Int. J. Adhes. Adhes.*, vol. 49, pp. 7–17, 2014, doi: 10.1016/j.ijadhadh.2013.12.001.

[64] S. Marzi, O. Hesebeck, M. Brede, and F. Kleiner, “A Rate-Dependent, Elasto-Plastic Cohesive Zone Mixed-Mode Model for Crash Analysis of Adhesively Bonded Joints,” *7th Eur. LS-DYNA Conf.*, pp. 1–11, 2009.

[65] S. Koralla, G. B. Gadekar, V. R. P. Nadella, and S. Dey, “Spot Weld Failure Prediction in Safety Simulations Using MAT-240 Material Model in LS-DYNA,” in *SAE Technical Paper Series*, 2015, vol. 1, doi: 10.4271/2015-26-0165.

[66] Livermore Software Technology Corporation, *LS-DYNA Keyword User’s Manual - Volume I*, R:6613. 2015.

[67] Livermore Software Technology Corporation, *LS-DYNA Keyword User’s Manual - Volume II*, R:6581. 2015.

[68] J. Wang, Y. Xia, Q. Zhou, and J. Zhang, “Simulation of Spot Weld Pullout by Modeling Failure Around Nugget,” in *SAE Technical Paper Series*, 2006, no. April, doi: 10.4271/2006-01-0532.

[69] S. Dancette, D. Fabrègue, V. Massardier, J. Merlin, T. Dupuy, and M. Bouzekri, “Experimental and modeling investigation of the failure resistance of Advanced High Strength Steels spot welds,” *Eng. Fract. Mech.*, vol. 78, no. 10, pp. 2259–2272, Jul. 2011, doi: 10.1016/j.engfracmech.2011.04.013.

[70] H. Ghassemi-Armaki, E. Biro, and S. Sadagopan, “Advanced Characterization of HAZ Softening of AHSS for Crash Modeling,” *ISIJ Int.*, vol. 57, no. 8, pp. 1451–1460, 2017, doi: 10.2355/isijinternational.isijint-2016-649.

[71] S. Zhang, “Approximate stress intensity factors and notch stresses for common spot-welded specimens,” *Weld. Res. Suppl.*, vol. 78, no. 9, pp. 173-s-179-s, 1999.

[72] S. Sommer and J. Maier, “Failure modeling of a self piercing riveted joint using LS-DYNA,” *8th Eur. LS-DYNA Conf.*, 2011.

[73] Q. Khan, H. Ghassemi-armaki, A. S. Gill, S. Zilincik, and A. Gawade, “Characterization and Modeling of Spot-Weld Joints with * MAT _ 100 _ DA Parameter Optimization using LS-OPT ® , and 3 Sheet Spot-weld Modeling Method Development in LS-DYNA ®,” in *15th International LS-DYNA Users Conference*, 2018, pp. 1–16.

[74] S. Bala, “Deformable Spotwelds in LS-DYNA for Impact and NVH Applications.”

[75] Y.-L. Lee and S. Balur, “Method of Predictiong Spot Weld Failure,” US 2013/0092663 A1, 2013.

[76] S. Marzi, O. Hesebeck, M. Brede, and F. Kleiner, “A Rate-Dependent Cohesive Zone Model for Adhesively Bonded Joints Loaded in Mode I,” *J. Adhes. Sci. Technol.*, vol. 23, no. 6, pp. 881–898, 2009, doi: 10.1163/156856109X411238.

[77] S. Marzi, O. Hesebeck, M. Brede, and F. Kleiner, “An End-Loaded Shear Joint (ELSJ) Specimen to Measure the Critical Energy Release Rate in Mode II of Tough, Structural Adhesive Joints,” *J. Adhes. Sci. Technol.*, vol. 23, no. 15, pp. 1883–1891, 2009, doi: 10.1163/016942409X12508517390716.

[78] M. Bier, C. Liebold, A. Haufe, and H. Klamser, “Evaluation of a Rate-Dependent , Elasto-Plastic Cohesive Zone Mixed-Mode Constitutive Model for Spot Weld Modeling,” *9th LS-DYNA Forum*, pp. 25–38, 2010.

[79] M. Bier and S. Sommer, “Simplified modeling of self-piercing riveted joints for crash simulation with a modified version of *CONSTRAINED_INTERPOLATION_SPOTWELD,” in *9th European LS-DYNA Conference*, 2013.

[80] M. Tamizi, M. Pouranvari, and M. Movahedi, “Welding metallurgy of martensitic advanced high strength steels during resistance spot welding,” *Sci. Technol. Weld. Join.*, vol. 22, no. 4, pp. 327–335, 2017, doi: 10.1080/13621718.2016.1240979.

[81] E. Nakayama, K. Okamura, M. Miyahara, M. Yoshida, K. Fukui, and H. Fujimoto, “Prediction of Strength of Spot-Welded Joints by Measurements of Local Mechanical Properties,” in *SAE Technical Paper Series*, 2003, vol. 1, pp. 313–318, doi: 10.4271/2003-01-2830.

[82] F. Seeger, G. Michel, and M. Blanquet, “Investigation of spot weld behavior using detailed modeling technique,” *7th LS-DYNA User Forum*, pp. 29–38, 2008.

[83] K. L. Nielsen, “3D modelling of plug failure in resistance spot welded shear-lab specimens (DP600-steel),” *Int. J. Fract.*, vol. 153, no. 2, pp. 125–139, 2008, doi: 10.1007/s10704-008-9305-4.

[84] X. Kong, Q. Yang, B. Li, G. Rothwell, R. English, and X. J. Ren, “Numerical study of strengths of spot-welded joints of steel,”

Mater. Des., vol. 29, no. 8, pp. 1554–1561, 2008, doi: 10.1016/j.matdes.2007.12.001.

[85] S. Burget and S. Sommer, "Modeling of deformation and failure behavior of dissimilar resistance spot welded joints under shear, axial and combined loading conditions," *13th Int. Conf. Fract.*, 2013.

[86] S. M. Zuniga and S. D. Sheppard, "Determining the constitutive properties of the heat-affected zone in a resistance spot weld," *Model. Simul. Mater. Sci. Eng.*, vol. 3, no. 3, pp. 391–416, 1995, doi: 10.1088/0965-0393/3/3/007.

[87] A. Mohamadizadeh, E. Biro, and M. Worswick, "Failure characterization and damage modeling of resistance spot welds in ultra-high strength hot stamped steel," no. July, 2019.

[88] A. Bardelcik, M. J. Worswick, S. Winkler, and M. A. Wells, "A strain rate sensitive constitutive model for quenched boron steel with tailored properties," *Int. J. Impact Eng.*, vol. 50, pp. 49–62, 2012, doi: 10.1016/j.ijimpeng.2012.06.007.

[89] S. Dancette, V. Massardier-jourdan, D. Fabrègue, J. Merlin, T. Dupuy, and M. Bouzekri, "HAZ Microstructures and Local Mechanical Properties of High Strength Steels Resistance Spot Welds," *ISIJ Int.*, vol. 51, no. 1, pp. 99–107, 2011, doi: 10.2355/isijinternational.51.99.

[90] E. Biro *et al.*, "Predicting Transient Softening in the Sub-Critical Heat-Affected Zone of Dual-Phase and Martensitic Steel Welds," *ISIJ Int.*, vol. 53, no. 1, pp. 110–118, 2013, doi: 10.2355/isijinternational.53.110.

[91] H. Rezayat, H. Ghassemi-Armaki, S. P. Bhat, S. Sadagopan, and S. S. Babu, "Constitutive properties and plastic instabilities in the heat-affected zones of advanced high-strength steel spot welds," *J. Mater. Sci.*, vol. 54, no. 7, pp. 5825–5843, Apr. 2019, doi: 10.1007/s10853-018-03276-9.

[92] H. Tao, W. Tong, L. G. Hector, and P. D. Zavattieri, "Uniaxial tensile and simple shear behavior of resistance spot-welded dual-phase steel joints," *J. Mater. Eng. Perform.*, vol. 17, no. 4, pp. 517–534, 2008, doi: 10.1007/s11665-007-9170-8.

[93] M. Gologanu, J.-B. Leblond, G. Perrin, and J. Devaux, "Recent Extensions of Gurson's Model for Porous Ductile Metals," *Contin. Micromechanics, CISM Courses Lect. No. 377*, pp. 61–130, 1997.

[94] N. Yurioka, "Physical metallurgy of steel weldability," *ISIJ Int.*, vol. 41, no. 6, pp. 566–570, 2001.

[95] N. Yurioka, H. Suzuki, S. Ohshita, and S. Saito, "Determination of Necessary Preheating Temperature in Steel Welding.," *Weld. J. (Miami, Fla)*, vol. 62, no. 6, 1983.

[96] T. Taylor, G. Fourlaris, P. Evans, and G. Bright, "New generation ultrahigh strength boron steel for automotive hot stamping technologies," *Mater. Sci. Technol.*, vol. 30, no. 7, pp. 818–826, 2014, doi: 10.1179/1743284713Y.0000000409.

[97] F. Krajcarz, A. F. Gourgues-Lorenzon, E. Lucas, and A. Pineau, "Fracture toughness of the molten zone of resistance spot welds," *Int. J. Fract.*, vol. 181, no. 2, pp. 209–226, 2013, doi: 10.1007/s10704-013-9836-1.

[98] F. Nikoosohbat, S. Kheirandish, M. Goodarzi, M. Pouranvari, and S. P. H. Marashi, "Microstructure and failure behaviour of resistance spot welded DP980 dual phase steel," *Mater. Sci. Technol.*, vol. 26, no. 6, pp. 738–744, 2010, doi: 10.1179/174328409X414995.

[99] M. Pouranvari, A. Abedi, P. Marashi, and M. Goodarzi, "Effect of expulsion on peak load and energy absorption of low carbon steel resistance spot welds," *Sci. Technol. Weld. Join.*, vol. 13, no. 1, pp. 39–43, 2008, doi: 10.1179/174329307X249342.

[100] Y. Li, Z. Lin, A. Jiang, and G. Chen, "Use of high strength steel sheet for lightweight and crashworthy car body," *Mater. Des.*, vol. 24, no. 3, pp. 177–182, 2003, doi: 10.1016/S0261-3069(03)00021-9.

[101] A. Abedini and P. Samadian, "Private Correspondence: Constitutive Behaviour of Ductibor® 1000." 2019.

[102] T. Rahmaan, A. Abedini, C. Butcher, N. Pathak, and M. J. Worswick, "Investigation into the shear stress, localization and fracture behaviour of DP600 and AA5182-O sheet metal alloys under elevated strain rates," *Int. J. Impact Eng.*, vol. 108, pp. 303–321, 2017, doi: 10.1016/j.ijimpeng.2017.04.006.

[103] A. Bardelcik, M. J. Worswick, and M. A. Wells, "The influence of martensite, bainite and ferrite on the as-quenched constitutive response of simultaneously quenched and deformed boron steel - Experiments and model," *Mater. Des.*, vol. 55, pp. 509–525, 2014, doi: 10.1016/j.matdes.2013.10.014.

[104] A. Abedini and P. Samadian, "Private Correspondence: Constitutive Behaviour of Ductibor® 500." 2018.

[105] Z. X. Gui, W. K. Liang, and Y. S. Zhang, "Formability of aluminum-silicon coated boron steel in hot stamping process," *Trans.*

Nonferrous Met. Soc. China (English Ed., vol. 24, no. 6, pp. 1750–1757, 2014, doi: 10.1016/S1003-6326(14)63249-0.

[106] R. G. Budynas, J. K. Nisbett, and J. E. Shigley, *Shigley's Mechanical Engineering Design*, 10th ed. New York: McGraw-Hill, 2015.

[107] R. George, A. Bardelcik, and M. J. Worswick, "Hot forming of boron steels using heated and cooled tooling for tailored properties," *J. Mater. Process. Technol.*, vol. 212, no. 11, pp. 2386–2399, 2012, doi: 10.1016/j.jmatprotec.2012.06.028.

[108] K. Omer, C. Butcher, and M. Worswick, "Characterization of heat transfer coefficient for non-isothermal elevated temperature forming of metal alloys," *Int. J. Mater. Form.*, 2019, doi: 10.1007/s12289-019-01478-3.

[109] ASTM, "ASTM E408 − 13: Standard Test Methods for Total Normal Emittance of Surfaces Using Inspection-Meter Techniques," *Annu. B. ASTM Stand.*, vol. 71, no. July 1971, pp. 4–6, 1996, doi: 10.1520/E0408-13.where.

[110] Plascore, "Plascore CrushLite." [Online]. Available: https://www.plascore.com/honeycomb/energy-absorbtion/crushlite/. [Accessed: 20-Feb-2020].

[111] ASTM, *ASTM E1820-15a: Standard Test Method for Measurement of Fracture Toughness*, no. November. 2015.

[112] A. Zhumagulov *et al.*, "High Rate Characterization of Three DP980 Steels," *EPJ Web Conf.*, vol. 183, p. 02060, 2018, doi: 10.1051/epjconf/201818302060.

Appendix A

Material Card Parameters

Table 21: **MAT_100_DA material card parameters.*

Material		ro [tonne/mm³]	e [MPa]	pr	true_t [mm]
1.2 mm	Ductibor® 500	7.89E-08	5000	0.3	0.85
	Ductibor® 1000	7.89E-08	5000	0.3	0.85
	Usibor® 1500	7.89E-08	200000	0.3	0.85
1.6 mm	Ductibor® 500	7.89E-08	6000	0.3	0.85
	Ductibor® 1000	7.89E-08	8000	0.3	0.85
	Usibor® 1500	7.89E-08	200000	0.3	0.85

Table 22: **DEFINE_CONNECTION_PROPERTIES material card parameters.*

Material		sigy [MPa]	etan [MPa]	sn [MPa]	sb [MPa]	ss [MPa]	exsn	exsb	exss	gfad [mJ/mm²]
1.2 mm	Ductibor® 500	750	380	260	1.00E+14	725	1	1.00E+14	1	400
	Ductibor® 1000	780	1500	235	1.00E+14	800	1	1.00E+14	1	192
	Usibor® 1500	1200	1200	182	1.00E+14	600	1	1.00E+14	1	230
1.6 mm	Ductibor® 500	1040	750	420	1.00E+14	910	1	1.00E+14	1	500
	Ductibor® 1000	900	6000	435	1.00E+14	875	1	1.00E+14	1	120
	Usibor® 1500	1500	900	251	1.00E+14	1050	1	1.00E+14	1	290

Table 23: **MAT_240 material card parameters.*

Material		ro [tonne/mm³]	emod [MPa]	gmod [MPa]	thick [mm]	g1c_0 [mJ/mm²]	t0 [MPa]	fg1	g2c_0 [mJ/mm²]	s0 [MPa]	fg2
1.2 mm	Ductibor® 500	7.89E-09	20000	1500	1	640	285	0.01	740	555	0.05
	Ductibor® 1000	7.89E-09	2500	1500	1	400	248	0.1	535	593	0.5
	Usibor® 1500	7.89E-09	200000	2800	1	390	140	0.01	240	473	0.1
1.6 mm	Ductibor® 500	7.89E-09	2500	2000	1	640	285	0.01	740	555	0.05
	Ductibor® 1000	7.89E-09	2500	2000	1	1130	433	0.1	420	742	0.3
	Usibor® 1500	7.89E-09	200000	2400	1	470	200	0.01	6670	1040	0.1

ITEM NO.	PART NUMBER	DESCRIPTION	QTY.
1	shear_wall	SIDE WALL 1.2mm - USE WITH C-CHANNEL	4
2	shear_connector	C CHANNEL - COMMON	1
3	shear_connector	C CHANNEL - COMMON - EXTRA INTERIOR SUPPORT	1
6	shear_cap	CLOSING CAP	2
7	shear_connector	C CHANNEL 2 - FOR 1.2mm SIDE WALL	1
8	shear_connector	C CHANNEL 2 - FOR 1.2mm SIDE WALL	1

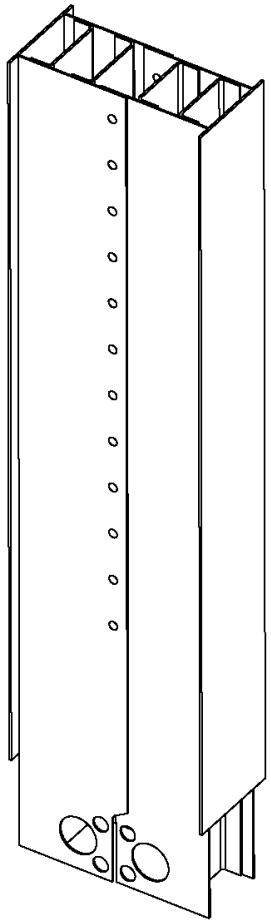

REFERENCE VIEW OF COMPLETED SPECIMEN

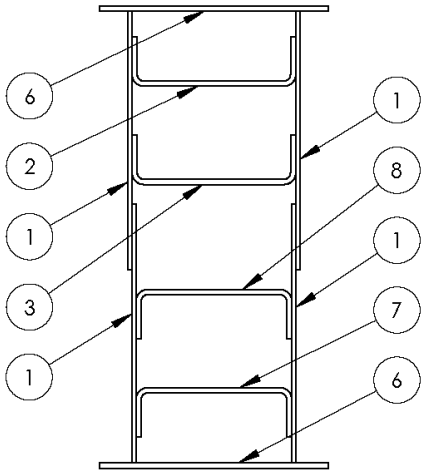

ITEM NO.	PART NUMBER	QTY	ASSEMBLY USED ON	
			1.2mm	1.6mm
1	shear_wall	4	•	•
2	shear_connector	1	•	•
3	shear_connector	1	•	•
4	shear_connector	1		•
5	shear_connector	1		•
6	shear_cap	2	•	•
7	shear_connector	1	•	
8	shear_connector	1	•	

NEXT ASSY	USED ON	
APPLICATION		DO NOT SCALE DRAWING

UNLESS OTHERWISE SPECIFIED:
DIMENSIONS ARE IN MM
TOLERANCES:
ONE PLACE DECIMAL ±0.5
TWO PLACE DECIMAL ±0.05
ANGULAR: BEND ±2
INTERPRET GEOMETRIC TOLERANCING PER:
MATERIAL
FINISH

	NAME	DATE
DRAWN	CT	2019-10-23
CHECKED		
ENG APPR.		
MFG APPR.		
Q.A.		

COMMENTS:

UNIVERSITY OF WATERLOO

TITLE:
RSW SHEAR SPECIMEN

SIZE	DWG. NO.	REV
A	shear_specimen_12final	1.7

SCALE: 1:4 | WEIGHT: | SHEET 1 OF 6

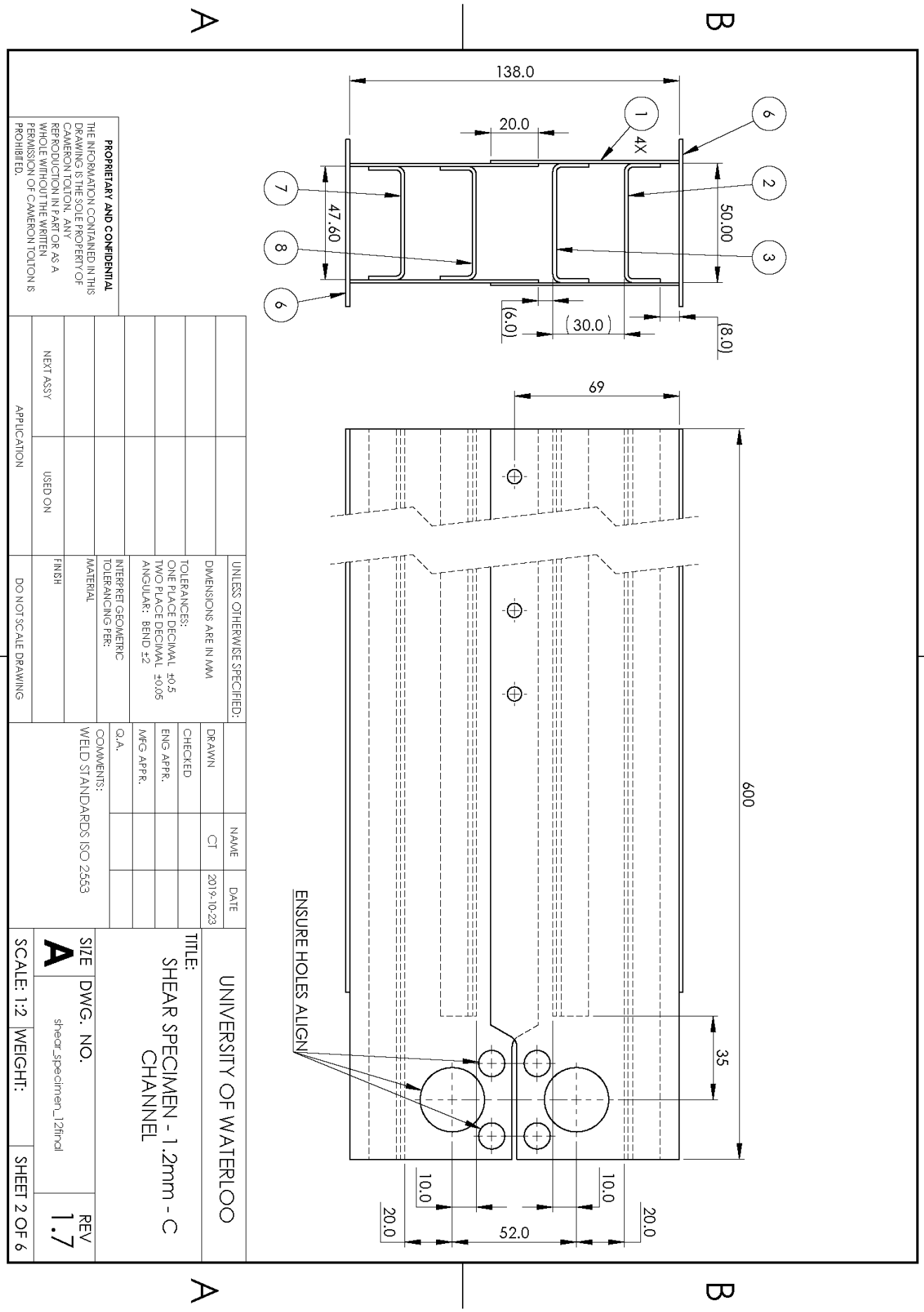
138.0
20.0
4X
50.00
47.60
(6.0)
30.0
(8.0)
69
600
35
ENSURE HOLES ALIGN
10.0
10.0
20.0
52.0
20.0
PROPRIETARY AND CONFIDENTIAL
THE INFORMATION CONTAINED IN THIS DRAWING IS THE SOLE PROPERTY OF CAMERON TOLTON. ANY REPRODUCTION IN PART OR AS A WHOLE WITHOUT THE WRITTEN PERMISSION OF CAMERON TOLTON IS PROHIBITED.
UNLESS OTHERWISE SPECIFIED:
DIMENSIONS ARE IN MM
TOLERANCES:
ONE PLACE DECIMAL ±0.5
TWO PLACE DECIMAL ±0.05
ANGULAR: BEND ±2
INTERPRET GEOMETRIC TOLERANCING PER:
MATERIAL
FINISH
DO NOT SCALE DRAWING
APPLICATION
USED ON
NEXT ASSY
NAME
DATE
DRAWN
CT
2019-10-23
CHECKED
ENG APPR.
MFG APPR.
Q.A.
COMMENTS:
WELD STANDARDS ISO 2553
UNIVERSITY OF WATERLOO
TITLE:
SHEAR SPECIMEN - 1.2mm - C CHANNEL
SIZE
A
DWG. NO.
shear_specimen_12final
REV
1.7
SCALE: 1:2
WEIGHT:
SHEET 2 OF 6

BUILD:

STEP 1) OVERLAP TWO SIDE WALLS
STEP 2) RESISTANCE SPOT WELD SHEETS TOGETHER
STEP 3) REPEAT STEPS 1-2
STEP 4) USE THE WALL CONNECTORS TO SPACE THE TWO NEW WALLS, ENSURING HOLES ALIGN
STEP 5) WELD WALL CONNECTORS INTO PLACE
STEP 6) WELD CLOSING CAPS INTO PLACE

TABLE 1: RESISTANCE SPOT WELD SCHEDULE

MATERIAL	FORCE	PRE-HEAT	MAIN WELD	HOLD TIME
ALL 1.2mm MATERIAL	770 lbf	8 kA - 33 ms	7 kA - 400 ms	200 ms

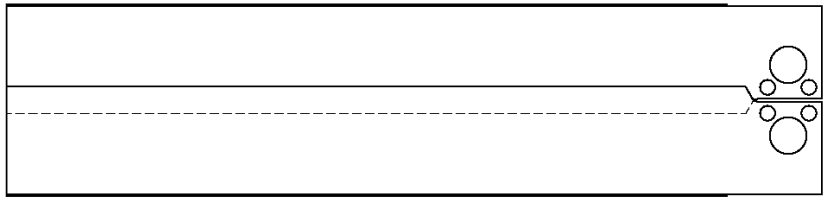

STEP 1

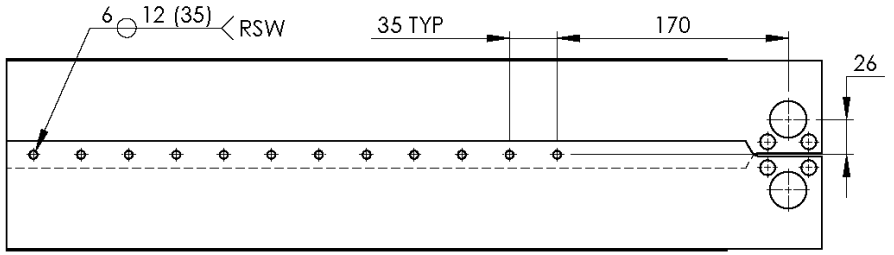

STEP 2

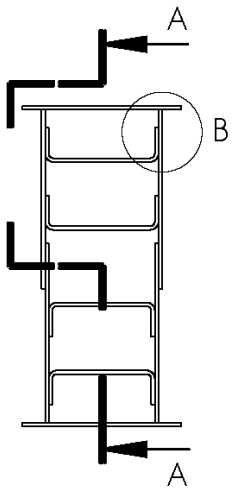

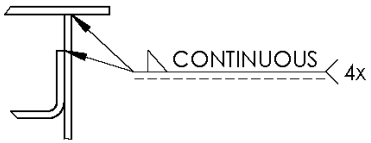

DETAIL B
SCALE 2 : 3

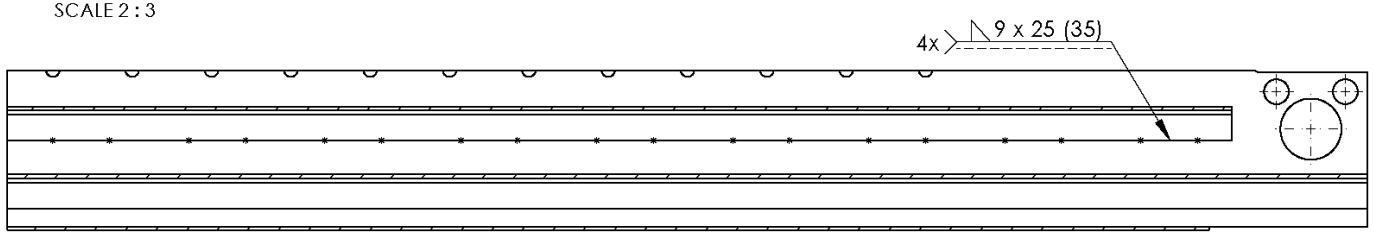

SECTION A-A
SCALE 1 : 3

STEP 5

		UNLESS OTHERWISE SPECIFIED:		NAME	DATE
		DIMENSIONS ARE IN MM TOLERANCES: ONE PLACE DECIMAL ±0.5 TWO PLACE DECIMAL ±0.05 ANGULAR: BEND ±2	DRAWN	CT	2019-10-23
			CHECKED		
			ENG APPR.		
			MFG APPR.		
		INTERPRET GEOMETRIC TOLERANCING PER:	Q.A.		
		MATERIAL	COMMENTS: WELD STANDARDS ISO 2553		
NEXT ASSY	USED ON	FINISH			
APPLICATION		DO NOT SCALE DRAWING			

UNIVERSITY OF WATERLOO

TITLE:

RSW SHEAR SPECIMEN - BUILD INSTRUCTIONS

SIZE	DWG. NO.	REV
A	shear_specimen_12final	1.7

SCALE: 1:5 | WEIGHT: | SHEET 3 OF 6

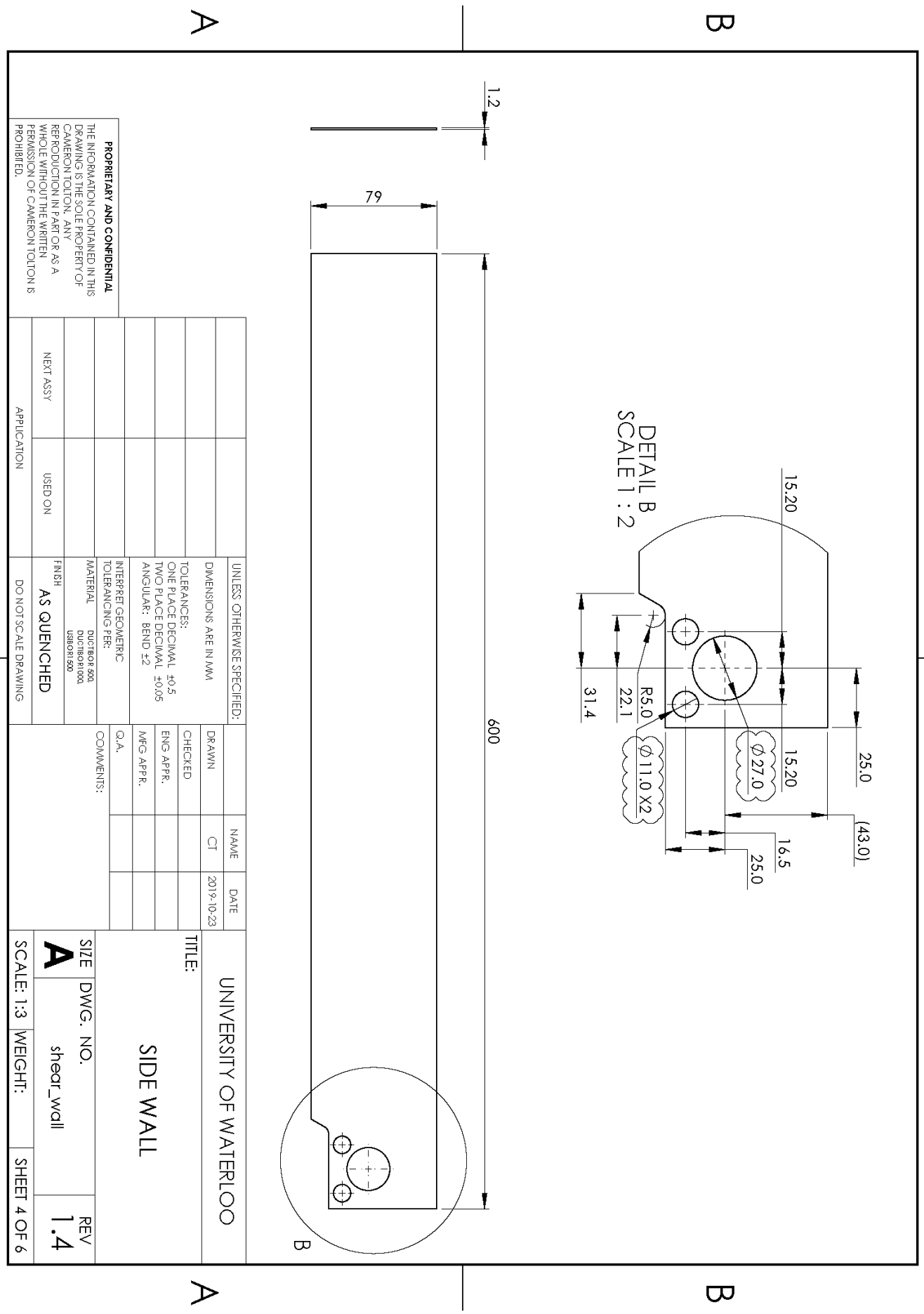
DETAIL B
SCALE 1 : 2
15.20
25.0
(43.0)
15.20
Ø27.0
16.5
25.0
R5.0
22.1
31.4
Ø11.0 X2
1.2
79
600
B
PROPRIETARY AND CONFIDENTIAL
THE INFORMATION CONTAINED IN THIS DRAWING IS THE SOLE PROPERTY OF CAMERON TOLTON. ANY REPRODUCTION IN PART OR AS A WHOLE WITHOUT THE WRITTEN PERMISSION OF CAMERON TOLTON IS PROHIBITED.
UNLESS OTHERWISE SPECIFIED:
DIMENSIONS ARE IN MM
TOLERANCES:
ONE PLACE DECIMAL ±0.5
TWO PLACE DECIMAL ±0.05
ANGULAR: BEND ±2
INTERPRET GEOMETRIC TOLERANCING PER:
MATERIAL
DUCTIBOR 500,
DUCTIBOR 1000,
USIBOR 1500
FINISH
AS QUENCHED
DO NOT SCALE DRAWING
APPLICATION
USED ON
NEXT ASSY
DRAWN
CHECKED
ENG APPR.
MFG APPR.
Q.A.
COMMENTS:
NAME
CT
DATE
2019-10-23
UNIVERSITY OF WATERLOO
TITLE:
SIDE WALL
SIZE
A
DWG. NO.
shear_wall
REV
1.4
SCALE: 1:3
WEIGHT:
SHEET 4 OF 6

ITEM NO.	CONFIGURATION NAME	DESCRIPTION	A	B	C
2	outer	C CHANNEL - COMMON	50	15	600
3	outer_offset_support	C CHANNEL - COMMON - EXTRA INTERIOR SUPPORT	50	15	540
7	inner_1.2	C CHANNEL 2 - FOR 1.2mm SIDE WALL	47.6	15	600
8	inner_1.2_offset_support	C CHANNEL 2 - FOR 1.2mm SIDE WALL	47.6	15	540

USE 1 EACH (4 TOTAL) WALL CONNECTORS TO MAKE 1 COMPLETE RSW SHEAR SPECIMEN

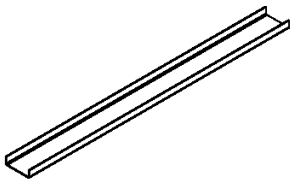

ISOMETRIC VIEW
SCALE 1:10

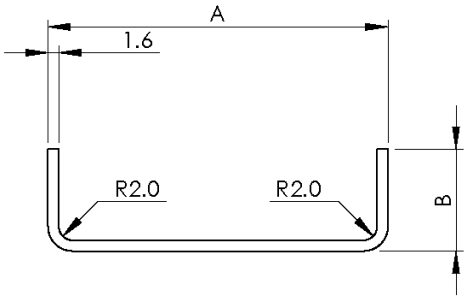

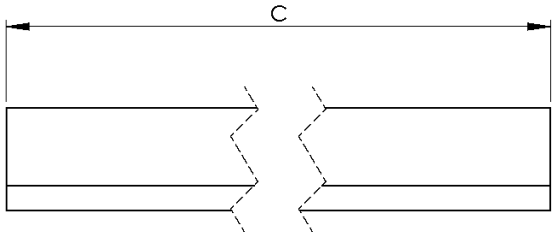

NEXT ASSY	USED ON	
APPLICATION		

UNLESS OTHERWISE SPECIFIED:
DIMENSIONS ARE IN MM
TOLERANCES:
ONE PLACE DECIMAL ±0.5
TWO PLACE DECIMAL ±0.05
ANGULAR: BEND ±2
INTERPRET GEOMETRIC TOLERANCING PER:
MATERIAL DP980
FINISH AS ROLLED
DO NOT SCALE DRAWING

	NAME	DATE
DRAWN	CT	2019-10-23
CHECKED		
ENG APPR.		
MFG APPR.		
Q.A.		

COMMENTS:

UNIVERSITY OF WATERLOO

TITLE:
WALL CONNECTOR

SIZE	DWG. NO.	REV
A	shear_connector	1.2

SCALE: 1:1 | WEIGHT: | SHEET 5 OF 6

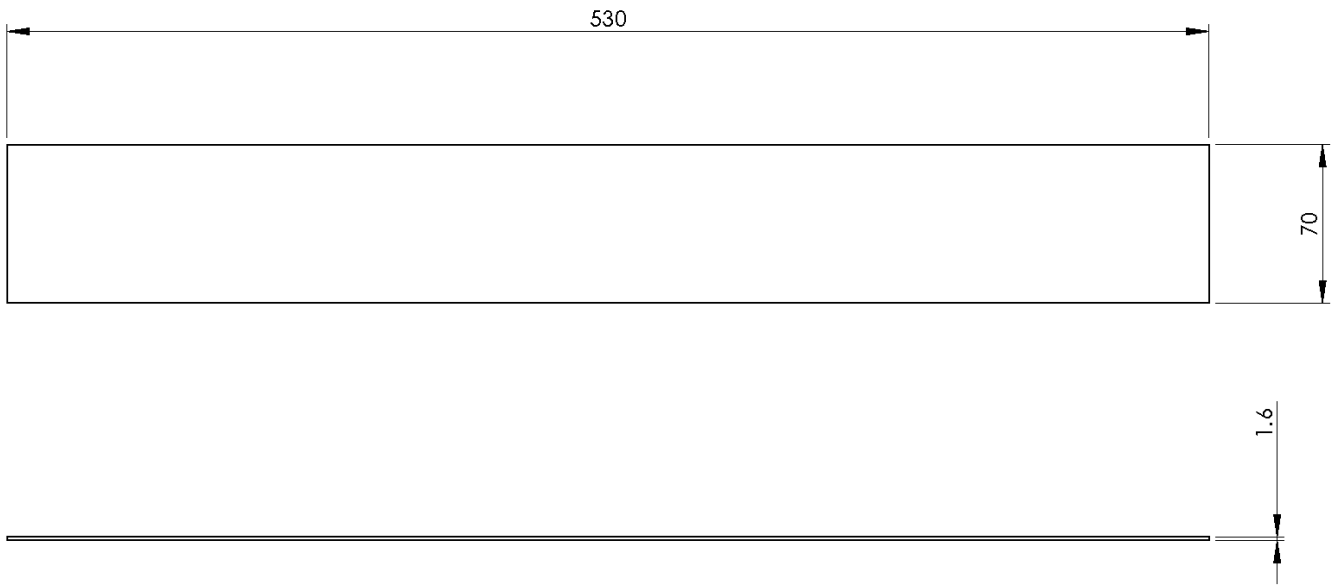

		UNLESS OTHERWISE SPECIFIED:		NAME	DATE
		DIMENSIONS ARE IN MM	DRAWN	CT	2019-01-22
		TOLERANCES: ONE PLACE DECIMAL ±0.5 TWO PLACE DECIMAL ±0.05 ANGULAR: BEND ±2	CHECKED		
			ENG APPR.		
			MFG APPR.		
		INTERPRET GEOMETRIC TOLERANCING PER:	Q.A.		
		MATERIAL DP 980	COMMENTS:		
NEXT ASSY	USED ON	FINISH AS ROLLED			
APPLICATION		DO NOT SCALE DRAWING			

UNIVERSITY OF WATERLOO

TITLE:

CLOSING CAP

SIZE	DWG. NO.	REV
A	shear_cap	1.0
SCALE: 1:3	WEIGHT:	SHEET 6 OF 6

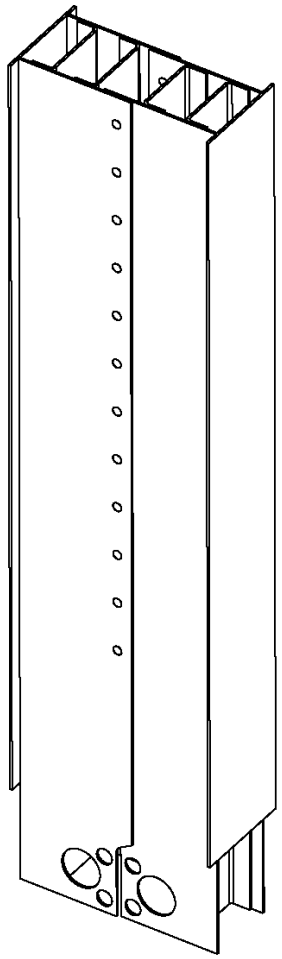

REFERENCE VIEW OF COMPLETED SPECIMEN

ITEM NO.	PART NUMBER	DESCRIPTION	QTY.
1	shear_wall	SIDE WALL 1.6mm - USE WITH C-CHANNEL	4
2	shear_connector	C CHANNEL - COMMON	1
3	shear_connector	C CHANNEL - COMMON - EXTRA INTERIOR SUPPORT	1
4	shear_connector	C CHANNEL 2 - FOR 1.6mm SIDE WALL	1
5	shear_connector	C CHANNEL 2 - FOR 1.6mm SIDE WALL - EXTRA INTERIOR SUPPORT	1
6	shear_cap	CLOSING CAP	2

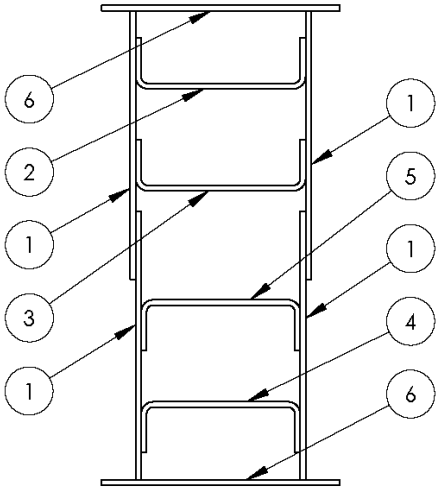

ITEM NO.	PART NUMBER	QTY	ASSEMBLY USED ON	
			1.2mm	1.6mm
1	shear_wall	4	•	•
2	shear_connector	1	•	•
3	shear_connector	1	•	•
4	shear_connector	1		•
5	shear_connector	1		•
6	shear_cap	2	•	•
7	shear_connector	1	•	
8	shear_connector	1	•	

NEXT ASSY	USED ON	
APPLICATION		

UNLESS OTHERWISE SPECIFIED:

DIMENSIONS ARE IN MM

TOLERANCES:
ONE PLACE DECIMAL ±0.5
TWO PLACE DECIMAL ±0.05
ANGULAR: BEND ±2

INTERPRET GEOMETRIC TOLERANCING PER:

MATERIAL

FINISH

DO NOT SCALE DRAWING

	NAME	DATE
DRAWN	CT	2019-10-23
CHECKED		
ENG APPR.		
MFG APPR.		
Q.A.		

COMMENTS:

UNIVERSITY OF WATERLOO

TITLE:

RSW SHEAR SPECIMEN

SIZE	DWG. NO.	REV
A	shear_specimen_16final	1.7

SCALE: 1:4 | WEIGHT: | SHEET 1 OF 6

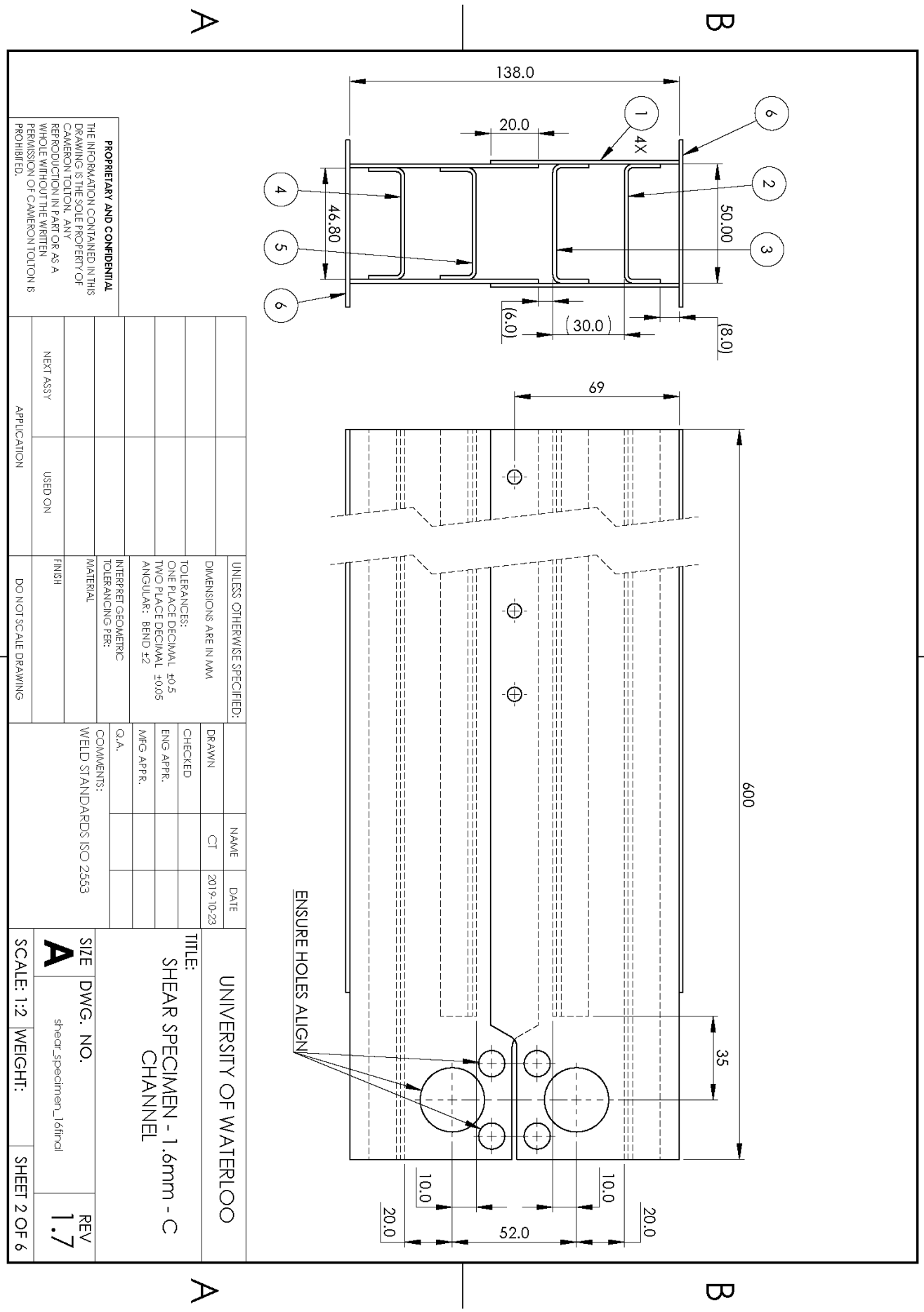
138.0
20.0
4X
50.00
46.80
(6.0)
30.0
(8.0)
69
600
35
ENSURE HOLES ALIGN
10.0
10.0
20.0
52.0
20.0
PROPRIETARY AND CONFIDENTIAL
THE INFORMATION CONTAINED IN THIS DRAWING IS THE SOLE PROPERTY OF CAMERON TOLTON. ANY REPRODUCTION IN PART OR AS A WHOLE WITHOUT THE WRITTEN PERMISSION OF CAMERON TOLTON IS PROHIBITED.
UNLESS OTHERWISE SPECIFIED:
DIMENSIONS ARE IN MM
TOLERANCES:
ONE PLACE DECIMAL ±0.5
TWO PLACE DECIMAL ±0.05
ANGULAR: BEND ±2
INTERPRET GEOMETRIC TOLERANCING PER:
MATERIAL
FINISH
DO NOT SCALE DRAWING
APPLICATION
USED ON
NEXT ASSY
DRAWN
CT
2019-10-23
CHECKED
ENG APPR.
MFG APPR.
Q.A.
COMMENTS:
WELD STANDARDS ISO 2553
UNIVERSITY OF WATERLOO
TITLE:
SHEAR SPECIMEN - 1.6mm - C CHANNEL
SIZE
A
DWG. NO.
shear_specimen_16final
REV
1.7
SCALE: 1:2
WEIGHT:
SHEET 2 OF 6

BUILD:

STEP 1) OVERLAP TWO SIDE WALLS
STEP 2) RESISTANCE SPOT WELD SHEETS TOGETHER
STEP 3) REPEAT STEPS 1-2
STEP 4) USE THE WALL CONNECTORS TO SPACE THE TWO NEW WALLS, ENSURING HOLES ALIGN
STEP 5) WELD WALL CONNECTORS INTO PLACE
STEP 6) WELD CLOSING CAPS INTO PLACE

TABLE 1: RESISTANCE SPOT WELD SCHEDULE

MATERIAL	FORCE	PRE-HEAT	MAIN WELD	HOLD TIME
1.6 mm Ductibor500/1000	900 lbf	10 kA - 33 ms	7 kA - 400 ms	200 ms
1.6 mm Usibor1500	770 lbf	10 kA - 33 ms	8 kA - 500 ms	200 ms

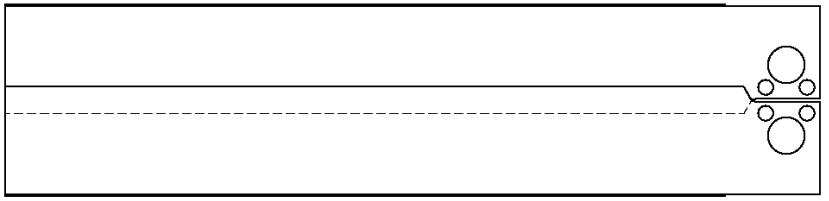

STEP 1

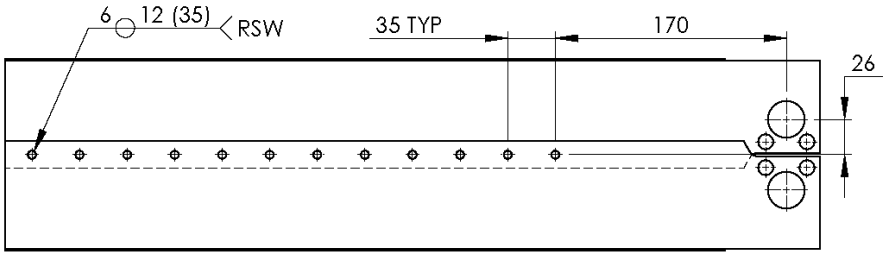

STEP 2

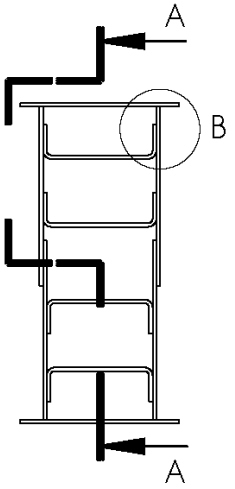

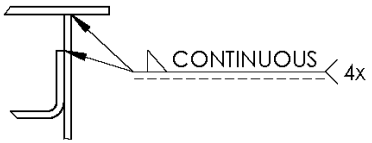

DETAIL B
SCALE 2 : 3

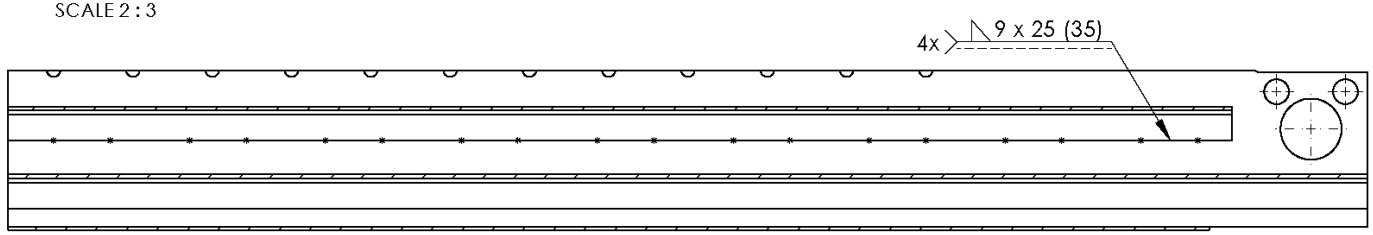

SECTION A-A
SCALE 1 : 3

STEP 5

		UNLESS OTHERWISE SPECIFIED:		NAME	DATE
		DIMENSIONS ARE IN MM	DRAWN	CT	2019-10-23
		TOLERANCES: ONE PLACE DECIMAL ±0.5 TWO PLACE DECIMAL ±0.05 ANGULAR: BEND ±2	CHECKED		
			ENG APPR.		
			MFG APPR.		
		INTERPRET GEOMETRIC TOLERANCING PER:	Q.A.		
		MATERIAL	COMMENTS: WELD STANDARDS ISO 2553		
NEXT ASSY	USED ON	FINISH			
APPLICATION		DO NOT SCALE DRAWING			

UNIVERSITY OF WATERLOO

TITLE:

RSW SHEAR SPECIMEN - BUILD INSTRUCTIONS

SIZE	DWG. NO.	REV
A	shear_specimen_16final	1.7

SCALE: 1:5 | WEIGHT: | SHEET 3 OF 6

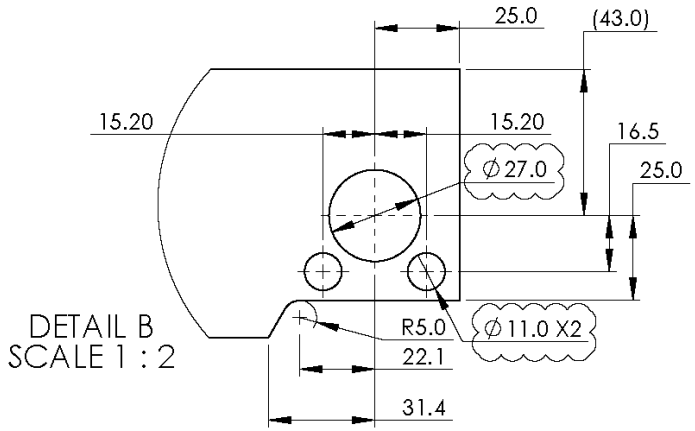

DETAIL B
SCALE 1 : 2

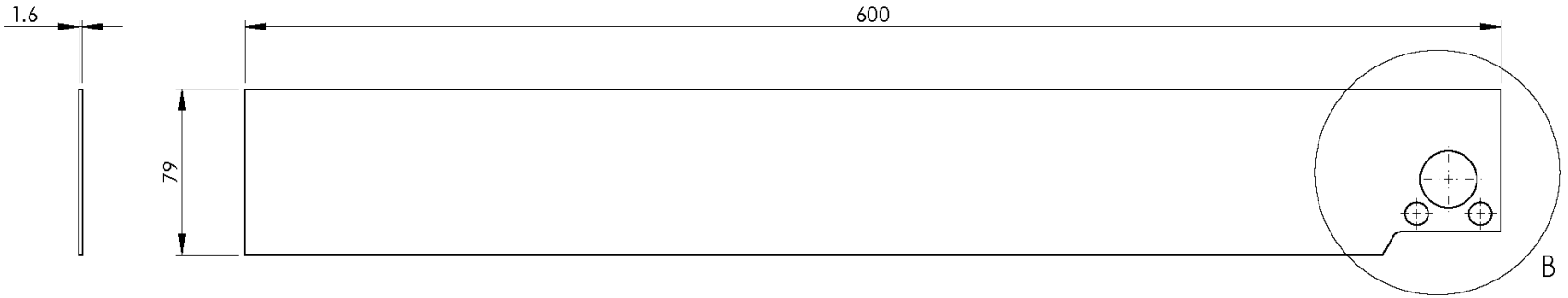

		UNLESS OTHERWISE SPECIFIED:		NAME	DATE
		DIMENSIONS ARE IN MM TOLERANCES: ONE PLACE DECIMAL ±0.5 TWO PLACE DECIMAL ±0.05 ANGULAR: BEND ±2	DRAWN	CT	2019-10-23
			CHECKED		
			ENG APPR.		
			MFG APPR.		
		INTERPRET GEOMETRIC TOLERANCING PER:	Q.A.		
		MATERIAL DUCTIBOR 500, DUCTIBOR1000, USIBOR1500	COMMENTS:		
NEXT ASSY	USED ON	FINISH AS QUENCHED			
APPLICATION		DO NOT SCALE DRAWING			

UNIVERSITY OF WATERLOO

TITLE:

SIDE WALL

SIZE	DWG. NO.	REV
A	shear_wall	1.4

SCALE: 1:3 | WEIGHT: | SHEET 4 OF 6

ITEM NO.	CONFIGURATION NAME	DESCRIPTION	A	B	C
2	outer	C CHANNEL - COMMON	50	15	600
3	outer_offset_support	C CHANNEL - COMMON - EXTRA INTERIOR SUPPORT	50	15	540
4	inner_1.6	C CHANNEL 2 - FOR 1.6mm SIDE W ALL	46.8	15	600
5	inner_1.6_offset_support	C CHANNEL 2 - FOR 1.6mm SIDE W ALL - EXTRA INTERIOR SUPPORT	46.8	15	540

USE 1 EACH (4 TOTAL) WALL CONNECTORS TO MAKE 1 COMPLETE RSW SHEAR SPECIMEN

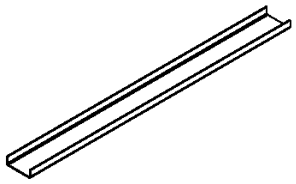

ISOMETRIC VIEW
SCALE 1:10

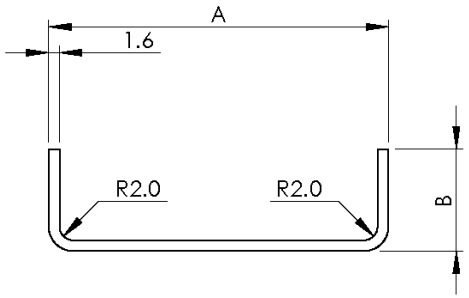

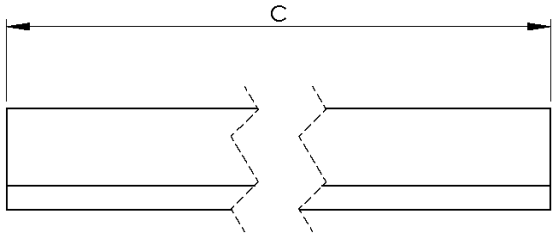

NEXT ASSY	USED ON	
APPLICATION		

UNLESS OTHERWISE SPECIFIED:
DIMENSIONS ARE IN MM
TOLERANCES:
ONE PLACE DECIMAL ±0.5
TWO PLACE DECIMAL ±0.05
ANGULAR: BEND ±2
INTERPRET GEOMETRIC TOLERANCING PER:
MATERIAL DP980
FINISH AS ROLLED
DO NOT SCALE DRAWING

	NAME	DATE
DRAWN	CT	2019-10-23
CHECKED		
ENG APPR.		
MFG APPR.		
Q.A.		

COMMENTS:

UNIVERSITY OF WATERLOO

TITLE:
WALL CONNECTOR

SIZE	DWG. NO.	REV
A	shear_connector	1.2

SCALE: 1:1 | WEIGHT: | SHEET 5 OF 6

		UNLESS OTHERWISE SPECIFIED:		NAME	DATE
		DIMENSIONS ARE IN MM	DRAWN	CT	2019-01-22
		TOLERANCES: ONE PLACE DECIMAL ±0.5 TWO PLACE DECIMAL ±0.05 ANGULAR: BEND ±2	CHECKED		
			ENG APPR.		
			MFG APPR.		
		INTERPRET GEOMETRIC TOLERANCING PER:	Q.A.		
		MATERIAL DP 980	COMMENTS:		
NEXT ASSY	USED ON	FINISH AS ROLLED			
APPLICATION		DO NOT SCALE DRAWING			

UNIVERSITY OF WATERLOO

TITLE:

CLOSING CAP

SIZE	DWG. NO.	REV
A	shear_cap	1.0

SCALE: 1:3	WEIGHT:	SHEET 6 OF 6